5-22-2006

Fluctuations, Phase Separation and Wetting Films near Liquid-Gas Critical Point

Ana Oprisan
University of New Orleans

FLUCTUATIONS, PHASE SEPARATION, AND WETTING FILMS NEAR LIQUID-GAS
CRITICAL POINT

A Dissertation

Submitted to the Graduate Faculty of the
University of New Orleans
in partial fulfillment of the
requirements for the degree of

Doctor of Philosophy
in
Engineering and Applied Science

by

Ana Oprisan

B.S. "Alexandru Ioan Cuza" University of Iasi, Romania, 1987
M.S. University of New Orleans, 2003

May 2006

Acknowledgements

Many people have inspired, guided, and helped me during my tenure as a doctoral student, and I would like to thank them all for a great graduate school experience. First and foremost I would like to thank my advisor, Dr. John Hegseth, for his supervision as my advisor throughout the time it took me to complete this research and write the dissertation. He challenged my thinking, writing and research skills and served as a teaching mentor and a role model. Without his insightful direction, many of the results presented here would not have been possible.

My dissertation committee deserves recognition for their time, valuable suggestions and support: Dr. Juliette Ioup for her continuous support and her willingness to read and make constructive suggestions during my research on this dissertation. I am grateful to her for that, for all the hours of consultation, suggestions enthusiasm and professionalism; Dr. Dimitrios Charalampidis for generously giving his time and expertise to better my work; Dr. Joseph Murphy for his insight and sound advise through this entire research; Dr. Jinke Tang for his kind words of support during my dissertation work; and Dr. Ralph Saxton for his help and support during my research.

I must acknowledge as well the many friends and colleagues that assisted and supported during my research and studies over the years. My special thanks go to our fiends Mrs. Kelly and Mr. Pavlos Petrou, Mrs. Yota and Mr. Sam Nicholopoulos for their optimism, friendship, hospitality and for always inspiring me with their advice. I am also grateful for the support and wisdom of Mrs. Diane and Mr. Nick Chronis during my graduate school at UNO. Furthermore I am grateful to my good friends Madalina and Costin Barbu for their friendship and support during my graduate work. My special thanks go to Maria and Coco Trusca for their hospitality and friendship. I am deeply indebted to Reverend Father Anthony Stratis, the Dean of the Holy Trinity Greek Orthodox Cathedral of New Orleans and to his wife Elenni for their friendship, hospitality and support.

My special thanks go to Dr. Seab, the Chair of the Physics Department, for the support he provided over the past years. I would like to extend my special thanks also to Mrs. Sandra Merz for making my studying at UNO a valuable life learning experience.

I am very grateful to Dr. Jeff Wragg from College of Charleston who took time from his busy schedule to revue the manuscript of the dissertation.

This dissertation is a result of a lifelong process of learning that has been difficult without the assistance, encouragements and moral support from my family, and my friends, from Romania.

Last, but far from least, I would like to express my deepest thanks to my husband Sorinel Oprisan for his continued support during the writing of this dissertation and to our children, Andra and Andrei Oprisan, who have been my greatest source of inspiration.

The strength of my family has been a tremendous boost to me. In recognition of this, I would like to dedicate this dissertation to my mother Aneta Tabirnac who passed away while I was in college 20 years ago. Her determination, personal strength and devotion have been passed on from generation to generation through the eternal power of love.

Table of Contents

Abstract

Gravity on Earth limits the study of the properties of pure fluids near critical point because they become stratified under their own weight. Near the critical point, all thermodynamic properties either diverge or converge and the heating and cooling cause instabilities of the convective flow as a consequence of the expansibility divergence.

In order to study boiling, fluctuation and phase separation processes near the critical point of pure fluids without the influence of the Earth's gravity, a number of experiments were performed in the weightlessness of Mir space station. The experimental setup called ALICE II instrument was designed to suppress sedimentation and buoyancy-driven flow. Another set of experiments were carried out on Earth using a carefully density matched system of deuterated methanol-cycloxexane to observe critical fluctuations directly.

The set of experiments performed on board of Mir space station studied boiling and wetting film dynamics during evaporation near the critical point of two pure fluids (sulfur hexafluoride and carbon dioxide) using a defocused grid method. The specially designed cell containing the pure fluid was heated and, as a result, a low contrast line appeared on the wetting film that corresponded to a sharp change in the thickness of the film. A large mechanical response was observed in response to the cell heating and we present quantitative results about the receding contact lines. It is found that the vapor recoil force is responsible for the receding contact line.

Local density fluctuations were observed by illuminating a cylindrical cell filled with the pure fluid near its liquid- gas critical point and recorded using a microscope and a video recorder. Microscopic fluctuations were analyzed both in sulfur hexafluoride and in a binary mixture of methanol cyclohexane. Using image processing techniques, we were able to estimate the properties of the fluid from the recorded images showing fluctuations of the transmitted and scattered light. We found that the histogram of an image can be fitted to a Gaussian relationship and by determining its width we were able to estimate the position of the critical point. The characteristic length of the fluctuations corresponding to the maximum of the radial average of the power spectrum was also estimated. The power law growth for the early stage of the phase separation was determined for two different temperature quenches in pure fluid and these results are in agreement with other experimental results and computational simulations.

1. Introduction

1.1.   Critical phenomena and critical exponents

In science, the word "critical" has different meanings. In this study, by "critical phenomena" we refer to phase transitions. The physical systems in this area are characterized by large susceptibility and strong correlation among the constituents. A characteristic of critical phenomena is the fact that simple laws acting at the microscopic level can produce complex macroscopic changes characterized by long-range correlation and self-similarity. Critical phenomena reveal cooperative behaviors resulting from multiple interactions between "microscopic" elements that construct a "macroscopic" self-similar state.

Gravity on Earth limits the study of pure fluids near the critical point because the compressibility diverges and fluids become stratified under their own weight. As a result, a bulk sample at critical point cannot be obtained on Earth, and any measured property is an averaged value rather than the local or instantaneous value of that property at the critical point [Moldover *et al.*, 1987; Beysens *et al.*, 1990]. In addition to gravitational stratification of fluids, convection instabilities determined by the divergence of expansibility near the critical temperature limits the accuracy of measurements. To overcome the aforementioned limitations, new experiments with fluids near the critical point were performed in microgravity [Moldover *et al.*, 1976]. The term "near-critical" refers to a region within a few tens of mK of the critical temperature, T_C. The liquid-vapor critical point is associated with a second order phase transition, meaning that the density varies continuously as the temperature changes.

The critical point (CP) is the terminal point on a line representing the fusion curve. Its coordinates are of the form (P_C, T_C, ρ_C), where P_C is the critical pressure, T_C is the critical temperature, and ρ_C is the critical density. Our study focuses on pure fluids for which a typical phase diagram is represented in Figure 1.1.1. Above the CP, only one phase exists; below the CP, both the gas and liquid phases coexist. Examples of similar phase diagrams are found for binary liquid mixtures and in the ferromagnetic-paramagnetic transition for iron at the Curie temperature [Stanley, 1971]. At low temperatures, there is a big difference between the liquid and gas densities ρ_L and ρ_G, but as the critical point is approached the difference vanishes.

The order parameter, introduced by Landau in 1937 [Landau *et al.*, 1969], is a useful tool to describe phase transition. For a pure fluid, the order parameter is described by:

$$\phi = (\rho - \rho_c)/\rho_c. \tag{1.1.1}$$

For a binary liquid mixture, the order parameter corresponds to the difference in concentration and is defined by:

$$\phi = c - c_c, \tag{1.1.2}$$

where c is the concentration of one of the two substances (A or B) and c_c is the corresponding concentration at the critical point.
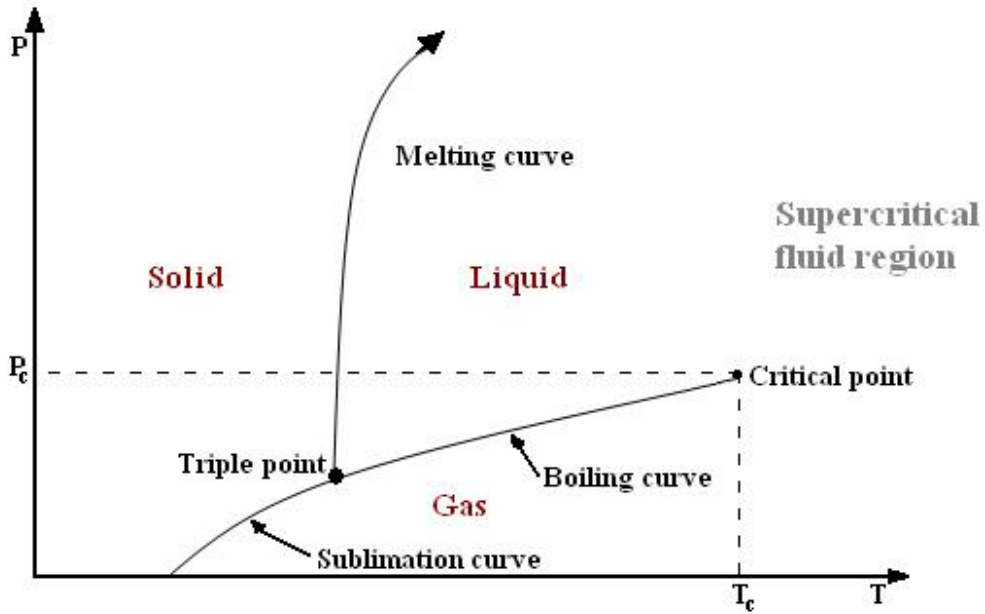
Figure 1.1.1. Generic phase diagram of a pure substance.

According to Landau's theory of the order parameter, the Helmholtz free energy, F, is expressed as a power expansion of T and ϕ, and for symmetry reasons [Beysens *et al.*, 1987], only the even powers are retained:

$$F(T,\ \phi) = F_0(T,0) + a/2(T-T_c)\phi^2 + b/4\phi^4 + \ldots \tag{1.1.3}$$

The equilibrium state can be found by minimizing the free energy, F, of the system:

$$\partial F/\partial \phi = 0, \tag{1.1.4}$$

which gives

$$\phi[a(T-T_c) + b\phi^2 + \ldots] = 0 \tag{1.1.5}$$

According to figure 1.1.2 two different solutions exist:

2

a) Above the critical temperature ($T > T_c$), there is only one stable state $\phi = 0$.

b) Below the critical temperature ($T < T_c$), there are two solutions

$$\phi^{\pm} = \pm(a/b)^{1/2}(T_c - T)^{1/2}. \tag{1.1.6}$$
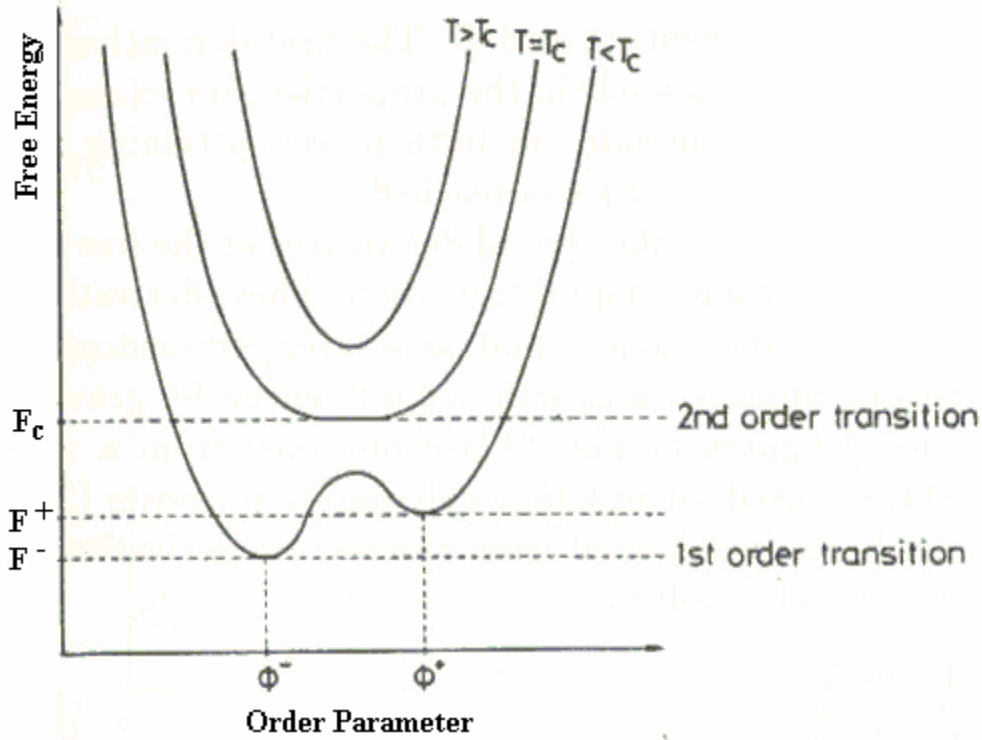
Figure 1.1.2.   Generic dependence of Helmholtz free energy on the order parameter,ϕ for a pure fluid [Beysens *et al.*, 1987].

The two solutions of equation (1.1.6) describe the coexistence curve of gas-liquid system and the miscibility curve for the binary liquid mixture. The behavior of the second derivative of the free energy (1.1.3) is strongly affected by the proximity of the critical point [Chimowitz, 2005]. For example, the isothermal compressibility, χ_T, is related to the second derivative of the free energy

$$\chi_T = 1/V(\partial^2 F/\partial V^2)_T \tag{1.1.7}$$

where V is the specific volume. This diverges as the critical point is approached. Furthermore, the heat capacity (C_p), represented in figure 1.1.3, which is the second derivative of the free energy with respect to temperature at a constant pressure, diverges at the critical point [Beysens *et al.*, 1987].

3
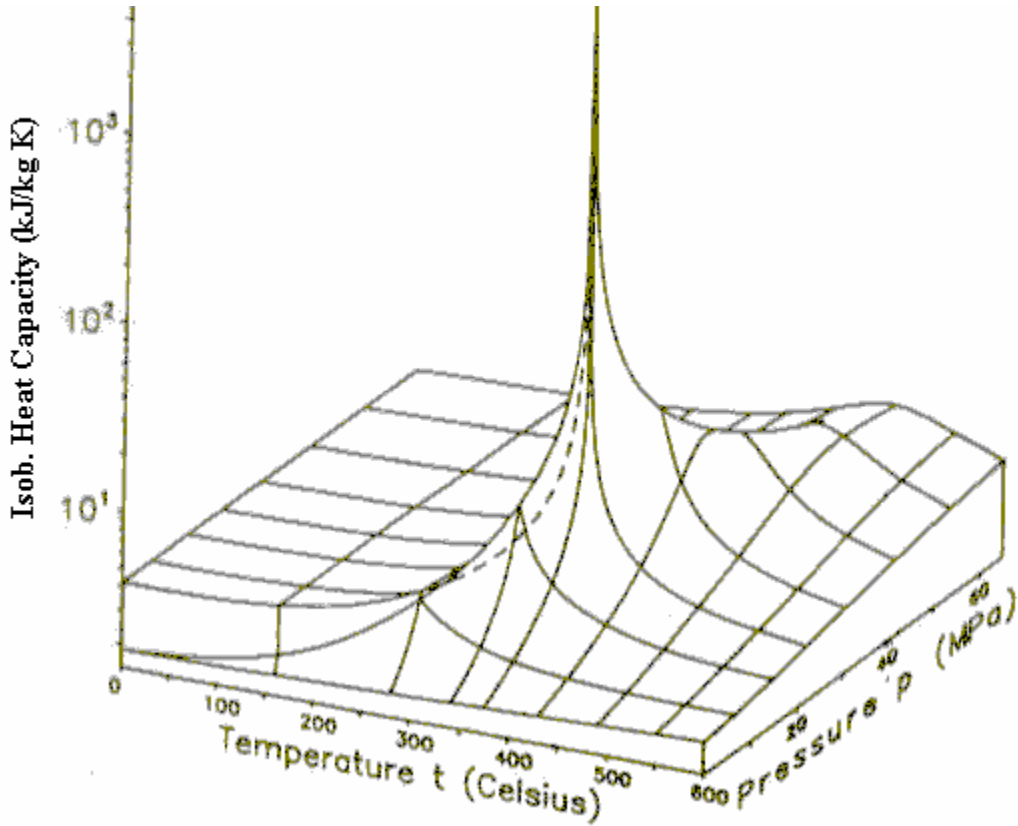
Figure 1.1.3. Critical anomaly in the specific heat at constant pressure measured in microgravity for SF$_6$ [Straub *et al.*, 1999].

During the past few decades, it has been found that the classical exponents are not valid near the critical point and strong theoretical and experimental efforts have been made to determine the effective power laws. These exponents are called the critical exponents because they describe the critical behavior very close to T_C.

The following power laws [Fisher, 1982] are related to the order parameter below the critical temperature $(T < T_C)$

Order parameter:	$\phi = \phi_0 \tau^\beta$,	(1.1.8)
Relative density:	$(\rho_L - \rho_G)/\rho_C = B_O \, \tau^\beta$,	(1.1.9)
Isothermal susceptibility:	$\chi_T = D_O \tau^{-\gamma}$,	(1.1.10)
Isochoric specific heat:	$C_V = A_O \tau^{-\alpha}$,	(1.1.11)
Surface tension:	$\sigma = \sigma_O \tau^\mu$,	(1.1.12)

where $\tau = (T - T_C)/T_C$ is the reduced temperature.

4

Table 1.1.1 gives a side-by-side comparison of critical exponents according to different experimental and theoretical methods.

Table 1.1.1. Values of critical exponents [Beysens *et al.*, 1987].

Critical exponents	β	δ	γ	α	ν	μ
Experiments (pure fluids)	0.32-0.36	4.2-4.6	1.15-1.26	0.110-0.098	0.625-0.635	1.26-1.3
Classical theory	1/2	3	1	0	1/2	1.5
Renormalization Group Theory	0.325	4.815	1.240	0.110	0.63	1.26

The critical exponents are related by so called scaling laws that can be deduced from thermodynamics and are confirmed by experiments and theory [Stanley, 1971]. The transport properties are enhanced near the critical point. For example, the thermal conductivity contains two terms: the normal thermal conductivity (λ_0) and the enhancement specific for the critical region ($\Delta\lambda$). The thermal conductivity is

$$\lambda = \lambda_0 \pm \Delta\lambda. \tag{1.1.13}$$

The enhancement of the thermal conductivity ($\Delta\lambda$) diverges asymptotically at the critical point [Green, 1971]. The mass diffusion coefficient is affected in a similar manner in the vicinity of the critical point.

1.2.   Interfaces-contact line

When a coexisting liquid-gas mixture of a pure fluid is heated to the gas phase, heat transport, convection, and interfacial processes occur in the two-phase fluid [Tong, 1997]. This process is called boiling and has many important applications because of the large heat transfer that it facilitates. Because many types of heat transfer technologies use this process, there are many empirical models of limited validity that are used to describe the boiling process. Many complications are caused by the buoyancy force due to gravity that lifts hot fluid and forces the lighter gas bubbles to nucleate on the hot surface. In the weightless environment of an orbiting space craft, the buoyancy force is negligible and allows the boiling process to be observed under simplified conditions [Hegseth *et al.*, 1998].

Near the liquid-gas critical point, material and thermal properties that play an important roll in the boiling process, such as the surface tension, liquid-gas density difference, and thermal diffusivity or expansively, vary considerably with temperature [Moldover *et al.*,1976]. These thermal properties vary according to well-known universal power laws that either converge (*i.e.*, the surface tension goes to zero) or diverge (*i.e.*, the isothermal compressibility goes to infinity). Near the critical temperature, T_C, the liquid phase has a zero contact angle with the solid boundary, and the phenomenon is called perfect wetting [Hegseth *et al.*, 2005]. In a boiling process where heat is applied, thus pushing the system slightly out of equilibrium, we can expect a perfectly wetted wall to dry from evaporation resulting in liquid-gas-solid contact lines. The same physics that makes perfect wetting at equilibrium will result in a well-defined boundary condition of zero contact-angle in the case where a contact line appears. The geometry of the walls of the cell significantly influences the dynamics of the bulk fluid [Straub *et al.*, 1987]. It can be compared to an extra phase that modifies their potentials.

A liquid droplet on a solid surface possesses three different interfaces [de Gennes, 1985] (Figure 1.2.1). The phases involved are: solid, liquid and vapor. The corresponding free energies for these three interfaces are: γ_{SL}, γ_{LV}, and, respectively γ_{SV}. The angle θ between the tangent plane and the solid–liquid interface is termed the angle of contact. The equilibrium position of the interface is described by the following equation:

$$\gamma_{SV} = \gamma_{SL} + \gamma_{LV} \cos \theta. \qquad (1.2.1)$$

6
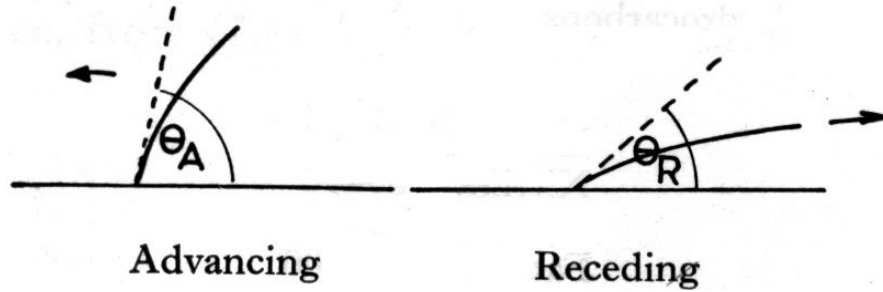
Figure 1.2.1.   A schematic representation of the wetting process of a solid surface by a liquid phase. The contact angle increases as the contact line advance and decreases as it recedes.

Equation (1.2.1) that relates the interfacial tension between phases is called Young's equation. If the contact angle is zero, then the liquid is said to "wet" the solid. If the contact angle (θ) is between zero and 90°, then the phenomenon is referred to as "imperfect wetting". Depending on whether the liquid is advancing or receding, the contact angle increases (θ_A) or decreases (θ_R). In certain situations, the contact line becomes anchored by defects [Hegseth *et al.*, 2002]. Even if the defects are restricted to a small area of the solid, the contact line can be perturbed much further.

The concept of wetting is important for the process of condensation of vapor on the surface of a solid. The attraction forces between the solid and liquid lead to a partial condensation, and a thin film of liquid forms on the surface of the solid. As the vapor approaches saturation, the film becomes thicker [Nikolayev *et al.*, 2001]. The liquid vapor interface may also have a total curvature

$$C = 1/R_1 + 1/R_2, \tag{1.2.2}$$

where R_1 and R_2 are the two radii of curvature at the two contact lines of the droplet. This curvature is associated with a pressure difference between the liquid and vapor phases according to the Laplace formula

$$\Delta P = \gamma C. \tag{1.2.3}$$

The curvature C in a liquid film depends on the thickness of the wetting film.

Let the system be on a coexistence curve where two phases can coexist and let the fluid be placed inside a cell. Near the critical point, the interfacial tension between liquid and gas [Nikolayev *et al.*, 1999] obeys a power law:

$$\sigma \sim [(T-T_c)/T_c]^\gamma, \tag{1.2.4}$$

where the critical exponent $\gamma = 1.28$. The difference between liquid and vapor vanishes at the critical point; therefore, the interface ceases to exist. In other words, the surface tension between the liquid and the vapor approaches zero as the temperature approaches the critical value. It was found experimentally [Widom, 1972] that the inverse of the interface thickness follows a power law near the critical temperature (Figure 1.2.2)

$$K^{-1} \sim [(\,T\text{-}T_c)/T_c\,]^{\nu}, \qquad\qquad (1.2.5)$$

where $\nu = 0.64$ is the universal critical exponent.
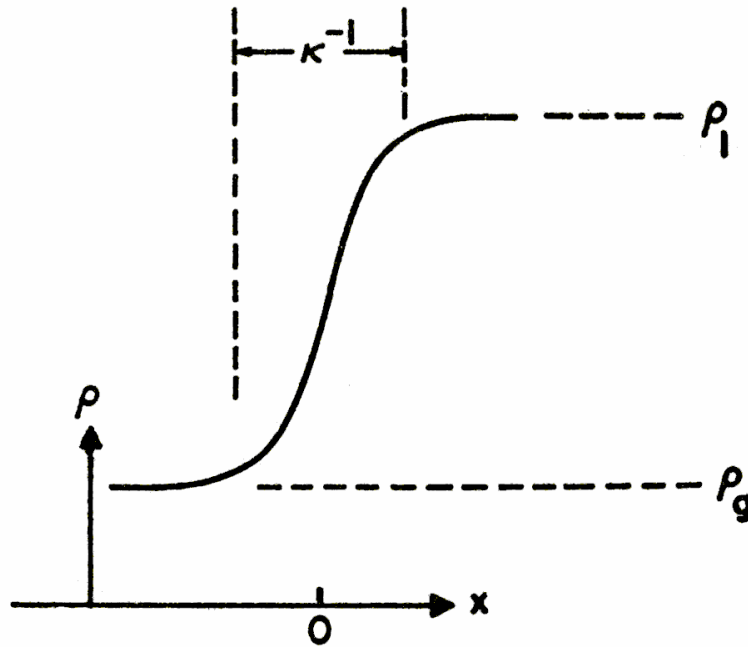
Figure 1.2.2.   The profile of the gas-liquid interface. The thickness of interface located at x = 0 and characterized by K^{-1}.

Vapor recoil force

Nikolayev suggested a new approach to the heat transfer near the triple vapor-liquid–solid contact line [Nikolayev *et al.*, 2003]. To calculate the expression of the vapor recoil force, they consider a portion of a liquid-gas interface with area A. The liquid mass Δm is heated during the Δt time interval [Nikolayev *et al.*, 2001]. The mass is related to the evaporated volume V_l by $\Delta m = \Delta V_l \rho_l$, where ρ_l is the liquid's density. Therefore, the liquid vapor interface displacement is $\Delta l = - n \Delta V_l / A$, where n is the unit vector normal to the interface directed toward the vapor (Figure 1.2.3).

8
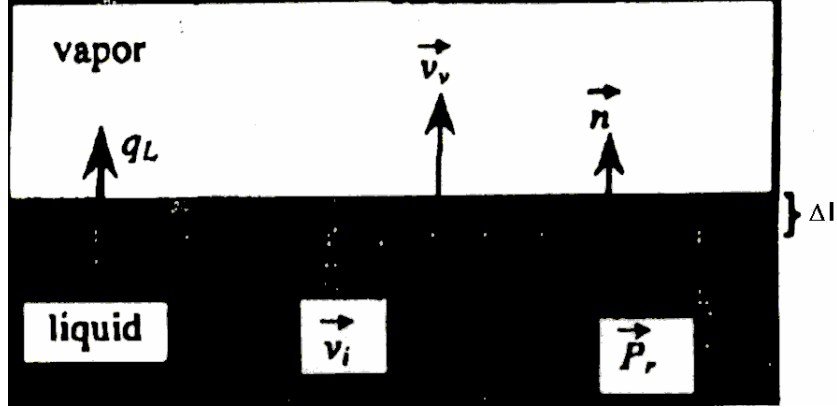
Figure 1.2.3. A schematic representation of the possible forces acting on a gas-liquid interface in a constant volume container.

Due to evaporation, the vapor's volume change is ΔV_v. Since the mass is conserved in a closed system

$$\Delta m = \Delta V_l \rho_l = \Delta V_v \rho_v. \tag{1.2.6}$$

Momentum conservation for this portion of the liquid–vapor interface is

$$\Delta m \, (v_i + v_v) + P_r \Delta t \, A = 0, \tag{1.2.7}$$

where P_r is the vapor recoil force per unit area of the interface, v_i is the interface's velocity, and v_v is the vapor's velocity. By substituting (1.2.6) into (1.2.7), the vapor recoil force can be written as

$$P_r = -\eta^2 (1/\rho_v - 1/\rho_l) n, \tag{1.2.8}$$

where the rate of evaporation $\eta = \Delta m/(A \Delta t)$. This quantity relates to the local heat flux q_l per unit area across the interface by the equation

$$q = H\eta, \tag{1.2.9}$$

where H is the latent heat of evaporation. Because the temperature gradient is strong in the vicinity of the contact line, q increases sharply near the contact line, and consequently, η and P_r also increase. According to (1.2.7) and (1.2.8), P_r is also large near the contact line and negligible on other parts of the bubble's surface. Therefore, under the action of the vapor recoil force, the dry spot under the gas bubble should spread to cover the heater's surface [Nikolayev *et al.*, 1999] (see Figure 1.2.4).

9

The shape of the bubble may be determined using a quasistatic approximation. Under such assumptions, the bubble's shape is defined only by the surface tension force and vapor recoil force

$$\sigma C = \Delta p + P_r, \qquad\qquad (1.2.10)$$

where C is the local curvature of the gas bubble, Δp is the difference pressure at the interface, and σ is the surface tension [Nikolayev *et al.*, 2001].
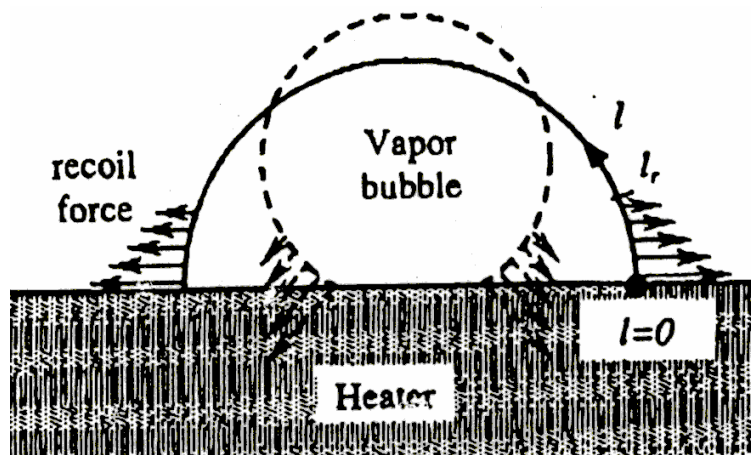
Figure 1.2.4   A schematic representation of the spreading process under the vapor recoil force influence.

1.3.   Critical fluctuations

During the past few decades, many theoretical and experimental approaches have been concentrated on the study of fluctuations in fluids subject to a stationary temperature gradient (∇T). It was found that the correlation of the functions is long-ranged because the detailed microscopic balance is violated [Kawasaki, 1975]. The theory of fluctuations in fluids that are in a macroscopic thermal equilibrium is well established [Lunacek, 1971]. Density fluctuations over time were probed experimentally by light scattering [Mountain, 1966; Ford, 1965]. The light scattering spectrum of a single-component fluid contains a central Rayleigh line, unshifted in frequency, resulting from fluctuations in entropy or temperature [Ohbayashi, 1978; Onuki, 1990]. For a two-component fluid, the local fluctuations give rise to a second Rayleigh component [Chimowitz, 2005]. The intensity of light scattered by the density fluctuations is proportional to the variation in the index of refraction. As the temperature gradient increases, the intensity of the fluctuations shows a significant enhancement [Li *et al.*, 1998]. The nonequilibrium enhancement of the concentration's fluctuations has been found to be proportional to $(\nabla T)^2/k^4$, where k is the wavenumber of the scattered light. The local observation of critical fluctuations allowed the morphology of the fluctuation to be studied by imaging the critical fluctuation of the order parameter (*M*) as first suggested by Debye and Jacobsen in 1963 [Debye *et al.*, 1968]. Recently, a number of binary fluids, such as isobutyric acid-water and methanole-cyclohexane, have been investigated, and only fluctuations in a range close to criticality were observed [Beysens *et al.*, 1990]. The images due to the refractive index fluctuation were interpreted as being formed by the interference between transmitted and scattered light. These fluctuations developed and vanished as time progressed and were temperature-dependent. The histograms were found to be of a Gaussian shape [Beysens *et al.*, 1990].

The existence of large density fluctuations was first documented by Andrew [Andrews, 1869] more than a hundred years ago. Andrews performed the first optical observation of density fluctuations near the critical point with a relatively primitive apparatus capable of revealing the critical opalescence due to the strong scattering of light by fluid. Critical opalescence is evidence of enhanced density fluctuations in the fluid near the critical point and is determined by the large compressibility of fluids in the critical region. According to Andrews, critical behavior is

determined by fluctuations and the increasing instability of the system approaching the critical point. Near the critical point, the fluctuations of the order parameter develop through the entire fluid. The distance measuring the spatial correlation is called the correlation length. As the critical point is approached, the correlation length increases according to

$$\xi = \xi_0 (T/T_c - 1)^{-\nu}, \tag{1.3.2}$$

where ξ_0 is a system-dependent correlation amplitude and ν is the universal exponent ($\nu = 0.63$). A two-dimensional illustration of increasing correlation length near T_c is shown in Figure 1.3.1. The density fluctuations are enhanced near the critical point because of the thermodynamic instability of the system. Many scattering experiments dealing with the critical behavior of gas-liquid and binary fluids systems were performed. Debye and Jacobsen [Debye *et al.*, 1968] reported the observation of the order parameter fluctuations in experiments during the early 1960s. They used the phase-contrast microscope technique to analyze concentration fluctuations that appear to be near the critical point of a polymer-solvent system of polystyrene and cyclohexane. In their experiment, the system containing the microscope and the sample was immersed in an air thermostat controlled within ± 0.02 K. This thermal accuracy did not allow for separate observation of critical fluctuations from the onset of phase separation. Direct observation of critical fluctuations was reported in 1989 [Guenoun *et al.*, 1989] in a number of binary fluids that belong to the same class as the 3D Ising model. In the experiments performed by Guenoun *et al*, the temperature stabilization provided by a water bath was in the range of 0.2 mK. A white light beam illuminated the cell and the image formed due to the interference of the transmitted light (E_T) with the scattered light (E_S)(Figure 1.3.2).
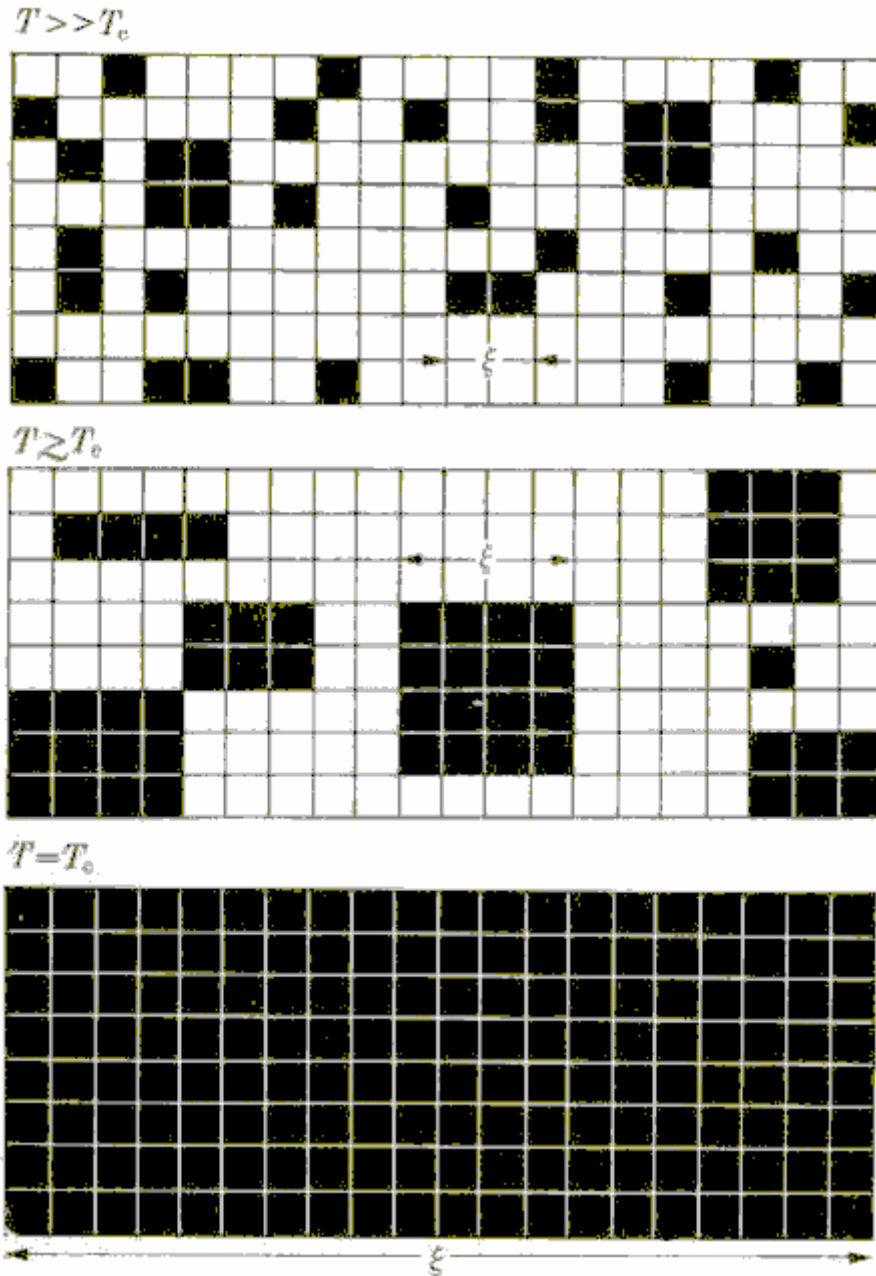
Figure 1.3.1. Two-dimensional sketch of a thermodynamics state of a fluid approaching its critical temperature [Stanley, 1971]**.** Black squares denote macroscopic regions of the system in the same thermodynamic state. The correlation length may be seen as "an island" of nearby macroscopic regions in the same thermodynamic state.

The change in the refractive index was proportional to the order parameter, which was considered to be the intensity in the image's plane (Figure 1.3.2). However, the intensity fluctuations are integrated over a volume, (*V*), which is defined by the product of the depth of the

field and the pixel area. Therefore, the intensity of one pixel is proportional to the average value of the order parameter (δM). The recorded images were corrected for the parasitic modulations by subtracting images taken under the same condition but at higher temperature so that the fluctuations were not visible anymore.
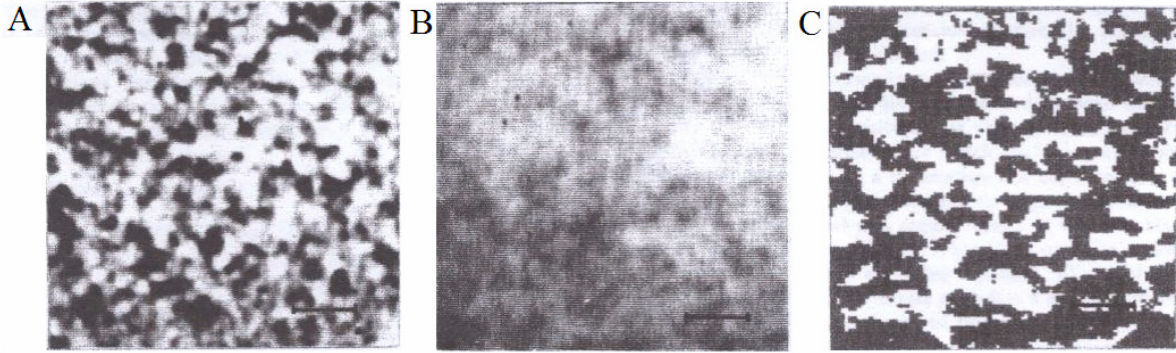
Figure 1.3.2. Concentration fluctuations in a binary fluid of isobutyric acid and water. (A) photos at $T\text{-}T_c$=1mK and (B) 16 mK (the horizontal bar corresponds to 40 μm); (C) photos at 1 mK digitized with two intensity levels [Guenoun *et al.*, 1989].

Guenoun *et al.* considered that the average of the order parameter over the volume V is a "block spin variable". The image intensity was assumed to be proportional to the order parameter fluctuations. The probability distribution of the intensity $P(\delta I)$ is given by:

$$P[\delta I(r)] \sim P[<\delta M(r)>] \sim exp\{[-(1/k_BT)\ F[<\delta M(r)>]]\}, \qquad (1.3.3)$$

with k_B is Boltzmann's constant and $F[<\delta M(r)>]$ is the free energy in the volume V in question. Using the above assumptions it was possible to directly determine δM dependence on F. It was found that the probability distribution function (PDF) of recorded images was Gaussian and that the images' widths are temperature dependent. The Fourier analysis of recorded images gave access to the structure factor of the fluctuation. Density fluctuations appear as domains whose intensities are different from the average value of the image and are detectable only near the critical point (Figure 1.3.2.). The cluster analysis has demonstrated the self-similarity of density fluctuations and has provided a measurement of their fractal exponent, which is D_f= 2.8 ± 0.1.

Other microscopic observations near the critical point have been reported by varying the optical techniques and image processing [Hegseth *et al.*, 2003]. Hegseth used a bench-top optical microscope with spatially coherent light to visualize concentration fluctuations in binary liquids near the critical point. The fluctuations were recorded on video tapes and the images processed

later on. Three different experimental media were placed in the focal plane of the optical system: (1) an opaque mask or dark field (DF), (2) a quarter wave plate or phase contrast microscopy (PC) or, (3) nothing or bright field microscopy (BF)(Figure 1.3.3). In conclusion, the temporal behavior of the fluctuations for PC and BF were similar, significant differences in the temporal behavior BF and DF were observed, and the DF images fluctuate much more rapidly.
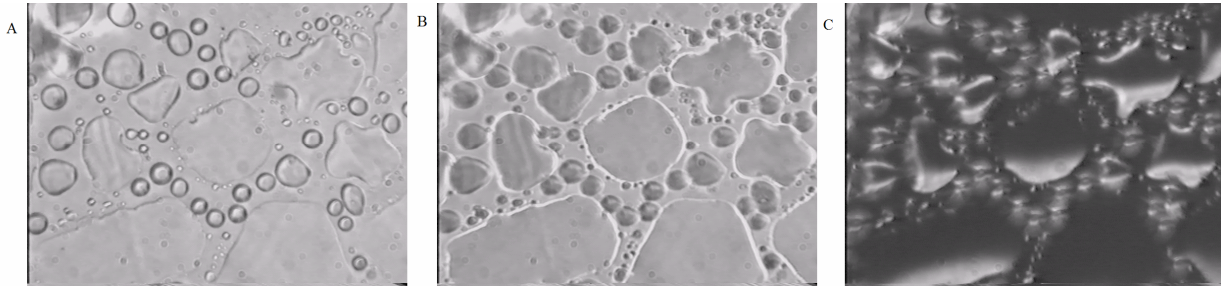
Figure 1.3.3. **Enhancement of fluctuating images in optical microscopy.** Typical fluctuations recorded from bright field (A), phase contrast (B), and dark field (C) experimental setups [Hegseth *et al*., 2003]

The image analyses provide valuable new information regarding the underlying statistical physics of the system. Based on the statistic of the patterns in microgravity, it was possible to infer the singular free energy and its behavior near the critical point. The mechanism of image formation was studied by applying a phase contrast and dark field filter to the microscope. The comparison among bright field, phase contrast and dark field images shows that between phase contrast images and bright field images, there are only slight differences (Figure 1.3.3). This result suggests that the fluctuating media is not a phase object, rather, the media acts like an amplitude object. Slightly below the critical temperature, the fluctuating fluid give rise to growing domains called generalized nucleation [Hegseth *et al*., 2000]. Other results regarding pure fluids reveal that the histograms of the recorded images can be fitted by a Gaussian function [Beysens *et al*., private communication].

1.4. Light scattering theory in fluids

The light scattering theory has been developed more than one hundred years ago and started with Einstein, who showed that the intensity of the scattered light determined by density fluctuations is proportional to the isothermal compressibility of the fluid. Over the past few decades, light scattering near the critical point has become an active topic because the variations in the scattered intensity are very large and visible to the naked eye. The fluid turns milky and the phenomenon is called critical opalescence. The underlying idea behind the theory of scattering is that the scattered light contains information about the fluid's density fluctuations over both time and space. The theoretical framework is provided by statistical mechanics and relates the intensity and the frequency distribution with the scattered light to the thermodynamic and transport properties of the fluid [Mountain, 1966].

Ornstein–Zernike theory

The density at an arbitrary point, *r,* in the fluid is defined by

$$n(r) = \sum_{i=1}^{N} \delta(r - r_i),$$ (1.4.1)

where r_i is the spatial coordinate of the ith particle and δ is the Dirac function. The average value of the density in a uniform system does not depend on the spatial position of a particle and has the expression:

$$\langle n(r) \rangle = \left\langle \frac{N}{V} \right\rangle = n,$$ (1.4.2)

where $\langle \ldots \rangle$ is the ensemble average. The correlation function measures the correlation density fluctuations at two positions, *r* and *r'*

$$G(r, r') = \left\langle \{n(r) - \langle n(r) \rangle\} \{n(r') - \langle n(r') \rangle\} \right\rangle.$$ (1.4.3)

For a spatially uniform system, equation (1.4.3) becomes

$$G(r - r') = \left\langle n(r)n(r') \right\rangle - n^2.$$ (1.4.4)

As the spatial separation, *|r-r'|*, between two points increases the correlation between their respective density fluctuations decreases. Stanley [Stanley, 1971] established the connection between the isothermal compressibility, K_T, and the fluctuations of the total number of particles in the system, which in turn is related to the correlation function

$$\left\langle (N - \langle N \rangle)^2 \right\rangle = \langle N^2 \rangle - \langle N \rangle^2, \tag{1.4.5}$$

where N is the number of particles at position r and time t, and $<...>$ is the temporal average at the specified position. The relation between the fluctuations of the number of particles and the isothermal compressibility is given by [Stanley, 1971]

$$\left\langle (N - \langle N \rangle)^2 \right\rangle = \frac{\langle N \rangle^2 k_B T}{V} K_T = \langle N \rangle n k_B T K_T, \tag{1.4.6}$$

where k_B is Boltzmann's constant, T is the temperature, V is the macroscopic volume, and K_T is the isothermal compressibility. For the ideal gas the compressibility is

$$K_T{}^0 = \frac{1}{n k_B T}, \tag{1.4.7}$$

Using (1.4.6) and (1.4.7), the ratio of the two compressibilities is

$$\frac{K_T}{K_T{}^0} = \frac{\left\langle (N - \langle N \rangle^2) \right\rangle}{\langle N \rangle}. \tag{1.4.8}$$

On the other hand, the correlation function relates to the fluctuations of the number of particles by

$$\left\langle (N - \langle N \rangle)^2 \right\rangle = \int dr \int dr' G(r - r') = V \int dr'' G(r''). \tag{1.4.9}$$

Therefore, based on (1.4.8) and (1.4.9), the compressibility and the correlation function are related by

$$\frac{K_T}{K_T{}^0} = \frac{1}{n} \int G(r) dr. \tag{1.4.10}$$

The last equation suggests that near the critical temperature T_c, a diverging compressibility corresponds to an increase in the correlation function. As a result, the correlation length increases and the density inhomogeneities scatter light more strongly thus leading to the critical opalescence phenomenon. When radiation of the incident wave vector k_0 is scattered by the fluid's atoms the scattered intensity $I_0(q)$ depends on the properties of the constituent atoms. Assuming a quasielastic interaction for scattering, the momentum transfer function can be written as [Ford, 1965]:

$$q = |q| = \frac{4\pi}{\lambda} \sin \frac{\theta}{2}, \tag{1.4.11}$$

17

where θ is the scattering angle and λ is the wavelength of the incident light. As the fluid's density increases, the observed scattering intensity $I(q)$ deviates from $I_0(q)$, and the reduced scattering intensity becomes very large at low angles

$$\frac{I(q)}{I_0(q)} = \frac{1}{n}\int dr e^{-iqr} G(r) = \frac{1}{n}S(q),$$ (1.4.12)

where $S(q)$ is the structure factor and is defined as the spatial Fourier transform of the correlation function. Near the critical point, the structure factor ($S(q)$) takes large values due to small values of q. The critical opalescence phenomenon was first studied theoretically by Ornstein and Zernike in 1914 [Ornstein *et al.*, 1914]. The first step in deriving the form factor according to Ornstein and Zernike theory is to substitute the density (1.4.1) into the correlation function (1.4.4)

$$G(r - r') = \left\langle \sum_{i=1}^{N}\sum_{j=1}^{N} \delta(r - r_i)\delta(r'-r_J) \right\rangle - n^2.$$ (1.4.13)

The correlation function (1.4.13) contains an autocorrelation term of the particle with itself (first term) and a correlation term between different particles (second term)

$$G(r - r') = n\delta(r - r') + n^2\Gamma(r - r'),$$ (1.4.14)

where $\Gamma(r\text{-}r^{'})$ is a dimensionless quantity. In order to compute the form factor from (1.4.12), the Fourier transform of (1.4.14) is required. Let $\hat{\Gamma}(q)$ be the Fourier transform, $\left(\int \Gamma(r)e^{-iqr}dr\right)$, of $\Gamma(r)$. The direct correlation function C(r) and its Fourier transform $\hat{C}(q)$ is defined by:

$$\hat{C}(q) = \frac{\hat{\Gamma}(q)}{1 + n\hat{\Gamma}(q)}.$$ (1.4.15)

At temperatures close to the critical temperature ($T{\to}T_C$), the function $\Gamma(r)$ became long-range as a result of the propagation of direct correlation and the Ornstein–Zernike integral becomes

$$\Gamma(r - r') = C(r - r') + n\int C(r - r'')\Gamma(r''-r')dr''.$$ (1.4.16)

The structure factor is:

$$S(q) = n + n^2\hat{\Gamma}(q).$$ (1.4.17)

For a small q, the scattered intensity is very nearly a Lorentzian and from (1. 4.14) and (1.4.15) the structure factor can be found as:

$$\frac{1}{n}S(q) = \frac{1}{1 - n\hat{C}(q)}, \qquad (1.4.18)$$

The function $\hat{C}(q)$ is short-range and can be expanded in a Taylor series about q=0 [Stanley, 1971]. Therefore

$$\frac{n}{S(q)} = 1 - n\hat{C}(q) = 1 - n\{\hat{C}(0) + \hat{c}_2(n,T)q^2 + O(q^4)\} =$$

$$\hat{c}_2(n,T)\{\frac{1 - n\hat{C}(0)}{\hat{c}_2(n,T)} - nq^2 + O(q^4)\} = R^2\{k_1^2 + q^2 + O(q^4)\}, \qquad (1.4.19)$$

where the integral $R^2 \equiv -n\hat{c}_2(n,T) \propto \int r^2 C(r)dr$ is directly related to the second moment

$C(r)$ and $k_1^2 = \dfrac{1 - n\hat{C}_0}{R^2}$ is related to the zeroth order moment.
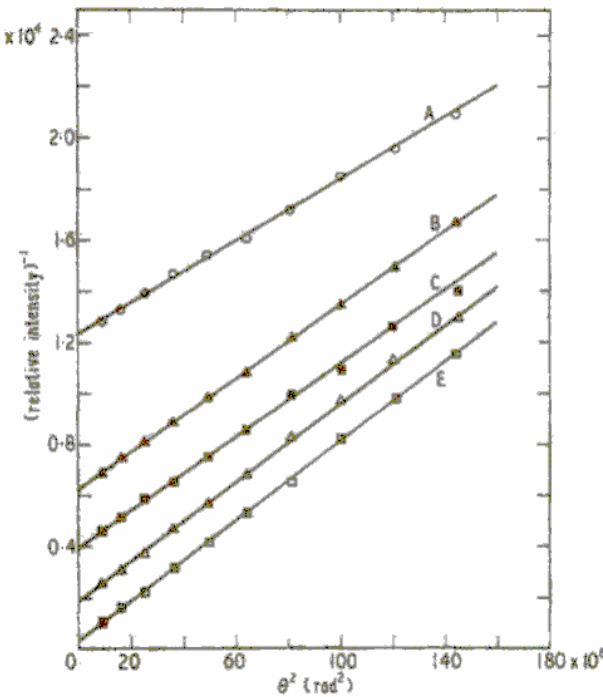
Figure 1.4.1. The dependence of the inverse scattering intensity on the scattering angle θ for Argon. Each curve represents different temperature on an isobar close to the critical temperature [Thomas, 1963].

The equation (1.4.19) predicts a relationship between the relative scattered intensity versus q^2 for different temperatures called Ornstein-Zernike-Debye curve. This predicted relationship was checked experimentally by Thomas and Schmidt for Argon (see figure 1.4.1, where the inverse relative intensity show a linear dependence on the scattering angle, θ [Thomas, 1963].

In Ornstein and Zernike's approximation, Taylor series terms higher than q^4 were neglected. The reduced intensity has a Lorentzian form

$$\frac{I(q)}{I^0(q)} = \frac{S(q)}{n} = \frac{R^{-2}}{k_1^2 + q^2} . \qquad (1.4.20)$$

The inverse Fourier transform of equation (1.4.20) gives the total correlation function

$$G(r) \approx \frac{1}{R^2} \frac{e^{-k_1 r}}{r} , \qquad (1.4.21)$$

where k_1 is the inverse correlation length $k_1 = \xi^{-1}$ with the property that $k_1 \to 0$ as $T \to T_c$. Fisher [Fisher, 1967] corrected the Ornstein-Zernike approximation by introducing a correctional exponent η less than 0.056 in three dimensional systems. It is a measure of the departure from the Ornstein-Zernike behavior. The modified Ornstein-Zernike-Debye correlation function is [Puglielly et al., 1970]

$$G(r) \approx \frac{1}{r^{1+\eta}} e^{-r/\xi} , \qquad (1.4.22)$$

Puglielly et al. measured the turbidity of SF_6 in the vicinity of the critical point and determined both the temperature dependence of the isothermal compressibility and the correlation length. A comparison of their isothermal compressibility estimations obtained from turbidity measurements with MacCormack [MacCormack, 1951] showed good agreement. The turbidity is given by the integral over all angles of light scattering intensity per unit length according to the Ornstein-Zernike theory

$$I(q) = A \frac{K_T \sin^2 \phi}{1 + (q\xi)^2} , \qquad (1.4.23)$$

and

$$A = \frac{\pi^2}{\lambda^4} \left(\frac{\rho \partial \varepsilon}{\partial \rho} \right)_T^2 K_B T , \qquad (1.4.24)$$

where K_T is the isothermal compressibility, q is the scattering vector, ϕ is the angle between the polarization vector of the incident light and the scattering wave vector, ξ is the correlation length and ρ is fluid density. By integrating (1.4.23) over all possible scattering angles, the turbidity becomes

$$\tau = \pi A K_T f(\alpha) , \qquad (1.4.25)$$

where $f(\alpha) = \left(\dfrac{2\alpha^2 + 2\alpha + 1}{\alpha^3} \right) \ln(1 + 2\alpha) - \dfrac{2(1 + \alpha)}{\alpha^2}$. Pugllielly [Pugllielly, 1970] relied on the

fact that the turbidity, τ, exhibits the same power law as the isothermal compressibility, K_T, and $f(\alpha)$ is nearly constant for a small α. Cannel [Cannel *et al.*, 1975] made measurements of the long range correlation length using two different light scattering techniques: (1) the differential method directly measuring the difference between the forward and backward scattered light, and (2) the turbidity measurements. The measurements are taken along the critical isochors which were found to fit the correlation length power law (see Figure 1.4.2). In order to compensate for the gravity-induced density gradient, the fluid was stirred, thus creating a state of uniform density throughout most of the cell.
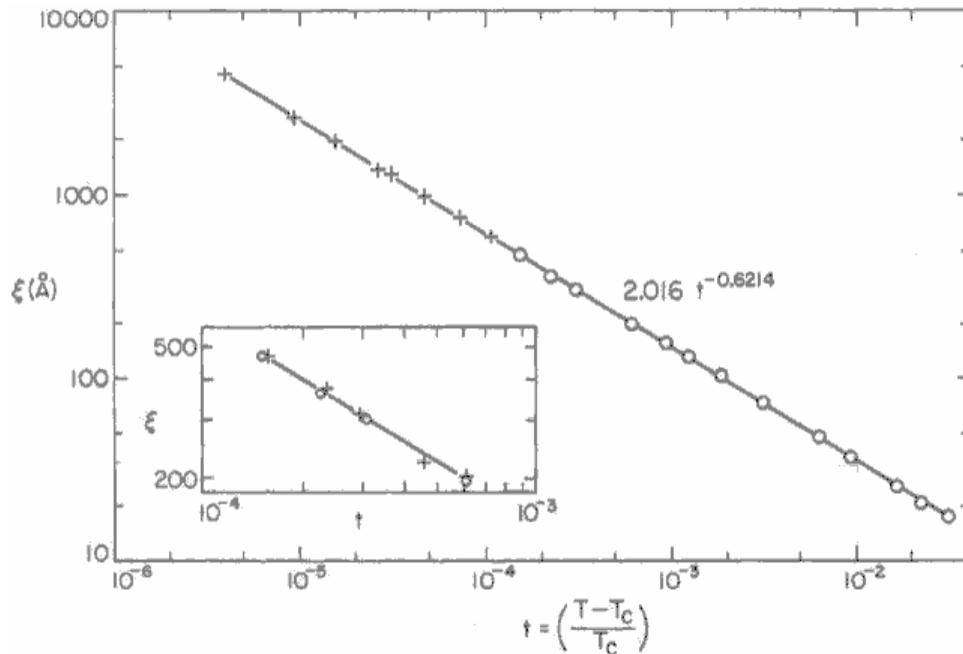
Figure 1.4.2. Long-range correlation length of SF$_6$ as a function of temperature on critical isochors. The crosses and the circles are the result of the turbidity method and differential intensity measurements.

Other experimental results using the light scattering techniques near the critical point of a ternary liquid mixture done by Ohbayashi [Ohbayashi, 1978] showed the universality of the critical exponent. The two power laws, one for the correlation length and the other for the isothermal compressibility, were also verified experimentally.

The effects of double scattering on the scattering intensity have been considered by a number of investigators [Chalyi, 1969; Oxtoby, 1974; Bray, 1975; Boots, 1976; Holm, 1977]. The effect of double scattering on the spectral distribution of scattering light has been investigated by Beysens [Beysens *et al.*, 1976, 1977] and Sorensen [Sorensen, 1977]. The effect of triple scattering or higher becomes very important in practice because most fluids are opaque near the critical point. Moldover *et al.* proposed three methods to reduce turbidity: (1) reduce the width (w) of the optical cell [Moldover *et al.*, 1979], (2) choose fluids with a smaller index of refraction, and (3) conduct the experiment at longer wavelength.

1.5.   Phase separation

Phase separation in a fluid and liquid mixture occurs when a sample is quenched from an initial temperature T_i characterized by a homogeneous state to another state temperature (T_f) such that one phase is no longer stable (see Figure 1.5.1).

Figure 1.5.1. Schematic representation of the phase diagram in the temperature (T) versus the order parameter (M).

Cahn and Hilliard [Cahn, 1965] were the first to study the process of phase separation in metallurgical systems. Phase separation is a nonlinear process and its kinetics have been investigated for a few decades by computer experiments using simple models [Puri, 1992; Broide, 1993; Bastea *et al.*, 1997; Martin, 1998] as well as theoretically [Siggia, 1979; Binder *et al.*, 1974; Swift, 1977; Nikolayev *et al.*, 1996] and experimentally [Chang *et al.*, 1979; Houessou *et al.*, 1985; Perrot *et al.*, 1994; Perrot *et al.*, 1999; Beysens *et al.*, 2000; Hegseth *et al.*, 2003; Xin-Liang *et al.*, 2005]. The thermodynamics stability of a fluid or a mixture is determined by the location of the minimum free energy in the temperature (T) versus the order parameter (ϕ) plane. The minimum of the free energy is determined by solving the extremum condition

$$\partial F/\partial \phi = 0. \qquad\qquad (1.5.1)$$

The implicit equation (1.5.1) describes the so-called coexistence curve (Figure 1.5.2B).

The thermodynamic stability of a phase is determined by the sign of the second derivative of the free energy $(\partial^2 F/\partial \phi^2)$ and the curve $\partial^2 F/\partial \phi^2 = 0$ defines the so-called "spinodal line" (Figure 1.5.2B). The region where the second derivative of the free energy with respect to the order

parameter is smaller than zero, $\partial^2 F/\partial\phi^2 < 0$, is thermodynamically unstable. The region between the two curves corresponds to the metastable case with $\partial^2 F/\partial\phi^2 > 0$. The previous classification was made according to the classical mean field theory [Papon, 2002].

Tanaka [Tanaka *et al.*, 1983] studied phase separation with an oligomer mixture between closely spaced plates. This type of arrangement was used in order to separate gravity effects from sedimentation and buoyancy. He observed two different kinetics of growth when the sizes of the domains were of the same order of magnitude as the thickness of the liquid mixture layer. The experimental setup introduced significant perturbations due to wetting from the plates so that the experiment could not reveal any bulk effects.

Depending on the thermal quench, two kinds of phenomena can occur below the coexistence curve (see Figure 1.5.2):

1) Inside the metastable region, phase separation is initiated by a nucleation process through spontaneous fluctuations or impurities (see figure 1.5.2). In this region, a nucleus of a critical size has to form before it is energetically favorable for it to grow. Nucleation and growth correspond to the metastable region of the phase diagram. If a fluctuation is large enough to overcome the energy barrier due to the interfacial processes, then a nucleus will appear and a new phase develops. The nucleation process is more likely to occur on a seed particle. An energy barrier always exists in the case of nucleation and growth and prevents the droplets with a radius smaller than a critical value *r** to grow so the domains appear disconnected. The growth law of the nucleus depends on its size and the number of droplets in the solution. It was experimentally confirmed [Chou *et al.*, 1979; Bayley, 1993; Perrot *et al.*, 1994; Perrot *et al.*, 1999; Onuki *et al.*, 1999] and theoretically proved [Lifshiftz, 1961; Siggia, 1976; Siggia, 1979; Bastea *et al.*, 1997] that the growth of a drop's radius follows a power law of the Lifshitz-Slyosov type: $r \sim t^{1/3}$.

2) Inside the unstable region, there is no energy barrier for the droplets to overcome and the system is unstable (see figure 1.5.2). The fastest growth is exhibited by the fluctuations whose sizes are of the order of the correlation length, ξ. A typical ring with a characteristic wavelength occurs when scattering techniques are used. Several minority domain growth mechanisms have been described [Guennoun *et al.*, 1987; Chou, 1979]. If the gravity effects are negligible and the volume fraction of the minority phase is very small ($\phi < 0.03$), then growth by diffusion as described earlier by Lifsitz and Slyosov characterizes the region. The growth law has a power law exponent of 1/3. Critical systems with a large volume fraction (ϕ) have been

24

studied by Wong and Kobler [Wong, 1978]. If $\phi > 0.10$, then a "slow" growth (characterized by the $t^{1/3}$ power law) is reported at early times and a faster growth at later times (see figure 1.5.4).
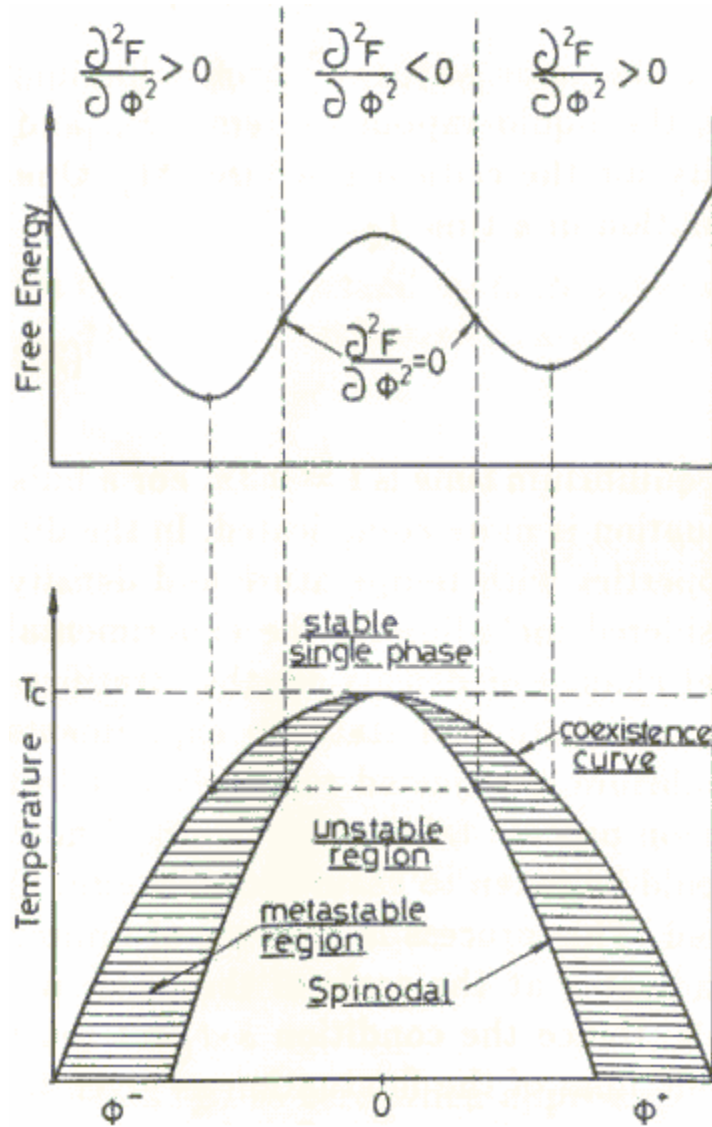
Figure 1.5.2. Schematic representation of phase equilibrium [Beysens *et al.*, 1987].

The fast growth at later times is due to sedimentation. Experiments done in microgravity with density matched binary liquids and pure fluid carbondioxide near the critical point have shown that interconnected (percolated) structures appear for a volume fraction of 0.5 [Garrabos *et al.*, 1992] (see Figure 1.5.4). At later periods during fluctuations growth, the characteristic time of these domains appear to have a linear growth in time (see figure 1.5.4). Densities matched in a binary fluid mixture have been used to study the growth law and the possible crossover between

the slow and fast growth laws [Chou *et al.*, 1979; Chu *et al.*, 1966; Chang, 1979]. The errors in these experiments were large, but it was still possible to delimitate the boundary between the slow ($r \propto t^{1/3}$) and fast ($r \propto t$) regimes for a critical volume fraction of $\phi > 0.30$. The threshold between the fast and slow growth was also reported by Perrot [Perrot *et al.*, 1994] in a pure fluid (SF_6) at low gravitational field. Using a volume fraction $\phi > 0.29$ and a thermal quench depth of 300 μK and 1000 μK, fast growth with interconnected patterns was reported (see figure 1.5.4). Slow growth with disconnected patterns occurred at smaller quench depth of 50 μK and 100 μK (see Figure 1.5.4). The result of this experiment proved that the volume fraction is the correct parameter to study the growth laws.

During the thermal quench from the homogeneous to the inhomogeneous state, fluids under Earth's gravity are affected by sedimentation and convection [Moldover *et al.*, 1979]. In the final stage of phase separation, the denser phase sinks to the bottom of the container. Wetting forces contribute to these changes, too. The nucleation process and late stage spinodal decomposition cannot be reached because of sedimentation. The role of interfacial tension remains uncertain for fluids near the critical point under Earth's gravity.

Figure 1.5.3. Phase separation in refrigerant R12 on Earth [Beysens *et al.*, 1987]
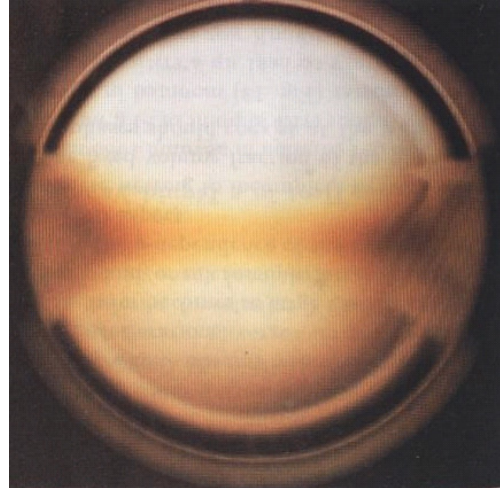
Figure 1.5.3 shows a sample of the refrigerant R12 when cooled from above the critical temperature ($T > T_C$). Critical opalescence is observed in the middle of the picture, and the fog from both sides demonstrates the phase separation as a dispersion of droplets. In the next stage, the phases will be decomposed by sedimentation.

The natural length scale for fluids near the critical point is the correlation length, which diverges according to the power law

$$\xi = \xi_0[(T-T_C)/T_C]^{-\upsilon}, \tag{1.5.2}$$

where $\upsilon = 0.63$ is a universal exponent, ξ_0 is a system-dependent amplitude, and T_C is the critical temperature. The experimental results can be represented on two master curves in reduced units $K_m^* = 2\pi\xi/L_m$ versus $t^* = t/t_\xi$, where $t_\xi = 6\pi\eta\xi^3/k_BT$,with η being the shear viscosity and k_B being Boltzmann's constant.
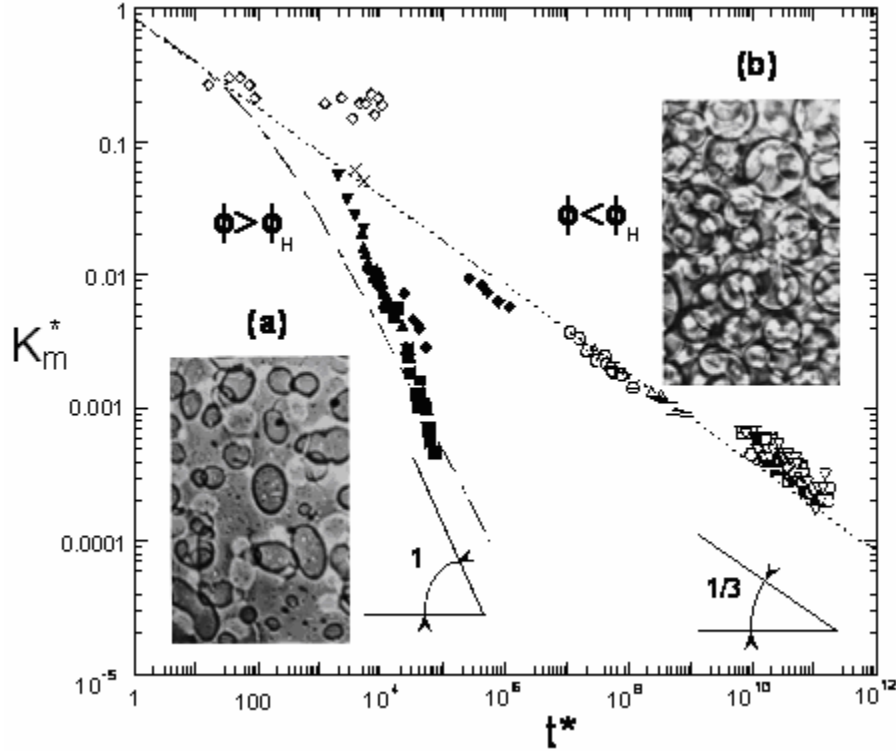
Figure 1.5.4. **Master curves of scaled wave number K_m^* versus scaled time t^*.** The two curves correspond to a liquid mixture with $\phi_H \sim 0.29$. The experiments for CO_2 and SF_6 under reduced gravity are recorded with a volume fraction between 0.50 and 0.13 and a temperature between 50 μK and 100 μK below T_C. (a) If $\phi > \phi_H$, then interconnected pattern of drops occurred. (b) If $\phi < \phi_H$, then the drops are isolated [Beysens *et al.*, 2000].

Scaling by proper units of length and time implies that all the data from different experiments and different systems can be cast on the same master curve. Late stages of growth can be observed only when the gravitational flow due to the difference in density of the phases is suppressed. A number of experiments under reduced gravity have been carried out [Beysens *et al.*, 1994, 2000]. The results show that the influence of convective flows and sedimentation were removed. Phase separation has been of great theoretical interest over the last several decades.

There have been investigations of kinetics and dynamics of phase transition from both the theoretical and experimental points of view [Guenoun *et al.*, 1994; Hegseth *et al.*, 1998; Lamorgese, 2005]. Siggia [Siggia, 1979] has initiated many attempts to explain the two growth laws from both theoretical and experimental perspectives. Several groups have done large scale numerical simulation in order to solve the coupled equations involving diffusion and hydrodynamics. These numerical simulations showed that an asymptotic growth law with an exponent greater then 1/3 results due to hydrodynamic effects and an exponent of 1/3 in the case of pure diffusion. A new theoretical attempt has been pursued by Nikolayev [Nikolaeyev *et al.*, 1997] to explain the existence of the two different regimes and their relation to the pattern morphology. According to Nikolayev [Nikolayev *et al.*, 1997], for a high equilibrium volume fraction, ϕ, droplet coalescence is a leading candidate for the growth mechanism at late times in both the "fast" and "slow" growth cases. In the "slow" growth case, the Brownian motion of the droplets determines a characteristic collision rate for the droplets. During their random motion, spherical droplets collide, coalesce and grow. This model corresponds to a diffusion limited growth because the time between two coalescence events is limited by droplet diffusion. In this case, the drop size obeys the asymptotic growth law $r \sim t^{1/3}$, where t is the time. The "fast" growth dominates at later times and is explained using a coalescence mechanism, which assumes that the droplets interact more strongly due to a lubrication flow. When two droplets coalesce they also induce another nearby droplet to coalesce through the lubrication flow. Subsequent coalescences follow each other and the average radius of the drop pattern grows more rapidly. If droplets are close together the hydrodynamic interaction may generate successive coalescence that creates the interconnected pattern. This mechanism is valid only when the volume fraction is high, so that the droplets are closely packed.

The basic idea of the numerical simulation of the drop coalescence [Nikolayev *et al.*, 1997] is that at the beginning of the simulation, the coalescence starts between two drops of size R that are at a distance ψ that corresponds to the interface thickness of the drop [Siggia, 1979]. Consider another drop at distance d_o from the spherical shell, which is defined as an aggregate of two coalescing drops (Figure 1.5.5.B).
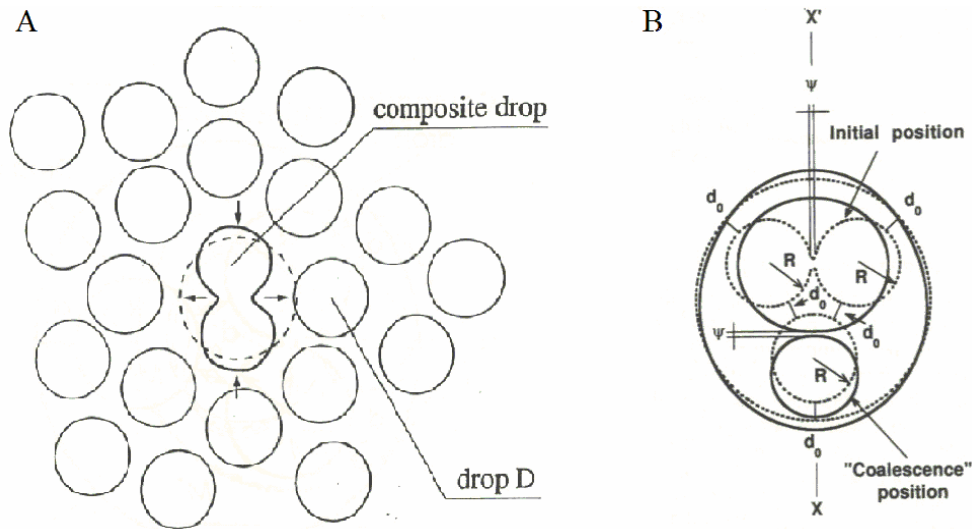
Figure 1.5.5. **Schematic representation of the drops pattern undergoing coalescence [Nikolayev, 1997].** (A) Droplets coming closer than a critical distance get into contact and then relax to a spherical surface to minimize the surface tension. (B) The position of the drop surfaces at the beginning (dotted line) and the end (solid line) of the simulation. ψ is the coalescence distance and d_0 is the initial distance between the drops.

The distance between the drops and the shell was also chosen to be d_o. The first important result in the simulation is that the first coalescence facilitates the coalescence between the composite drop and the neighboring drops. At the beginning of the evolution, two droplets are considered at a distance smaller than ψ and, as a result, they form a "composite drop". A nearby drop D (Figure 1.5.5A) is pushed away and deforms the spherical shell. As a result, the shell undergoes a deformation and then relaxes because the surface tension is finite. Consequently, the composite drop and the neighboring drops will approach each other during this stage. This means that the lubrication interactions with the surrounding drops cause the composite and the neighboring drops to attract each other. This process of coalescence-induced-coalescence is possible only when the distance between drops is less than a critical value [Nikolayev *et al.*, 1997]. Using this model, it was proved that the growth law is linear and the pattern is interconnected.

1.6. Hydrodynamic model of phase separation

Phase separation dynamics for pure fluids and binary mixtures is a nonequlibrium process exhibiting features such as domain growth and pattern formation. In a typical experiment, a system in a homogeneous state is quenched inside the coexistence curve. Depending on the quench position, two different patterns could appear: for a near critical quench, convoluted domains of each component are formed; while in an off critical quench, droplets of minority phase form within the majority phase background. A Brownian mechanism was first considered by Smoluchovchi [von Smoluchowski, 1917] for coagulation of colloids. According to such a model, the droplets collide during their Brownian motion and the total surface energy of the system is lowered. This model was applied by Binder and Stauffer [Binder, 1974] and Siggia [Siggia, 1979] by considering a drop of radius a_1, fixed at the origin of the reference frame, in an uniform cloud containing n_2 drops of radius a_2 per volume (see Figure 1.6.1).
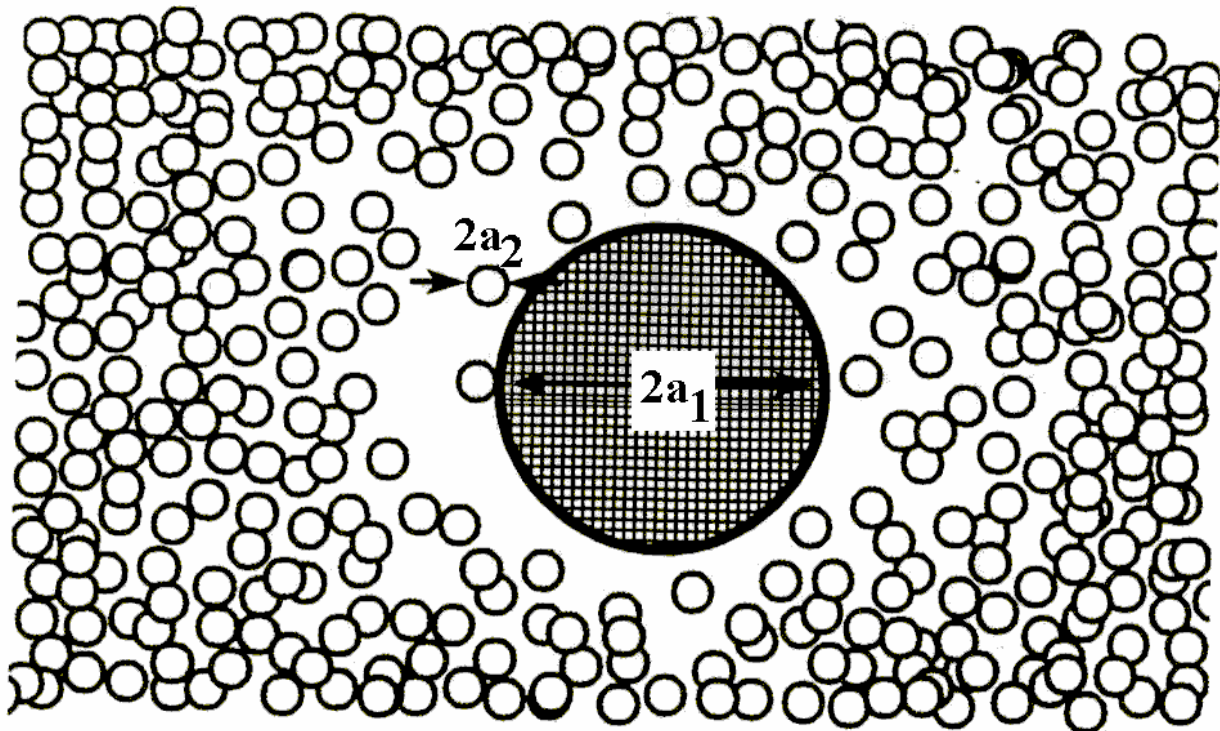
Figure 1.6.1. Schematic representation of drops growth mechanism based on Brownian motion mechanism [Hegseth *et al.*, 1998].

At steady state, the radial distribution of the drops follows from a solution of:

$$\nabla^2 n_2 = 0, \tag{1.6.1}$$

with boundary conditions $n_2 = 0$ at $r = a_1 + a_2$ and $n_2 = n_0$ at $r \to \infty$. The solution is

$$n_2(r) = n_0[1 - (a_1 + a_2)], \tag{1.6.2}$$

and the flux (I) of particles at $a_1 + a_2$ is given by:

$$I = \int D_2 \frac{dn_2}{dr} \Big|_{r=a_1+a_2} da = D_2 4\pi n_0 (a_1 + a_2), \tag{1.6.3}$$

where $D_2 = \dfrac{K_B T}{6\pi\eta a_2}$ is the diffusion constant of the spherical drop undergoing Brownian

motion and I is the total number of drops of radius a_2 colliding with all fixed drops of radius a_1 per unit time. Considering the interaction between the two populations of drops during their motion, the total flux of particles is:

$$I = I_1 + I_2 = 4\pi(D_1 + D_2)(a_1 + a_2)n_1 n_2. \tag{1.6.4}$$

Let us consider the following simplified case:

$$D_1 = D_2 = D; \; n_1 = n_2 = n; \; a_1 = a_2 = \langle a \rangle. \tag{1.6.5}$$

Using the flux given by (1.6.4) and the conditions (1.6.5), the stationary distribution of the number of particles is

$$\frac{dn}{dt} = -16\pi D\langle a \rangle n^2. \tag{1.6.6}$$

Since $D<a>$ is time-independent, the solution of (1.6.6) is

$$a^3 - a_0^{\,3} = 12D\langle a \rangle(t - t_0), \tag{1.6.7}$$

or $a \propto t^{1/3}$. The previous argument did not consider the hydrodynamic interaction between the drops. Siggia [Siggia, 1979] found by considering the hydrodynamic interaction that the relative diffusion constant is smaller than the one used above and depends on the separation between the drops. According to Siggia, the corrected rate of collision per unit volume due to Brownian motion is

$$N_B = 16\pi Dan^2 f(\phi), \tag{1.6.8}$$

where the factor $f(\phi)$ accounts for the hydrodynamic effect. This factor is related to the ratio of the viscosities of the liquids inside and outside the drops and the average distance between drops and, therefore, depends on volume fraction ϕ. Zang and Davis [Zang, 1991] calculated this

correction in the dilute limit. Near the critical point, the viscosities of the two phases are equal and the factor $f(\phi)$ is equal to 0.56. The number of droplets decreases as a result of coalescence with the rate

$$\frac{dn}{dt} = -N_B.$$
(1.6.9)

The hydrodynamic approach was used to explain the kinetics of the interconnected domain and the origin of t^1 growth law by Siggia [Siggia, 1979]. He associated the growth rate with the rate of evolution of the unstable fluctuations.

Another research group used the coupled equation of hydrodynamics and diffusion to explain the motion of droplets caused by a concentration gradient. They did not consider the translational motion due to the pressure gradient which is very important when we have a high volume fraction [Kawasaki, 1983].

Nikolayev [Nikolayev *et al.*, 1996, 1997] developed a different approach by suggesting that coalescence between two drops induces coalescence when the distance between the drops is less then the coalescence limit, resulting in a chain reaction of coalescence. They use the term "coalescence-induced-coalescence", which was first introduced by Tanaka [Tanaka, 1994]. The surface tension of drops is considered to be the same for all interfaces. If the drops are close enough and the distance does not exceed the coalescence limit, then in the presence of the lubrication forces the droplets interact and a new elongated droplet is produced (see figure 1.6.2).
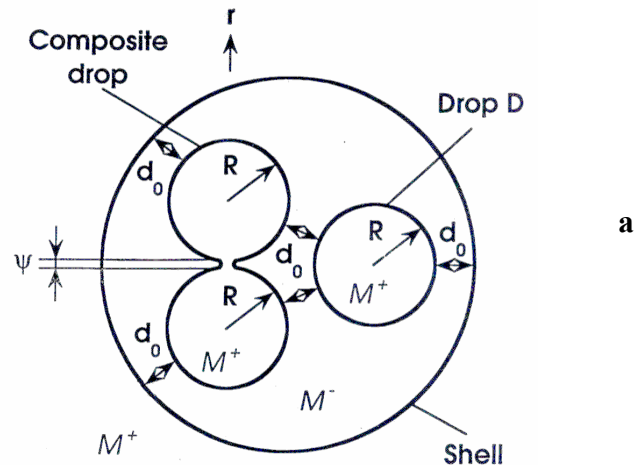
Figure 1.6.2.   Schematic representation of a shell model [Hegseth *et al.*, 1998].

At a high volume fraction, the droplets are tightly packed and the composite drops do not have time to relax so another coalescence take place resulting in an interconnected pattern (see figure

1.6.2). On the other hand, if the droplets are far apart ($d_0/R \gg 1$), the second coalescence never occurs. The average coalescence time is the time between consecutive coalescences

$$t_c = \alpha \eta R / \sigma, \tag{1.6.10}$$

where σ is the surface tension coefficient, η is the coefficient of viscosity, R is the droplet's radius, and α is the coalescence constant. The volume fraction, ϕ, of the minority phase is related to d_0/R by:

$$\phi = b[1 + d_0 / 2R]^{-3}, \tag{1.6.11}$$

where b is a constant depending on the spatial arrangement of the drops. In the coalescence-induced-coalescence model, the radius of the droplets grows with each coalescences according to the following recursive relationship

$$R^{(i+1)} = \beta R^{(i)}, \tag{1.6.12}$$

where $\beta \sim 1.1$. After n successive coalescences the time and the droplet radius are:

$$t = t_c^{(0)} + t_c^{(1)} + t_c^{(2)} + t_c^{(3)} + ... + t_c^{(n-1)} = (\alpha \eta / \sigma)[R^{(0)} + R^{(1)} + R^{(2)} + ... + R^{(n-1)}] \Leftrightarrow$$

$$t = (\alpha \eta / \sigma)R^{(0)}(1 - \beta^n) / (1 - \beta), \tag{1.6.13}$$

and

$$R = \beta^{(n)} R^{(0)} = R^{(0)} + (\beta - 1)(\sigma / \eta)t. \tag{1.6.14}$$

The last equation shows the linear time dependence of the droplet's radius specific for packed domains. Nikolaev [Nikolayev et al., 1996] explained the decrease in the number of droplets through a competitive mechanism between the Brownian diffusion and hydrodynamic interactions. According to Nikolayev [Nikolayev et al., 1997], the rate of change of droplets is

$$\frac{dn}{dt} = -(N_B + N_H). \tag{1.6.15}$$

In practice, for $\phi > \phi_H$, the droplets grow according to the hydrodynamic mechanism. For $\phi < \phi_H$, the droplet's growth is determined only by the Brownian interaction. The transition between the two regimes is sharp and occurs at the threshold volume fraction $\phi = 0.26$. As the authors mentioned [Nikolayev et al., 1997], this model applies to any system involving growth of droplets due to coalescence of liquid drops inside another fluid.

1.7.   Image processing background

With computers becoming less expensive and more powerful, applications for image processing have become widespread [Jahne, 1997]. An image is a function f of two variables (x, y) that represent the plane coordinates. The amplitude $f(x, y)$ is called the intensity or gray level of the image at point (x, y). The amplitude of a given image will be an integer or a real number. The former is a result of quantization process that converts a continuous range to a discrete number of gray levels. The two-dimensional continuous image $f(x,y)$ is divided into N rows and M columns. The intersection of a row and a column is called a pixel (see figure 1.7.1).
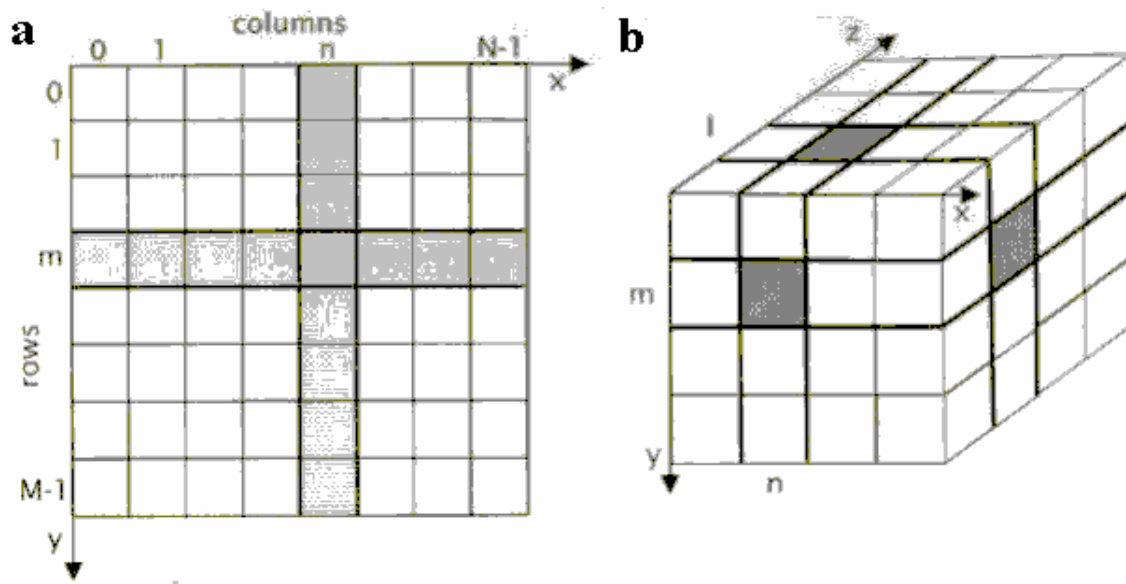
Figure 1.7.1.   Schematic representation of digital images. (a) Discrete arrays with two indices represent a rectangular grid assimilated to a two-dimensional image and (b) array with three indices are assimilated to a three-dimensional image [Jahne, 1997].

Each pixel has an associated value that represents the average brightness or gray level for a monochromatic image. With a large pixel size, the spatial resolution is poor and the gray value discontinuities are significant. On the other hand, for a small pixel size the effect becomes less intense for the visual system. A histogram of a digital image is a discrete function $g(r_k) = n_k$ where r_k is the kth gray level and n_k is the number of pixels in the image with gray level r_k. The histogram can be normalized by dividing each value by the total number of pixels n. The gray level in a given image can be seen as a random variable in the interval $(0, 1)$. The descriptor of a

continuous variable is its probability density function (PDF). The general characteristics for an image can be extracted from the density probability function of its gray level. As an example, predominantly dark images would have a PDF like the one shown in Figure 17.2 a, while the PDF of a bright one would most likely resemble the one in Figure 1.7.2b.
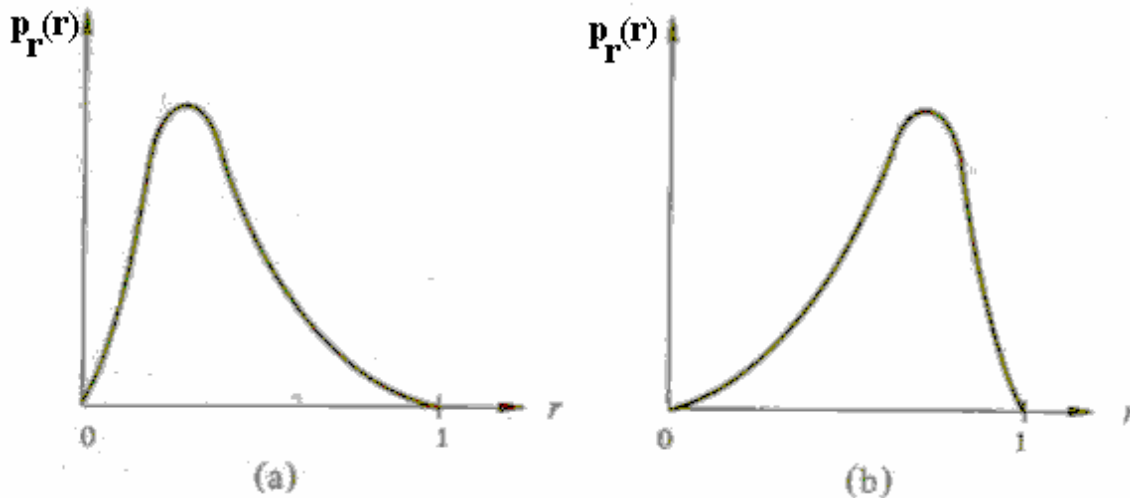
Figure 1.7.2. Normalized histograms for two-dimensional images. Gray level probability density function of (a) a "dark" image, and (b) a "light" image [Jahne, 1997].

Histograms are the basis for many spatial processing techniques useful in image enhancement [Jain, 1990; Gonzalez, 2002]. The purpose of image enhancement is to perform a series of operations such that the final image is more suitable for a specific application than the original. Image enhancement is classifiable into two broad categories: 1) spatial domain and 2) frequency domain methods. The spatial domain methods are related to direct pixel manipulation in an image. The frequency domain processing techniques operate on the Fourier transform of an image. Spatial filtering is an operation done directly on an image. One of the objectives for this method is noise reduction [Gonzalez, 2002]. The process of spatial filtering using an average filter consists in moving the filter from point to point in an image and averaging the pixels within a small neighborhood. By replacing the value of every pixel with an average value, the final image would have less of a sharp transition in the gray level. In this case, the filter produces isotropic smoothing and there is no shift in the image location. An undesirable effect in using a moving average filter is blurring of edges. A spatial averaging filter in which all the coefficients are equal is called a box filter. Here is a simplified example of a 3x3 box filter:

$$R = \frac{1}{9} \times \begin{vmatrix} 1 & 1 & 1 \\ 1 & 1 & 1 \\ 1 & 1 & 1 \end{vmatrix}.$$

The local smoothing effect depends on the filter size. As an example, for a filter size of A = 3(3=number of rows=number of columns), the image blurring would be limited to "this dimension". The effects of smoothing using filter of variable size are illustrated in Figure 1.7.3. Only details that are approximately the same size as the filter are affected because the size of the filter establishes the relative size of the objects that will be blended with the background. The purpose of this operation is to eliminate objects based on their intensity [Gonzalez, 2002]. A complementary enhancement of digital images uses frequency domain manipulations. The mathematical tools used to represent image processing in frequency domain are related to the Fourier Transform (FT). The FT produces another representation of a signal, specifically a representation as a weighted sum of complex exponentials. Because of Euler's formula:

$$e^{jq} = \cos(q) + j\sin(q), \tag{1.7.1}$$

where $j^2 = -1$, we can say that the FT produces a representation of a two-dimensional image as a weighted sum of sine and cosine functions. The defining formulas for the continuous forward Fourier and the inverse transforms [Hecht, 2000] are as follows.
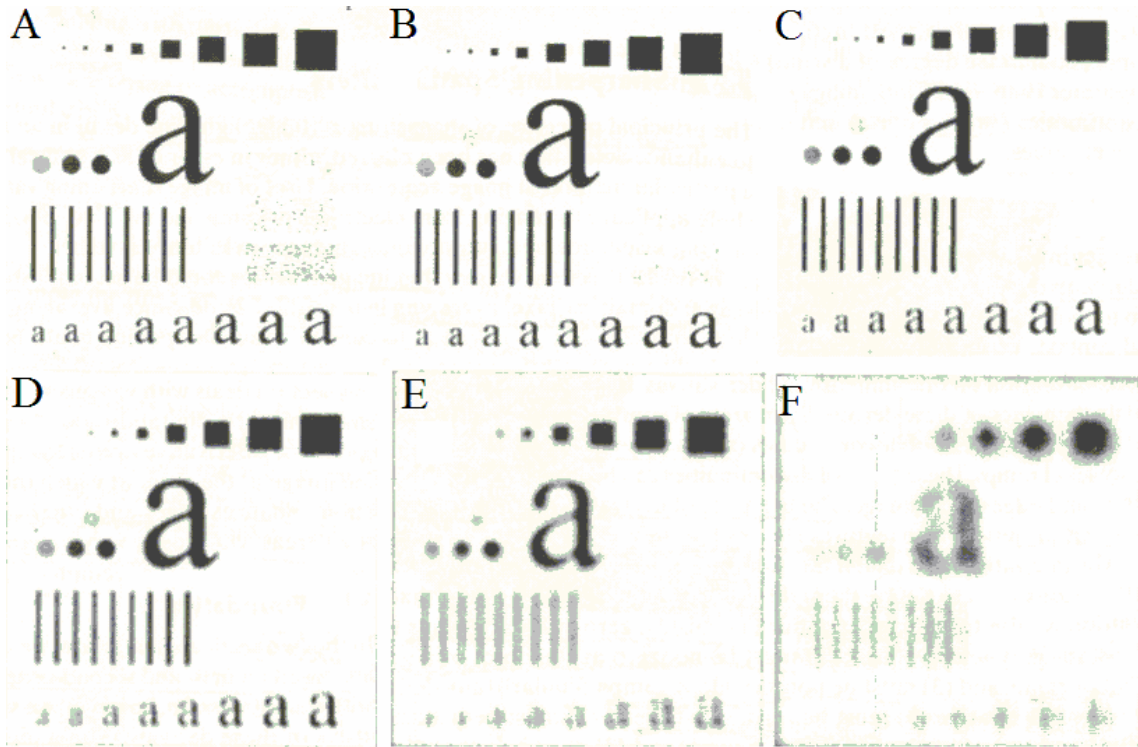
Figure 1.7.3. Image noise reduction using averaging filter. Result of smoothing of the original image (500x500 pixels) with an average filter mask of sizes A = 3, 5, 9, 15, 35 and 45 [Gonzalez, 2002].

Forward:
$$F(u,v) = \int\limits_{-\infty}^{+\infty}\int\limits_{-\infty}^{+\infty} f(x,y)e^{-j(ux+vy)}\,dx\,dy\,. \qquad (1.7.5)$$

Inverse:
$$f(x,y) = \frac{1}{4\pi^2}\int\limits_{-\infty}^{+\infty}\int\limits_{-\infty}^{+\infty} F(u,v)e^{-j(ux+vy)}\,du\,dv\,. \qquad (1.7.6)$$

The corresponding Fourier transforms for a two-dimensional discrete data are:

Forward:
$$F(\Omega,\Psi) = \sum_{m=-\infty}^{\infty}\sum_{n=-\infty}^{\infty} f[m,n]e^{-j(\Omega m+\Psi n)}\,. \qquad (1.7.7)$$

Inverse:
$$f[m,n] = \frac{1}{4\pi^2}\sum_{\Omega=-\infty}^{\infty}\sum_{\Psi=-\infty}^{\infty} F(\Omega,\Psi)e^{j(\Omega m+\Psi n)}\,. \qquad (1.7.8)$$

The following are some of the most relevant properties of Fourier transforms for digital image processing.

1) The Fourier transform is, in general, a complex function of the real frequency variables. The transform can be written in terms of its magnitude and phase.

$$F(u,v) = |F(u,v)|e^{j\varphi(u,v)}, \qquad\qquad F(\Omega,\Psi) = |F(\Omega,\Psi)|e^{j\varphi(\Omega,\Psi)}. \qquad (1.7.9)$$

2) A 2D image can also be complex and thus written in terms of its magnitude and phase.

$$f(x,y) = |f(x,y)|e^{j\phi(x,y)}, \qquad\qquad f[m,n] = |f[m,n]|e^{j\phi[m,n]}. \qquad (1.7.10)$$

3) A 2D real image, f [m, n] has a Hermitian Fourier transform F(Ω, ψ).

$$F(u,v) = F^*(-u,-v), \qquad\qquad F(\Omega,\Psi) = F^*(-\Omega,-\Psi). \qquad (1.7.11)$$

The symbol (*) indicates the complex conjugate. For real images, the magnitude is even and the phase is odd:

$$|F(u,v)| = |F(-u,-v)|, \qquad\qquad \varphi(u,v) = -\varphi(-u,-v). \qquad (1.7.12)$$

$$|F(\Omega,\Psi)| = |F(-\Omega,-\Psi)|, \qquad\qquad \varphi(\Omega,\Psi) = -\varphi(-\Omega,-\Psi). \qquad (1.7.13)$$

4) If a 2D image is real and even, then the Fourier transform is real and even.

$$F(u,v) = F(-u,-v), \qquad\qquad F(\Omega,\Psi) = F(-\Omega,-\Psi). \qquad (1.7.14)$$

5) The Fourier transform in discrete space, $F(\Omega,\Psi)$, is periodic in both Ω and Ψ. Both periods are 2π.

$$F(\Omega + 2\pi j, \Psi + 2\pi k) = F(\Omega,\Psi), \qquad (1.7.15)$$

with *j, k* integers.

If Δx and Δy are the spatial sample intervals then the frequency sample intervals Δu and Δv are given by:

$$\Delta u = \frac{1}{M\Delta x}, \qquad\qquad \Delta v = \frac{1}{N\Delta y}, \qquad (1.7.16)$$

where *M* and *N* represent the image size in pixels.

An example of a connection between spatial and frequency domains is shown in Figure 1.7.4.
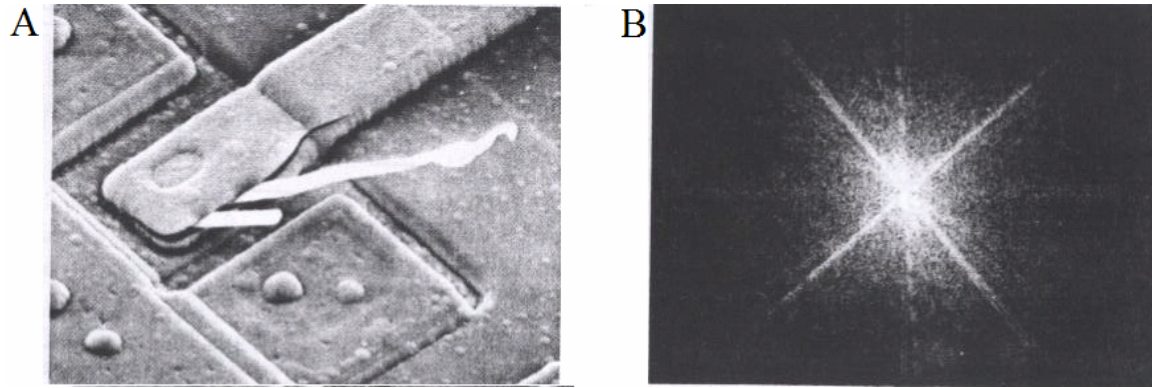
Figure 1.7.4. A damaged electric circuit (A) and its Fourier spectrum (B) [Gonzalez, 2002]. This is a typical association between spatial and frequency domain.

2. Fluctuations and phase separation

2.1. Pure fluids

A large number of experiments dealing with the critical behavior of gas-liquid mixtures and binary fluid systems have been performed. Many experiments used light scattering to visualize the fluctuations of the fluid's density. Fluids near the critical point are affected by gravity because the compressibility of the fluid is very large near the critical point. Therefore, due to the gravitational field, the fluid compresses under its own weight and stratifies. Any measurements of thermodynamics properties made on a cell of finite height in a gravitational field will actually measure a macroscopic average property of the fluid over different densities rather than the precise property approaching the critical point. Experiments in microgravity eliminate the complication due to the fluid compressibility near the critical point. Therefore, space experiments have enabled new phenomena to be discovered as a result of the removal of convection, sedimentation and buoyancy phenomena.

Density fluctuations cause local deviations in the intensity of transmitted or scattered light from the average intensity of the image. The visualization of fluctuations provides important information about the statistical physics of cooperative phenomena that take place at the microscopic level. Near the liquid-gas critical point, the density fluctuations determine the fluctuations in the transmitted or scattered light through a transparent medium and, therefore, can be directly observed using microscopy techniques. In Earth-based experiments, the average size of fluctuations is limited by gravity. In the microgravity environment, direct fluctuation in space and time were recorded by using the ALICE II instruments. We present results of microscopic density fluctuations of pure fluids under microgravity conditions. There were five different experiments performed on the Mir space station (see section 2.1.1). The fifth experiment on growth and morphology in supercritical fluids (GMSF) was dedicated to phase separation [Hegseth *et al*., 2000].

2.1.1. Experimental setup

The study of fluctuation growth and their morphology in supercritical fluids (GMSF) was the subject of a series of experiments onboard the Mir space station. The purpose of the experiments was to study the behavior of liquid-gas mixtures very close to their critical point. These experiments were performed on the Mir space station between December 12, 1998 and January 8, 1999 using the ALICE II facility. A series of seven experiments were performed to study the following three topics:

1) Boiling

2) Phase separation

3) Fluctuations.

In the boiling experiments, a two-phase liquid-gas mixture consisting of a single bubble was heated to a supercritical state above the critical temperature. In some cases, the gas bubble was slightly pushed against the side-wall of the cell to vary the gas pressure and in other cases it was not.

In the phase separation experiments, a fluid above the critical temperature was quenched by quickly decreasing its temperature such that a minority phase of droplets grew inside the majority phase. Because liquids always wet a solid surface, these experiments were arranged so that the gas bubbles grew inside the liquid phase.

Finally, the fluctuation experiments visualized the density fluctuations very close to the critical point. These seven experiments used five different cells that were enclosed in thermostats. Tables 2.1.1.1 and 2.1.1.2 summarize the relevant information concerning the cells used in these experiments [Hegseth *et al*., 2000].

Table 2.1.1.1. The geometric characteristic of the cells used in microgravity conditions along with the corresponding fluids under investigation and the type of constrains (constant or variable volume).

Thermostat	Fluid	Properties	Cell thickness (mm)
Th31	SF_6	constant volume no thermistors	3.016
Th33	SF_6	constant volume no thermistors	1.664
Th34	SF_6	variable volume, 3 thermistors	4.340
Th37	CO_2	variable volume, 3 thermistors	2.204
Th38	SF_6	variable volume, 3 thermistors, immersion micro.	1.000

Table 2.1.1.2. Different experiments performed using the thermostats listed in Table 2.1.1.1. Each experiment was designed with an appropriate order parameter value for the purpose of studying specific critical phenomena (boiling, phase separation, and fluctuations).

Exp. No.	Thermostat	Duration	Order parameter $M=(\rho-\rho_c)/\rho_c$	Boiling	Phase Separation	Fluctuations
1	37	4 h	0	X		
2	33	3 h	0.7%	X		
3	31	5 h 39 min	0.2%	X		
4a	37	4 h	1.87%	X		
4b	37	4 h	4.90%	X		
5	34	206 h	0.02 & 0.46%	XX	XX	
6	37	4 h	-3.5%	X		
7	38	234 h	0%	X	X	X

The fluctuation and phase separation in the supercritical fluid was visualized in the fifth experiment performed using the cell and thermostat number 34 (Th34). The cell containing the fluid under study consisted of a cylindrical shell made of a thin copper alloy encapsulating a layer of SF_6 sandwiched between two sapphire windows (Fig. 2.1.1.1).
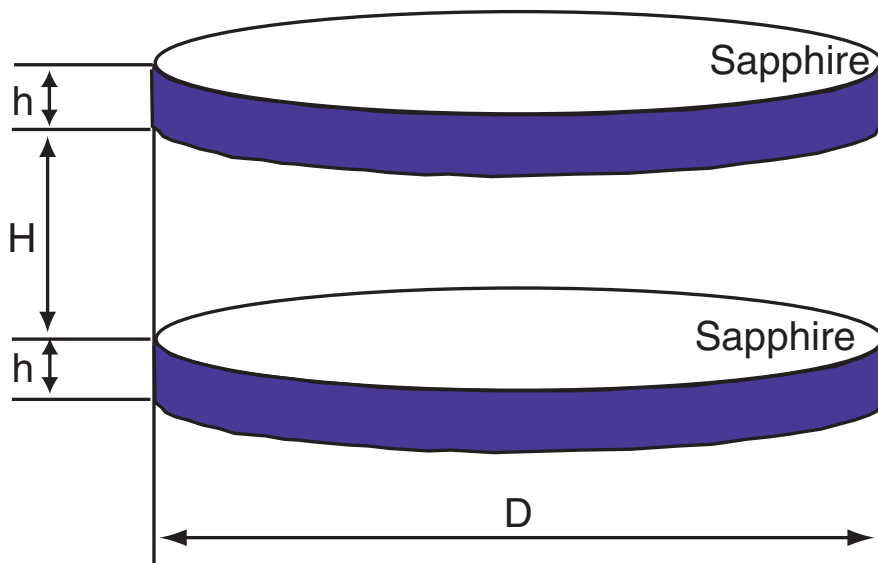
Figure 2.1.1.1. A schematic representation of the experimental cell encapsulating a layer of SF$_6$ between two sapphire cylinders. The thickness of the sapphire windows was h = 10 mm and the thickness of the fluid is listed in Table 2.1.1.1. same as cell and thermostat 34.
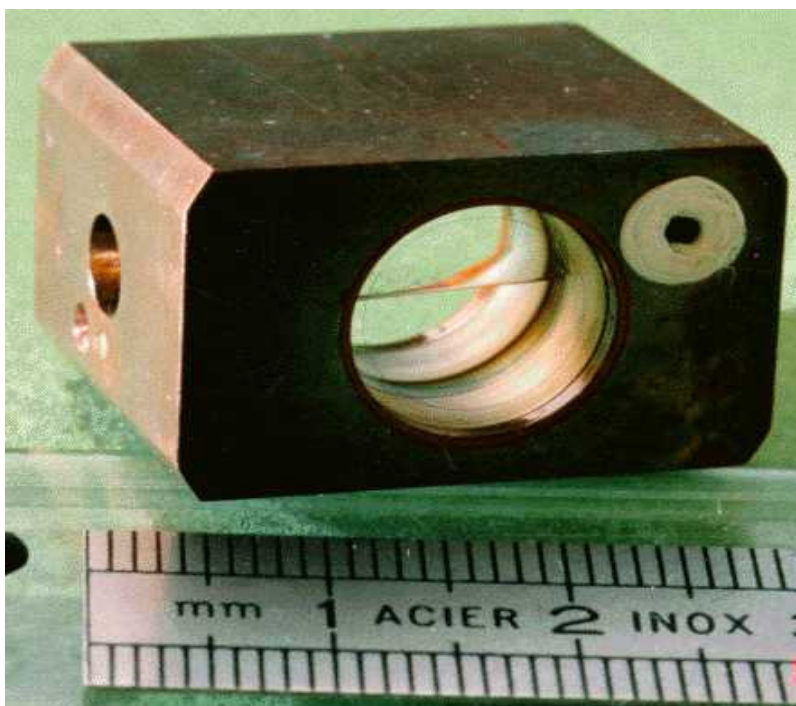
Figure 2.1.1.2. Sample cell unit (SCU) containing a fluid between two sapphire windows and a CuBeCo alloy housing.

The diameter of the cylindrical cell containing thermostat Th34 is $D = 12$ mm, the thickness of the SF$_6$ layer is $H = 4.34$ mm, and the aspect ratio is $\Gamma = D/L = 2.765$. One of the advantages of the thick cell is that the phase separation can be observed for a long time and the clusters of the minority phase can grow to a large size before wetting effects from the wall can influence them. Another advantage of the tick cells is that they allow the three thermistors to be located away from any thermal boundary layer that may exist at the walls. The volume enclosed by the cylindrical cell contained pure fluid with a density close to the critical density (see Table 2.1.1.2). This cell is placed inside of a copper sample cell unit (Fig. 2.1.1.2) that is, in turn, placed inside a thermostat (Fig. 2.1.1.3). The thermostat is especially designed for thermal control and aligned with the ALICE II optical instrument.
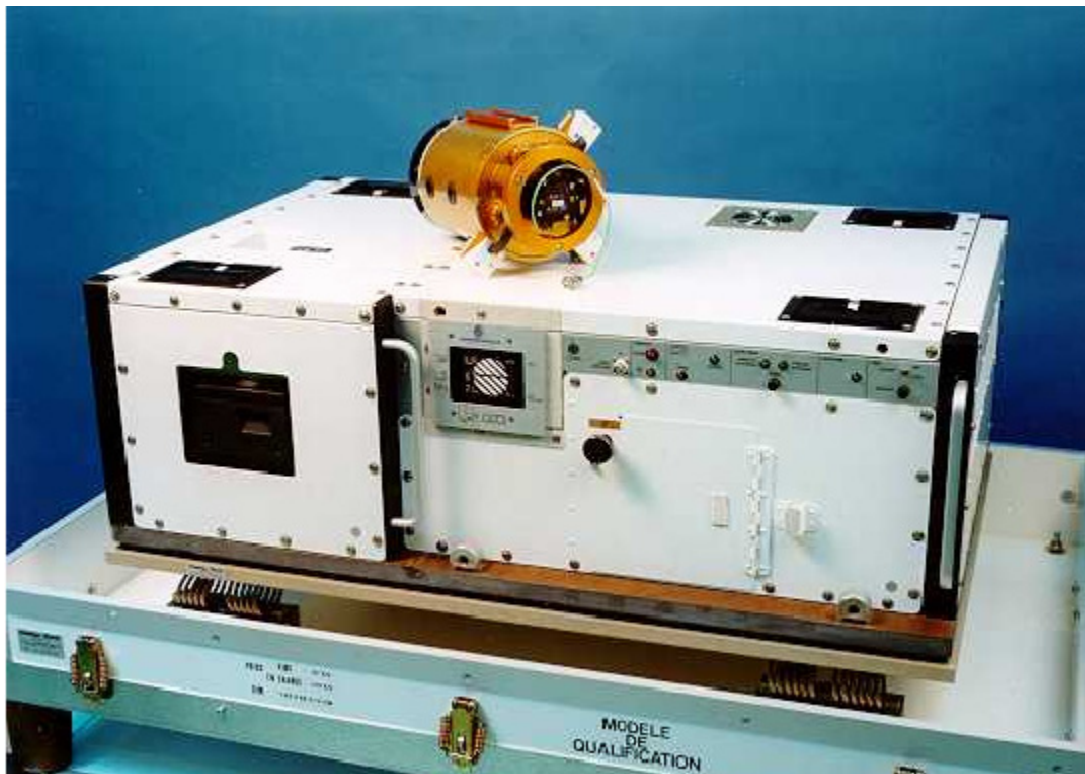
Figure 2.1.1.3.   ALICE II external view. An ALICE II instrument contains the thermostat, SCU and the optical apparatus.

The thermostat is specially designed to ensure a precise thermal control and is aligned with the optical instruments. The high precision temperature control is accomplished using three concentric thermal shields (Figs. 2.1.1.3 and 2.1.1.4). The inner shield has a foil heater around it

and a thermistor for thermal control. It also contains the SCU and six Peltier elements in contact with the SCU for thermal control. The SCU also uses two types of thermistors, one for temperature control and the other for temperature measurement, T_m. The thermistors Th1, Th2, Th3 are located inside the cell as shown in Fig. 2.1.1.5.
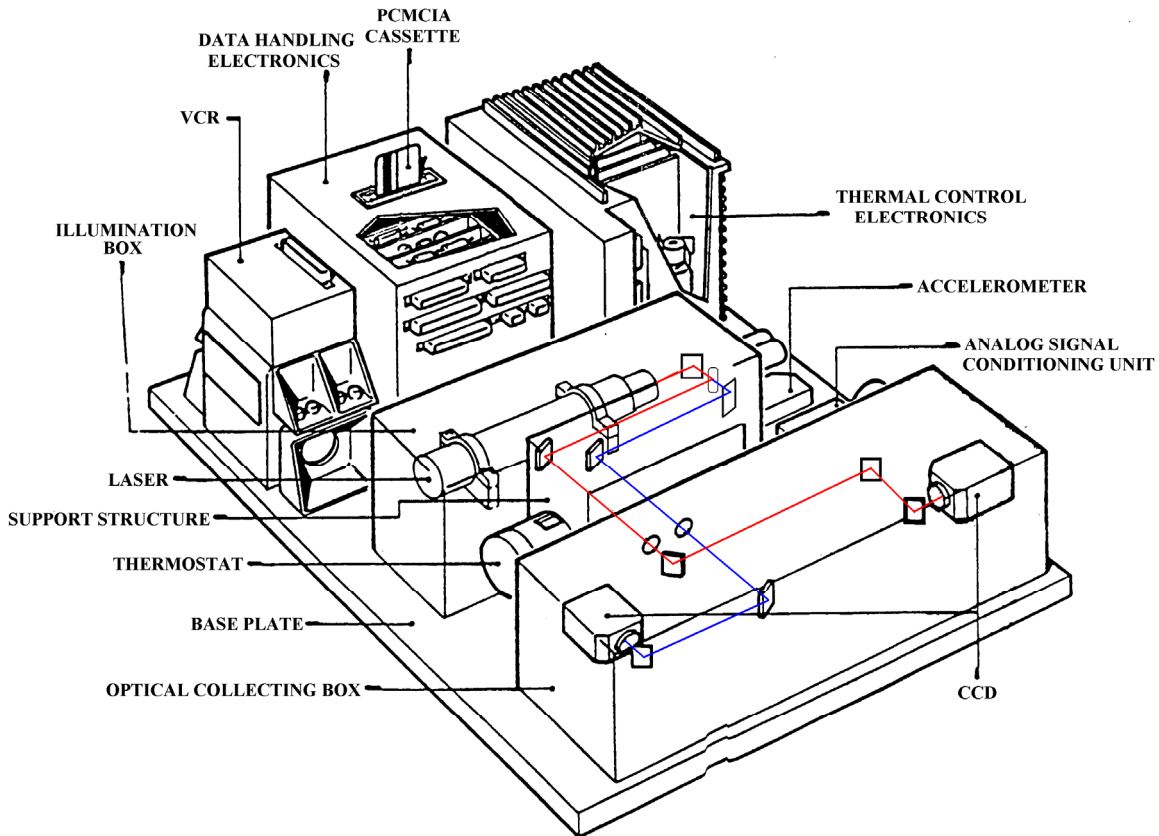
Figure 2.1.1.4. Physical layout of ALICE II instruments.

Several sets of thermal quenches were performed from the one phase region into the two phase region that resulted in phase separation. The SF_6 cell marked Th34 (Table 2.1.1.1) was used twice in two runs of the GMSF experiment. The first set of quenches consisted of a large 3.6 mK temperature quench through the expected critical temperature T_c. The second set of experiments consisted of 0.3 mK temperature quenches that stepped through the same temperature interval as the large quench. The third set of experiments consisted of 0.1 mK quenches (the lower limit of ALICE II's temperature measurement) that stepped through the same temperature range. The density of the cell was initially prepared at the critical density with the order parameter M = (ρ-

45

$\rho_c)/\rho = 0.0\pm0.02\%$, and at M = 0.46%. The first run at this density produced two kinds of fluid separation, one in the large temperature quench of 3.6 mK (Fig. 2.1.1.6) and the other in the last 0.3 mK temperature quench. The large temperature quench (3.6 mK) is shown in Fig. 2.1.5.

Figure 2.1.1.5. Full view of cell image. The image recorded by a CCD camera showing the full view of the cell and the locations of the three thermistors (Th1, Th2, Th3) inside the cell. These thermistors are all at approximately the same temperature.
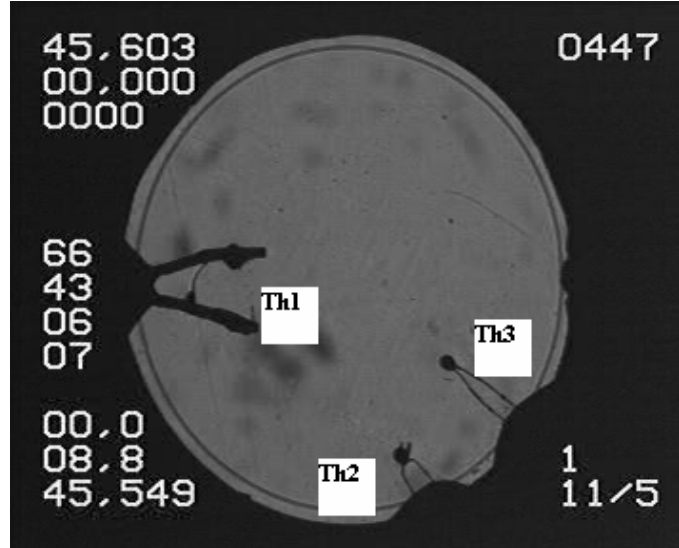
The thermistors Th$_1$, Th2, and Th$_3$ are all at approximately the same temperature. The measurement thermistor T$_m$ was placed inside the SCU such that T$_m$ represents only approximately the temperature inside the fluid phase.
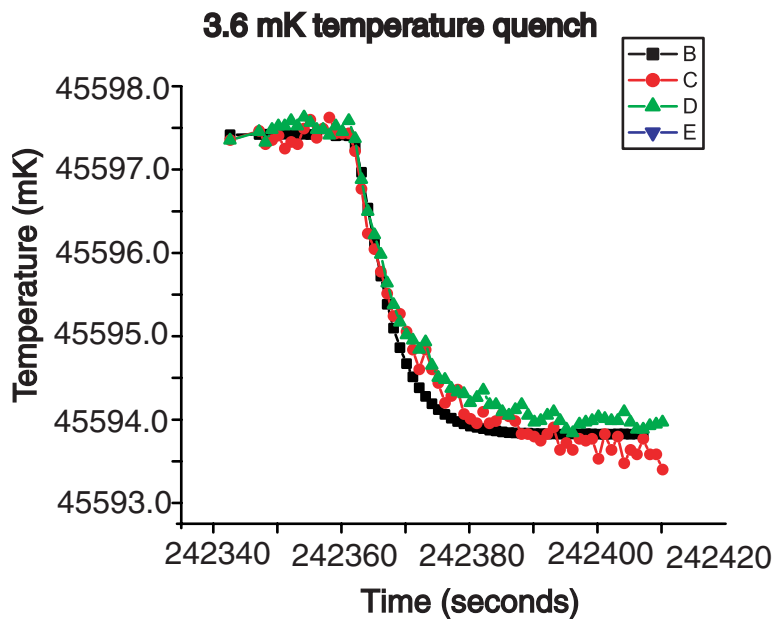
Figure 2.1.1.6. Time course of the temperature inside the fluid phase during the large temperature quench (3.6 mK). The error in temperature measurement by internal thermistors Th$_1$ (C), Th$_2$ (D), and Th$_3$ (E) is of the order of 1 mK. Thermistor T$_m$ recordings are plotted with black square (B).

The second set of quenches resulting in the 0.3 mK temperature quench through the critical temperature did not result in homogeneous separation of the fluid. The 0.3 mK quenches stepped in the same range as the large 3.6 mK quench (Fig. 2.1.1.7). Because the fluid separated on the last 0.3 mK quench, we concluded that the critical temperature T_c was very near the bottom of the 3.6 mK range of the first large quench.

The last quench in the series of 0.3 mK quenches recorded by T_m steps through the critical temperature T_c (Fig. 2.1.1.7.B). Near the critical point, the minority domain grows directly from the fluctuations. The density fluctuations are visualized through light transmission normal to the windows using a LED light source at 633 nm and an optical microscope of a 3.1 μm resolution.
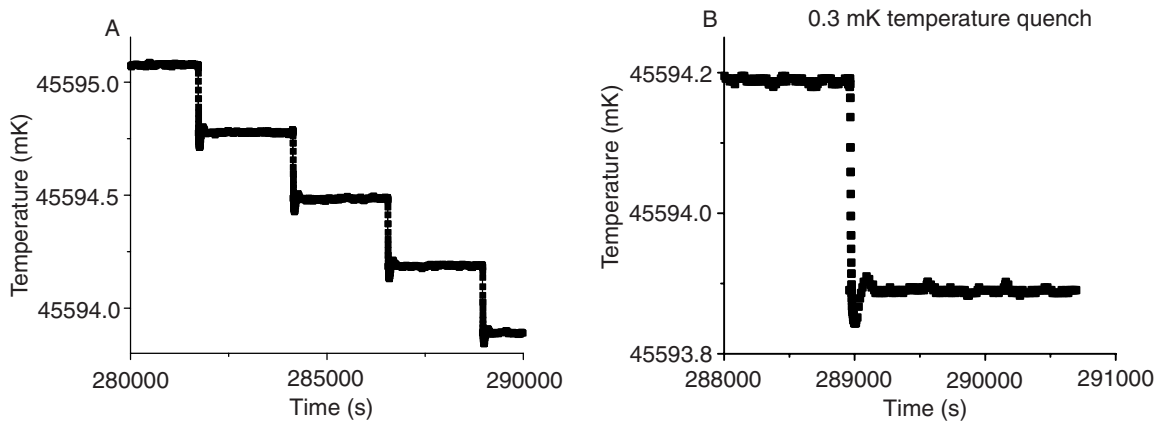
Figure 2.1.1.7.   Multiple small temperature quenches (0.3 mK) inside a large (3.6 mK) temperature quench. (A) Time course of the temperature inside the fluid phase during the 3.6 mK temperature quench. (B) The last 0.3 mK quench is important in the study of fluctuations because it steps through the critical temperature.

2.1.2 Methods

The pure fluid under investigation was SF_6, which exhibits critical behavior when both the temperature and the density are near the critical point. The pure fluid is placed in a constant volume cell (see section 2.1.1.). The increase in the fluctuations correlation size is manifested by an increase in the intensity of the scattered light. When the fluctuation size approaches the size of the light's wavelength, the density fluctuations strongly scatter light. This phenomenon produces the visual effect called critical opalescence [Andrew, 1869; Stanley, 1971]. In this microgravity experiment using SF_6, the temperature of the working fluid is quenched from a one-phase supercritical fluid (above the critical temperature) to a two-phase mixture (below the critical temperature). The same cell filled with SF_6 was used for two runs consisting of two sets of temperature quenches. The first set consisted of a large 3.6 mK temperature quench and the second set consisted of temperature quenches of 0.3 mK that stepped through the same range as the large quench. Before the 3.6 mK temperature quench, the cell was maintained at 1 K above the critical temperature T_c until it equilibrated to a homogeneous state. This procedure was repeated for 0.3 mK temperature quenches protocol.

Figure 2.1.2.1. Temperatures measured at the copper sample cell by the measurement thermistor at successive time intervals for the 0.3 mK temperature quench. Each square corresponds to a recorded image and successive frames were captured 33 ms apart.
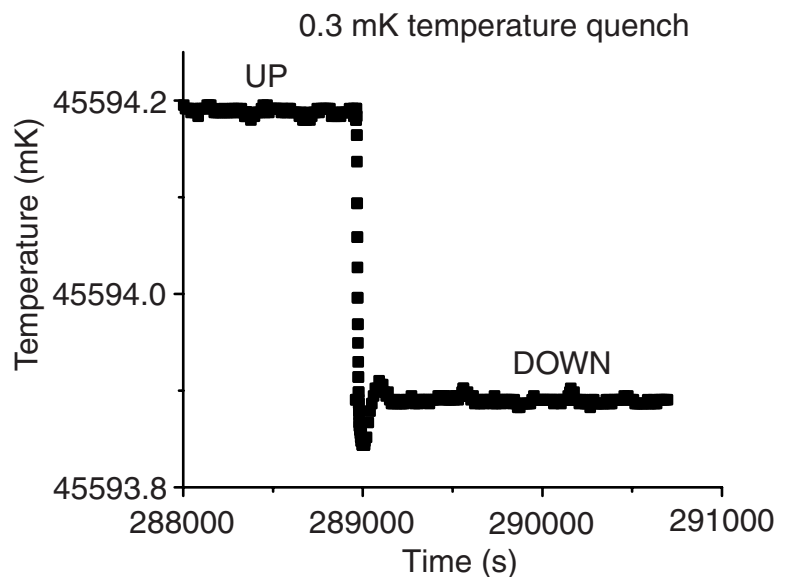
In the case of the 0.3 mK temperature quench experiment, the images were divided in two groups: the "Up" group that corresponds to the plateau marked UP on Fig. 2.1.2.1 and the "Down" group that corresponds to the plateau marked DOWN on Fig. 2.1.2.1. For the "Up"

region, we captured 200 frames from the original video record, while the "Down" region contains 575 frames. The time interval between successive frames is 3.3 ms. The video recording for the 0.3 mK temperature quench experiment started when the fluid was very turbid due to critical opalescence. The spatial size of fluctuations grew on the last part of the "Down" plateau and eventually the fluid separates into gas and liquid phases.

2.1.2.1. Image before enhancement

The spatial and temporal fluctuations in pure fluids were video taped and stored in MPEG format using the ALICE II instruments on the Mir space station during the fifth experiment of GMSF. ALICE II is a specially designed device for the study of the thermodynamic properties of transparent media by optical methods. The ALICE II device is equipped with high precision thermometry to precisely place the fluid near the critical point. ALICE II automatically tagged the time and the temperatures at the copper sample cell and critical temperature for the pure fluid on each video frame.
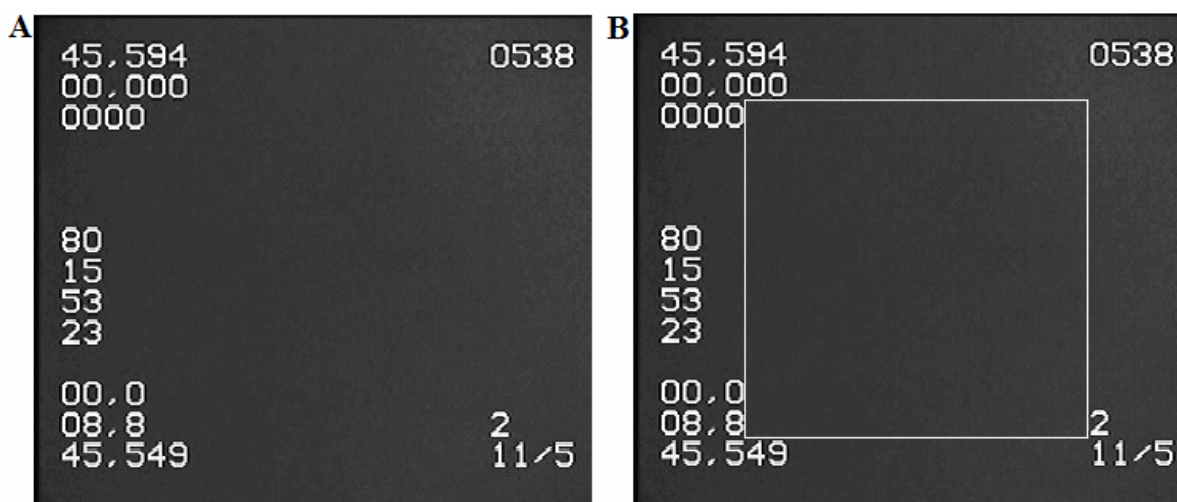
Figure 2.1.2.2. Snapshot of the cell marked with the ALICE II device. (A) The numbers on the upper left corner indicate the temperature in the copper sample cell and the numbers on the lower left corner indicate the critical temperature for SF_6. The numbers on the middle left position represent the time of the video recording in hours (80), minutes (15), seconds (53) and tenths of seconds (23) measured from an arbitrary time reference. The upper right number is the frame number and the lower right numbers indicate the date of the recording. This image is dark because of the high turbidity due to the critical opalescence phenomena near the critical point. (B) The inner rectangle with white borders shows the cropped 190 x 190 pixels image used for subsequent digital image processing.

We designed automated image processing routines in MATLAB to analyze the image data from this experiment.

The first step in processing the images was to convert the frames from true color to double format in order to use MATLAB's FFT routines (Fig. 2.1.2.3.A). To avoid introducing spurious frequencies in the resultant FFT spectrum due to the automatically marked numbers on the original frames (Fig. 2.1.2.2.A), we cropped the original frame to a square of maximum

possible area (Fig. 2.1.2.2.B). Therefore, the original 256 x 256 pixels frame allowed us to crop 190 x 190 pixels clean image (free of white digits marked by ALICE II).
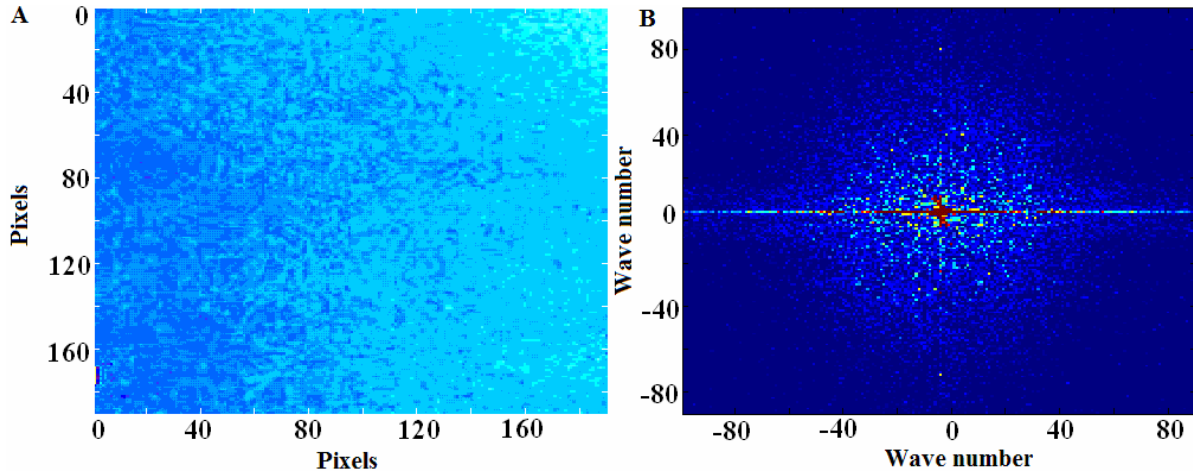
Figure 2.1.2.3.   Recorded image and the corresponding two-dimensional Fast Fourier Transform. (A) Cropped image of 190 x 190 pixels that eliminates the white numbers automatically marked by the ALICE II. This image was converted from true color to double and shows a significant difference in contrast between the left and right side of panel A. (B) Color-coded two-dimensional power spectrum of the cropped image represented in the frequency (wave numbers) domain. Red color represents high amplitude values in the power-spectrum and blue indicates low amplitude values. The presence of non-uniform illumination in the image is reflected in the central line along the x-direction, visible in the power spectrum. The DC component is present in the center of the power spectrum and shown by the intense red color (high Fourier amplitude).

The second step in our image processing strategy was to obtain the two-dimensional Fast Fourier Transform (FFT) of the cropped image (Fig. 2.1.2.3.B).

Finally, after removing the DC component, we computed the radial average of the power spectrum. Since the two-dimensional FFT of the image (Fig. 2.1.2.3.B) has radial symmetry with the center at the DC component, we averaged the power spectrum at each fixed wave number. In other words, starting from the center of the power spectrum, we computed the average power spectrum's amplitude along circles surrounding the DC component (Fig. 2.1.2.4.A). The computed average amplitudes were plotted versus the wave numbers (Fig. 2.1.2.4.B). The example in Fig. 2.1.2.4 shows the circular path of radius $k = 20$ (Fig. 2.1.2.4.A) used to compute the average amplitude of the power spectrum. The vertical arrow on Fig. 2.1.2.4.B at wave number 20 shows the corresponding average amplitude of the power spectrum on the circular path marked on Fig. 2.1.2.4.A. Since the radial average of the two-dimensional power spectrum

has significant variations we used a polynomial interpolation to smooth the variations and to extract the most probable wave numbers, which is the local maximum of the polynomial interpolation, present in the original image (Fig. 2.1.2.4.B).
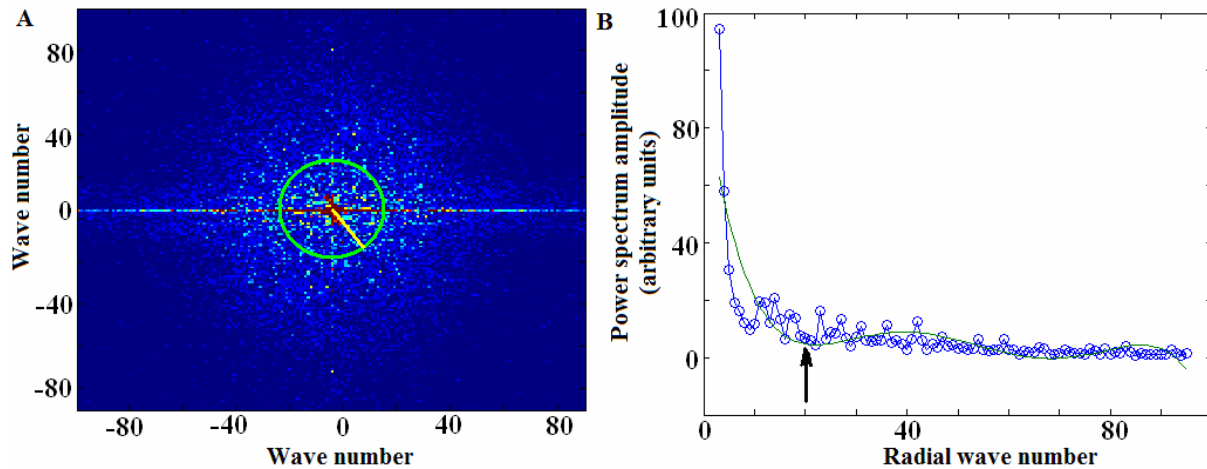
Figure 2.1.2.4.   Radial average of a two-dimensional power spectrum. (A) The color-coded power spectrum has a circular symmetry. The radial average of the power spectrum is the average power computed along a circular path (yellow circle) centered on the DC component. (B) Radial average (open circles) shows a few peaks that suggest possible spatially correlated domains in the original image. The polynomial fit (continuous line) smooth the radial average and indicates the most probable wave number associated to the FFT.

However, the results found using the aforementioned steps were not satisfactory for our purpose due to the significant optical noise present. Therefore we tested different noise-reduction techniques.

The principal objective of the next section is to enhance the image using both spatial domain and frequency domain methods. The term spatial domain refers to the image itself and the approaches in this category are based on direct manipulation of the pixels' intensity [Gonzalez, 2002]. Image processing techniques in the frequency domain are based on modifying the Fourier transform of the original image [Jahne, 2002].

2.1.2.2.   Multiple-image average background

The method of multiple-images average was suggested by Wu *et al.* [Wu *et al.*, 1995] and consists in defining the background image for the whole experiment as the average image over a series of images. Wu *et al.* [Wu *et al.*, 1995] explained that such an averaging is required because the system's dimension, which in our experiments was about 533 μm, is small enough to be susceptible to noise. Wu *et al.* [Wu *et al.*, 1995] used 128 background images (each image was the average of 16 images) to compute the average background. Because of experimental limitations, only 30 images were available for computing the average background in our experiments. The color-coded power spectrum of a set of 32 images shows a significant DC component and high frequency fluctuations concentrated along the horizontal axis (Fig. 2.1.2.5.A). In order to reduce the contribution of the optical noise to the power spectrum, we computed an average background image above the critical temperature (1 K above T_c) to ensure that the fluctuations were weak (Fig 2.1.2.5.B). The average background image was subsequently subtracted from the set of averaged images under investigation (Fig. 2.1.2.5.A) and the result was divided by the average background image. This scaled (normalized) image is called the image without noise and its corresponding power spectrum is shown in Fig 2.1.2.5.C. The ringing in the x-direction may be caused by the small number of frames used in averaging the background images. The frequency domain radial average of the image without noise for integer values of the wave number and the corresponding least-mean-square polynomial fit are shown in Fig 2.1.2.5.D. The method of multiple images background gives superior results regarding the image quality after noise reduction compared to the simple power spectrum method described in the previous section. At the same time, the small number of available background images is the leading cause of enhancement of small fluctuations present above the critical temperature. This method was only applied to the "Down" region. In the "Up" region this method was not very effective in improving the quality of the images because the bandwidth of the optical noise overlapped with the high frequency fluctuations present near the critical point.
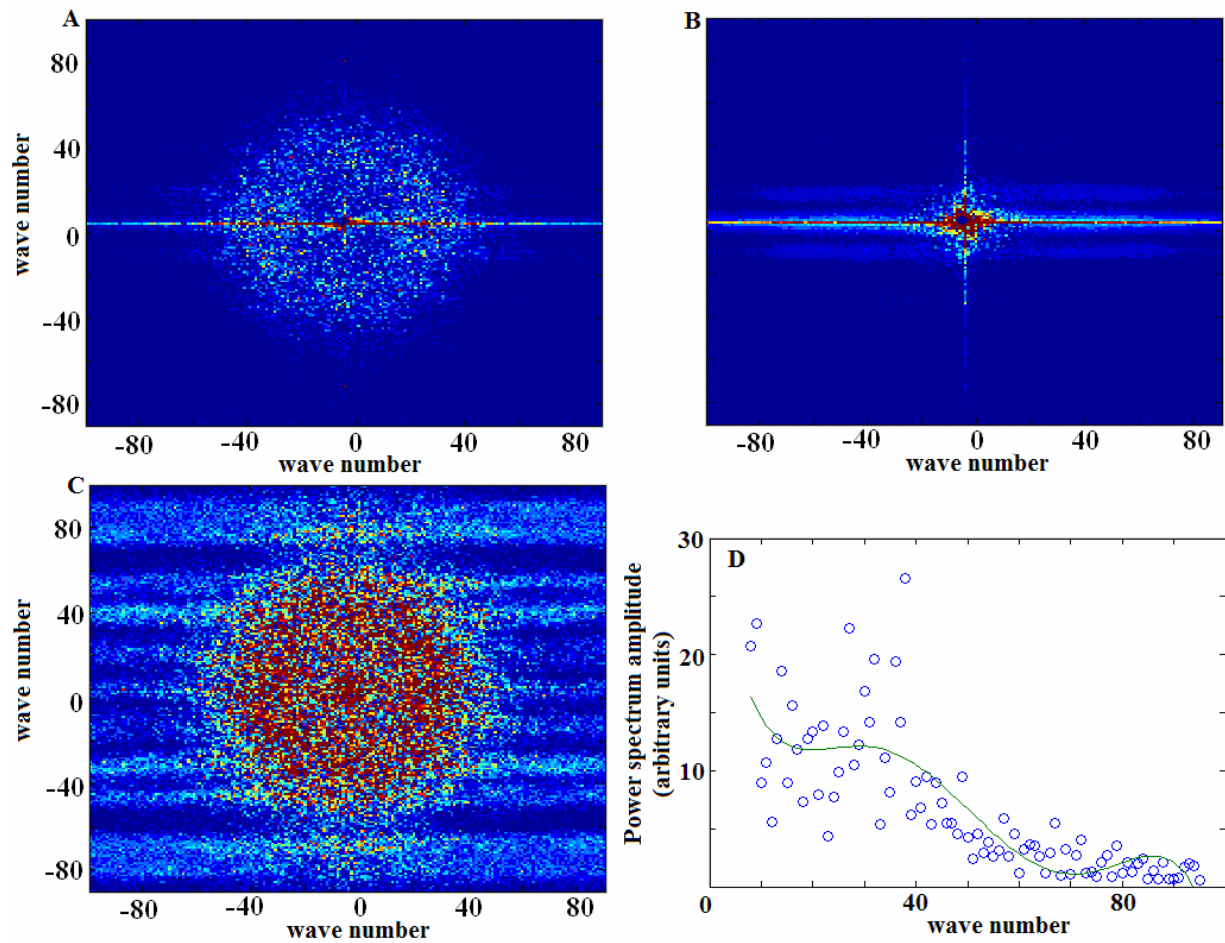
Figure 2.1.2.5. **Multiple-images background method.** (A) Color-coded power spectrum for the average of 32 images in the "Down" region. Noise frequencies are present in the power spectrum and determine a horizontal line. (B) Color-coded power spectrum for the average background images over 30 images taken well above the critical point. In this case the power spectrum shows no ring for $T \gg T_c$, which means no fluctuation away from the critical point.(C) Color-coded power spectrum for normalized image without noise shows an improvement in power spectrum quality reflected in an almost complete removal of frequencies related to optical noise. (D) Radial average of the power spectrum for image without noise (open circles) at integer values of the wave number and the corresponding polynomial fit (continuous line). The position of the local maximum values of the polynomial fit indicates the most probable wave numbers in the frequency domain and corresponds to the spatial periodicities present in the original image.

54

2.1.2.3.   Single-image background

This method uses as a background image an image recorded at a temperature well above the critical temperature to ensure that the fluctuations are negligible and only the optical noise is present. To enhance the fluctuations present at the critical temperature and to reduce optical noise, the background image is subtracted from each image of interest. This method was used by Guenoun *et al.* [Guenoun *et al.*, 1989] to study the fluctuations near the critical point in a mixture of isobutyric acid and water. In this particular example we used image number 130 as our background image and subtracted it from the image of interest. The new image is called the image without background and the brightness in the upper left corner is different from that in the lower right corner (Fig. 2.1.2.6.A). The most significant improvement consists in eliminating the bright line along the horizontal direction in the FFT spectrum (Fig. 2.1.2.6.B). The above improvement allows for a more accurate computation of the radial average of the power spectrum (Fig. 2.1.2.6.C).
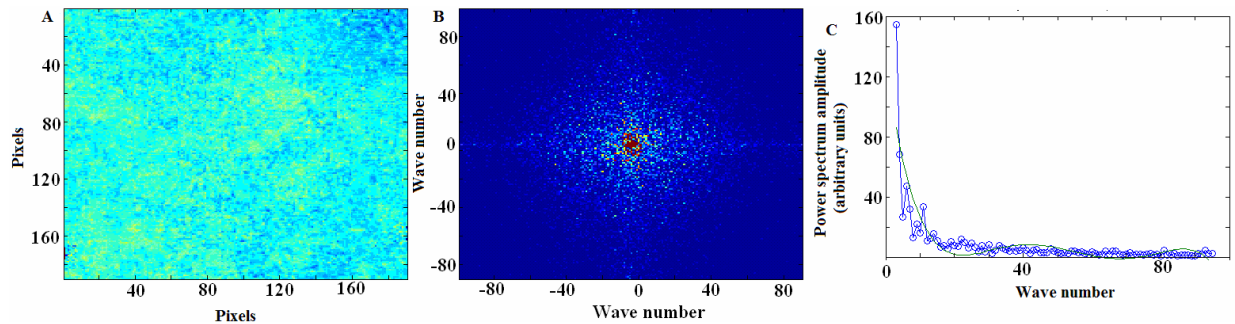
Figure 2.1.2.6.   Single-image background methods for fluctuation enhancement and noise reduction. (A) The enhanced image obtained from the noisy image after the background image was subtracted from the image of interest. (B) In the color-coded power spectrum of the enhanced image, the horizontal bright line seen in Fig. 2.1.2.4.A that was presumably determined by the optical noise is completely eliminated. (C) The radial average of the two-dimensional power spectrum shows the two weakest peaks at wave numbers 5 and 10 (similar to Fig. 2.1.2.5.B).

2.1.3. Results regarding fluctuations

2.1.3.1.   Image processing of "Up" region

Image processing tools such as padding, filtering and Fast Fourier Transforms (FFT) were used to extract information regarding fluctuations from the recorded images. The video recording of the "Up" region has intensity fluctuations over a very small spatial distance close to the resolution of the movie. At the same time, the optical noise is also shore-range and overlaps with the intensity fluctuations determined by actual density fluctuations taking place inside the fluid. Therefore, subtracting a background image is not very effective in reducing the optical noise for the "Up" region. As a result, the first step in image processing of "Up" region was to use a linear filter called an average filter or n-point smoothing to reduce the effect of noise. The idea behind this smoothing filter is straightforward. Because random noise typically consists of sharp transitions in gray levels the most obvious application of smoothing is noise reduction. By replacing the value of every pixel in the original (noisy) image by the average of the gray levels in a certain user-defined neighborhood, the "sharp" transitions in gray level were reduced. However, an undesirable side effect of filtering is blurring the edges. Usually, the moving average filters have odd sizes because it gives the gray level value of the pixel (x,y) in an image based on the gray level values of a symmetric neighborhood. For example, a filter of size three means that the value of the pixel at coordinates (x,y) is determined by the gray level values of the 3 x 3 square centered at (x,y). Different moving average filter sizes were used to test their influence on the FFT power spectrum. We used filters of odd sizes (5, 7, 9, 11, 19, and 27) and the corresponding fluctuation images and power spectra for each filter are shown in Fig. 2.1.3.1. For the purpose of noise reduction, the filter of size A = 9 pixels proved to give the clearest contour of the color-coded FFT power spectrum. The peak value of the wave number (k_m) of the radial average of the power spectrum varies with the size of the averaging filter (Table 2.1.3.1). A the plot of k_m versus the filter's size revealed the existence of a switching region between the smoothening without cutting short range fluctuations and severe filtering revealing only large scale fluctuations (Fig. 2.1.3.2). For relative small values of the filter's size (less than ten units), the wave number is relatively high (Fig. 2.1.3.2.A) and quickly decreasing (Fig. 2.1.3.2.B) with

the increase of the filter's size. This suggests that while the filter is still effective in smoothening the images it also allows the small range fluctuations (high wave number values) to pass.
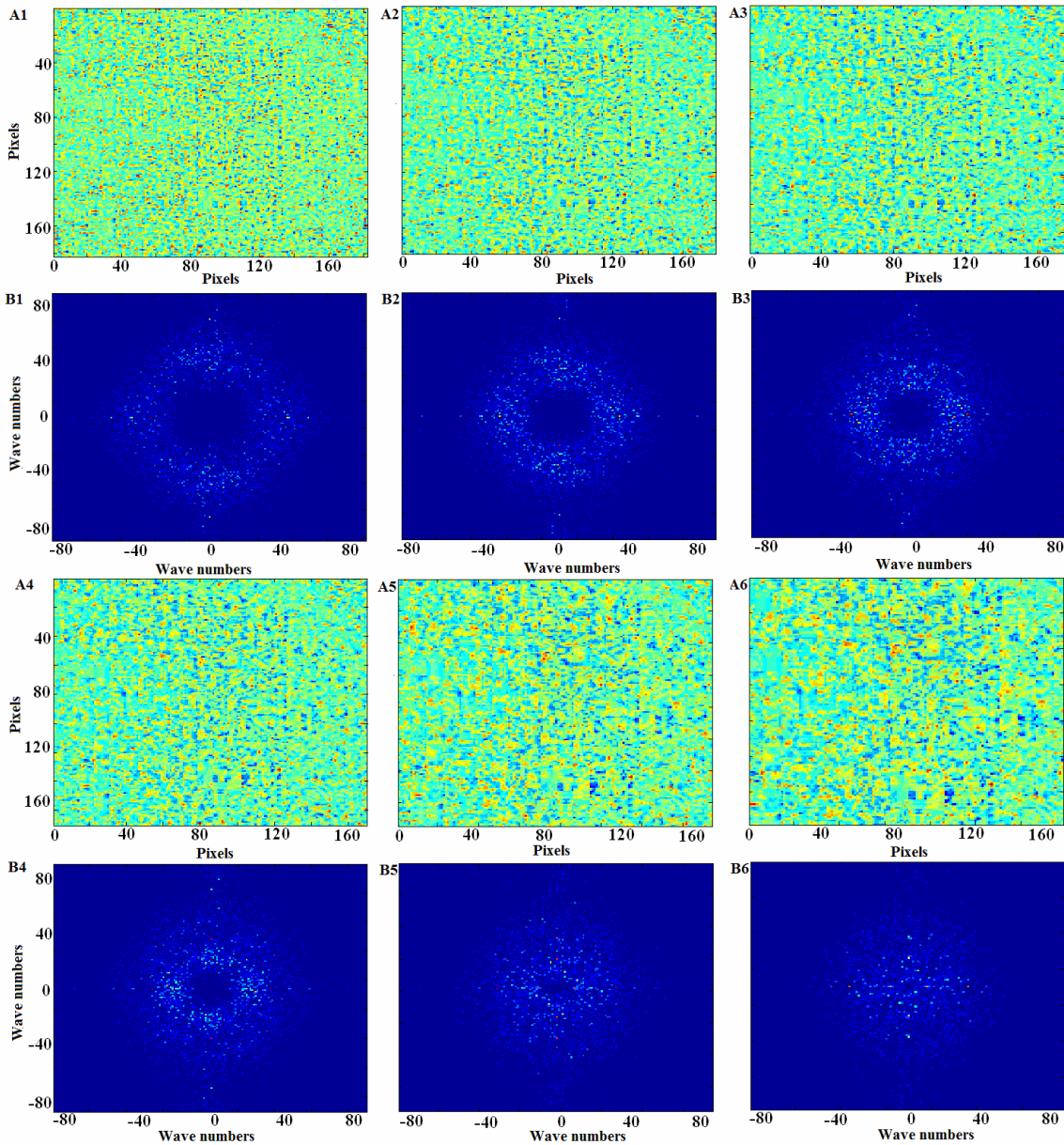
Figure 2.1.3.1.   Enhancing the image quality and reducing the noise by spatial domain filtering. The effect of the averaging filter's size in the spatial domain (panels A) and in the frequency domain (panels B). N-point smoothing filters of sizes 5, 7, 9, 11, 19, and 27 were applied to the same image. The best structure of the power spectrum was revealed for a filter of size 9 (panels A3 and B3).

At one end, the filter size of three units gives the largest wave number, which we believe, is mostly due to the noise and very short scale fluctuations. At the other end of the same region of relatively high slope (Fig. 2.1.3.2.B), a filter size around ten units filtered most of the short scale fluctuations, including optical noise, and is still capturing fluctuations over an intermediate range.

Table 2.1.3.1. The dependence of the wave number corresponding to the peak of the radial average of the power spectrum (k_m) on the size of the averaging filter A.

A	0		3	5	7	9	11	13	15	17	19	21	23	25	27	29	31	33	35
k_m	3		64	43	34	27	22	20	18	17	16	15	13	11	10	9	8	5	3
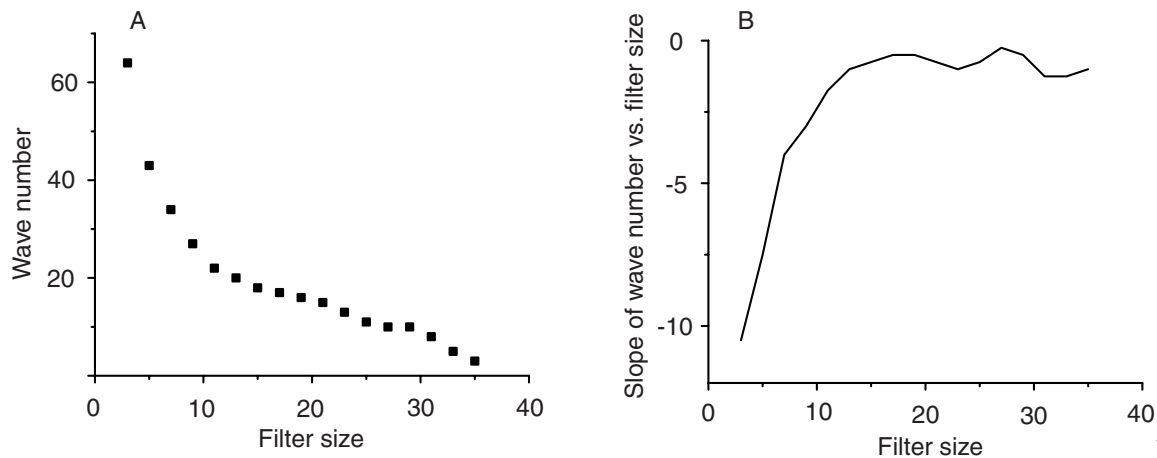
Figure 2.1.3.2. Wave number dependence on the size of the averaging filter. (A) A small size of the averaging filter reveals small scale fluctuations with large values of the wave number whereas for large values of the averaging filter only large scale fluctuations are detected. (B) The slope of the wave number versus the size of the averaging filter indicates the existence of two separate regions and the cutoff is around the filter size of nine units.

For a filter size over ten units, the wave number only slowly decreases by increasing the filter's size and reflects that fact that only long range fluctuations (small wave numbers) can be visualized. At the same time, small changes in the wave number over a wide range of filter's sizes is an indication of a too severe filtering and high uncertainty about the spatial localization of fluctuations.

The second step towards fluctuations visualization was to subtract the filtered (blurred) image from the original image. The resulting image is called the fluctuation image (Fig. 2.1.3.2).
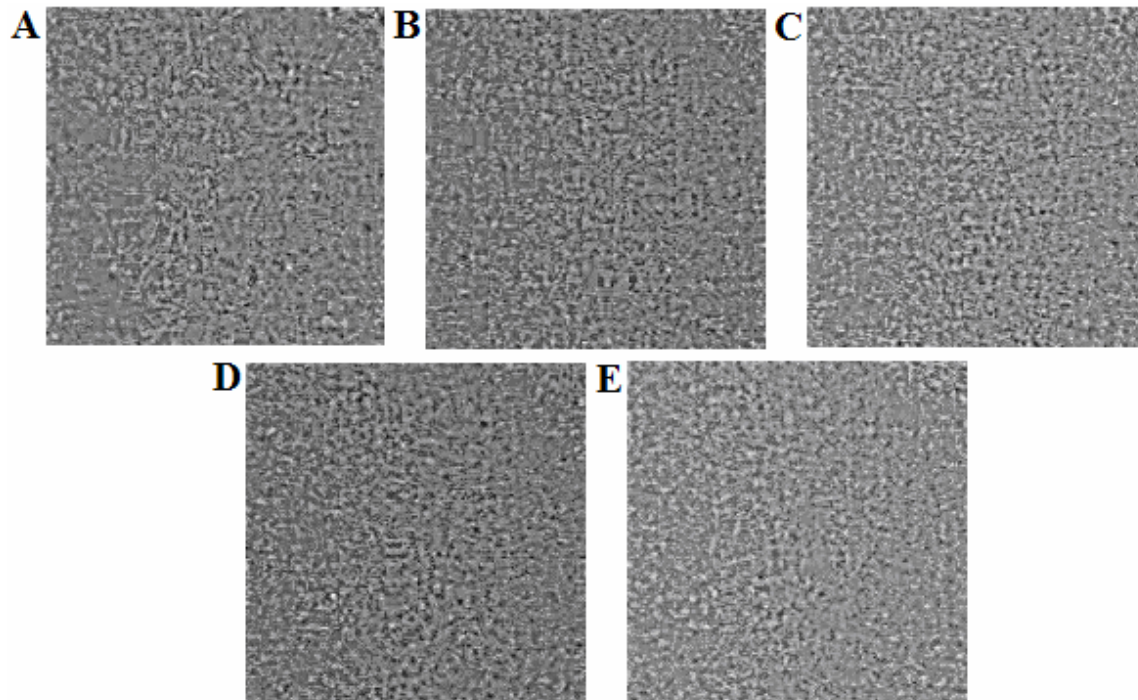
Figure 2.1.3.3. **Fluctuation images obtained by subtracting the filtered (blurred) image from the original image**. The images correspond to frames 100 (A), 120 (B), 140 (C), 160 (D), and 180 (E) of the "Up" region.

The third step in our analysis of the video recordings was to obtain the power spectrum for the fluctuation images such as those shown in Fig. 2.1.3.3. We used an in-house designed program written in Matlab for this task. The power spectrum corresponding to fluctuating images 100, 120, 140, 160, and 180 of the "Up" region are shown in Fig. 2.1.3.4. The minimum amplitude of the power spectrum is represented in blue and the maximum amplitude in red with intermediate amplitudes shown as corresponding intermediate colors.

Finally, the fourth step was to compute the radial average of the power spectrum. Based on the radial symmetry of the FFT power spectrum (Fig. 2.1.3.4), we averaged the distribution of the FFT along all radii centered on the DC component of the FFT. The broad peak in the plot of the radial average of the power spectrum corresponding to the ring in the power spectrum is shown in Fig 2.1.3.5. In order to estimate the wave number associated with the broad peak in each FFT power spectrum we used a fifth order polynomial interpolation plotted by the continuous red line in Fig. 2.1.3.5. We determined the order of the polynomial by trial and error. The polynomial degree was successively increased until we found the minimum polynomial

degree that gave the same estimate of the dimensionless wave number associated with the maximum of the broad peak in the power spectrum (k_m).
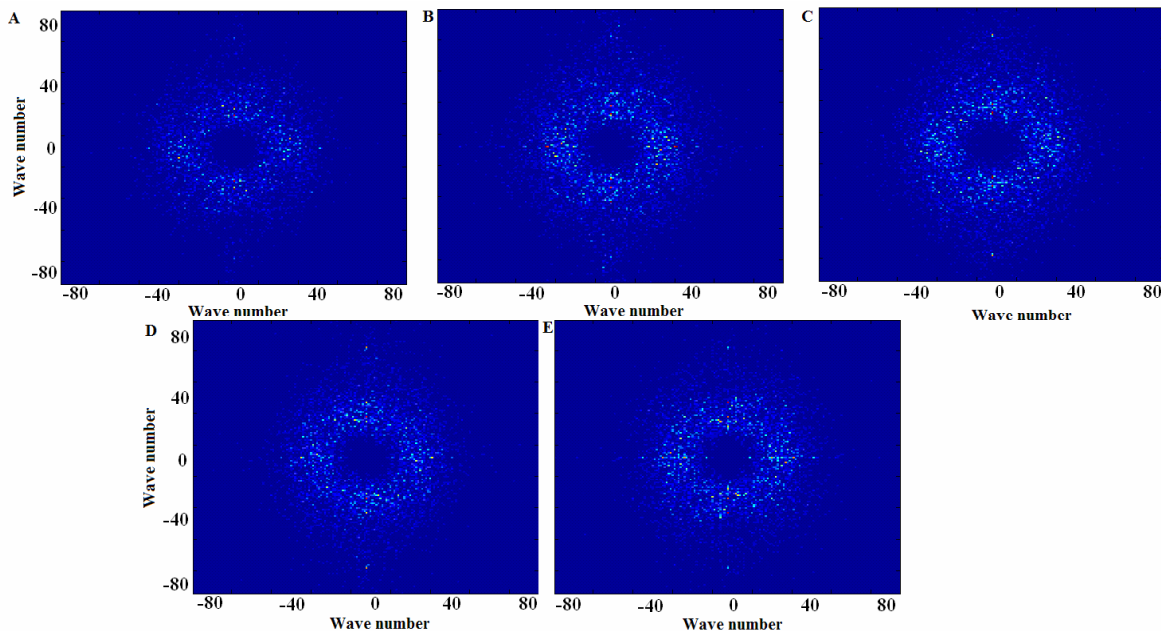
Figure 2.1.3.4. Color-coded power spectra corresponding to the fluctuating images of "Up" region (see Figure 2.1.3.3.) show a dark ring corresponding to randomly oriented structures. The power spectrum has a distinctive structure with a "ring" of significantly high amplitudes.
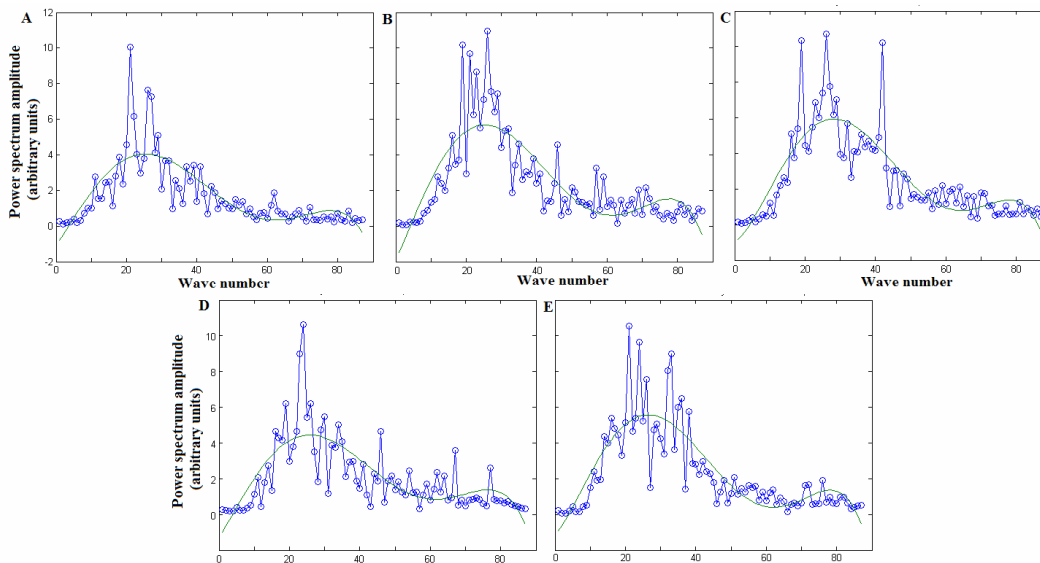
Figure 2.1.3.5. Radial average of the power spectra obtained for fluctuation images in "Up" region. The images indices were 100, 120, 140, 160, and 180. Circles mark the radial average for an integer value of the wave numbers. The continuous line shows the polynomial interpolation used to estimate the wave number associated with the maximum of the broad peak in the power spectrum (k_m).

2.1.3.2.   Critical temperature estimation based on characteristic length

The most probable radial average of the power spectrum obtained according to the method described in the previous section is related to the characteristic length of the fluctuations. The relationship between the spatial and frequency domains is [Gonzalez, 2002]

$$k = k_m/(N \, \Delta x), \qquad\qquad (2.1.3.1)$$

where N is the total number of pixels in the image, $\Delta x = 3.1$ μm represents the image resolution in the spatial domain, and k_m represents the dimensionless value of the maximum of the broad peak in the radial average power spectrum shown in Fig. 2.1.3.4. The original image contained 190 x 190 pixels and was filtered with an optimal n-point smoothing filter of dimension A = 9 pixels. As a result, a border region of A pixels was removed all around the initial image. Therefore, the power spectrum was computed for the resultant image of only 172 x 172 pixels (N = 172). The value for the wave vector is related to the characteristic length of the correlated fluctuations (λ) as follows

$$k = 1/\lambda. \qquad\qquad (2.1.3.2)$$

For example, for a value of $k_m = 29$ arbitrary units in Fig. 2.1.3.4.B and an image size of $N = 172$ pixels with 1 pixel corresponding to 3.1 μm the characteristic length of the correlated fluctuations (λ) is 17.79 μm. We analyzed more than 200 images for the "Up" region and determined that there is a very slight tendency of the estimated wave number k_m to increase over time. A linear regression gave as a slope of 0.008 ± 0.001 wave numbers/image index that accounts for the spread of the wave numbers between 27 and 30 with an average of $k_{m,average} = 28.94 \pm 0.07$ and corresponding average characteristic length of $\lambda_{average} = 18.44 \pm 0.05$ μm. The characteristic length determined from the radial average FFT spectrum according to (2.1.3.2) is about five pixels and reflects the emergence of long-range coherent behavior near the critical point.

Stanley [Stanley, 1971] showed that near the critical point, the correlation length also follows a power law

$$\xi = \xi_0 \, [(T-T_c)/T_c]^{-\nu}, \qquad\qquad (2.1.3.3)$$

where the scaling coefficient of the correlation length is $\xi_0 = 1.8 \; 10^{-10}$ m, $T_c = 318.687$ K, and $\nu = 0.633$ for SF_6 [Moldover *et al.*, 1979]. Based on (2.1.3.3) and the hypothesis that the characteristic length, λ, obtained from the radial average of the power spectrum of the image is

the same as the correlation length, ξ, we estimated the average temperature difference $\Delta T_\lambda = T - T_c = T_c(\xi_0/\lambda_{average})^{1/\nu} = 3.87 \pm 0.02$ μK, where the index λ reflects the fact that the estimated ΔT is based on the characteristic length. The estimated temperature ΔT_λ is too small to be detected by ALICE II instruments. The method is definitely limited by finite size effects that strongly dominate the dynamics of the fluid near the critical point. In particular, very close to the critical point the correlation length and the characteristic length diverge to infinity. However, since the experiment is performed using a finite cell the key to understanding of critical phenomena in finite physical systems is the ration λ/L, where L is the characteristic geometric dimension of the cell. Since the estimated correlation length was about five pixels and the characteristic length $L = 172$ pixels then $\lambda/L \approx 3\%$, which is significant and cannot be neglected. Therefore, the equation (2.1.3.3) must be corrected to take into account finite size effects and cannot be used directly to estimate the temperature difference $\Delta T = T - T_c$.

2.1.3.3. Estimation of critical temperature based on the histogram of the image

In the previous section 2.1.3.2, we suggested that finite size effects significantly limit our ability to estimate the temperature of a near-critical fluid from the radial average of the power spectrum of the image. As a result, every method based on spatial correlation of measurable quantities near the critical point must take into consideration appropriate corrections imposed by the finite size of the physical system under investigation. To avoid such a shortcoming there is the option of defining measurable quantities not specifically related to a certain position in the recorded image. One such method that does not take into consideration the spatial position of a pixel in the recorded image is the histogram method.

The hypotheses we made when using the histogram method for the estimation of the critical temperature was that the intensity of the scattered light is proportional to the variation in the density of the fluid

$$<\Delta I^2>/I_0^2 = c^2 <\Delta\rho^2>/\rho_c^2, \qquad (2.1.3.4)$$

where c is a dimensionless temperature-dependent coefficient. We hypothesized that the local density fluctuations, $<\delta\rho^2> = <\Delta\rho^2>/\rho_c^2$, can be determined by measuring the fluctuations of the intensity of scattered light, $<\delta I^2> = <\Delta I^2>/I_0^2$. According to Domb [Domb, 1996], the density fluctuations are related to the isothermal compressibility according to the following relationship

$$<\Delta\rho^2>/\rho_c^2 = k_B T_c k_T/V, \qquad (2.1.3.5)$$

where k_B is Boltzmann's constant, ρ_c is the critical density, T_c is the critical temperature, V is the volume of fluid covering one pixel (3.1 μm) in the recording image at a depth of $t_0 = 1.9$ μm, and k_T is the isothermal compressibility. Near the critical point, the isothermal compressibility of a fluid is given by the power law [Puglielli *et al.*, 1970]

$$k_T = k_0[(T-T_c)/T_c]^{-\gamma}, \qquad (2.1.3.6)$$

where $k_0 = 1.33\ 10^{-8}$ m^2/N, $\gamma = 1.19$ for SF$_6$ [Moldover *et al.*, 1979]. By substituting (2.1.3.6) into (2.1.3.5) and the result into (2.1.3.4), the relative temperature, $\Delta T = (T-T_c)/T_c$, can be estimated by measuring the variance of the scattered light intensity:

$$\Delta T = T-T_c = T_c\ (k_0 k_B T_c/(V<\delta\rho^2>))^{1/\gamma} = T_c\ (k_0 k_B T_c c^2/(V<\delta I^2>))^{1/\gamma}. \quad (2.1.3.7)$$

The equation (2.1.3.7) is the basis for temperature estimation based on measured intensity fluctuations of the scattered light and has the advantage of avoiding any reference to the spatial

correlation of the pixels in the recorded image, which will be affected by the finite size of the physical system. However, two important observations must be made:

1) The CCD camera records gray levels corresponding to scattered light intensity and, as a result, we determine the variance of the gray levels in the recorded image and not the variance of the intensity of the scattered light. According to Kammoun *et al.* [Kammoun *et al.*, 1992] and Guenoun *et al.* [Guenon, *et al.* 1993], the variance of the gray levels in the background image, $\sigma_{background}$, is proportional to the gain of the camera $\Gamma \propto \sigma_{background}$. Therefore, appropriate calibration must be performed [Kammoun *et al.*, 1992] to directly link the gray level $i = 1, 2, \ldots, 256$ and the corresponding light intensity I scattered by the fluid

$$I \propto i^2/\Gamma \propto i^2/\sigma_{background}. \tag{2.1.3.8}$$

2) The proportionality constant c in (2.1.3.4) and (2.1.3.7) is temperature-dependent. As a result, (2.1.3.7) is an implicit equation that can be used to determine the temperature of the fluid provided that we are able to calibrate the CCD camera such that the correspondence between the gray levels, i, and the intensity, I, of the light received by the camera can be inferred from experiments.

Taking into account the above two observations, we derived two complementary methods for estimating the relative temperature of a fluid based on the histogram of the recorded images.

First, by considering the variation of the scattered light intensity in (2.1.3.8) around the average value of the gray levels $<i>$ we get

$$<\delta I> \propto <i> \sqrt{<(\delta i)^2>}/\sigma_{background} = <i> \sigma_i/\sigma_{background}, \tag{2.1.3.9}$$

where σ_i is the variance of the analyzed image. By substituting (2.1.3.9) into (2.1.3.4) one finds that a small density fluctuation induces a change in the scattered light intensity that can be estimated using the average gray scale intensity, $<i>$, and the variance, σ_i, of the recorded picture of the cell

$$\delta\rho = b <i> \sigma_i/\sigma_{background}, \tag{2.1.3.10}$$

where b is a calibration constant. In order to determine the calibration constant b we used images recorded at the beginning of the experiment at temperatures higher than the critical temperature, and estimated the corresponding average gray level intensity, $<i_0>$, and variance, $\sigma_{i,0}$. The calibration constant is

$$b = \delta\rho_0 \, \sigma_{background}/(<i_0> \sigma_{i,0}), \tag{2.1.3.11}$$

where $\delta\rho_0 = (\rho - \rho_c)/\rho_c = 0.0 \pm 0.02\%$ at the beginning of the experiment. Finally, substituting the calibration constant (2.1.3.11) into (2.1.3.10) we determined the local density fluctuations $<\delta\rho>$ using the average gray levels intensity, $<i>$, and the variance, σ_i, of the histogram of a recorded images

$$\delta\rho = \delta\rho_0 <i> \sigma_i/(<i_0> \sigma_{i,0}). \tag{2.1.3.12}$$

After substituting (2.1.3.12) into (2.1.3.5) and the result into (2.1.3.6) it was possible to derive an explicit relationship for the relative temperature of the fluid:

$$\Delta T_i = T - T_c = T_c \left(\frac{k_0 k_B T_c}{V \delta\rho_0^2} \frac{\langle i_0 \rangle \sigma_{i,0}}{\langle i \rangle \sigma_i} \right)^{1/\gamma} = \frac{0.0220514}{\left(\langle i \rangle \sigma_i \right)^{1/\gamma}}, \tag{2.1.3.13}$$

where $k_0 = 1.33 \ 10^{-8} \ m^2/N$, $k_B = 1.38 \ 10^{-23} \ J/K$ is Boltzmann's constant, $T_c = 318.687$ K and $\gamma = 1.19$ for SF_6 [Moldover et al., 1979], V is the volume corresponding to an image area of 1 pixel = 3.1 μm and a field depth of $t_0 = 1.9$ μm, $V = 3.1$ μm x 3.1 μm x 1.9 μm = $1.76 \ 10^{-17} \ m^3$. The depth of focus is $t_0 \approx \lambda/(4 \ NA^2)$, where the wavelength of the laser light was $\lambda_0 = 633$ nm and the numerical aperture of the optical system $NA = 0.2$ [Hegseth et al., 2003]. We used 36 background frames extracted from the video recording to find the average of the gray levels intensity $<i_0> = 129 \pm 2$ with a variance $\sigma_{i,0} = 21.3 \pm 0.6$. The range of average background intensity $<i_0>$ was between 108 and 155, and the range for the variance $\sigma_{i,0}$ of the histograms was between 14 and 29. For the fluctuation images shown in Fig. 2.1.3.2 the corresponding average and variances for the gray level intensities are listed in Table 2.1.3.

Table 2.1.3.2. The average gray level intensities and variances obtained from the histograms of the images shown in Fig. 2.1.3.2. The estimated temperature ΔT_i is based on the gray level calibration from histogram measurements.

Image Index	$<i>$ (gray level)	σ_i (gray level)	ΔT_i (μK)
100	122	25	46.75
120	118	26	45.25
140	134	28	38.11
160	114	26	47.05
180	136	26	40.93

Based on the complete set of data, which is only partly shown in table 2.1.3.2, the estimated temperature difference is $\Delta T_i = 46.39 \pm 0.05$ μK with a range between 37.98 μK and 68.71 μK.

This temperature is within the temperature quench separating the "Up" and "Down" regions, which was 300 µK and included the critical point.

The second histogram-based method for temperature estimation uses the fact that the intensity of the scattered light is proportional to the local fluctuation of fluid density, according to (2.1.3.4), and the fact that the density fluctuations can be related to the isothermal compressibility, according to (2.1.3.5). By substituting (2.1.3.5) into (2.1.3.4) one obtains an implicit expression for the fluid temperature

$$\sigma_I^2 = c^2(T)\, k_B\, T_c\, k_T/V, \tag{2.1.3.14}$$

where σ_I is the variance of the intensity of the scattered light, $c(T)$ is a temperature-dependent coefficient, k_B is Boltzmann's constant, T_c is the critical temperature, and V is the volume of fluid associated with 1 pixel in the recorded image.

The histograms of the fluctuation image shown in Fig. 2.1.3.5 have a normalized Gaussian shape given by

$$y = y_0 + A_{histo}\, e^{-\frac{(x-x_c)^2}{2\sigma_i^2}}, \tag{2.1.3.15}$$

where A_{histo} is the area under the histogram and the parameter σ_i is the variance of gray level intensity, $<\delta i^2>$, in the recorded image.

By using (2.1.3.14) it is possible to determine the relative temperature variation $(T-T_c)/T_c$ based on the histograms of the images and the values of the constants listed in Table 2.1.3.3. However, there are two key issues involved in our novel method for temperature estimation from the histogram of the recorded images:

1) The determination of the temperature-dependent proportionality constant $c(T)$.

2) The calibration of the CCD camera to establish the correspondence between the intensity of the light, I, and the recorded gray level i.

In order to determine the temperature-dependent proportionality constant, c, we refer to Ornstein-Zerinke theory of light scattering [Ornstein and Zernike, 1914; Fisher, 1964; Landay and Lifshitz, 1960]. The attenuation of the light intensity passing through a very thick optical medium of thickness t_0 is determined by $I = I_0 e^{-ht_0}$, where I_0 is the intensity of the incident light and h is called the coefficient of extinction.
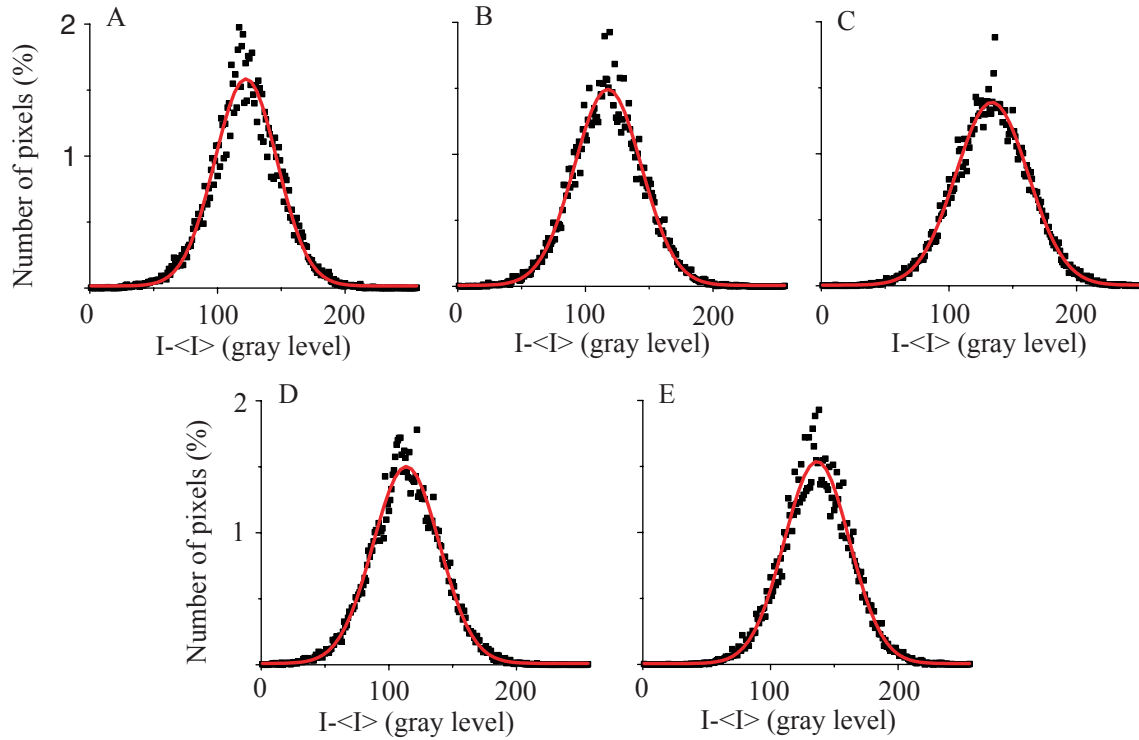
Figure 2.1.3.5. Histograms of the gray level distribution for the fluctuation images. The horizontal axis represents the gray levels from 0 to 255. The vertical axis represents the percentage of the total number of pixels corresponding to a certain gray level. The continuous line represents the Gaussian fit of the experimental histogram (filled squares). The corresponding fluctuation images are shown in Fig. 2.1.3.2.

Table 2.1.3.3. Important material data and critical exponents for methanol-cyclohexane and SF_6. η is the shear viscosity, ξ_0 is the coefficient of the correlation length in (2.1.3.3), k_0 is the coefficient of the isothermal compressibility in (2.1.3.6), c_c is the critical concentration (methanol-cyclohexane only), ρ_c is the critical density, T_c is the critical temperature, and ν and γ are critical exponents.

System	η $(10^{-4} Pas)$	ξ_0 (nm)	k_0 $(10^{-9} Pa^{-1})$	c_c	ρ_c $(Kg.m^{-3})$	T_c (K)	ν	γ
CC*-Me	7.5	0.330		0.71		317.6		
SF_6	0.40	0.1892	12.203		737	318.7	0.63	1.2

The extinction coefficient measures the fraction of the incident light that is scattered per unit length along the optical axis. For a thin layer, the fractional intensity variation is $\delta I = \Delta I/I_0 = (I_0 - I)/I_0 = h\, t_0$. At each image point, the total light scattered out of the imaging field is $h = A\, k_T\, f(\theta_0, k_0\xi)$, where the factor A is defined by [Ford *et al.*, 1965]

$$A = \frac{\pi^2 k_B T_c}{2\lambda_0^{\ 4}} \left(\rho \frac{\partial n^2}{\partial \rho} \right)^2, \qquad (2.1.3.16)$$

k_T is the isothermal compressibility, and the factor f is given by

$$\begin{aligned} f(\theta_0, k_0 \xi) &= 2\pi \int_{\theta_0}^{\pi} \frac{1 + \cos\theta}{1 + 4k_0^{\ 2} \xi^2 \sin^2 \frac{\theta}{2}} \sin\theta d\theta \\ &= 2\pi \int_{\theta_0}^{\pi} \frac{1 + \cos\theta}{1 + 16\pi^2 \left(\frac{\xi}{\lambda_0} \right)^2 \sin^2 \frac{\theta}{2}} \sin\theta d\theta \end{aligned} \qquad (2.1.3.17)$$

Based on experimental design data, the angular aperture was $\theta_0 = 16.7°$, the wave number of the laser light used was $k_0 = 2\pi/\lambda_0$ with $\lambda_0 = 633$ nm, and the value of the factor f was numerically evaluated in Mathematica. In agreement with the results stated in the previous section based on the power spectrum of the analyzed images, the average value of the correlation length was $\xi_{average} = 17.85 \pm 0.05$ μm and the numeric value for the factor f was $f = (5.76 \pm 0.03)*10^{-4}$.

According to Hegseth *et al.* [private communication, 2003], the intensity fluctuations and density are related through variations of the extinction coefficient as follows

$$\delta I = \delta(ht_0) = t_0 \frac{\partial h}{\partial \rho} \delta\rho = f \cdot t_0 \cdot \left(A \frac{\partial k_T}{\partial \rho} + k_T \frac{\partial A}{\partial \rho} \right) = k_T \left(-\frac{A}{\rho} + \frac{\partial A}{\partial \rho} \right) \delta\rho, \qquad (2.1.3.18)$$

where we used the fact that $\dfrac{\partial k_T}{\partial \rho} = -\dfrac{k_T}{\rho}$. In order to compute the coefficient A and its derivative, we used the Lorenz-Lorenz formula

$$\rho = \mu \frac{n^2 - 1}{n^2 + 2}, \qquad (2.1.3.19)$$

with $\mu = 1.275 \ 10^4$ kg/m^3, according to Jany and Straub [1987]. From (2.1.3.19) we get

$$n^2 = -\frac{2\rho + \mu}{\rho - \mu}, \qquad (2.1.3.20)$$

and its derivative is

$$\frac{\partial n^2}{\partial \rho} = \frac{3\mu}{(\rho - \mu)^2}. \qquad (2.1.3.21)$$

Based on (2.1.3.21) and (2.1.3.19), one finds

$$\rho\frac{\partial n^2}{\partial\rho} = \rho\frac{3\mu}{(\rho-\mu)^2} = \mu\frac{n^2-1}{n^2+2}\frac{3\mu}{\left(\mu\dfrac{n^2-1}{n^2+2}-\mu\right)^2} = \frac{(n^2-1)(n^2+2)}{3},\quad (2.1.3.22)$$

such that the variation of (2.1.3.22) gives

$$\delta\left(\rho\frac{\partial n^2}{\partial\rho}\right) = \delta\left(\rho\frac{3\mu}{(\rho-\mu)^2}\right) = -\frac{3\mu(\rho+\mu)}{(\rho-\mu)^3}\delta\rho.\qquad (2.1.3.23)$$

By substituting (2.1.3.19) into (2.1.3.23) we get

$$\delta\left(\rho\frac{\partial n^2}{\partial\rho}\right) = -\frac{3\mu(\rho+\mu)}{(\rho-\mu)^3}\delta\rho = -\frac{3\mu\left(\mu\dfrac{n^2-1}{n^2+2}+\mu\right)}{\left(\mu\dfrac{n^2-1}{n^2+2}-\mu\right)^3}\delta\rho =$$

$$\frac{(2n^2+1)(n^2+2)^2}{9\mu}\delta\rho.\qquad (2.1.3.24)$$

Based on (2.1.3.16), the variation of A is

$$\delta A = \delta\left(\frac{\pi^2 k_B T_c}{2\lambda_0^4}\left(\rho\frac{\partial n^2}{\partial\rho}\right)^2\right) = \frac{\pi^2 k_B T_c}{2\lambda_0^4}\delta\left(\rho\frac{\partial n^2}{\partial\rho}\right)^2 =$$

$$\frac{\pi^2 k_B T_c}{2\lambda_0^4}2\rho\frac{\partial n^2}{\partial\rho}\delta\left(\rho\frac{\partial n^2}{\partial\rho}\right).\qquad (2.1.3.25)$$

By substituting (2.1.3.22) and (2.1.3.24) into (2.1.3.25) we get

$$\delta A = \frac{\pi^2 k_B T_c}{2\lambda_0^4}2\rho\frac{\partial n^2}{\partial\rho}\delta\left(\rho\frac{\partial n^2}{\partial\rho}\right) =$$

$$\frac{\pi^2 k_B T_c}{2\lambda_0^4}2\frac{(n^2-1)(n^2+2)}{3}\frac{(2n^2+1)(n^2+2)^2}{9\mu}\delta\rho =\qquad (2.1.3.26)$$

$$\frac{\pi^2 k_B T_c}{\lambda_0^4}\frac{(2n^2+1)(n^2+2)^3(n^2-1)}{27\mu}\delta\rho.$$

Using the definition (2.1.3.16) and the formula (2.1.3.22) we found

$$\frac{A}{\rho} = \frac{1}{\rho}\frac{\pi^2 k_B T_c}{2\lambda_0{}^4}\left(\rho\frac{\partial n^2}{\partial \rho}\right)^2 = \frac{1}{\rho}\frac{\pi^2 k_B T_c}{2\lambda_0{}^4}\left(\rho\frac{3\mu}{(\rho-\mu)^2}\right)^2 =$$

$$\frac{\pi^2 k_B T_c}{2\lambda_0{}^4}\frac{9\rho\mu^2}{(\rho-\mu)^4} = \frac{\pi^2 k_B T_c}{2\lambda_0{}^4}\frac{9\mu\frac{n^2-1}{n^2+2}\mu^2}{\left(\mu\frac{n^2-1}{n^2+2}-\mu\right)^4} = \qquad (2.1.3.27)$$

$$\frac{\pi^2 k_B T_c}{2\lambda_0{}^4}\frac{(n^2-1)(n^2+2)^3}{9\mu},$$

and from (2.1.3.26)

$$\frac{\partial A}{\partial \rho} = \frac{\pi^2 k_B T_c}{\lambda_0{}^4}\frac{(2n^2+1)(n^2+2)^3(n^2-1)}{27\mu}. \qquad (2.1.3.28)$$

Based on (2.1.3.27) and (2.1.3.28), one get

$$-\frac{A}{\rho}+\frac{\partial A}{\partial \rho} = -\frac{\pi^2 k_B T_c}{2\lambda_0{}^4}\frac{(n^2-1)(n^2+2)^3}{9\mu}+\frac{\pi^2 k_B T_c}{\lambda_0{}^4}\frac{(2n^2+1)(n^2+2)^3(n^2-1)}{27\mu} =$$

$$\frac{\pi^2 k_B T_c}{2\lambda_0{}^4}\frac{(n^2+2)^3(n^2-1)}{9\mu}\left(-1+2\frac{(2n^2+1)}{3}\right) = \qquad (2.1.3.29)$$

$$\frac{\pi^2 k_B T_c}{2\lambda_0{}^4}\frac{(n^2+2)^3(n^2-1)(4n^2-1)}{27\mu}.$$

Finally, we are able to identify the temperature-dependent constant as

$$c = f\cdot t_0\cdot k_T\cdot\frac{\pi^2 k_B T_c}{2\lambda_0{}^4}\frac{(n^2+2)^3(n^2-1)(4n^2-1)}{27}\frac{\rho_c}{\mu}. \qquad (2.1.3.30)$$

By substituting the coefficient c into (2.1.3.14) and assuming that the index of refraction is constant and equal to the critical refraction index, it is possible to derive an explicit expression for the temperature difference ΔT_I:

$$\Delta T_I = T_c\left(\frac{1}{K_0}\left(\langle\delta I^2\rangle\frac{(2\lambda_0{}^4 27\mu)^2 V}{k_B T_c\rho_c^2\left(f\cdot t_0\cdot\pi^2 k_B T_c(n^2+2)^3(n^2-1)(4n^2-1)\right)^2}\right)^{1/3}\right)^{-1/\gamma} =$$

$$= T_c\left(K_0^3\frac{k_B T_c\rho_c^2\left(f\cdot t_0\cdot\pi^2 k_B T_c(n^2+2)^3(n^2-1)(4n^2-1)\right)^2}{(2\lambda_0{}^4 27\mu)^2 V\langle\delta I^2\rangle}\right)^{1/3\gamma} \qquad (2.1.3.31)$$

where $k_0 = 1.33 \; 10^{-8}$ m^2/N, $t_0 = 1.9$ μm, n = 1.1, $\lambda_0 = 633$ nm, $\mu = 1.275 \; 10^4$ kg/m^3, $V = 1.8259$ 10^{-17} m^3, $T_c = 318.687$ K, $f = (5.6681 \div 6.3545)*10^{-4}$, $\gamma = 1.24$, $\rho_c = 730$ kg/m^3. The above relationship reduced to

$$\Delta T_I = 0.01067 <\delta I^2>^{-1/3\gamma} \text{ μK}. \tag{2.1.3.32}$$

The novelty of this method is that the temperature variations $\Delta T_I = (T-T_c)/T_c$ can be determined using only the histogram of the images. However, the estimation of the proportionality constant between the variation of intensity of the scattered light, $<\delta I^2>$, and the variance of the gray levels recorded by the CDD, $<\delta i^2>$, is not trivial, and the calibration data could not be obtained for this experiment.

Similar results can be obtained starting from thermodynamic considerations (see section 2.2.1) [Landau, 1969] that lead to the probability distribution function of the density fluctuations

$p(\delta\rho) = \dfrac{1}{\sqrt{2\pi}\sigma_\rho} e^{-\frac{\delta\rho^2}{2\sigma_\rho^2}}$ and, based on (2.1.3.14), to the corresponding density fluctuation for the

intensity of the scattered light $p(\delta I) = \dfrac{c}{\sqrt{2\pi}\sigma_I} e^{-\frac{\delta I^2}{2\sigma_I^2}}$. Since the histogram of the gray levels in the

recorded images is also Gaussian, according to (2.1.3.15), we have $p(\delta i) = \dfrac{1}{\sqrt{2\pi}\sigma_i} e^{-\frac{\delta i^2}{2\sigma_i^2}}$. Since

the probability distribution function for the scattered light intensity and for the gray level histogram is proportional, let us consider that $\delta I = \chi \; \delta i$, where χ is an undetermined scaling factor. By determining the amplitude of the Gaussian fit from the histogram amplitude $A_{histo} =$

$\dfrac{1}{\sqrt{2\pi}\sigma_i} = \dfrac{\chi}{\sqrt{2\pi}\sigma_I}$ we can actually determine $\sigma_I = \dfrac{\chi}{\sqrt{2\pi}A_{histo}}$ and substitute it into (2.1.3.32).

Again, the estimation of the temperature cannot be completed unless the proportionality factor χ is known.

The temperature estimation based on (2.1.3.31) assumes that the refractive index is constant. However, explicit temperature-dependence can be established for the refractive index based on (2.1.3.20) and the fact that the density of the fluid near the critical point follows the power law [Moldover *et al.*, 1979]

$$\rho = B \; [(T-T_c)/T_c]^\beta, \tag{2.1.3.33}$$

where $B = 1.827$ kg/m^3 and $\beta = 0.355$. As a result, the refractive index becomes

$$n^2 = \frac{2B\tau^\beta + \mu}{\mu - B\tau^\beta},$$

(2.1.3.34)

where the reduced temperature is $\tau = (T-T_c)/T_c$. By substituting (2.1.3.34) into (2.1.3.30) and using (2.1.3.14) we obtain an implicit relationship that determines the reduced temperature $\tau = (T-T_c)/T_c$

$$\langle \delta I^2 \rangle = \left(f \cdot t_0 \cdot \frac{9\pi^2}{2\lambda_0^4} \frac{\mu^3 B\tau^\beta \left(3B\tau^\beta + \mu\right) \rho_c}{\left(\mu - B\tau^\beta\right)^5} \frac{\rho_c}{\mu} \right)^2 \frac{\left(k_B T_c k_0 \tau^{-\gamma}\right)^3}{V}.$$

(2.1.3.35)

2.1.3.4. The universality scaling exponent

In section 2.1.3.2 we found that the estimated temperature of the fluid based on the characteristic length λ obtained from the maximum of the radial average of the power spectrum is $\Delta T_\lambda = 3.87 \pm 0.02$ µK, which is too small to be detected by ALICE II instruments. One possible explanation is that the finite size effects are significant near the critical point and limit the applicability of the power law (2.1.3.3). Based on section 2.1.3.3 results, we have a more realistic estimate of the fluid's temperature from the histogram of the images as $\Delta T_i = 46.39 \pm 0.05$ µK with a range between 37.98 µK and 68.71 µK, which is within the temperature quench of 300 µK separating the "Up" and "Down" regions. Based on this new estimate of the temperature, ΔT_i, the average value for the correlation length from (2.1.3.3) is $\xi_i = 4.17 \pm 0.02$ µm, which is about a pixel's dimension of 3.1 µm. The index i for the correlation length emphasizes that the value was derived using the estimated temperature from the gray level histograms. Based on the determined correlation length ξ_i and the characteristic length λ it is possible to compute a dimensionless quantity called the reduced wave number k^* and the corresponding dimensionless reduced time (t^*) [Perrot *et al*., 1994]

$$k^* = \xi/\lambda, \qquad\qquad t^* = t/t_\xi, \qquad\qquad (2.1.3.36)$$

where $t_\xi = 6\ \xi^3\ \pi\ \eta/k_B T_c = 1.71442\ 10^{17}\ \xi^3$ and η is the shear viscosities listed on Table 2.1.3.2. Fig. 2.1.3.6 shows the temporal evolution of the wave number determined using the radial average of the power spectrum. The wave number is almost constant for the duration of the "Up" plateau. The plot of the wave number k versus time t, according to data in Table 2.1.3.3 shows a linear dependence.

Table 2.1.3.4 includes a few of the values for the time, temperature, characteristic length, λ, correlation length, ξ, reduced wave vector, k^*, and reduced time, t^*, used in Fig. 2.1.3.6. The selected values listed in table 2.1.3.4 clearly indicate that the wave number k is almost practically constant over the entire time interval of the experiment.

Figure 2.1.3.6. **Temporal dependence of the wave number above the critical temperature.** The wave number is almost constant during the entire duration of "Up" plateau.
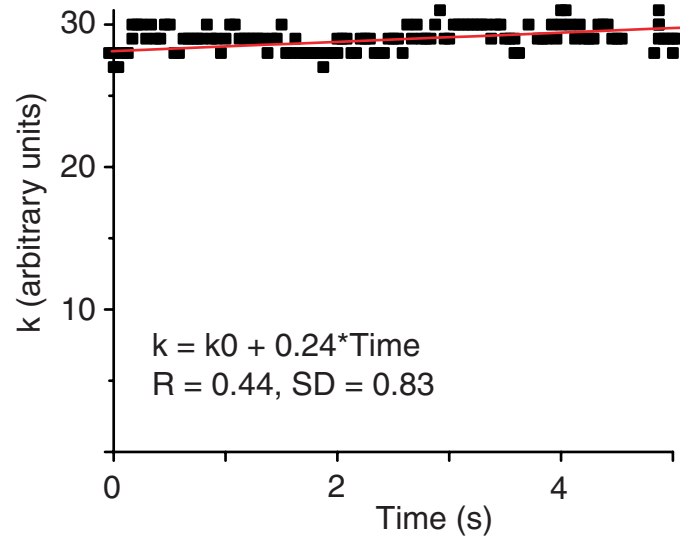
Table 2.1.3.4. Temporal dependence of the wave number. Experimental data indicate that the wave number is almost constant over the entire "Up" plateau. The average gray level intensity $\langle i \rangle$ and the variance σ_i of the recorded image are both measured in gray levels. The corresponding temperature based on the histogram measurements was computed according to (2.1.3.13) $\Delta T = \dfrac{0.0220514}{\left(\langle i \rangle \sigma_i\right)^{1/\gamma}}$. The absolute time measured from the beginning of the experiment is $t + 288950$ (s). The characteristic length was computed using the values of the maximum wave number obtained from the radial average of the power spectrum according to $\lambda = 533.2/k_m$, the correlation length was computed based on $\xi = \xi_0(\Delta T/T_c)^{-\nu}$, and the characteristic time was computed using $t_\xi = 1.71442 \cdot 10^{17} \, \xi^3$.

Image	$\langle i \rangle$	σ_i	ΔT (μK)	t (s)	k_m	λ (μm)	ξ (μm)	t_ξ (s)
100	122	24	46.75	3.96	28	19.04	4.12	12.00
110	134	23	46.11	4.25	29	18.39	4.18	12.33
120	118	26	45.25	4.58	28	19.04	4.21	12.78
130	132	25	42.89	4.96	29	18.39	4.35	14.16
140	134	28	38.11	5.25	30	17.77	4.69	17.75
150	125	25	45.47	5.58	29	18.39	4.19	12.66
160	114	26	47.04	5.96	29	18.39	4.11	11.86
170	119	28	42.86	6.25	29	18.39	4.36	14.18
180	136	26	40.93	6.83	29	18.39	4.49	15.49
190	132	28	38.93	6.96	29	18.39	4.63	17.05

2.1.3.5. Temporal evolution of fluctuations

The image in Fig. 2.1.3.7 is the same as the gray level image in Fig. 2.1.3.2.C except that it was saved as a true color image to show the domains more clearly of positive and negative density fluctuations. The fluctuations are still microscopic but they are correlated over a long distance.
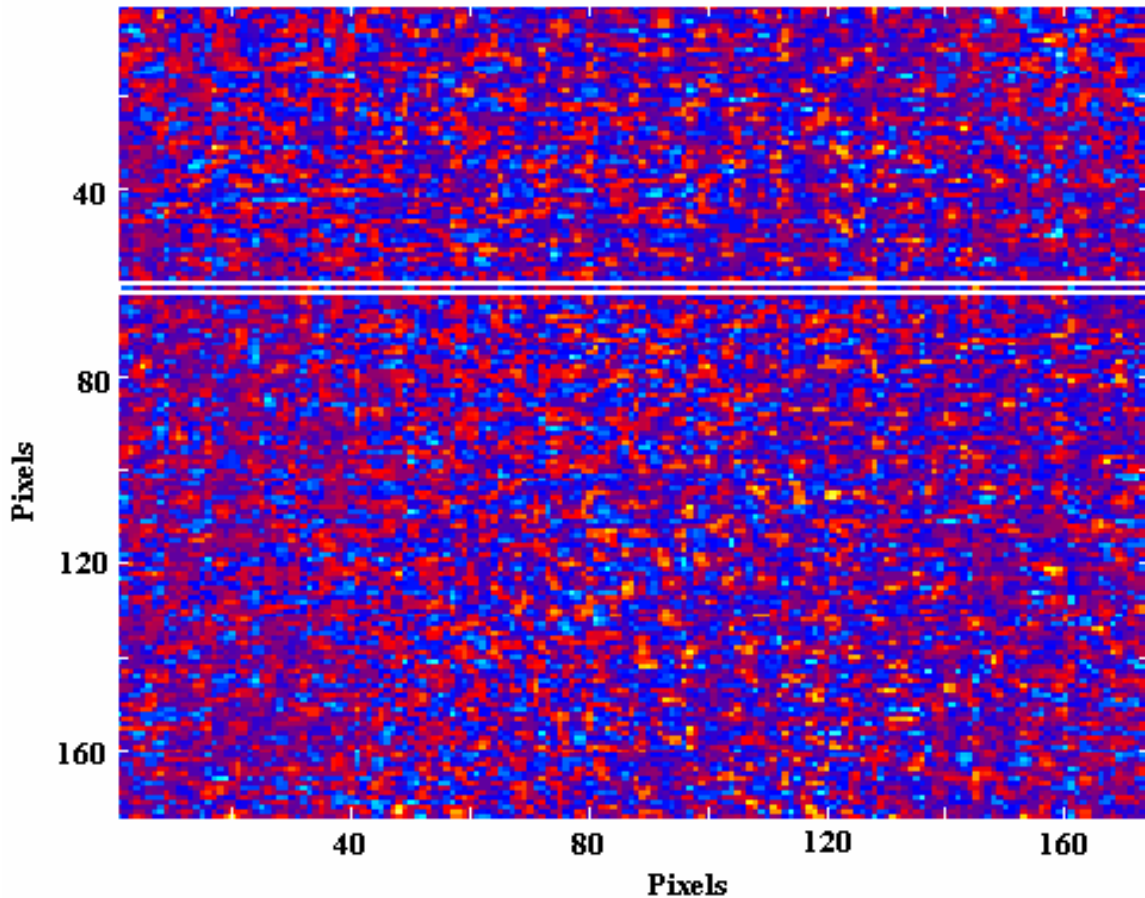
Figure 2.1.3.7. True color image of fluctuations image obtained by subtracting the filtered (blurred) image from the original image. The image index is 140 in the "Up" region.

The long range correlations near the critical point manifest a domain of higher density (positive correlation) with very strong light scattering. Lower density regions (negative correlation) scatter less light (Fig. 2.1.3.7). These scattering domains can be easily visualized because scattering more light is equivalent to a reduction in the transmitted light [Beysens *et al*., 1988].
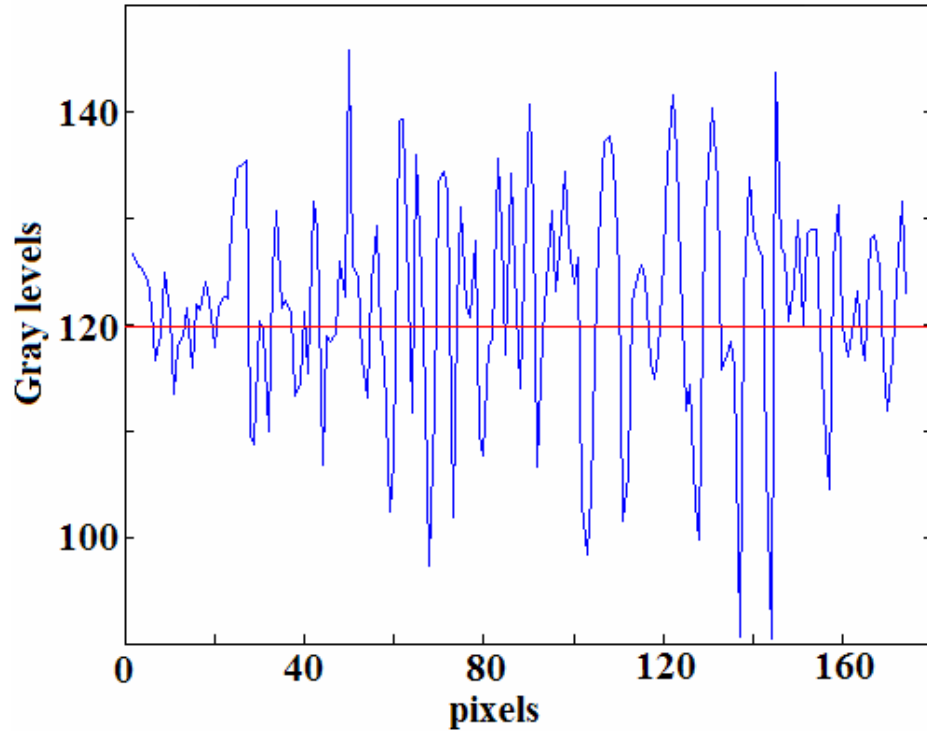
Figure 2.1.3.8. **Local spatial fluctuation of gray levels.** Fluctuations in the gray levels are evidence of local intensity deviation from the average intensity (horizontal continuous line) of the image.
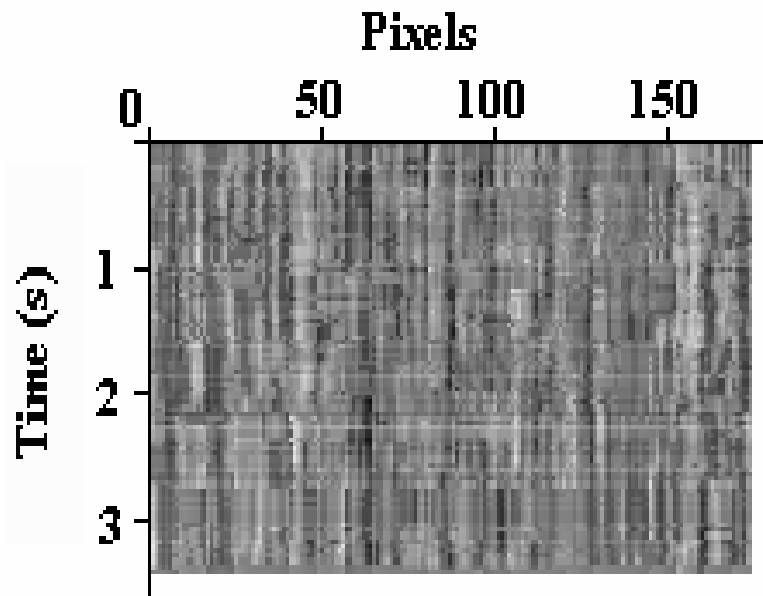
Figure 2.1.3.9. **Temporal fluctuations of gray levels at a given position**. One-pixel wide line sections through successive frames stacked on top of each other determine a space-time diagram for a row of pixels in the box in Figure 2.1.3.7.

Direct visualization of density fluctuations near the critical point can be obtained by displaying one-dimensional intensity sections, such as that shown in Fig. 2.1.3.9, sequentially in time on a 2D frame at successive times. Line sections of one pixel width taken from successive images, such as that shown in Fig. 2.1.3.7, are stacked on top of each other to produce a space-time image such as in Fig. 2.1.3.9.

The vertical lines of constant gray levels aligned with the temporal axis indicate a density fluctuation that is persistent over time. The recording started above the critical point. Significantly long lasting fluctuations are easy to identify near the pixel positions 40 and 150 on Fig. 2.1.3.9. Beyond $t = 2$ seconds in Fig. 2.1.3.9, there are no persistent fluctuations. The above qualitative analysis of the space-temporal diagram shown in Fig. 2.1.3.9 can be converted into quantitative analysis of the temporal structure of fluctuation images based on the FFT method. For this purpose, we recorded the intensity of the scattered light at a particular position $[x,y]$ in a frame at successive times. The time series associated with the pixel at position $[x,y]$ was subsequently analyzed by computing the FFT and the corresponding power spectrum in order to determine the relevant temporal correlations manifested as dominant and persistent frequency peaks. In order to reduce the optical noise, we computed the average intensity at pixel position $[x,y]$. The average was computed over a square of side L (= 2, 4, 8, 16, and 32) pixels centered at $[x,y]$. Unless otherwise stated, the temporal series correspond to the central pixel of the frame and the temporal resolution of $\Delta t = 33$ ms corresponds to the time interval between successive frames in the video recording of the experiment. We found that by increasing the area of the square over which we average the light intensity, some peaks in the power spectrum disappear but others persist over a wide range of values for the filter size L. While the spurious peaks could be related to local fluctuations, the persistent peaks in the frequency domain are clear indication of in-phase long range temporal correlations. We identified (see Fig. 2.1.3.10) the following persistent frequencies $f^* = 10$, 18, and 45 in arbitrary units. The corresponding frequencies in Hz are given by [Gonzales, 2002]

$$f = f^*/(N \, \Delta t), \tag{2.1.3.37}$$

where $N = 101$ represents the number of frames that were used for the time series and $\Delta t = 33$ ms is the time interval between consecutive frames. Using (2.1.3.37), we found that the persistent frequencies for all averaging squares of sizes 2, 4, 8, 16 and 32 pixels are 3.23, 5.34, 9.50, and 13.36 Hz, respectively. Based on fluctuations visualization in the images the first two

frequencies (3.23 and 5.34 Hz) correspond to fluctuation lifetime and the last two (9.50 and 13.36 Hz) correspond to the noisy horizontal lines.
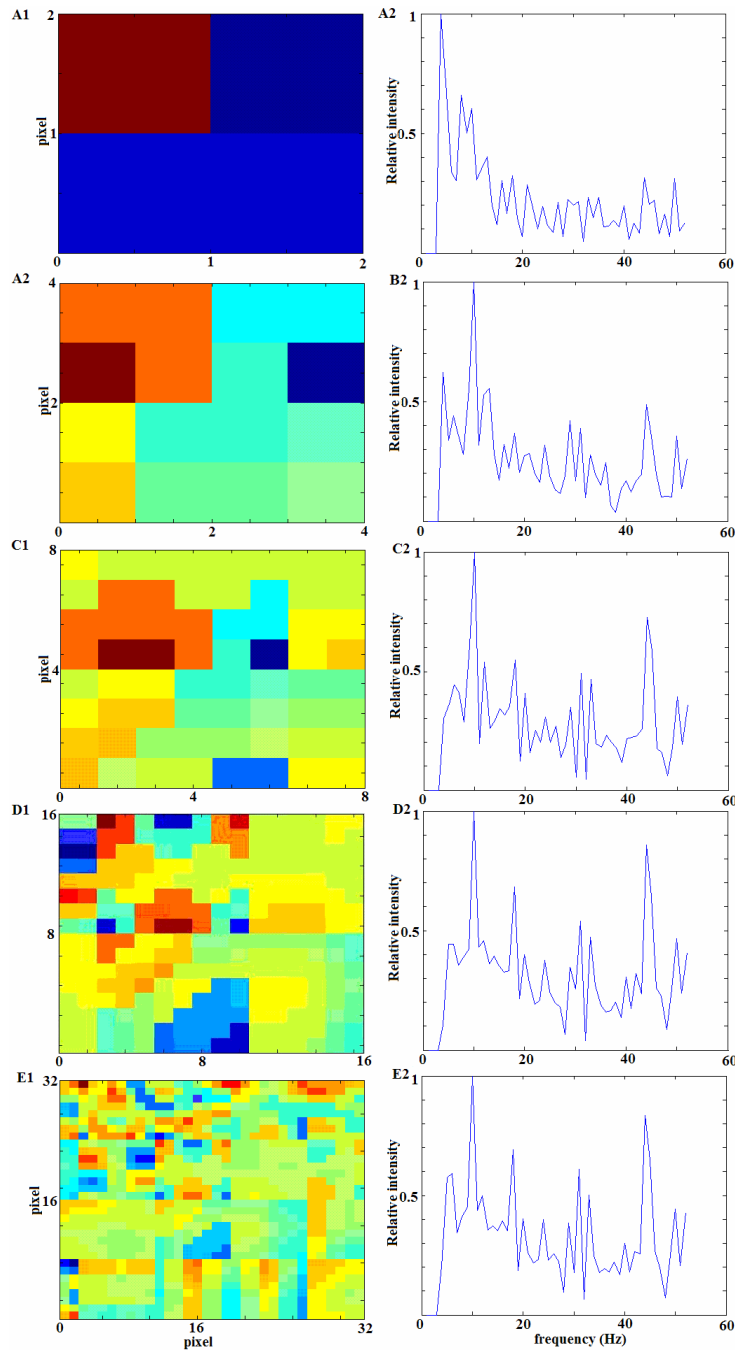
Figure 2.1.3.10. Spatial renormalization of local fluctuations. The intensity at the central pixel of successive frames is used to generate a temporal series. The intensity at the central pixel is the average over a square of 2 pixels (A), 4 pixels (B), 8 pixels (C), 16 pixels (D), and, 32 pixels (E). The right panels represent the corresponding power spectrum of the time series. The persistent frequencies are at 10, 18, and 45 arbitrary units.

2.1.3.6.   Image processing of "Down" region

The second flat region for the 0.3 mK quench is called the "Down" region (Fig. 2.1.1.1). We analyzed the images using the same filtering (averaging) methods described in section 2.1.3.1 for the image processing of the "Up" region.
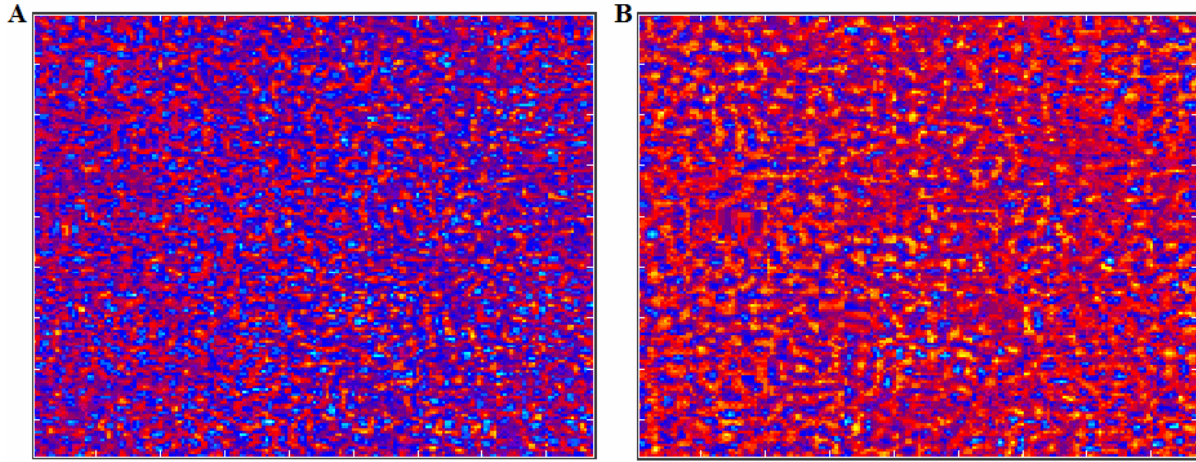
Figure 2.1.3.11.   Qualitative analysis of the growth of the fluctuations for the "Down" region. At the beginning of the "Down" region (A) the fluctuations are weak, and toward the end of the plateau (B) the minority phase grows from the fluctuations leading to large inter-connected clusters.

It appears that near the critical point the minority phase domain grows directly from the fluctuations. Fluctuations are shown as local intensity variations from the average intensity of the picture. The shape of the fluctuation domains [Guenoun, 1989] can be easily visualized by dividing the image into regions with bright clusters (red clusters in Fig. 2.1.3.11), and dark clusters (blue clusters in Fig. 2.1.3.11). In Fig. 2.1.3.11 the bright and dark fluctuation clusters appear as highly interconnected domains. During the phase separation the fluctuations grow larger and larger and percolate over the entire image [Kadanoff, 2000]. In mean field theory, the process of phase separation occurs when large fluctuations with a small interfacial energy barrier make it possible for each fluctuation to become a nucleation site. This process is called generalized nucleation. The fluid separates gas from liquid and the droplets appear.

        To evaluate quantitative information from fluctuation images, we followed the same procedure as in the previous sections. The optical noise was reduced by subtracting from the

image under consideration an image that was processed using a moving average filter of size A = 9. The result, called the fluctuation image, of size 172 x 172 pixels is shown in Fig. 2.1.3.12.
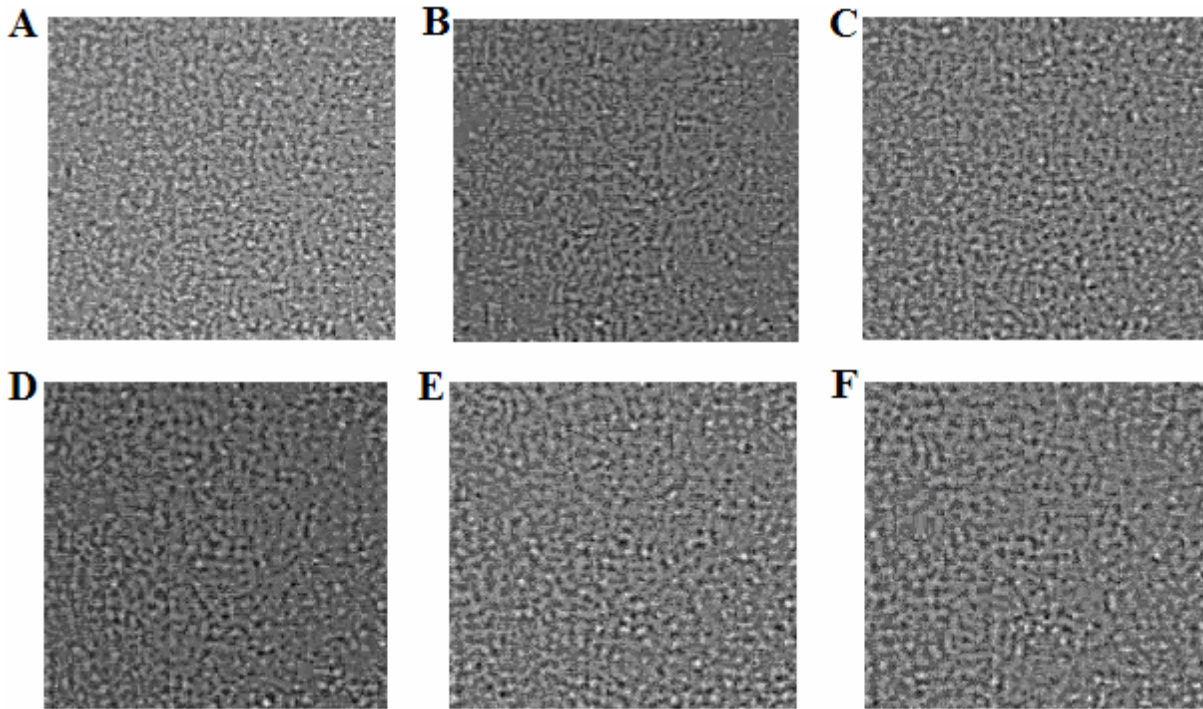
Figure 2.1.3.12. Fluctuation images of "Down" plateau. The frames used were 100 (A), 200 (B), 300 (C), 400 (D), 500 (E), and 575 (F) of the "Down" region.

The power spectrum for the fluctuation images reveals a broad ring in the wave number space whose radius decreases as the image index (time) increases. The ring is brighter than that for the "Up" region.

We also computed and plotted the radial average of the power spectrum and estimated the position of the broad peak k_m. Based on equation (2.1.3.1) and (2.1.3.2), we determined the characteristic length λ. As the image index increases, the corresponding k_m number gets smaller and the characteristic length increases, suggesting a significantly increased correlation between the local fluctuations.
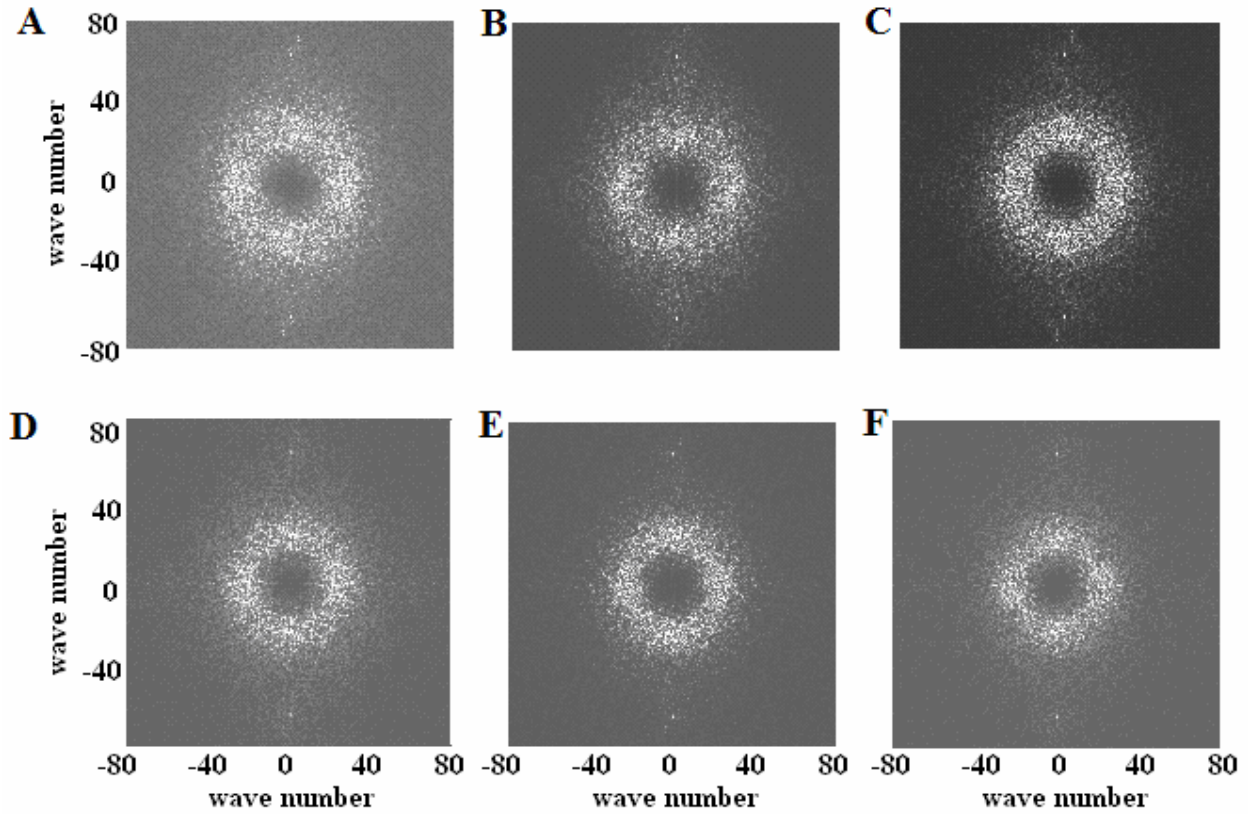
Figure 2.1.3.13. **Power spectra of "Down" plateau.** The power spectra correspond to fluctuation images shown in Fig. 2.1.3.12. The power spectrum ring shrinks as the image number increases, suggesting an increase of the characteristic length λ.
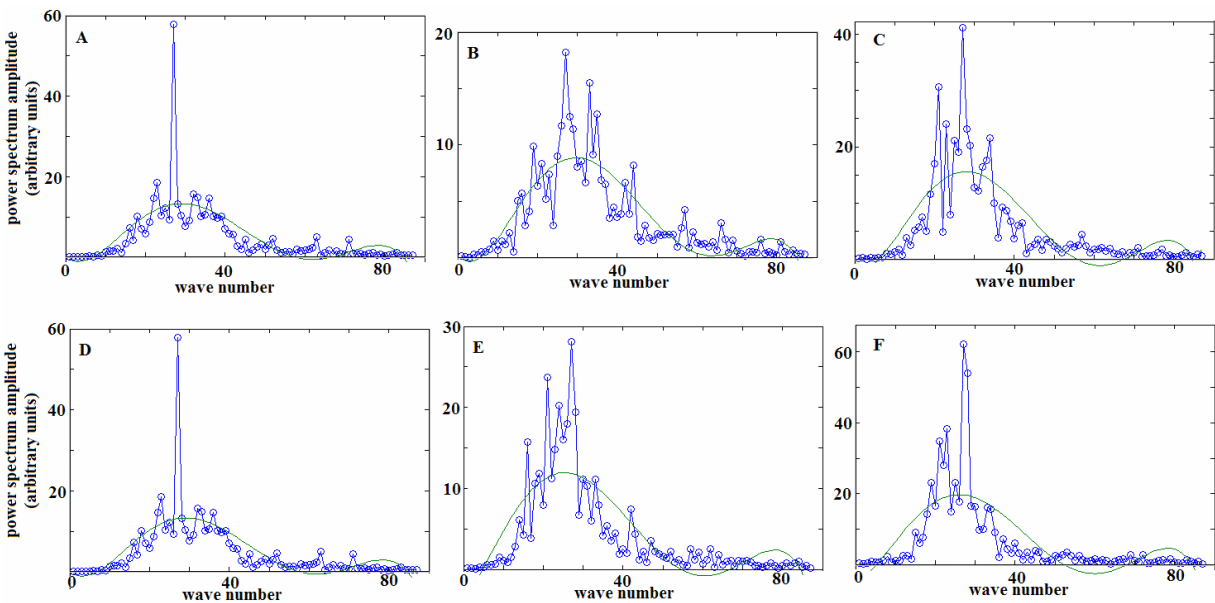
Figure 2.1.3.14. Radial average of the power spectra of "Down" plateau. The corresponding fluctuation images were 100(A), 200(B), 300(C), 400(D), 500(E), and 575(F) of the "Down"

82

region. The maximum of the broad peak is displaced towards lower wave numbers compared to the values for the "Up" region (Fig. 2.1.3.4).

The corresponding wave number for the position of the maximum of the broad peak, k_m, was estimated using a polynomial fit to the radial average of the power spectra (Fig 2.1.3.14). For example, according to equation (2.1.3.1) and (2.1.3.2), a value of $k_m = 31$ arbitrary units corresponds to a characteristic length λ of 16.64 µm.

2.1.3.7. Estimation of critical temperature based on the histogram of the image

Similar to the "Up" region, the distribution of the gray levels for the fluctuation images in the "Down" region is also Gaussian. The corresponding histograms for the fluctuation images in Fig. 2.1.3.12 are plotted in Fig. 2.1.3.15.
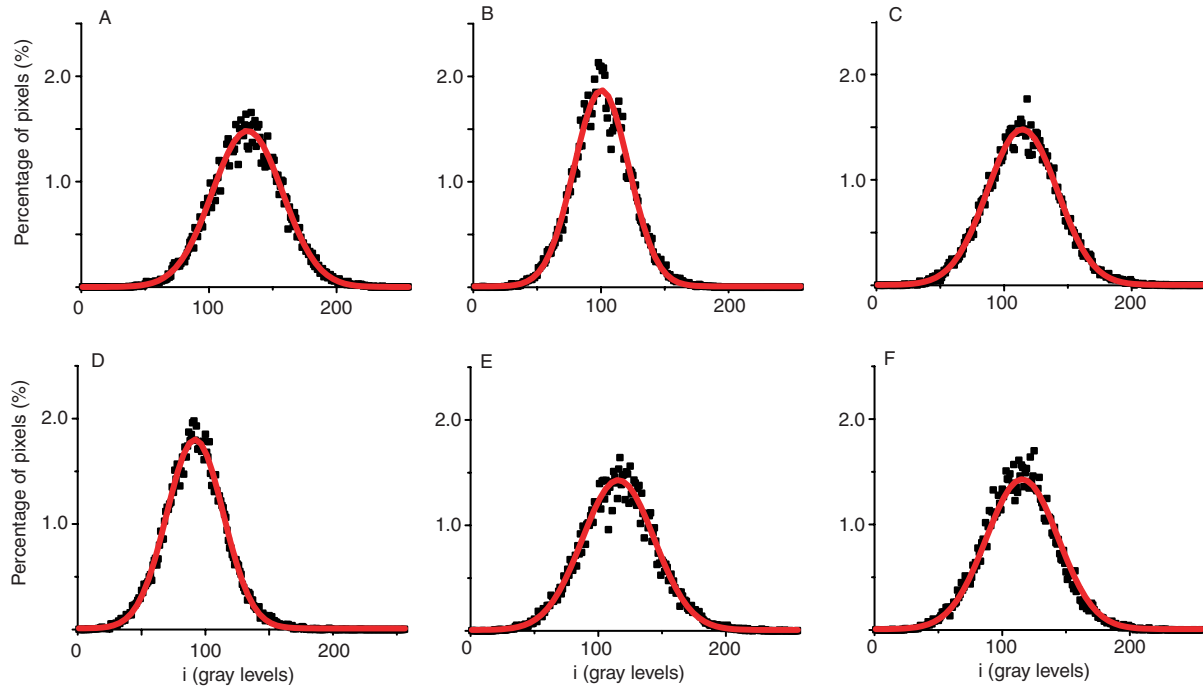
Figure 2.1.3.15. **Histograms of images of "Down" plateau.** Histograms of the gray level intensities (filled squares) have been fitted with a Gaussian curve (continuous line). The horizontal axis represents the gray scale levels and the vertical axis represents the percentage of the number of pixels having a given gray level. These histograms correspond to the fluctuation images 100, 200, 300, 400, 500, and 575 in the "Down" region. The statistics tests for the Gaussian fit are (A) $\chi^2 = 0.00337$, $R^2 = 0.987$; (B) $\chi^2 = 0.00548$, $R^2 = 0.985$; (C) $\chi^2 = 0.00208$, $R^2 = 0.992$; (D) $\chi^2 = 0.00214$, $R^2 = 0.994$; (E) $\chi^2 = 0.00435$, $R^2 = 0.983$; (F) $\chi^2 = 0.00435$, $R^2 = 0.983$.

As in section 2.1.3.3, we assumed that the variation of the scattered light intensity, $<\delta I>$, is proportional to the average value of the gray levels $<i>$, according to (2.1.3.9), and that a small fluctuation, $\delta\rho$, of the fluid density induces a change in the scattered light intensity that can be measured from average gray scale intensity, according to (2.1.3.10). The calibration constant b in (2.1.3.11) is the same as for the "Up" region because we used the same cell with the same initial density $\delta\rho_0 = (\rho - \rho_c)/\rho_c = 0.0 \pm 0.02\%$ at the beginning of the experiment. Consequently, we

assume that the same formula (2.1.3.13) will determine the relative temperature of the fluid in the "Down" region, based on histogram measurements:

$$\Delta T_i = T\text{-}T_c = T_c \left(\frac{k_0 k_B T_c}{V \delta \rho_0^2} \frac{\langle i_0 \rangle \sigma_{i,0}}{\langle i \rangle \sigma_i} \right)^{1/\gamma} = \frac{0.0220514}{\left(\langle i \rangle \sigma_i \right)^{1/\gamma}} , \qquad (2.1.3.38)$$

where $k_0 = 1.33 \ 10^{-8}$ m^2/N, $k_B = 1.38 \ 10^{-23}$ J/K is Boltzmann's constant, $T_c = 318.687$ K and $\gamma = 1.19$ for SF$_6$ [Moldover *et al.*, 1979], V is the volume corresponding to an image area of 1 pixel = 3.1 μm and a field depth of $t_0 = 1.9$ μm, $V = 3.1$ μm x 3.1 μm x 1.9 μm = 1.76 10^{-17} m^3. We used the same 36 background images with an average of gray level intensity $\langle i_0 \rangle = 129 \pm 2$ with variance $\sigma_{i,0} = 21.3 \pm 0.6$. The range of average background intensity $\langle i_0 \rangle$ was between 108 and 155 and the range for the variance $\sigma_{i,0}$ of the histograms was between 14 and 29. For the fluctuation images shown in Fig. 2.1.3.12 the corresponding averages and variances for the gray level intensities are listed in table 2.1.3.5.

Table 2.1.3.5. The average gray level intensities and variances obtained from the histograms of the images shown in Fig. 2.1.3.12. The estimated temperature ΔT_i is based on the gray levels calibration from histogram measurements.

Image	$\langle i \rangle$ (gray level)	σ_i (gray level)	ΔT_i (μK)
100	130	27	40.16
200	101	22	61.38
300	114	27	44.92
400	92	22	64.31
500	116	28	43.44
575	114	27	45.36

Based on the complete set of video recordings, we found that the average gray level intensity was $\langle i \rangle = 114 \pm 9$, the variance was $\sigma_i = 26 \pm 2$, and the estimated temperature difference was $\Delta T_i = 46.74 \pm 0.03$ μK with a range from 36.19 μK to 67.32 μK. This temperature is within the temperature quench separating the "Up" and "Down" regions, which was 300 μK and included the critical point.

2.1.3.8.   The universality scaling exponent

Following the same procedure as for the "Up" region and using equations (2.1.3.2), (2.1.3.3), (2.1.3.4) and (2.1.3.5), the variation in temperature can be determined (see Table 4 in the Appendix). The experimental results for the 0.3 mK quench for the "Down" region are reported in Figure 2.1.3.16 in reduced units $k^* = \xi/\lambda$ and $t^* = t/t_\xi$. The data are a reasonable fit to the "universal" curve with a regression coefficient of -0.921. The power law follows $t^{-0.330}$ growth for SF_6 and is similar to the power law found for the early stage of growth for shallow quenches, which is $t^{-1/3}$ [Chou et al., 1979].
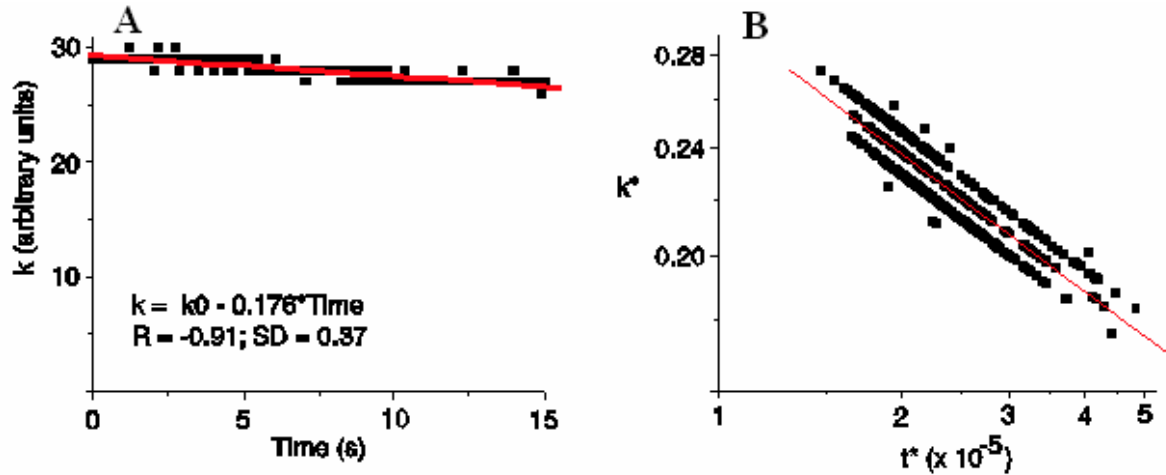
Figure 2.1.3.16.   Early growth law in pure fluid (SF_6) when gravity effects are absent. The slowly changing wave number (panel A) is an indication slow growth of fluctuations that can be captured in a log-log plot of the scaled wave vector k^* versus the reduced time t^*. The power law of the "Down" region at 0.3 mK temperature quench shows an exponent of -0.330 ± 0.006 (panel B).

The advantage of using the scaled units k^* and t^*, is that any results obtained with liquids and fluids at different temperature quench depths can be plotted on the same axis, thus demonstrating scaling and universality in phase separation phenomena.

2.1.3.9. Temporal evolution of fluctuations

The local fluctuation evolutions are recorded in Fig. 2.1.3.19.
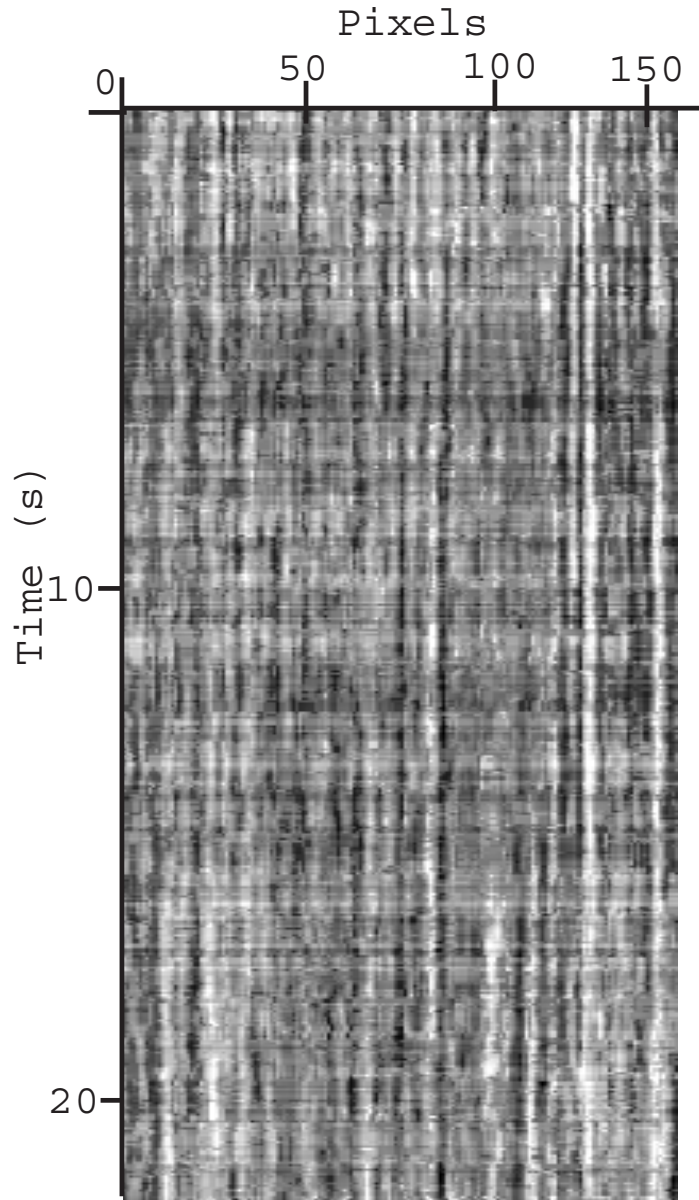
Figure 2.1.3.19. Temporal evolution of fluctuation of a one-dimensional section through successive frames of the recording. Significantly persistent temporal fluctuations (vertical lines of constant gray level) lasting for more than 10 s can be identified around pixel position 125. The display contains 475 sequences 3.3 ms apart. The thermal fluctuation growth gives rise to phase separation.

2.1.4. Results regarding phase separation

Phase separation in liquid mixture and pure fluid is a common process that occurs in many areas of natural science, engineering and industry [Papon, 2001]. Phase separation is also important in material processing because the final properties of the material depend on the final morphology when phase separation is done [Gunton, 1983].

The phase separating process is investigated by performing thermal quenching of 3.6 mK from the one phase region to the two phase region. Usually under ordinary gravity conditions the growth process is greatly affected by convection and sedimentation which inevitably drive the denser fluid downward and the lighter upward. A number of experiments [Garrabos *et al.*, 1992]; [Perrot *et al.*, 1999] under reduced gravity with a near density-matched binary mixture of partially deuterated cyclohexane and methanol(C*M) and pure fluid CO_2 and SF6 have been done. Results from these works support the universality approach for phase ordering in fluids and in a liquid mixture. Two types of morphologies have been previously reported: slow growth with disconnected droplets [Cumming, 1992] and fast growth with interconnected droplets [Jayalakshmi, 1992]. The slow growth appears when a cluster of droplets embedded in the majority phase is disconnected. In this case the growth law (the relationship between the characteristic dimension of droplets and time) is $k* \approx t*^{1/3}$ [Perrot *et al.*, 1994]. Fast growths have been shown to appear when the volumes of the phases are equal and the droplet pattern is interconnected. In this case the sizes of the droplet grow linearly in time. The parameter which determines the transition between these regimes is the volume fraction of the minority phase [Perrot *et al.*, 1999]. These previous results have also estimated the volume fraction where the transition from slow to fast growth occurs.

Phase separation was studied in a binary mixture. Two different stages were determined:

   a) an early stage where the exponent for the power law is 1/3 and the experimental results [Chou *et al.*, 1979] were in good agreement the theoretical models of Kawasaki [Kawasaki, 1983] and Siggia [Siggia, 1979]

   b) a late stage with an exponent of 1, as expected from the hydrodynamics effects.

Both stages were found Bastea and Lebowitz [Bastea, 1997] by three dimensional simulations using a Monte Carlo method.

2.1.4.1. Morphology of phase separation for SF$_6$

We report experimental results with pure fluid SF$_6$ at critical density using the SCU cell in the GMSF program [Hegseth *et al.*, 2000]. Thermostat number 34 was used in this experiment to record the temperature inside the cell. Before the 3.6 mK quench the cell was heated to 1 K above the critical temperature T$_c$ where it equilibrate to a homogeneous state. The 3.6 mK temperature quench is shown in Fig. 2.1.1.5. As is seen in Fig. 2.1.4.1.A, the fluid separates after the temperature quench. The bright and dark spots are cluster of droplets with high and low density, respectively. A microscope was used to record the detailed morphology of a small area of the original image (Fig. 2.1.4.1.B).
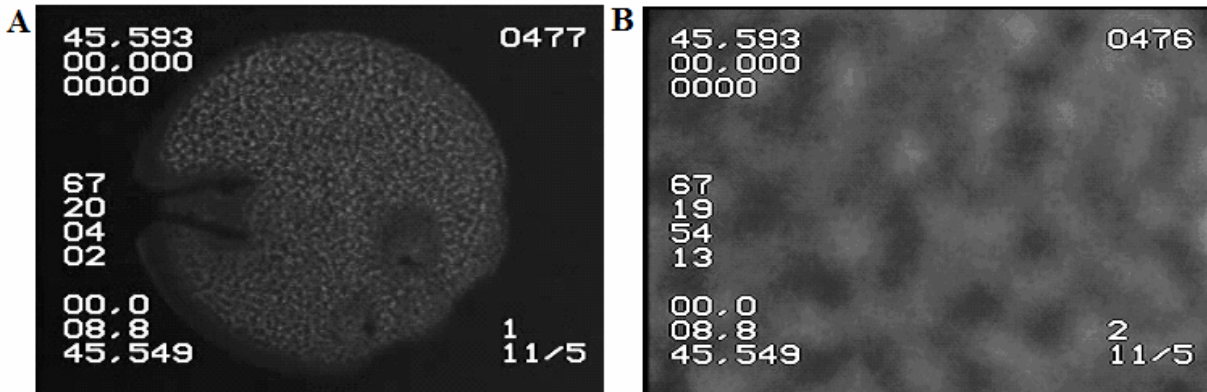
Figure 2.1.4.1. Phase separation. Full (A) and microscopic (B) views of the sample cell after a 3.6 mK temperature quench. The presence of the three thermistors inside the cell creates distortion in the image (dark spots around thermistors). The fluid separation in gas and liquid can be observed as domains of different brightness. The bright and dark spots of the interconnected domain are the basis of the quantitative analysis that we develop hereafter.

2.1.4.2.   Macroscopic view of phase separation for SF$_6$

We analyzed 436 full view frames (see Fig. 2.1.4.1.A) from the original video recording of the experiment.

First, following the same procedure of image enhancement as in section 2.1.3, the power spectra of filtered and non-filtered images (Figure 2.1.4.2) were determined. The enhancement of the filtered image (Fig2.1.4.2.B) resulted not only in a clearer "ring", but also the horizontal and vertical lines related to the optical noise were removed.
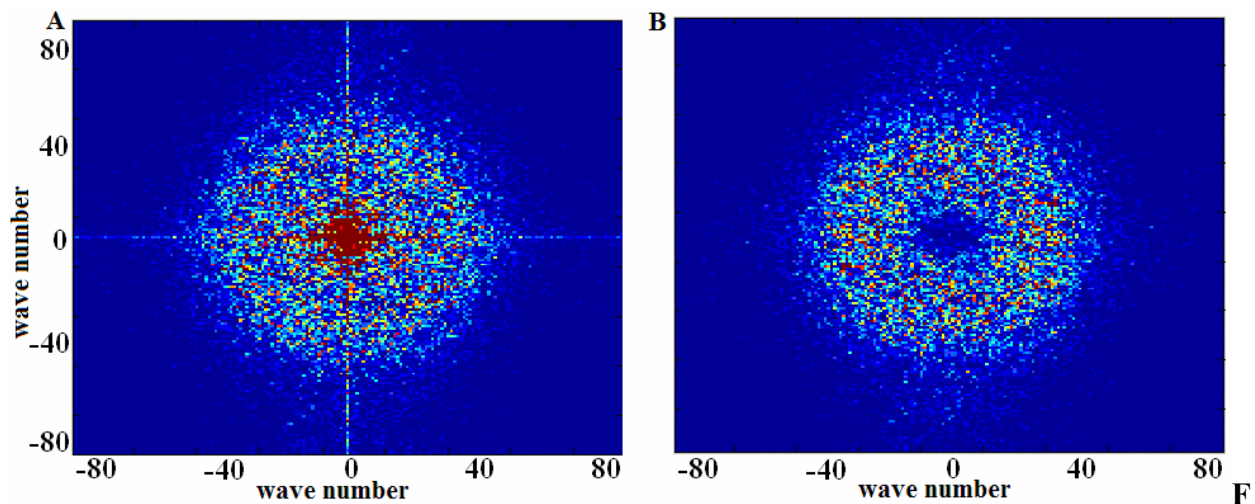
igure 2.1.4.2.   Power spectra of full view images. Power spectra for non-filtered (A) and filtered (B) full view image shown in Fig. 2.1.4.1.A. By trial and error we found that the optimal sizes of the moving average filter to be nine.

For digital image processing purpose, the image obtained by subtracting the filtered image from the original image was called the "phase separating image" (Fig. 2.1.4.3).
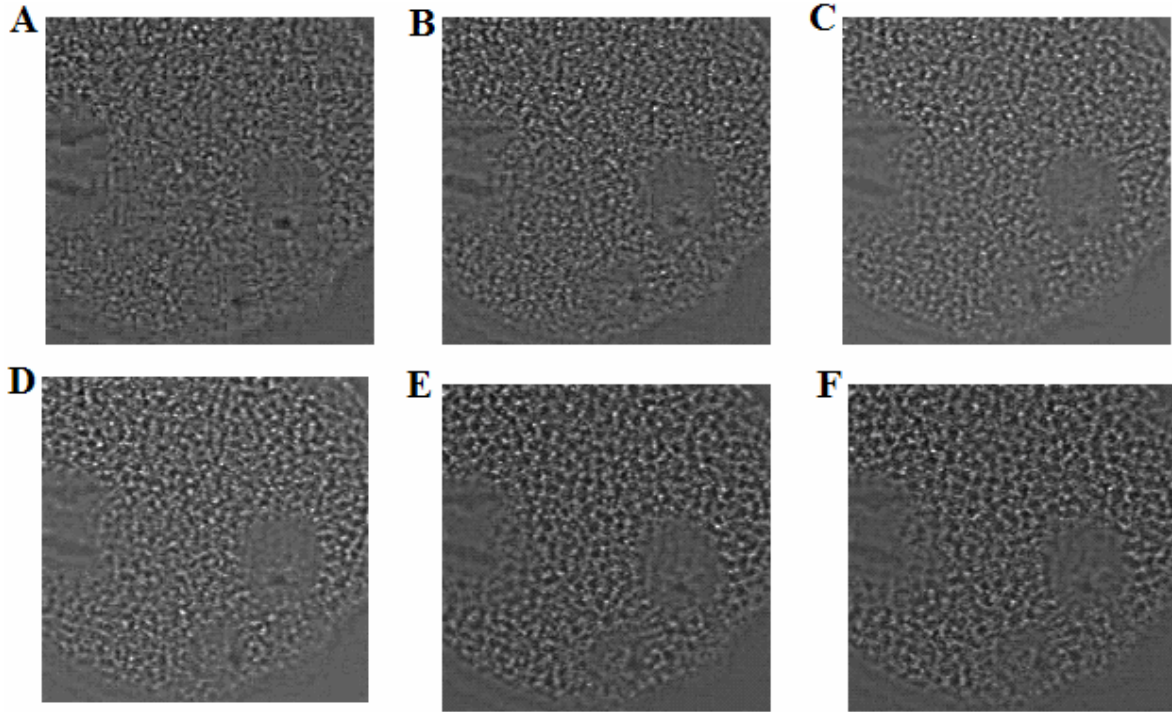
Figure 2.1.4.3.   Phase separating images obtained by subtracting the filtered (blurred) image from the original image for the full view case. The images correspond to frames 2019 (A), 2119 (B), 2200 (C), 2250(D), 2320 (E) and 2440 (F). As can be observed toward the top of each image the phase separation increases from image 2019 to image 2440.

In order to find quantitative information from the phase separating images, we computed their power spectra (Fig. 2.1.4.4). The ring is broader in the beginning of the sequence and becomes narrower as we approach the end of the sequence. This means that the corresponding wave numbers are larger at first and decrease toward the end of the temperature quench [Hegseth *et al.*, 2002]. Since the wave number is inversely proportional to the characteristic length of the clusters in the image, the characteristic length increases as the phase separation progresses.

For each frame in the full view of the phase separation region (frames 2019 to 2440), we extracted a typical size of the fluctuating domain, called characteristic length, λ related to the wave number through equation (2.1.3.1) and (2.1.3.2) from section 2.1.3. As the image index (time) increases, the estimated maximum of the radial average of the power spectrum, k_m, gets smaller. In order to estimate the wave number associated with the broad peak in each power spectrum we used a fifth order polynomial interpolation of the radial average of the power spectrum. The computed radial average of the power spectra and the corresponding polynomial fit are shown in Fig. 2.1.4.5.
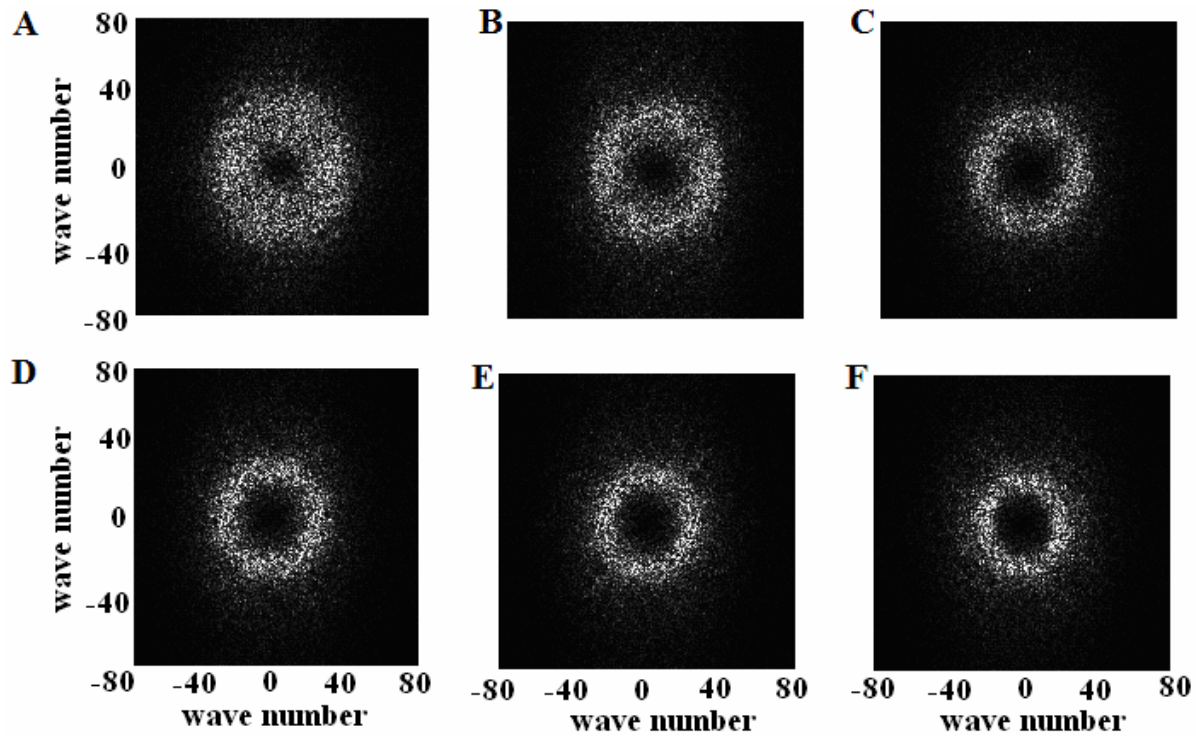
Figure 2.1.4.4.   Power spectra corresponding to full view phase separating images in Fig. 2.1.4.3. The thickness of the ring decreases as the time increases, and the wave number decreases as we move toward the end of the sequence.
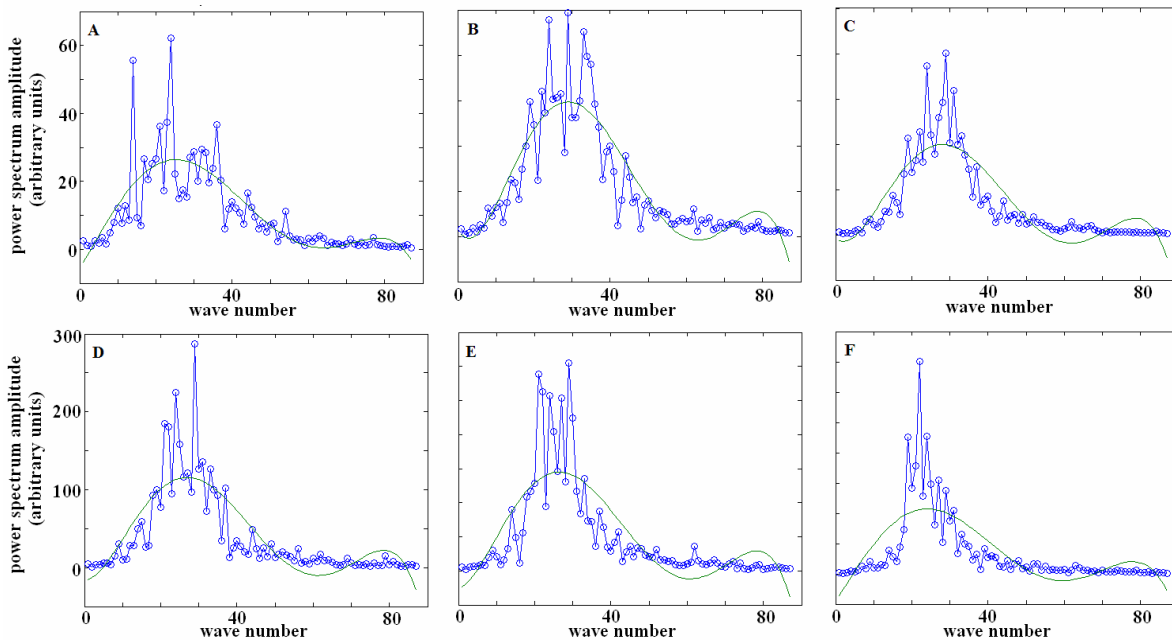
Figure 2.1.4.5.   Radial average of the power spectra corresponding to full view phase separating images 2019 (A), 2119 (B), 2200 (C), 2250 (D), 2320 (E), and 2440 (F). The circles indicate the radial average of the power spectra and the continuous green line shows the fifth order polynomial interpolation used to find the peak (maximum value) associated with the wave number.

The corresponding histograms of the full view fluctuating images in Fig. 2.1.4.3 contain information about the gray level distribution (Fig. 2.1.4.5) used to determine the scaled variable k^* and t^* (Table 2.1.4.1).

Table 2.1.4.1.   Experimental data used to plot the power law relationship between the reduced wave number k^* and the reduce time t^* for full view images. The average gray level intensity $<i>$ and the variance σ_i of the recorded image are both measured in gray levels. The corresponding temperature based on the histogram measurements was computed according to (2.1.3.13) $\Delta T = \dfrac{0.0220514}{\left(\langle i\rangle \sigma_i\right)^{1/\gamma}}$. The absolute time measured from the beginning of the experiment is $t + 242396.(3)$ (s). The characteristic length was computed using the values of the maximum wave number obtained from the radial average of the power spectra according to $\lambda = (174$ pixels x 3.1 µm/pixel$)/k_m = 539.4/k_m$, the correlation length was computed based on $\xi = \xi_0(\Delta T/T_c)^{-\nu}$, and the characteristic time was computed using $t_\xi = 1.71442 \ 10^{17} \ \xi^3$. The reduced wave numbers k^* in the table were obtained using ξ/λ and the reduced time t* was computed using $(t/t_\xi - 17675.85) \ 10^{-5}$.

Image	$<i>$	σ_i	ΔT (µK)	t (s)	k_m	λ (µm)	ξ (µm)	t_ξ (s)	k^*	t^*
2020	79	15	57.55	0.00	27	19.98	3.61	8.07	0.18	0.12
2040	79	16	55.61	0.67	28	19.26	3.69	8.61	0.19	0.10
2080	80	15	57.89	2.00	30	17.98	3.59	7.97	0.20	0.13
2120	77	16	55.00	3.37	29	18.60	3.72	9.79	0.20	0.10
2160	88	16	50.34	4.67	28	19.26	3.95	10.54	0.20	0.05
2200	88	14	55.84	6.00	28	19.26	3.68	8.55	0.19	0.11
2240	90	16	48.65	7.38	28	19.24	4.02	11.12	0.21	0.04
2280	74	15	60.05	8.67	28	19.26	3.51	7.43	0.18	0.15
2320	83	17	49.66	10.0	28	19.26	3.97	10.70	0.21	0.05
2360	86	16	52.18	11.4	27	19.98	3.84	9.73	0.19	0.07

Using equation (2.1.3.8) and (2.1.3.9) from section 2.1.3 we determined the characteristic length ξ. Following a similar procedure with that previously described in section 2.1.3, we plot the growth law in scaled k^* versus t^* (see equation (2.1.3.11) of the 2.1.3 section) and a few values listed in Table 2.1.4.1. The scaling law derived from the experimental data for the 3.6 mK temperature quench is reported in Fig. 2.1.4.7. The average temperature obtained using the data extracted from the histograms is $\Delta T_{Full\ view} = 56.4 \pm 0.3$ µK with a range between 43.6 µK and 78.8 µK.
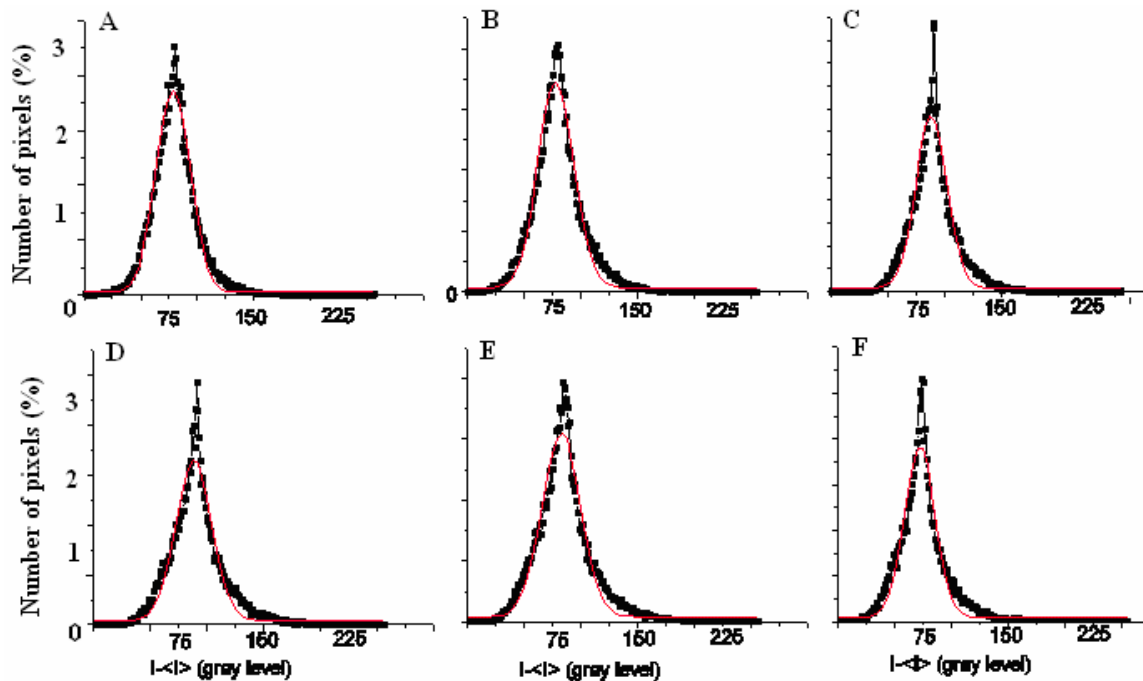
Figure 2.1.4.6.   Distribution of gray level intensities for the full view filtered images. The horizontal axis represents the gray scale from 0 to 255 and the vertical axis represents the percentage of the pixels corresponding to a certain gray level. The red continuous line represents the Gaussian fit to the histogram.

Figure 2.1.4.7.   Scaling law for full view images in reduced units *k* versus t*. The data fit reasonably well to the early stage growth curve. The continuous line is a linear fit to the experimental data with a slope of -0.348 ± 0.007 and linear correlation R = -0.933 over 184 images.
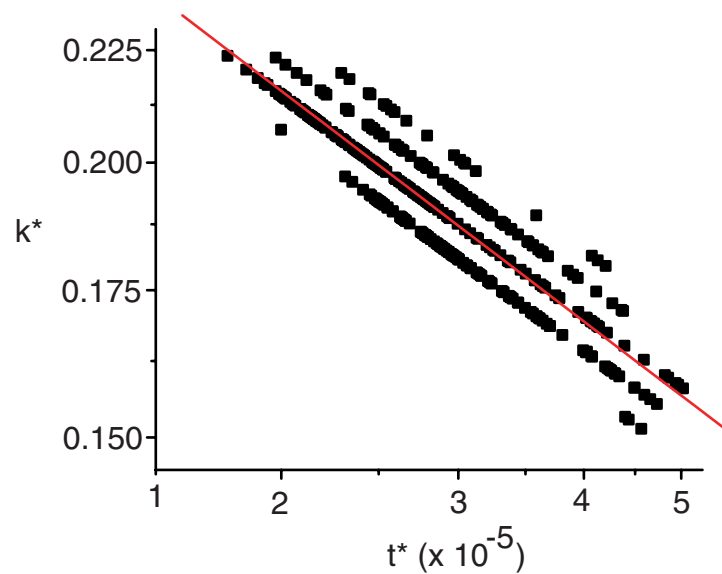
2.1.4.3. Microscopic view of phase separation for SF$_6$

We extracted 586 microscopic view frames from the original video record of the experiment. In order to avoid including the automatically marked numbers on each frame, in our analysis we cropped all frames to obtain a square image with the maximum possible area. In the 192 x 192 pixels clear images, the density varies from high (dark clusters) to low (bright clusters) as seen in Fig. 2.1.4.1.B. A true color counterpart of the previous snapshot (Fig. 2.1.4.8.A) shows that the density changes gradually from high to low values.
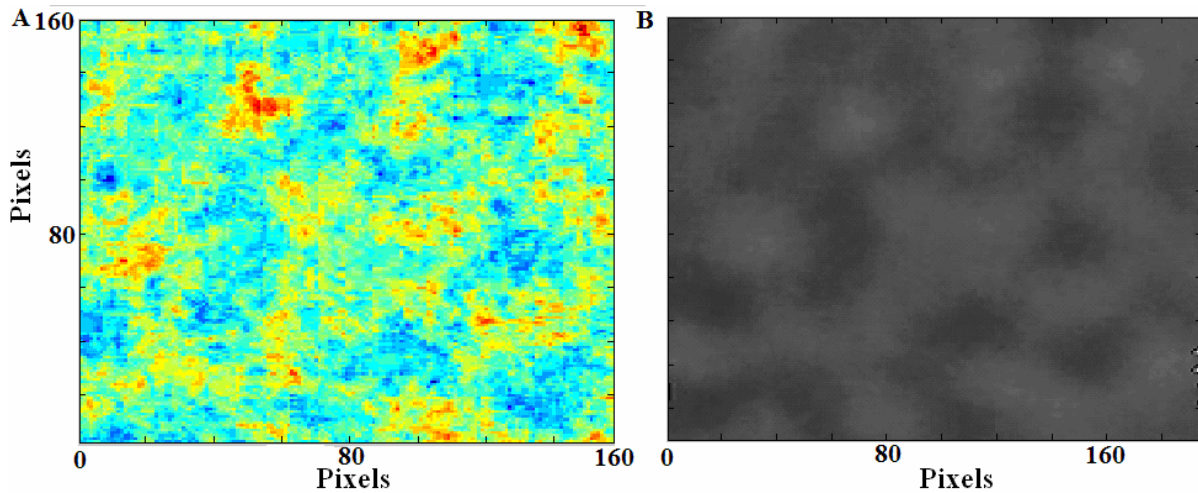
Figure 2.1.4.8. Clusters of pixels reveal domains of growing fluctuations. The true color image shows the gradually change in density (A). Density changes are visualized by bright (low density) and dark (high density) spots in the microscopic image (B).

As a representative example, we determined the power spectra of a specific image (image 1964 of microscopic view). Both the power spectrum for the original image and the filtered images were computed. Comparison of the two power spectra shows the presence of noise in the original image (bright horizontal and vertical lines).

In section 2.1.3, we found that the power spectra always have a bright ring [Goldman *et al.*, 2004]. We analyzed all 586 microscopic views and found that the ring does not have a clear contour as seen in the fluctuation section. Following the same procedure highlighted in the previous subsection for the macroscopic view, we also investigated the existence of a power law between the reduced wave number k^* and the reduced time t^*. The average temperature obtained

using the data extracted from the histograms is $\Delta T_{\text{microscopic view}} = 29.4 \pm 0.4$ μK with a range between 20.0 μK and 86.9 μK.
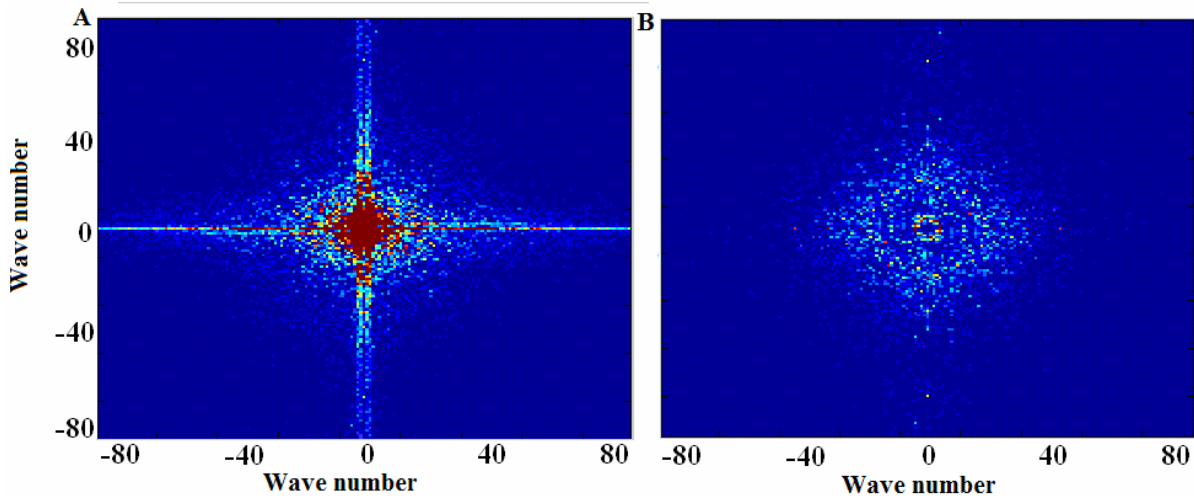
Figure 2.1.4.9. Power spectra of original (A) and filtered (B) images for microscopic view. The horizontal and vertical lines along the center of the power spectra (A) are evidence of the optical noise in the image.

Table 2.1.4.2. Experimental data from all 586 frames were used to plot the power law relationship between the reduced wave number $k*$ and the reduce time $t*$ for microscopic view images. The average gray level intensity $<i>$ and the variance σ_i of the recorded image are both measured in gray levels. The corresponding temperature based on the histogram measurements was computed according to (2.1.3.13) $\Delta T = \dfrac{0.0220514}{\left(\langle i \rangle \sigma_i\right)^{1/\gamma}}$. The absolute time measured from the beginning of the experiment is $t + 242376.08(3)$ (s). The characteristic length was computed using the value of the maximum wave number obtained from the radial average of the power spectrum according to $\lambda = (174 \text{ pixels} * 3.1 \text{ μm})/k_m = 539.4/k_m$, the correlation length was computed based on $\xi = \xi_0(\Delta T/T_c)^{-\nu}$, and the characteristic time was computed using $t_\xi = 1.71442$ $10^{17} \xi^3$. The reduced wave numbers $k*$ in the table were obtained using ξ/λ and the reduced time $t*$ was computed using $(t/t_\xi - 1000740)\,10^{-6}$.

Image	$<i>$	σ_i	ΔT (μK)	t (s)	k_m	λ (μm)	ξ (μm)	t_ξ (s)	$k*$	$t*$
1450	125	21	282	1.25	30	19.84	1.31	0.386	6.607	0.373
1500	131	25	229	2.92	29	20.52	1.49	0.575	7.293	0.579
1550	130	24	241	4.58	28	21.26	1.45	0.519	6.805	0.534
1600	128	13	415	6.25	25	23.81	1.02	0.184	4.297	0.319
1650	115	23	269	7.92	27	22.04	1.35	0.421	6.121	0.425
1700	136	27	210	9.58	27	22.04	1.58	0.679	7.177	0.644
1750	125	26	233	11.3	23	25.88	1.48	0.556	5.720	0.565
1800	142	24	219	12.9	20	29.76	1.54	0.626	5.175	0.614

Based on Table 2.1.4.2 we plotted the reduced wave number k* versus the reduced time t* in order to extract the scaling law for the microscopic view. The exponent of the power law was -0.28 ± 0.01 with a linear regression coefficient R = -0.74 (black squares in panel A of Fig. 2.1.4.9) for the region of almost constant or slowly decreasing wave numbers (panel B of Fig. 2.1.4.9, time interval between 0 and 10 seconds). A slow decrease in wave number is equivalent to a slow increase in the correlation length and determines a slow grow of fluctuations. The fact that the exponent for the macroscopic view (-0.348 ± 0.007) is close to the above exponent for the microscopic view constitutes experimental evidence of the scale invariance of the fluctuations. If the rate of change of wave number is significant (see panel B of Fig. 2.1.4.9, time interval above 10 seconds), then the slope of the scaled wave numbers versus scaled times is significantly larger (red circles in panel A, Fig. 2.1.4.9) compared to the slow growth regime.
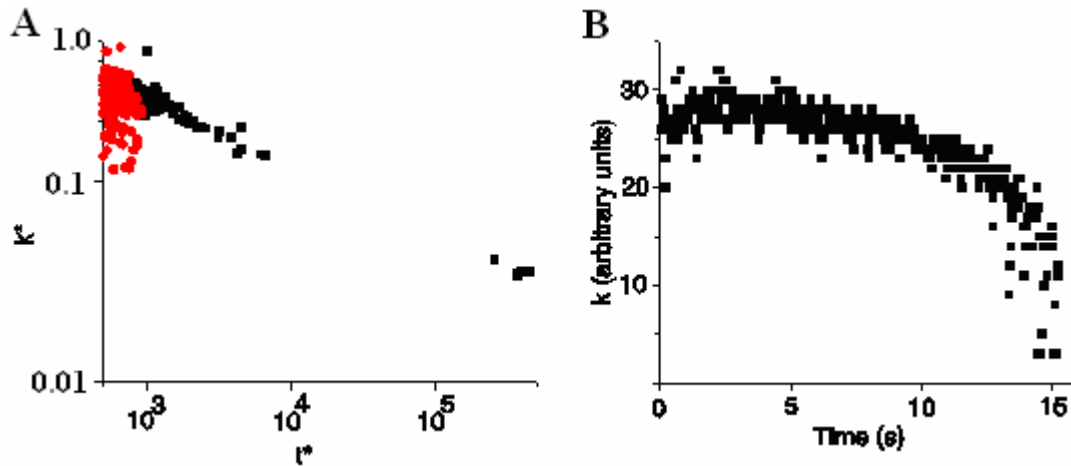
Figure 2.1.4.9. **Slow and fast growing fluctuations.** The plot of *k** versus *t** shows two different power laws: a small slope (black squares in panel A) corresponding to slowly changing wave numbers (time interval 0 to 10 seconds in panel B) and a significantly larger slope (red circles in panel A) corresponding to a fast change in the wave numbers for time intervals above 10 seconds. The closeness in the slope values of the two power laws for the slow growing macroscopic and microscopic views demonstrates the invariance of the scale.

2.1.5. Conclusions

According to Stanley [Stanley, 1971], the correlation length follows a power law near the critical point

$$\xi = \xi_0 \left[(T-T_c)/T_c \right]^{-\nu}, \tag{2.1.5.1}$$

where the scaling coefficient of the correlation length is $\xi_0 = 1.8 \, 10^{-10}$ m, $T_c = 318.687$ K, and $\nu = 0.633$ for SF_6 [Moldover *et al.*, 1979]. However, the scaling factor is $\xi_0 = \xi_{0,Down}$ for $T < T_c$ and $\xi_0 = \xi_{0,Up}$ for $T > T_c$. Sengers and Sengers [1978], and Moldover *et al.* [Moldover, 1979] explicitly derived the ratio $\xi_{0,Up}/\xi_{0,Down}$ for the cubic model of SF_6 and compared their findings to the values for the Ising model near the critical point [Aharony and Hohenberg, 1976; Tarko and Fisher, 1975] $\xi_{0,Down}/\xi_{0,Up} = 0.512857$ and the Landau-Ginzburg-Wilson model [Brezin *et al.*, 1976] $\xi_{0,Down}/\xi_{0,Up} = 0.52281$.

Based on direct measurements of the wave number from the radial average of the power spectrum, we extracted the characteristic length and found that if the power law (2.1.5.1) is valid, then the resultant temperature difference was too small to be detected by the instruments on ALICE II (see section 2.1.3.2). One possible explanation is that the finite size effects are significant near the critical point and alter the expression of the scaling factor ξ_0. However, if we assume that both $\xi_{0,Up}$ and $\xi_{0,Down}$ are modified near the critical point according to the same (unknown) relationship then their ratio should be independent of any finite size effects. As a result, it is possible to estimate the position of the critical point inside the 300 µK temperature quench by taking the ratio of the characteristic lengths derived directly from the maximum values of the averaged power spectra.

Let us assume that the critical point is somewhere between T_{Up} and T_{Down} at a distance x from the upper temperature plateau (Fig. 2.1.5.1).

$$T_{Up} = T_c + x \, (T_{Up} - T_{Down}) = T_c + x\Delta T, \tag{2.1.5.1}$$

and

$$T_{Down} = T_c - (1-x) \, (T_{Up} - T_{Down}) = T_c - (1-x)\Delta T, \tag{2.1.5.2}$$

The correlation length on "Up" plateau is simply:

$$\xi_{UP} = \xi_{0,Up} \left(\frac{T_{UP} - T_c}{T_c} \right)^{-\gamma} = \xi_{0,Up} \left(\frac{x\Delta T}{T_c} \right)^{-\gamma}, \tag{2.1.5.3}$$

and similarly on "Down" plateau

$$\xi_{Down} = \xi_{0,Down}\left(\frac{T_c - T_{Down}}{T_c}\right)^{-\gamma} = \xi_{0,Down}\left(\frac{(1-x)\Delta T}{T_c}\right)^{-\gamma}. \qquad (2.1.5.4)$$

The ratio of (2.1.5.3) and (2.1.5.4) is

$$\frac{\xi_{Up}}{\xi_{Down}} = \frac{\xi_{0,Up}}{\xi_{0,Down}}\left(\frac{x}{1-x}\right)^{-\gamma}, \qquad (2.1.5.5)$$

which can be used to determine the position x of critical temperature by computing the ratio of the correlation lengths on "Up" and "Down" plateau.

$$x = \frac{1}{1 + \left(\dfrac{\xi_{Up}}{\xi_{0,Up}}\dfrac{\xi_{0,Down}}{\xi_{Down}}\right)^{1/\gamma}}. \qquad (2.1.5.6)$$

From the radial average of the power spectrum we determined the most probable value of the wave number (k). By assuming that $\xi \propto 1/k$ the relationship (2.1.5.6) becomes

$$x = \frac{1}{1 + \left(\dfrac{k_{Down}}{k_{UP}}\dfrac{\xi_{0,Down}}{\xi_{0,Up}}\right)^{1/\gamma}}. \qquad (2.1.5.7)$$

Figure 2.1.5.1. The temperature profile includes the critical temperature T_c whose exact location can be inferred from the correlation length.
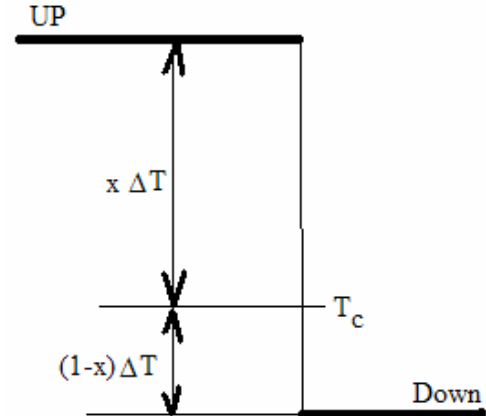
The images analyzed gave us $26 \leq k_{Up} \leq 31$ with a mean value of $k_{Up} = 28.94194 \pm 0.0745$ and $26 \leq k_{Down} \leq 30$ with a mean value $k_{Down} = 27.95 \pm 0.04$. Based only on the mean values $k_{Down}/k_{Up} = 0.965727$, we estimated that the mean value for the critical point is $x = 0.6379$ ($0.604 \leq x \leq 0.664$) using data from the Ising model and $x = 0.6344$ ($0.601 \leq x \leq 0.660$) using data from the Landau-Ginzburg-Wilson model. This suggests that the critical temperature is closer to the

"Down" plateau temperature. Its position could be determined precisely based on measurements of the maximum value of the wave number from the radial average of the Fourier power spectra. The advantage of using the ratio of correlation lengths is that we do not need to explicitly define the coefficients of proportionality between ξ and k. As a result, a ratio ξ_{Up}/ξ_{Down} simply converts to k_{Down}/k_{Up} and can be computed without any difficulties. However, in order to determine correctly the absolute value of ξ based on values obtained for k we must convert frequency domain values of k back to spatial domain values for ξ.
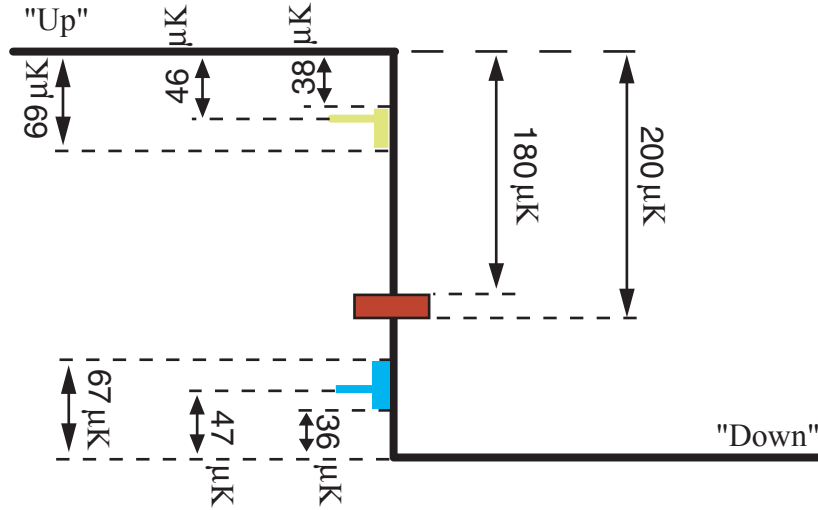
Figure 2.1.5.2.   The estimated position of the critical temperature inside the 300 μK temperature quench. The values on the left side are based on equation (2.1.3.13) that establishes a relationship between the temperature difference and the parameters evaluated from the histogram of the image. For the "Up" region the average temperature difference was 46 μK measured with respect to the "Up" region temperature, while using images for the "Down" region the histogram method gave an average temperature difference of 47 μK measured with respect to the "Down" region temperature. Based on the ratios of the characteristic lengths we determined that the critical temperature should be in the range 180-200 μK measured with respect to the "Up" reference (red square).

Fig. 2.1.5.2 suggests that the critical temperature is between 38 μK and 69 μK measured with respect to the temperature of the "Up" region as estimated using the average gray level intensity and variances extracted directly from the histograms of the recorded images according to equation (2.1.3.13)

$$\Delta T_i = T\text{-}T_c = T_c \left(\frac{k_0 k_B T_c}{V \delta \rho_0^{\,2}} \frac{\langle i_0 \rangle \sigma_{i,0}}{\langle i \rangle \sigma_i} \right)^{1/\gamma} = \frac{0.0220514}{\left(\langle i \rangle \sigma_i \right)^{1/\gamma}} \,.$$

Using the histogram method for the "Down" region we found that the temperature difference is in the range of 36 μK to 67 μK measured with respect to the "Down" reference temperature. Finally, based on the ratio of the wave numbers obtained from the average power spectrum for "Up" and "Down" region we found that the critical temperature is in the range 100-120 μK measured with respect to the temperature of the "Down" region (on the right side of the ramp in Fig. 2.1.5.2).

2.2. Binary liquid

The presence of a gravitational field leads to practical limitations of the interpretation of critical phenomena experiments in fluids near the gas-liquid critical point [Moldover *et al*., 1987]. Gravity induces a density gradient near the critical point [Teichner, 1904; Baehr,1954]. For example, the effect of sedimentation is seen in experiments with phase separating liquids when performed under the influence of gravity. The effect of sedimentation was reduced in a fluctuating binary mixture [Hegseth *et al*., 2003] using a density matched mixture of methanol and partially deuterated cylcohexane (CC*-Me) with a critical concentration of 71% by weight.

2.2.1. Light scattering and Gaussian fluctuations

In the simple case of parallel incident light arriving at a cell filled with a homogeneous transparent medium (see Fig. 2.2.1.1) all the transmitted light can be focused at the focal point. In this case, only the phase of the transmitted light is affected by the local density fluctuations in the fluid. A different situation occurs when the incident light passes through a non-homogeneous medium with local variations in the refractive index δn. In this case, the interaction of the incident light with the non-homogeneous medium may be understood as a light scattering process that produces the image. The scattering of light means absorption of energy from an incident wave by a non-homogeneous medium and reemission of some portion of the electromagnetic energy. Although scattering appears to be similar to absorption, it is a much more complex phenomenon [Hecht, 2001]. Due to multiple scattering processes, only a fraction of the incident radiation reenters the original beam of light. The total amount of scattered light and the angular distribution are related to the optical properties of the scattering medium. At the microscopic level, the incident radiation produces excitation of the molecular polarizability that causes a radiation of the electromagnetic wave. The well separated centers act independently (incoherently) and the net radiance is the sum of their individual irradiances. The scattering of the incident light is caused by the fluctuation centers that are related to small changes in the density of the medium, which, in turn, determines the local variations of the index of refraction δn. As a result, the local density variations induce local changes in the image brightness because of the modifications in the propagation of light inside the medium. The visualization of

102

fluctuations is based on the interference between the scattered and transmitted light [Guenoun *et al.*, 1989]. In the vicinity of the critical point, the intensities of the transmitted and scattered light have become comparable and the contrast is maximized. The effect of multiple scattering can lower the contrast in the fluctuation pattern. To reduce the effect of multiple scattering, the sample can be made thinner [Beysens *et al.*, 1978]. We assume that there is no light absorption and the variations in intensity of the images are determined by the light scattering. The dark and bright regions in the scattering images are areas of more or less light scattered due to the local fluctuations of the mixture concentration. The fluctuations evolve in time, and a typical fluctuation lasts a few seconds.

As we will show in section 2.2.2.2., the histograms corresponding to BF, PC, and DF images exhibit Gaussian statistics (Figs. 2.2.2.5, 2.2.2.6 and 2.2.2.7). This characteristic can be traced back to the thermodynamic theory of fluctuations [Landau, 1969]. According to the order parameter theory of critical phenomena [Landau, 1969], far from the critical temperature T_c, the probability *p(M)dM* for a small but macroscopic subsystem to have the order parameter M in the ranges *M* and *M+dM* is:

$$p(M)dM = A\exp\left[-\frac{1}{2}\left(\frac{\partial^2 F}{\partial M^2}\right)_0 \delta M^2 + \frac{1}{4}\left(\frac{\partial^4 F}{\partial M^4}\right)_0 \delta M^4 + O(\delta M^6)\right]dM, \quad (2.2.1.1)$$

where A is normalization constant, F is the free energy of the system that was expanded about its minimum, and only the even powers are retained in the probability distribution function. For temperatures far from the critical point, the coefficient $\left(\frac{\partial^2 F}{\partial M^2}\right)_0$ is large and, as a result, the quadratic factor in (2.2.1.1) is dominant. Since we correlated the fluctuations in the order parameter (the mixture concentration) with the fluctuations in the intensity of the scattered light, the histogram of the image should also be Gaussian. If the concentration of the fluid elements fluctuates, then a small change in the index of refraction occurs and a change in the phase of scattered electric field is expected. The changes in the refractive index of the fluid produce changes in the optical path of the transmitted and scattered light.

2.2.2. Experimental setup

The methanol and cyclohexane binary liquid [Hegseth *et al.*,2003] is located between two 10 mm diameter sapphire windows (8.5 mm thick) separated by a gold-coated 3 mm thick brass spacer. The sample is placed in a larger copper housing with a diameter of 6 cm and length of 6 cm. Although the cell is filled with a mixture slightly off the critical concentration $c = (c_c - 0.01) \pm 0.002$, it is well within the concentration range $|c-c_c| < 0.05$ where fluctuations are visible [Guenoun *et al.*, 1989]. In order to conveniently use the optical microscopy system shown in Figure 2.2.1.1, Hegseth [Hegseth *et al.*, 2003] designed a thermal control system that uses air convection and radiation for heat transfer. The copper housing of the cell contains two thermistors for temperature measurement and control. To avoid local heating from the thermistors, temperature measurements are never taken more often than every 30 seconds. The cell is temperature controlled due to its placement near the center of an aluminum cylinder of diameter $D = 10$ cm and length $L = 18$ cm that has a foil heater glued to its exterior. Heat is continuously applied to the system with a computer controlled power supply. The space between these cylinders is filled with air so that heat is exchanged with the inner copper housing only through radiation and convection. Two holes in the heating cylinder, aligned with the optical axis of the cell, allow light to enter and leave the sample fluid. To prevent convective cooling of the sample's cell windows, these holes are closed at both ends. To provide a constant ambient temperature for the inner cylinder, two more thermal shields made of 7 cm thick polystyrene surround the heating cylinder. The walls of these rectangular polystyrene boxes are attached with silicone glue to provide an outer box with inner dimension 50 cm x 40 cm x 50 cm and an inner box with inner dimension 24 cm x 24 cm x 30 cm. Light enters and leaves these shields through plexiglas windows. These boxes provide two layers of shielding, except for the bottom which has only one layer, so that the optical support for the heating cylinder, the magnification lens, and the quarter wave plate can enter these boxes. The temperature of the air between these boxes is also computer controlled. The heater is placed near the top of the space between these thermal shields in order to create stable temperature gradient in this space such that the midpoint temperature was at an ambient temperature of approximately $T_C - 5°$ C to within $1°$ C. As shown in Figure 2.2.2.1, the optical bench supports all the optical elements used for optical observation. The light

source is provided by a halogen lamp. A collimator produces a parallel beam of light of diameter d = 2.5 cm, which is collected and focused into a 0.8 mm pinhole by two 7.8 mm diameter plan-convex lens. The pinhole is at the input focal point of a 50 mm lens. The central portion of the beam with a diameter of 1 cm travels through the sample cell. Although this wide band source results in a small coherence time and a longitudinal coherence length of approximately 1 μm, the geometry of the setup gives a spatial coherence of approximately 120 μm in the microscope object plane. The sample cell position is adjusted along the optical axis by moving the bottom support using a translation stage of the heating cylinder that also contains the sample cell. The light input to the heating cylinder passes through a small glass covered hole and the output light travels through a 50 mm magnifying lens. The space between the cylinder and the lens is filled with a polystyrene spacer that allows for relative movement along the optical axis of the cell, the heating cylinder and the lens in order to adjust the position of the object plane in the sample cell. This optical setup constitutes the bright-field (BF) experimental arrangement.

Two other methods of microscopy were also used as shown in Figure 2.2.2.1. These methods require further treatment of the output light before the image is formed on the CCD. The treatments were applied at the focal point for the output light of the magnification lens L_3. The second method, called phase contrast (PC), consisted of passing the light through a mica quarter-wave-plate of 1 cm diameter. The light that passes through this plate is retarded by a phase of $\pi/2$ radians relative to what it would have been had it not passed through. This has the effect of rotating the electric field vector of the input light by 90°. The light that is focused on this plate is primarily that part of the incoming wave field that is called the transmitted light, *i.e*, the part of the incoming parallel light wave forward scattered by fluctuations of the refractive index. The light that does not pass through this plate is also scattered by fluctuations but its electric field vector is not rotated. By rotating the electric field vector of the transmitted light at the lens output focal plane, the wave at the detector will be the superposition of two waves that interact and make phase objects visible by converting a phase difference into an intensity variation. The third treatment, called dark-field (DF), used a 7 mm diameter opaque disk, placed at the output focal point of the magnification lens L_3 (Fig. 2.2.2.1), to block the transmitted beam and allow only the scattered beam to enter the CCD array. These elements were positioned in the focal plane using the same support. The support consisted of an aluminum ring with three 2 mm wide arms that held the quarter-wave-plate at the center of the ring and in the plane of the ring.

The opaque disk was glued to one of the arms such that it was also in the plane of the ring. The plane of this support was positioned perpendicular to the optical axis and connected to a translation stage. The stage allowed the support to be displaced perpendicular to the optical axis such that: 1) the light would pass through the focus unaltered, leading to BF, 2) the light near the focus would pass through the quarter-wave-plate leading to PC, and 3) light would be blocked at the focus by the opaque disk, leading to DF. This allowed the three optical techniques to be changed inside by adjusting the translation stage. Since the method of separating the scattered and transmitted light in the binary liquid setup is not the same as that normally used in commercial microscopes, the system was tested first with images of phase separated droplets. Figure 2.2.2.2 A-C shows images of phase separated methanol droplets using the three optical techniques [Hegseth *et al.*, 2003]. PC clearly increases the contrast of the droplet interface, and shows that a change in the optical phase between the liquid and the gas which is not visible in the BF image (Fig. 2.2.2.2 A) is converted into an intensity change in the PC image (Fig. 2.2.2.2 B). DF produces the same object but with a completely different intensity distribution over the droplet (Fig. 2.2.2.2 C).
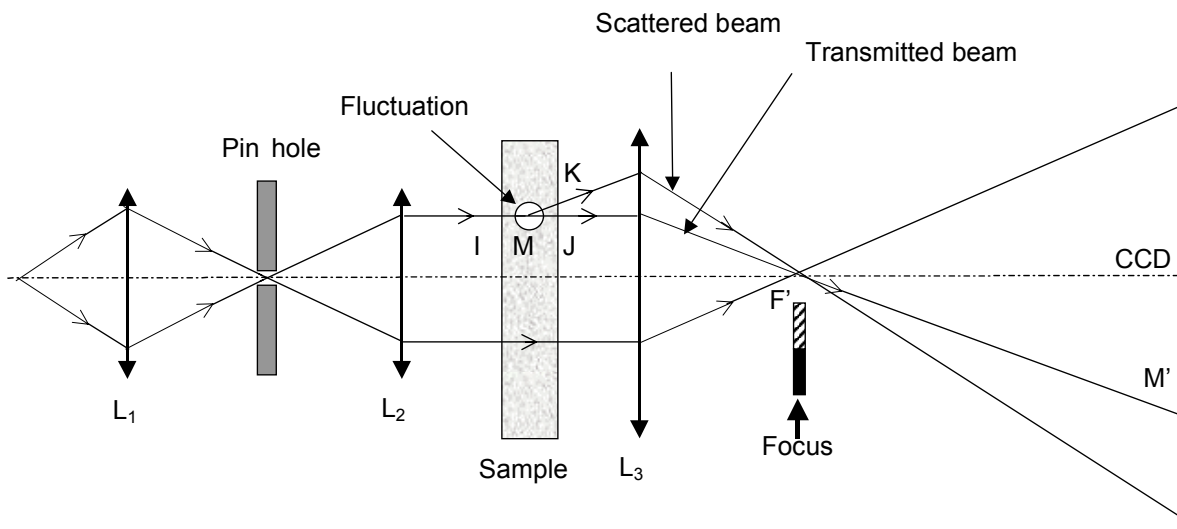
Figure 2.2.2.1.   The optical microscopy system used in the binary mixture. The white light source and a collimator produced a beam of light which is focused onto an 0.8 mm pinhole by a 50 mm lens. The fluctuations in the sample scattered the beam of light. Magnification is provided by a high quality photographic lens(L_3) of numerical apperture 1.2.

106

The cell was heated above the critical temperature T_C (T_C = 46.64° C) to approximately 50° C. At this temperature the cell was thoroughly mixed and allowed to settle for at least 12 hours to ensure that the liquid mixture was homogenous. The temperature was then decreased toward the critical point in temperature quenches. The temperature quenches, ΔT, were of 1 K in magnitude far from the critical temperature and 1 mK closer to the critical point. The temperature control system achieved stability as high as 0.1 mK over 12 hours and was primarily limited by room temperature fluctuations. Because these quenches often resulted in as much as a 20% undershoot and the stability was 0.1 mK, the temperature quenches were limited to 1 mK.
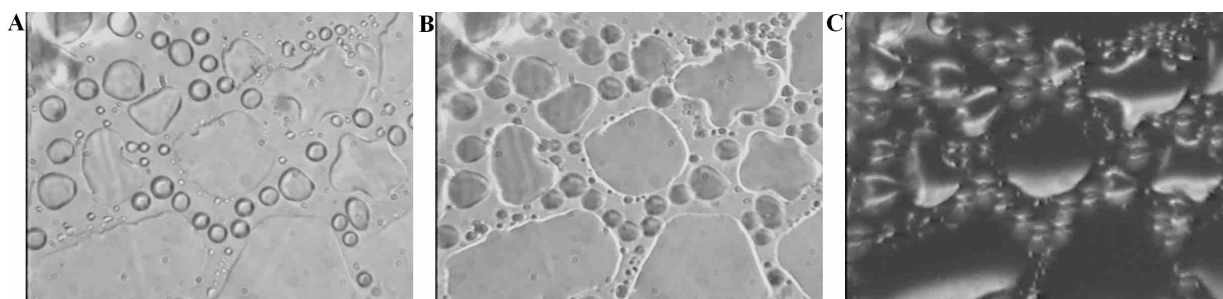
Figure 2.2.2.2. Optical microscopy and image enhancement. (A) Bright field (BF) image of the fluctuations in a liquid mixture produced by the scattering centers. (B) Phase contrast (PC) gray scale image produced by using a quarter wave plate and (C) Dark field (DF) gray scale image produced by placing an opaque object at the focus of L_3 in the optical system (Fig. 2.2.2.1).

To determine the critical temperature, video images were recorded in order to identify the fluid phase separation after a temperature quench. The phase separation was relatively fast, producing high contrast domains that grew over time. The critical point could be measured to within 0.5 mK with the 1 mK quenches. The identification of the fluctuations in the images was verified by waiting for over 12 hours at T_c+0.5 mK. During this time interval the fluctuations retained the same character and no phase separation was found. After each quench, the temperature was allowed to equilibrate for at least 20 minutes before recording the video images of the fluctuations on an HI8 VCR with full field resolution. At each temperature, BF, PC, and DF images were recorded for 1 minute each. The recorded video images were time tagged to correlate with the temperature data that was also time tagged.

2.2.3. Methods and results

As has been mention in the experimental section, the fluid studied is a binary fluid that exhibits critical behavior when the temperature and concentration are near the critical point. The binary liquid used in this experiment is a mixture of methanol and partially deuterated cylcohexane such that one of them is at a known critical concentration c_c [Houessou, 1985; Guenoun,1989]. The order parameter of the system is $M = c - c_c$, where c is the concentration of one of the chemical species. The increase in the fluctuation correlation size is manifested in a region near the critical point of the scattered light. As the critical point is approached more light is scattered because of the concentration fluctuation; the phenomenon is called critical opalescence. Long range fluctuations and other important thermodynamic properties of interest can be estimated by performing light-scattering experiments [Cannel, 1975; Ohbayaski, 1978; Joshua, 1985; Gammon, 1987].
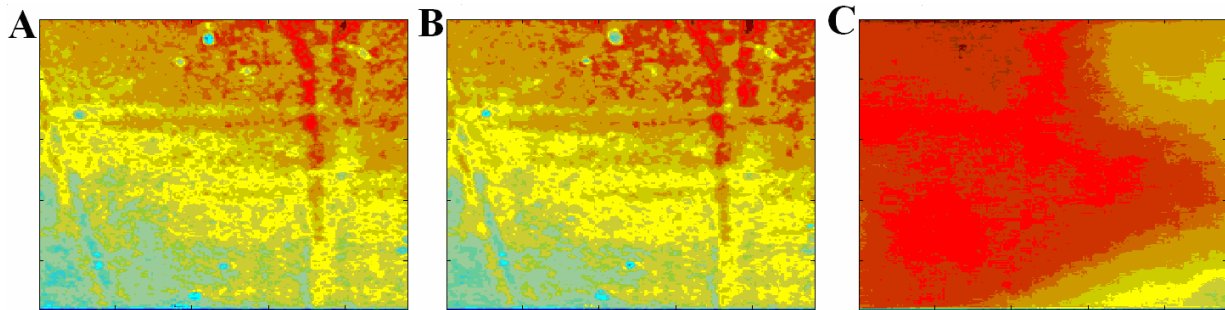
Figure 2.2.3.1.   Image enhancement using color adjustment. True color images of bright field (A), phase contrast (B) and dark field (C) for one example of fluctuating image. Bright field (BF) and phase contrast (PC) have a very similar appearance and both contain the same information about the statistics of the fluctuations. The dark field (DF) image contains information about the fluctuations at a completely different wave number scale compared to BF and PC.

2.2.3.1. The effect of different filters on image contrast

The images recorded with the methods described in section 2.2.2 exhibit spatial domain varying intensities. The images produced in the system were not uniform due to noise from dust. This optical noise gives non-uniform background intensity in addition to the intensity variation from fluctuation. To correct for the noise, we use the same method as for pure fluids (see section 2.1) and subtract an image filtered with a moving average filter from the image of interest. In this case, the fluctuations in the image do not contribute to the image background. Figure 2.2.3.2 shows enhanced images using a moving average filter to smooth the sharp transitions in the original image Fig. 2.2.3.1 for the bright field BF (A), phase contrast PC (B), and dark field DF (C) filters. All three images were taken in sequence at the same temperature and correspond to the three techniques described in the experimental section 2.2.2.
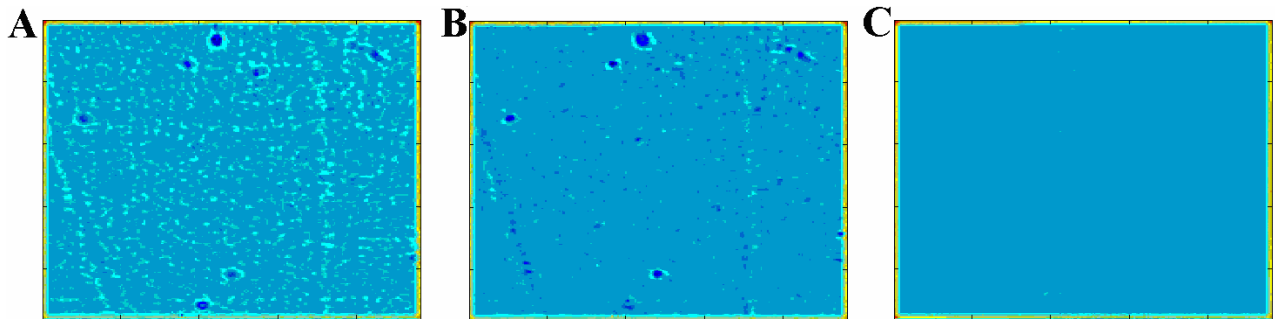
Figure 2.2.3.2.   Enhanced images using a moving average n-point smoothing filter with an optimal size of 9 pixels (same method as in section 2.1.2 BF (A), PC (B), and DF (C).
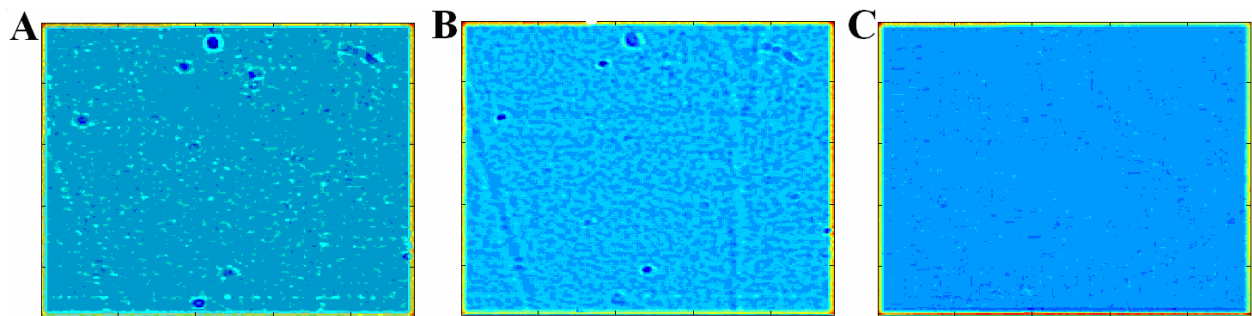
Figure 2.2.3.3.   Enhanced images with incident red light using a moving average filter. The optimal n-point smoothing filter of size 9 was used to filter the images for BF (A), PC (B), and DF (C).

109

Similar experiments were performed by inserting a red filter in the path of the incident light. The contrast of the BF and PC increased because of the red filter. Recorded images using the red filter placed in front of the incident light were also analyzed with the moving average filter. As a result of this new red filter, the incident light was attenuated and the contrast increased for the BF and PC images, as can be seen in Fig. 2.2.3.3.

A third set of experiments was performed by using a circular polarizer placed in front of the incident light instead of either "nothing" or a red filter.
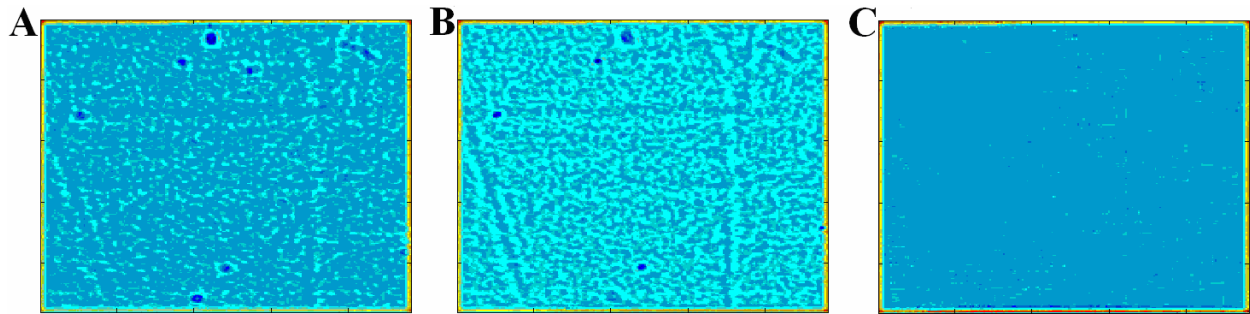
Figure 2.2.3.4.   Enhanced images in the case of incident light treated with a circular polarizer, after averaging with a moving average filter of size 9. BF (A), PC (B), and DF (C).

The images obtained in Fig. 2.2.3.4 show that the interfaces of the fluctuations are much darker as compared to the image background and, therefore, clearly visible. It can be observed in the DF images treated using the circular polarizer that the contrast for the fluctuations is clearly visible compared to nothing (Fig. 2.2.3.2) or red filter (Fig. 2.2.3.3).

2.2.3.2. The histogram method

Histograms of the images corresponding to the three different techniques (bright field –BF, phase contrast – PC, and dark field - DF) are plotted in Fig. 2.2.3.5 with no filter inserted. The horizontal axis represents the gray levels between 0 and 255 and the vertical axis represents the percentage of the total number of pixels in the images with a given gray level. The original image size was 240 x 240 pixels but because the moving average filter distorts the borders of the final image it was cropped again to eliminate the distortions so that the final size of the image was 222 x 222 pixels.

Figure 2.2.3.5. Histogram of gray level intensities without any filter for the incident light. Points are BF (filled square), PC (red circle), and DF (green triangles).The horizontal axis is the gray level with values between 0 and 255 and the vertical axis represents the percentage of the total number of pixels with a given gray level.
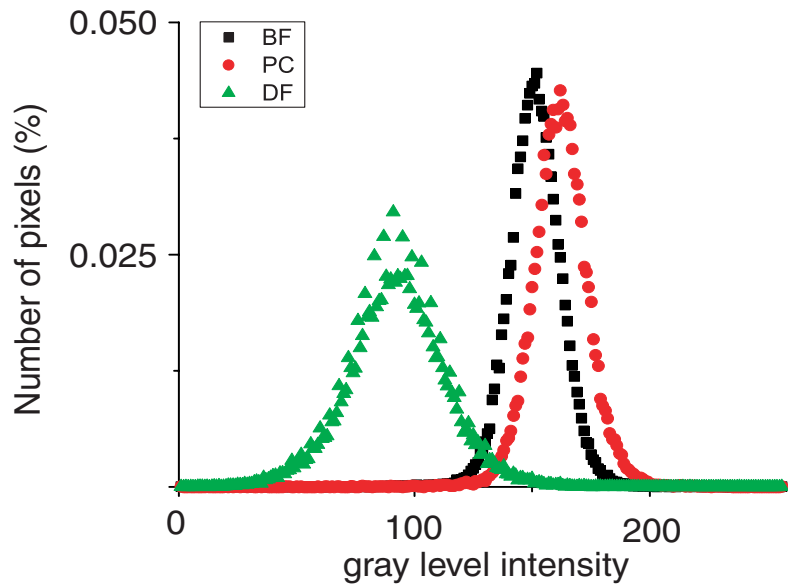
The widths of the distributions for the case of "nothing" (Fig. 2.2.3.5) were $\sigma_{i,BF} = 10.23 \pm 0.03$ (BF), $\sigma_{i,PC} = 10.57 \pm 0.04$ (PC), and $\sigma_{i,DF} = 18.3 \pm 0.2$ (DF) and the corresponding statistical tests for the Gaussian fit were:$\chi_{BF} = 1.35\ 10^{-7}$, $R_{BF}^2 = 0.998$; $\chi_{PC} = 2.23\ 10^{-7}$, $R_{PC}^2 = 0.998$, and $\chi_{DF} = 9.36\ 10^{-7}$, $R_{DF}^2 = 0.982$. According to the histograms in Fig. 2.2.3.5, there is a slight difference between the BF and PC, in the sense that the contrast increases in the latter. Both BF and PC histograms follow a Gaussian distribution, which is consistent with the interference mechanism for the formation of the fluctuating image. The small shift in intensity between BF and PC may be caused by absorption in the mica wave plate that is slightly opaque, the wave plate wedges and the mounting pieces for the wave-plate. Overall, there is a clear increase in the contrast of the PC image as can be seen in the Fig. 2.2.3.2. The DF histogram is shifted toward the lower gray levels and both the shape and the amplitude are quite different from the BF and PC

histograms. This difference lies in the fact that the transmitted light is blocked for the DF case. The direct visualization of the DF images suggests that an extinction process from scattering must contribute to the formation of the images in this case.

For the case of red filter treatment (Fig. 2.2.3.3), the shift between the two histograms corresponding to BF and PC in the original image Fig. 2.2.3.2 disappears and the two histograms overlap (Fig. 2.2.3.6). At the same time, the amplitude and the contrast of the DF histogram increases and approaches the BF and PC images contrast. The histograms corresponding to the BF and PC maintain the same Gaussian shape while the DF histogram has a shape closer to an exponential distribution.

Figure 2.2.3.6. Histograms corresponding to images recorded after the treatment of the incident light with a red filter. The BF and PC histogram have the same contrast and overlap (black squares and red circles), while the DF (green triangles) histogram has a different shape than in the normal incident light.
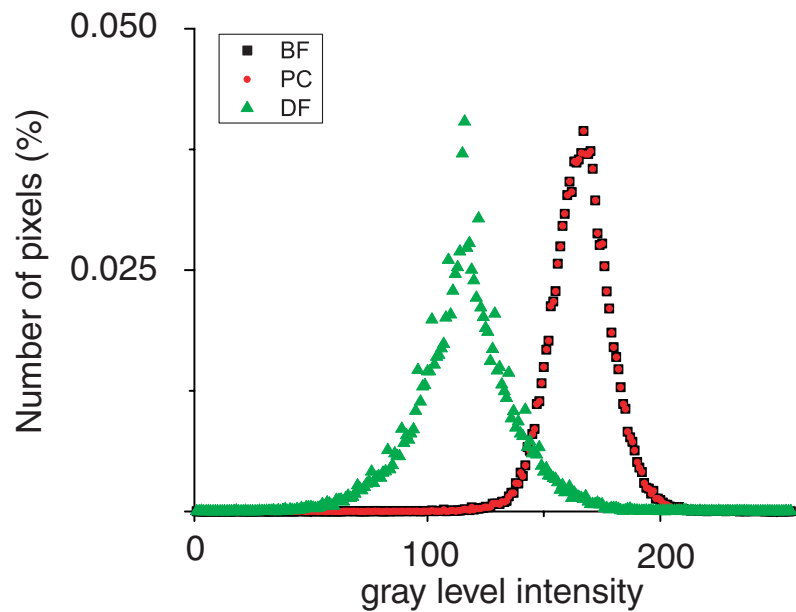
The widths of the distributions for the case of red filter (Fig. 2.2.3.6) were $\sigma_{i,BF} = 11.75 \pm 0.05$ (BF), $\sigma_{i,PC} = 11.75 \pm 0.05$ (PC), and $\sigma_{i,DF} = 15.9 \pm 0.3$ (DF) and the corresponding statistical tests for the Gaussian fit were: $\chi_{BF} = 1.98 \ 10^{-7}$, $R_{BF}^2 = 0.998$; $\chi_{PC} = 1.98 \ 10^{-7}$, $R_{PC}^2 = 0.998$, and $\chi_{DF} = 3.06 \ 10^{-6}$, $R_{DF}^2 = 0.947$. According to the histograms in Fig. 2.2.3.6, the widths of the distributions have a slight increase when the red filter is applied.

A third set of experiments was performed by using a circular polarizer placed in front of the incident light instead of either nothing (Fig. 2.2.3.2) or a red filter (Fig. 2.2.3.3). The widths of the distributions for the case of circular polarizer filter (Fig. 2.2.3.7) were $\sigma_{i,BF} = 10.88 \pm 0.04$ (BF), $\sigma_{i,PC} = 10.96 \pm 0.03$ (PC), and $\sigma_{i,DF} = 13.9 \pm 0.4$ (DF) and the corresponding statistical tests for the Gaussian fit were: $\chi_{BF} = 1.61 \ 10^{-7}$, $R_{BF}^2 = 0.998$; $\chi_{PC} = 9.70 \ 10^{-8}$, $R_{PC}^2 = 0.999$, and $\chi_{DF} =$

4.68 10^{-6}, R_{DF}^2 = 0.906. The fluctuation images obtained after using the moving average filter are shown in Fig. 2.2.3.4. The contrast in these images changed in comparison with the experiment with the red filter. The corresponding histograms for the circular polarized treatment of the incident light are shown in Fig. 2.2.3.7.

Figure 2.2.3.7. Histograms corresponding to images recorded after the treatment of the incident light with a circular polarizer. The histograms of images from Fig. 2.2.3.4 show a Gaussian distribution for BF (filled squares) and PC (red circles). The DF histogram (green triangles) has a slightly different distribution.
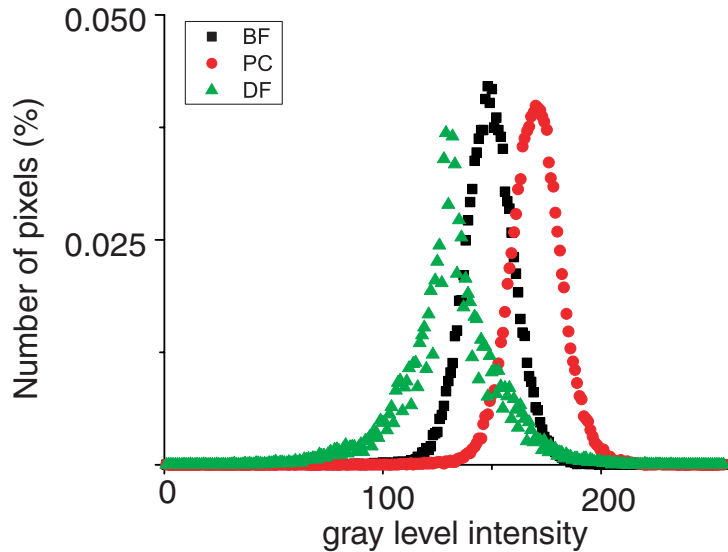
A side by side comparison between the widths of the Gaussian distribution using the three different methods for BF, PC and DF is presented in Fig. 2.2.3.8. These plots show the variance of the histograms (vertical axis) versus the corresponding image index (horizontal axis) for all images we analyzed. The widths were found by fitting the histograms of the images to Gaussians.
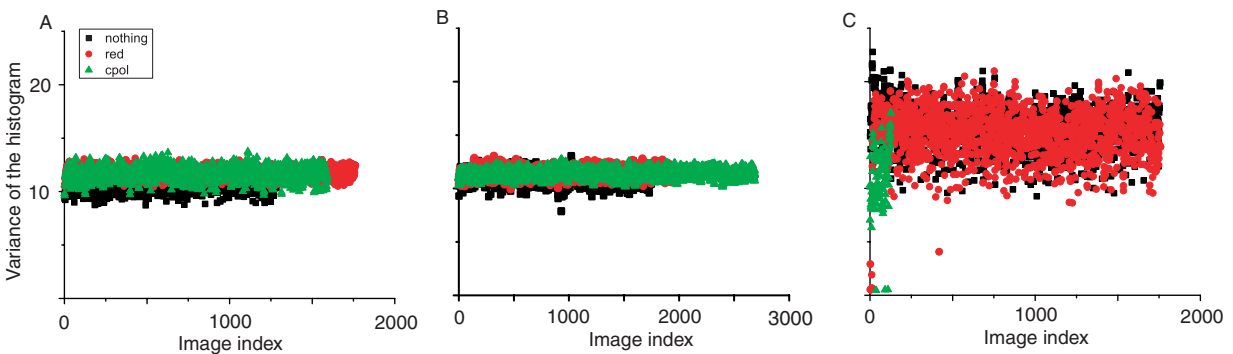
Figure 2.2.3.8. The variances of the histograms depend on the special filter used. For the BF (A), PC (B), and DF (C) using the three different methods to treat the incident light: "nothing"-black squares, the red filter-red circles and circular polarizer-green triangles. The variance of the histograms varies significantly.

113

For BF (Fig. 2.2.3.8.A) in the case of the red filter, the average width of the histograms over the total number of available images was $\sigma_{red} = 11.86 \pm 0.01$ gray levels, which is a bit larger but with a narrower range compared to the circular polarized case with $\sigma_{cpol} = 11.72 \pm 0.02$. The widths of the histograms for the BF without any filter are smaller, $\sigma_{nothing} = 10.71 \pm 0.01$ gray levels compared to BF with the red and circular polarizer filters. The widths of the histograms for the PC (Fig 2.2.3.8.B) circular polarized is narrower $\sigma_{cpol} = 11.476 \pm 0.007$ gray levels, compared to the PC with the red filter, $\sigma_{red} = = 11.63 \pm 0.01$ gray levels. The widths of the histograms have even smaller values for the PC with nothing, $\sigma_{nothing} = 11.19 \pm 0.001$ gray levels. The distinctive feature of the widths of the histograms for the DF is the large dispersion (Fig. 2.2.3.8.C). In the case of the DF circular polarized experiment, the widths have the smallest range $\sigma_{cpol} = 10.94 \pm 0.3$ gray levels, compared to the DF with nothing, $\sigma_{nothing} = 15.70 \pm 0.04$ gray levels, and DF with the red filter, $\sigma_{red} = 15.09 \pm 0.06$ gray levels.

2.2.3.3. Experimental renormalization of fluctuations

We considered sample images (BF-nothing, PC-nothing, and DF-nothing) of size 240 pixels by 240 pixels and studied the effect of different n-point smoothing filter size, such as A = 3, 5, 7, 9, 11, 13, 17, 19, 27, 29, 35, and 39 on the histograms. This corresponds to coarse graining the fluctuations on large blocks of pixels of size $L = A*b$ where b is the resolution associated with one pixel (in this experiment 1 pixel = 2.2µm). The plot of the half-width of the histogram (σ) versus the filter size (L) shows two different regions of qualitatively different behavior of the resultant histogram with respect to the size of the filter.
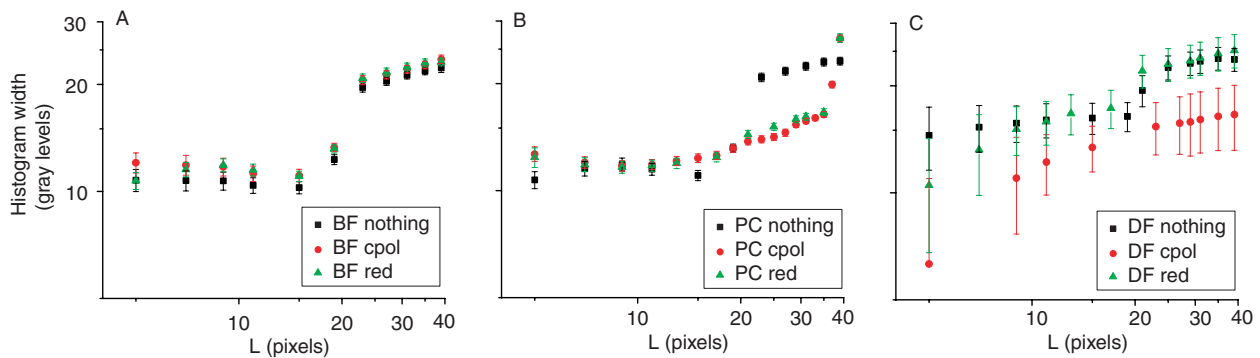
Figure 2.2.3.9. **Experimental renormalization of the enhanced images.** Plot of the width σ of the histograms versus the size of the averaging filter L for the BF (A), PC (B), and DF (C) on a log-log scale. Two qualitatively different regions can be observed for L ≤ 16 pixels and L > 20 pixels.

The fluctuations are averaged over blocks of size $L \times L$. In the case of the bright field (BF), two different regions can be distinguished on the plot in Fig. 2.2.3.9A: for the filter size L ≤ 16pixels, the variance, σ, of the histograms saturates because of the correlation between fluctuation while for a filter L > 20 pixels, the variance, σ varies as $1/L^x$ regardless of the treatment of the incident light by a red filter or a circular polarizer. The exponent x was 0.24 ± 0.01 and the linear regression coefficient was R = 0.997. The phase contrast (PC) histograms with no light treatment show a significant jump around L = 16 pixels (Fig. 2.2.3.9.B) similar to the case of the bright field. However, both red filter and circular polarizer treatment of the incident light smoothes the transition diagram in Fig. 2.2.3.9B, although the two regions are still clearly separated: for low filter size L ≤16 pixels there is an almost no dependence of the histogram width on the averaging filter size, while for large filter size, L > 20, the histogram width is still proportional to 1/L. For

the dark field technique, the histograms for both the case of no filter and the red filter the two regions in the transition diagram are clearly separated and resemble the general structure shown in Fig. 2.2.3.9.A. In the case of the circular polarization treatment for the incident light (Fig. 2.2.3.9.C – red circles), the log-log plot clearly separates into two regions around the transition size of L =16 pixels. On both sides of the bifurcation point the histograms width is proportional to $1/L^x$ with different positive exponents: for low values of the averaging filter $x = 0.7 \pm 0.1$ with a linear regression coefficient of $R = 0.973$, and for high values of L the exponent is $x = 0.154 \pm 0.007$ with a linear regression coefficient of $R = 0.996$.

2.2.3.4. Power spectrum method

Since the optical system is affected by noise, in order to find the fluctuation image, the moving average filter (a low pass filter) was applied to the original image and then that image was subtracted from the original image (Fig. 2.2.3.2). The power spectrums of the original images in Fig. 2.2.3.1 have significant contribution in the high frequencies indicated by the strong vertical band corresponding to noise.
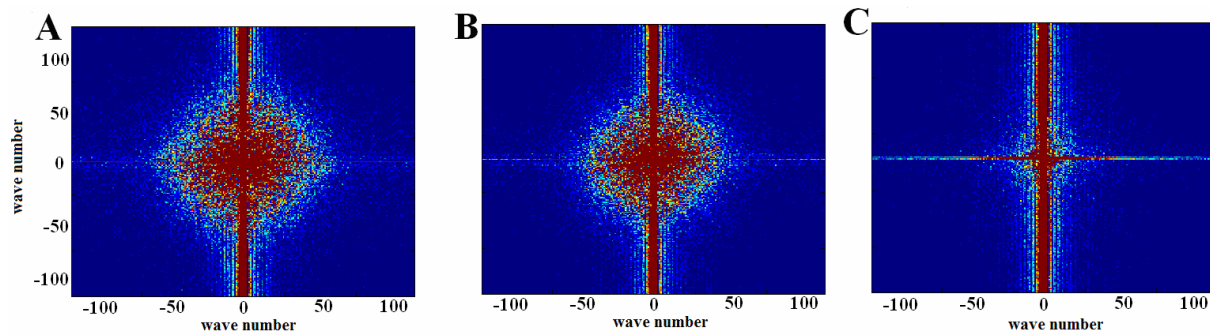
Figure 2.2.3.10. Power spectra and the light treatment in optical microscopy. In the power spectra plots of the original images (Fig. 2.2.3.1) for the BF (A), PC (B), and DF (C) techniques, strong DC components along the y axis and a smaller DC component along the x axis indicate significant optical noise.
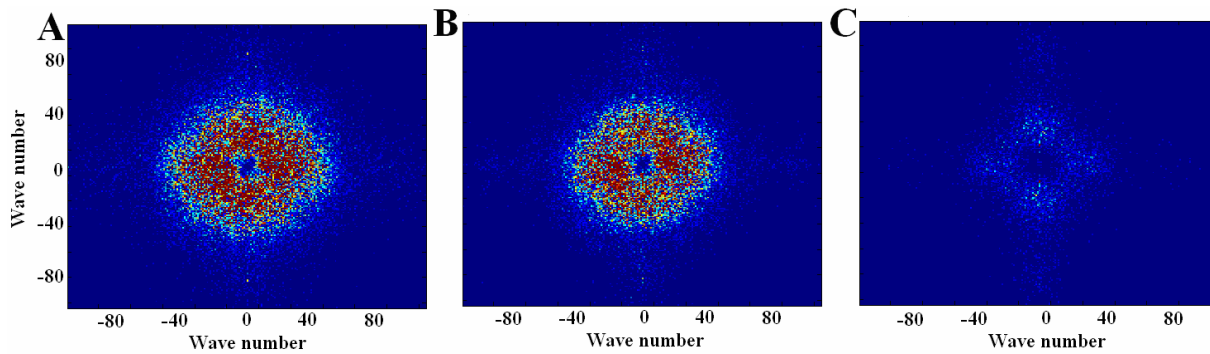
Figure 2.2.3.11.   Power spectra in optical microscopy enhanced by averaging filter. The filtered images corresponding to the filtered images shown in Fig. 2.2.3.2. Both the BF (A) and PC (B) power spectra illustrate the presence of the fluctuation in the image by a distinct bright ring in wave numbers space. In contrast, the power spectrum for the DF (C) shows a much weaker ring as a result of small scale fluctuations.

On the other hand, the average filter can still preserve the fluctuations in the original images (Fig. 2.2.3.1) and, at the same time, reduce the optical noise, as shown by the FFT of the filtered images in Fig. 2.2.3.11.

We use the same method as discussed in section 2.1 to find the characteristic length of the fluctuations. First, we determine the maximum value of the wave number corresponding to the maximum of the radial power spectrum (k_m). In the following, we refer only to the BF, PC, and DF techiques with no filter (nothing), as opposed to the experiments performed with a red filter or a circular polarizer. The relationship between the spatial and frequency domain is [Gonzales, 2002]

$$k = k_m /(N \, \Delta x), \quad\quad\quad (2.2.3.1)$$

where N is the total number of pixels in the image along one direction, Δx represents the image resolution in the spatial domain, and k_m represents the dimensionless value of the maximum of the broad peak in the power spectrum shown in Fig. 2.2.3.12. The spatial resolution in this experiment was $\Delta x = 2.2$ µm/pixel and the original image contained 240 x 240 pixels. By using an optimal n-point smoothing filter of dimension A = 9 pixels, a border region of A pixels was removed all around the initial image. Therefore, the power spectrum was computed for the resultant image of only 222 x 222 pixels (N = 222). The value for the wave vector is related to the characteristic length of the fluctuations (λ) as follows

$$k = 1/\lambda. \quad\quad\quad (2.2.3.2)$$
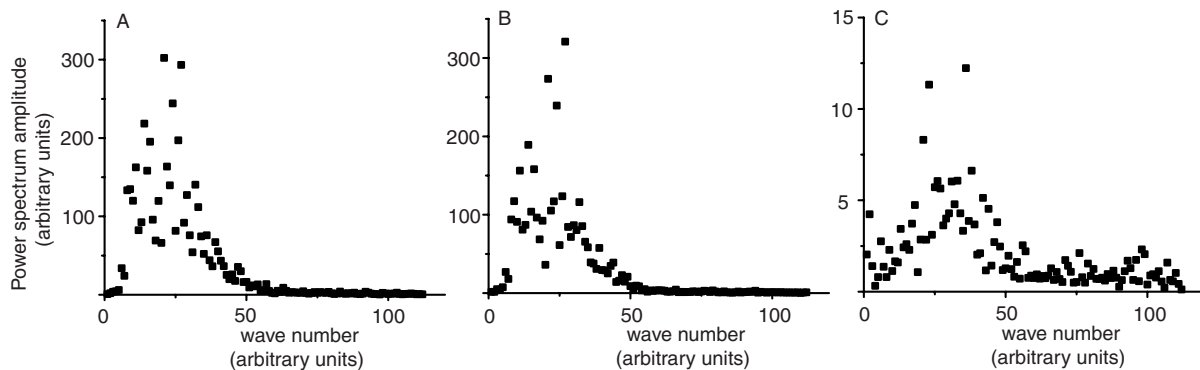
Figure 2.2.3.12. **Power spectra of fluctuating images in optical microscopy.** The radial power spectra show a peak corresponding to the ring in the Fig. 2.2.3.11.The radial averages of the power spectra for BF (A) and PC (B) are very similar whereas for DF (C) the amplitude of the power spectrum is much smaller.

For example, for a value of $k_m = 23$ arbitrary units for the BF images and an image size of $N = 222$ pixels with a resolution of 2.2 µm/pixel, the corresponding characteristic length (λ) is 21.23 µm.

The amplitude of the power spectra and the peak value of the wave number k_m for BF is $k_m = 23$ and for PC is $k_m = 22$. In contrast, the DF has not only a smaller amplitude of the power spectra but also a greater value for the wave number corresponding to the maximum of the power spectra, $k_m = 28$. A statistical analysis of the distribution of the wave numbers k_m for all available images showed that the wave vector values are close to each other for the BF and PC images while for the DF technique the wave numbers are spread over a broader range. The DF technique eliminates the low values of the wave numbers in the power spectra.
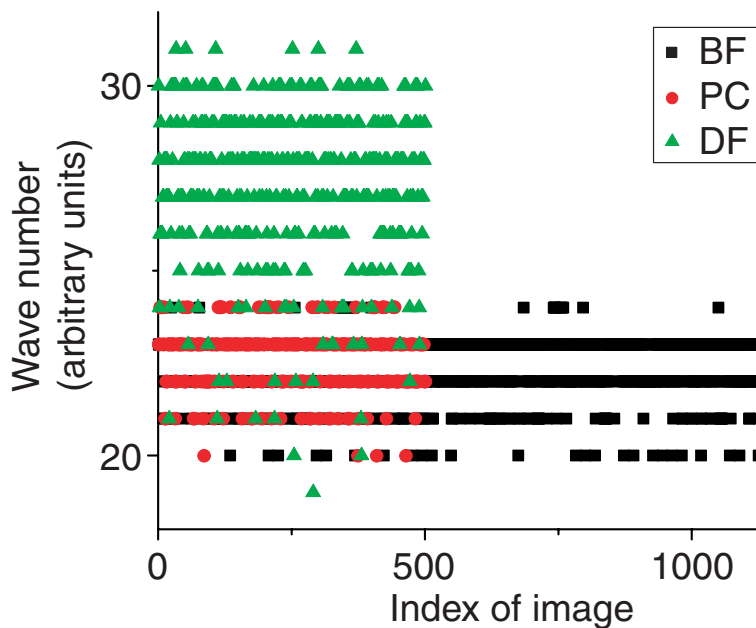
Figure 2.2.3.13.   Wave numbers filtered by different light treatments. The wave numbers corresponding to the maximum of the radial power spectra versus the image index show similar values for BF (black squares) and PC (red circles). The wave vector for the DF extends to a much higher values for the wave numbers with a larger dispersion (green triangles).

The average wave number corresponding to the maximum of the radial averaged power spectrum for the 1200 BF images is $k_{BF} = 22.5 \pm 0.8$, which is close to the average value for 500 PC images $k_{PC} = 22.7 \pm 0.8$. The average wave number for 500 images obtained using the DF technique is $k_{DF} = 27 \pm 2$ (Fig. 2.2.3.13).

119

Additional information can be extracted from the average radial power spectra by plotting Fig. 2.2.3.12 in log-log coordinates and retaining only high wave numbers (small characteristic length). The log-log plot (Fig. 2.2.3.14) shows that both BF and PC have an almost linear dependence on log k with almost identical slopes, while the power spectrum for the DF images presents a significantly smaller slope for the linear fit.
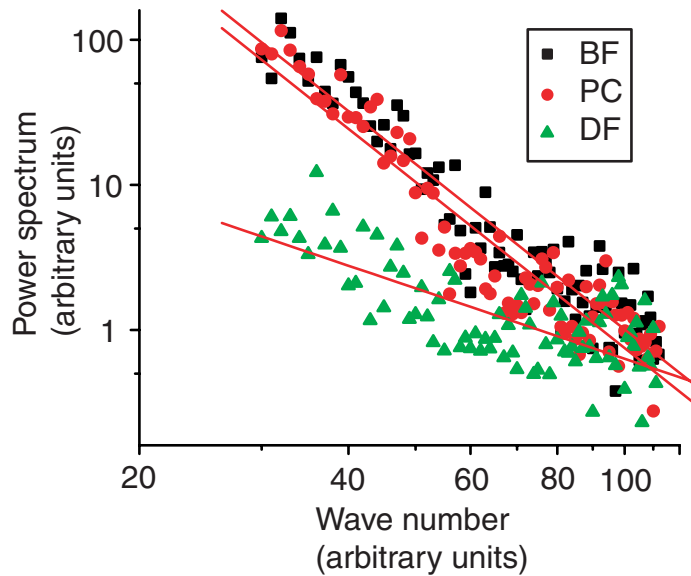
Figure 2.2.3.14.   Log-log plot of the radial average of the power spectrum versus the wave number. The linear relationship for high values of the wave numbers suggests that the fluctuations are self similar on multiple spatial scales.

The power law fit in Fig. 2.2.3.14 gives the exponent for the BF technique to be $m = -3.8 \pm 0.1$ with a linear regression coefficient of $R = -0.945$. For the PC technique the exponent is $m = -3.8 \pm 0.2$ with a linear regression coefficient of $R = -0.939$. In contrast, the DF images have a lower exponent of $m = -1.6 \pm 0.2$ with a linear regression coefficient of $R = -0.730$ because this technique suppresses the lower wave numbers.

We also found that the averaging filter alters the histograms of the original images (Fig. 2.2.3.15). The histograms corresponding to the original images (black squares in Fig. 2.2.3.15) are bimodal, whereas the filtered histograms are always Gaussian (red circles).

The DF image has a different distribution of gray levels because the opaque object blocks the transmitted light and low wave numbers are suppressed. For the DF case, only the scattered

light is recorded by the CCD. In the DF images, the large slow fluctuations are absent and only small fluctuations lasting 1-2 seconds are visible.
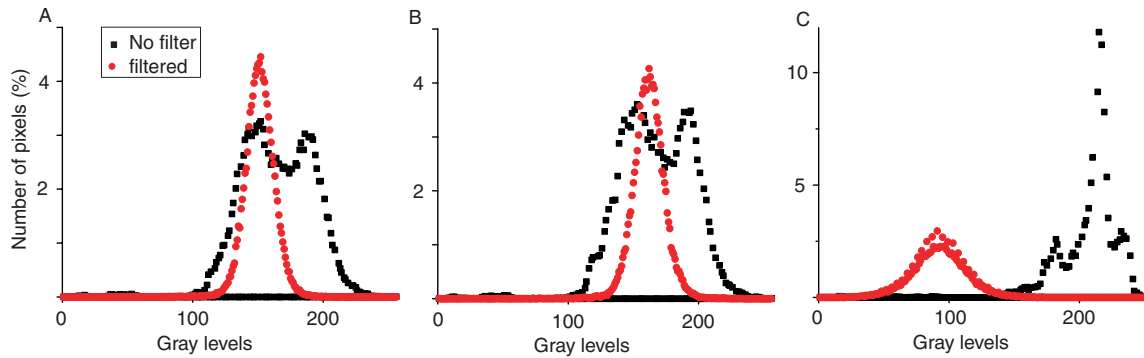
Figure 2.2.3.15. Bimodal distribution for fluctuations. The moving average filter eliminates the bimodal character of the original histograms (black squares) and transforms them into a Gaussian shape (red circles). These histograms correspond to BF(A), PC(B) and DF(C).

2.2.4. Conclusions

The observation and analysis of fluctuations near the critical point in real time and space is an important issue in the critical point phenomena. This important aspect is related to statistical physics and to microscopic image formation. Image formation is due to the interference between the transmitted light and the scattered light by the refractive index fluctuation. Using three different techniques, bright field, phase contrast, and dark field, we investigated a liquid mixture system (mixture of methanol and partially deuterated cylcohexane(CC^{*}-Me)). Three different recordings were made for each of the described techniques (BF, PC, and DF) using different light filters termed: "nothing," red filter, and circular polarizer.

The recorded images (original) and the filtered images corresponding to BF, PC, and DF exhibit intensity variation in the spatial domain. Image analysis finds similarities in the image formation for BF and PC, but differences for DF. A contrast increase in the BF, PC, and DF was observed for recorded images using the red filter and the circular polarizer when the noise was reduced with a moving average filter.

After noise reduction was applied to all images (BF, PC, and DF), we found that the probability distribution functions are Gaussian for the BF and PC and that the distribution is different for DF not only in amplitude but also in the tail of the distribution for the red filter, "nothing", and the circular polarizer. The widths for the probability distributions were recorded (BF, PC and DF) for a series of images using three different cases for the incident light (red filter, "nothing," and circular polarizer). The DF width distribution shows a distinctive feature in magnitude for all the aforementioned filters as compared to the BF and PC. The discussion of image formation exceeds the purpose of this research. However, the fluctuations in these images can be explained using percolation theory [Stauffer, 1997], and this approach will be the topic of another study. The power spectra corresponding to images recorded with these techniques show the existence of large fluctuations in these images and their connection to generalized nucleation. Fluctuations recorded in these images are evidence of self-similarity in real space.

3. Wetting films in pure fluids near boiling point

If a pure fluid with coexisting gas and liquid phases is heated past its boiling point, then a complex process of fluid dynamics, interfacial phenomena, and heat transfer takes place [Tong, 1997]. This process is greatly complicated by thermal convection and buoyancy due to gravity. If the gas bubble grows sufficiently, then the buoyancy overcomes the surface tension and the bubble moves upward. In weightlessness, the buoyancy force is eliminated.

Close to the critical point, many thermodynamic properties, including the surface tension, vary according to the well-known universal power law [Green, 1971; Moldover *et al*., 1979] and the fluids exhibit perfect wetting of almost any solid. In a boiling process involving heat transfer to a two-phase fluid, sandwiched between two sapphire windows a perfectly wetted wall dries from evaporation resulting in liquid-gas-solid triple contact lines.

3.1. Experimental setup and measurements

The experiments were conducted with a pure fluid whose initial temperature was slightly below the critical temperature and whose density was nearly critical, so that the gas and liquid phases coexisted. The experiments were performed in weightlessness on the MIR space station on the French/American GMSF mission using the ALICE-II instruments [Garrabos *et al.*, 2000]. These instruments were specially designed to obtain high precision temperature control with a stability of ≈15 µK over 50 hours and repeatability of ≈40 µK over 7 days. The ALICE-II instruments suppress buoyancy driven flows and gravitational constraints on the liquid gas interface. A thin constant volume cell, filled with sulfur hexafluoride (SF_6), produces a considerable constraint on the bubble and allows the entire bubble to be observed as heat is applied [Hegseth *et al.*, 2002] (Figure 3.1.1).
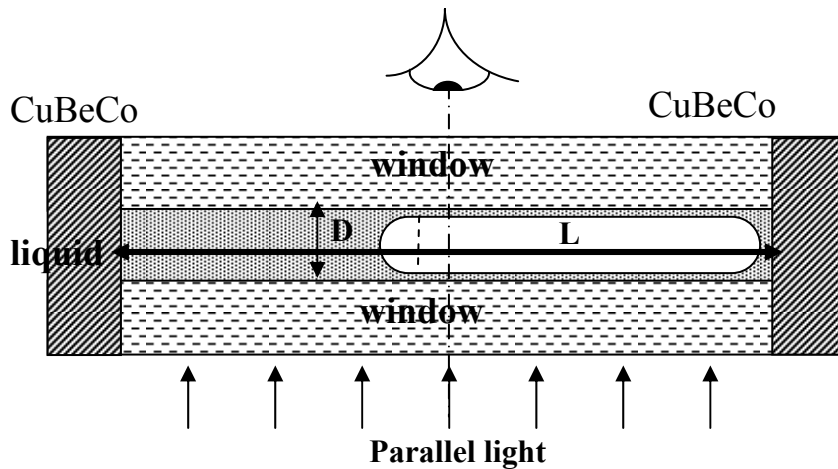
Figure 3.1.1.   A cross-section of the cylindrical sample cell. The fluid volume is contained between two sapphire windows and a CuBeCo alloy ring. A semi-circular liquid-gas meniscus between the two parallel windows appears dark in the images because the liquid-gas meniscus refracts the normally incident parallel light away from the cell axis.

To place the samples near the critical point, constant mass cells are prepared with a high precision density, to 0.02%, by observing the volume fraction change of the cells as a function of temperature on the ground [Green, 1971]. Similar ground based experiments were done before these experiments, yielding completely different results [Gurfein *et al.*, 1991] in the presence of gravity. The cylindrical cell shown in Figure 3.1.1 is 12 mm in diameter and 1.664 mm thick

while each sapphire window is 9 mm thick. A 10 mm diameter ring was engraved on one of the sapphire windows of each cell in order to calibrate the size of the visible area of the cell image. The sample cell was placed inside a copper housing, which in turn, was placed inside a thermostat. These cells were heated linearly in time while the liquid-gas interface was visualized through light transmission normal to the windows. The temperature profile consisted of two ramps with a constant temperature plateau between them, as shown in Figure 3.3.1.A. An initial temperature ramp at a rate of 8.7 mK/s is followed by approximately 40 minutes of constant temperature. Another ramp of 7.4 mK/second is then imposed and the critical point is crossed.

Heat was pumped into and out of the sample cell unit using six Peltier elements. The temperature was sampled every second with a resolution of 1 μK [Garrabos *et al.*, 2001]. Although the cell was manufactured with high precision, the cell's windows could not be placed exactly parallel because the windows are pressed and glued in the copper housing leaving a glue layer. As a result, the gas bubble takes an off-center position (Figures 3.1.1 and 3.1.2) as discussed in [Garrabos *et al.*, 2001].

Figure 3.1.2. Full view of cell. The fluid (sulfur hexafluoride) volume is contained between two sapphire windows and a CuBeCo alloy housing.
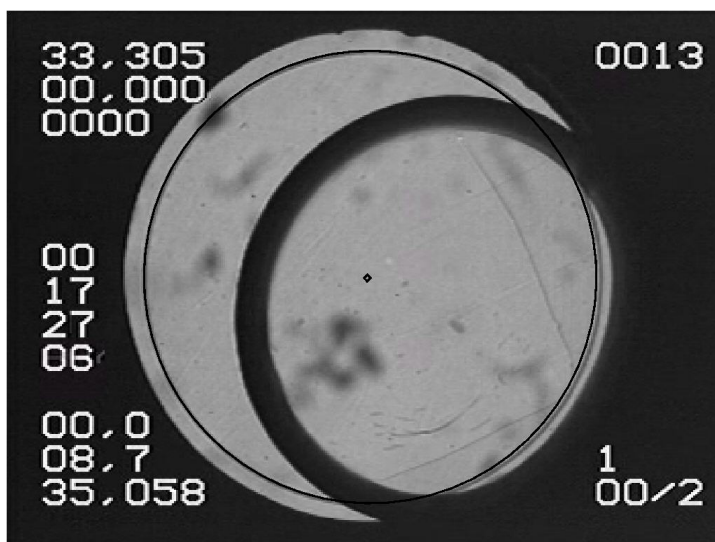
Because the contact angle is zero near the critical point the liquid-gas meniscus between the two parallel windows forms an interface with a semicircular cross section between the windows as shown in Figure 3.1.2. We have verified by ray tracing that all of normally incident light on the meniscus is refracted out the field of view. We also note that some of the fluid volume near each cell's edge is blocked by glue that was used in manufacturing cells. Nevertheless, we can find

each cell's center and each cell's edge because there is a 10mm diameter reference etching on the sapphire windows that is concentric with the cell (see figure 3.1.2 and figure 3.1.3.B).
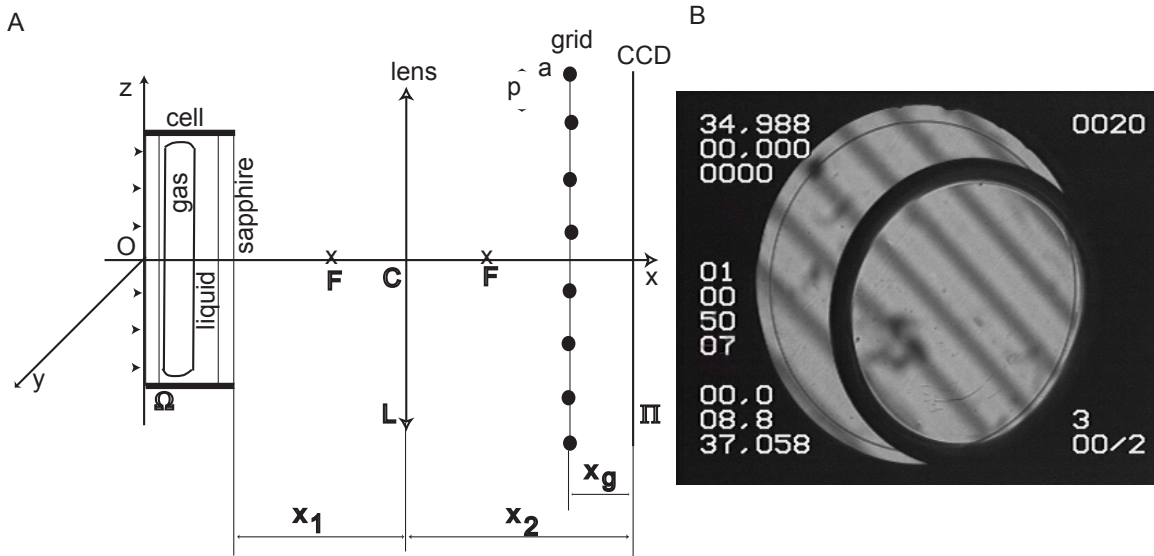
Figure 3.1.3. A) A schematic representation of the optical system and the cell. B) A reference image recorded by the CCD camera corresponding to a flat gas-liquid interface. The cell consists of a 12 mm diameter cylinder made of CuBeCo containing a 1.664 mm thin layer of SF_6 sandwiched between two sapphire windows (9 mm thick). The convergent lens, L, that has a focal point F and a center C, projects the out-of-focus grid image on the CCD plane Π.

The explanation for the recorded image on the CCD plane Π is as follows [Gurfein, 1991]. A plane wave propagating in the x-direction illuminates a phase object (Ω) that is a single bubble in a thin constant mass cell filled with fluid near its critical density (Figure 3.1.3A). An image of Ω is projected onto a plane Π by a lens L. A grid made up of equally spaced straight wires with periodicity p and thickness a is placed perpendicular to the optical axis x, and parallel to the y-axis, between the lens L and CCD camera Π [Gurfein, 1991]. The origin of the x-axis is taken as the entry-side of the cell Ω (point O). The distance between Ω and the lens L is x_1 and the distance from L to Π is x_2. Therefore, the magnification of the optical system is given by $\gamma = x_2/x_1$. The distance from the grid to the plane Π is x_g. If the gas-liquid interface is flat (see Figure 3.1.3A), then the incident rays parallel to the optical axis Ox would remain parallel to the optical axis after they cross the cell. The resultant image of the grid shadow is not distorted (Figure 3.1.3B). The only indication of the cell presence is the dark gas-liquid interface because the

meniscus refracts the normally incident light away from the cell's axis and out of the optical system

During the heating process, two phenomena take place inside the cell. First, a triple contact line between sapphire, gas, and liquid (Figure 3.1.4A) occurs. Because the copper conducts heat faster than sapphire the evaporation is stronger at the part of the interface closer to the copper heating wall. As explained by Hegseth [Hegseth *et al.*, 2002], the tilted sapphire window pushes the bubble to the side-wall leading to a contact between the bubble and the copper wall, *i.e.*, there is a thin liquid layer between the gas bubble and the copper side-wall. Second, during the temperature increase toward the critical temperature, T_c, liquid evaporation leads to the gas bubble spreading phenomenon with a contact angle shown of about 120° (Figure 3.1.4B).
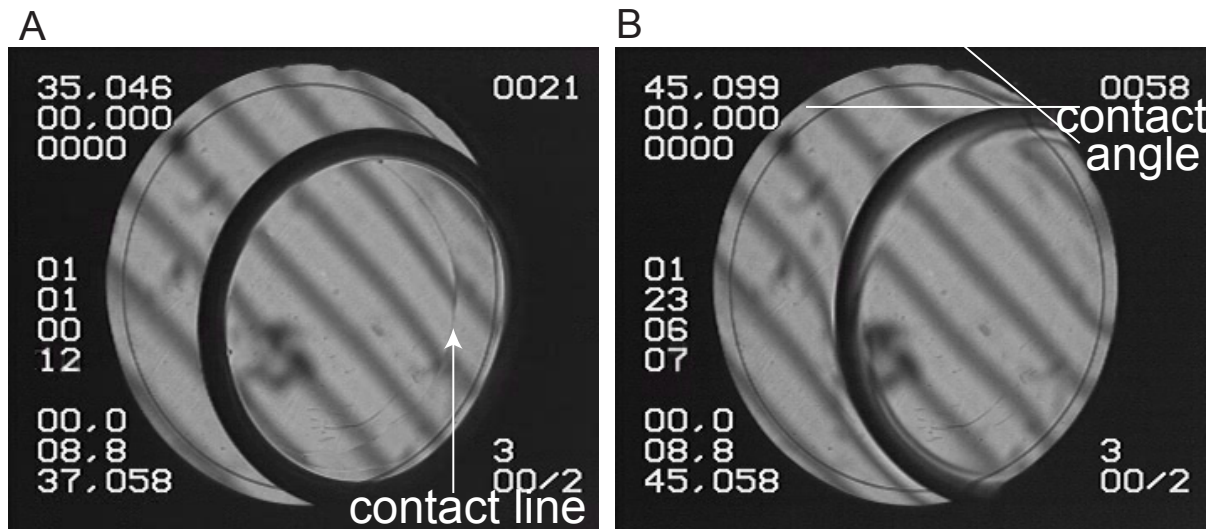
Figure 3.1.4.   Triple contact line formation. (A) The evaporation of the liquid film between the sapphire window(s) and the gas bubble leads to a triple contact line close to the critical temperature T_c. (B) The heat transfer through the copper cell wall leads to a rapid evaporation of the thin liquid film and a rapids change in the contact angle.

The analysis of the gas-liquid interface demonstrates the existence of the differential recoil vapor force [Palmer, 1976]. Besides the spreading that takes place at the copper wall, there is a similar process of liquid evaporation at the two sapphire windows. The evaporation of the thin fluid film between the sapphire windows and the gas bubble leads to the triple contact line (Figure 3.1.4A). Although the two processes are similar the major difference consists in a much

higher heat transfer through the copper wall than through the sapphire window. As a result, the speed of contact line motion is smaller than the rate of change of the contact angle.

3.2. Methods

The principle of the measurement is as follows. In the presence of any liquid-gas interface along the z-axis in the phase object (cell) Ω, the incident rays are deflected from their original direction. The deformation of the wave front causes a displacement or a distortion of the shadow of the grid on plane Π. The wetting condition of the interface at the wall requires a concave curvature near the wall while the flat interface away from the contact line requires convex curvature. We assume that between these edges of the contact line a linear approximation of the shape is a reasonable simplification that allows the estimation of the film thickness. Using this wedge model, the shadow displacement depends on the angle of the interface, as shown qualitatively in Figure 3.2.1. If the gas bubble interface is flat ($\alpha = 0$), then the incident ray I_0, which is parallel to the optical axes, remains parallel to the optical axis after it crosses the cell and reaches the convergent system L at I_1'. This ray is further refracted and hits the CCD plane at I_1". The ray tracing program we wrote uses a large number N (10^3 - 10^6) of equally spaced incident rays and computes for each incident ray the position of the point of incidence on the CCD plane. If the refracted ray passed between the grid lines, then the incidence point on the CCD plane is marked "white", meaning that the corresponding pixel is turned white. If it happened that the refracted ray hit a grid line its intersection with the CCD plane is marked "black", meaning that the corresponding pixel is turned black. This way we get the out-of-focus image of the grid by ray tracing (Figure 3.1.3B). If the gas-liquid interface is tilted ($\alpha \neq 0$), then the incident light suffers successive refractions at the gas-liquid interface (Figure 3.2.1, point I_1), liquid-sapphire interface (Figure 3.2.1, point I_2), and, sapphire-air interface (Figure 3.2.1, point I_3). As a result, the emergent ray leaves the cell at the height z_3 with an angle r_3. Assuming that the refraction angle r_3 is small, the convergent system would finally form the image on the CCD plane at I_6. We use the same ray tracing algorithm to find the new out-of focus grid shadow. In the example shown in Figure 3.2.1, if the gas-liquid interface is flat then the initial ray I_0 hits a line of the grid at I_5 and determines a shadow point ("black" pixel) at I_6.
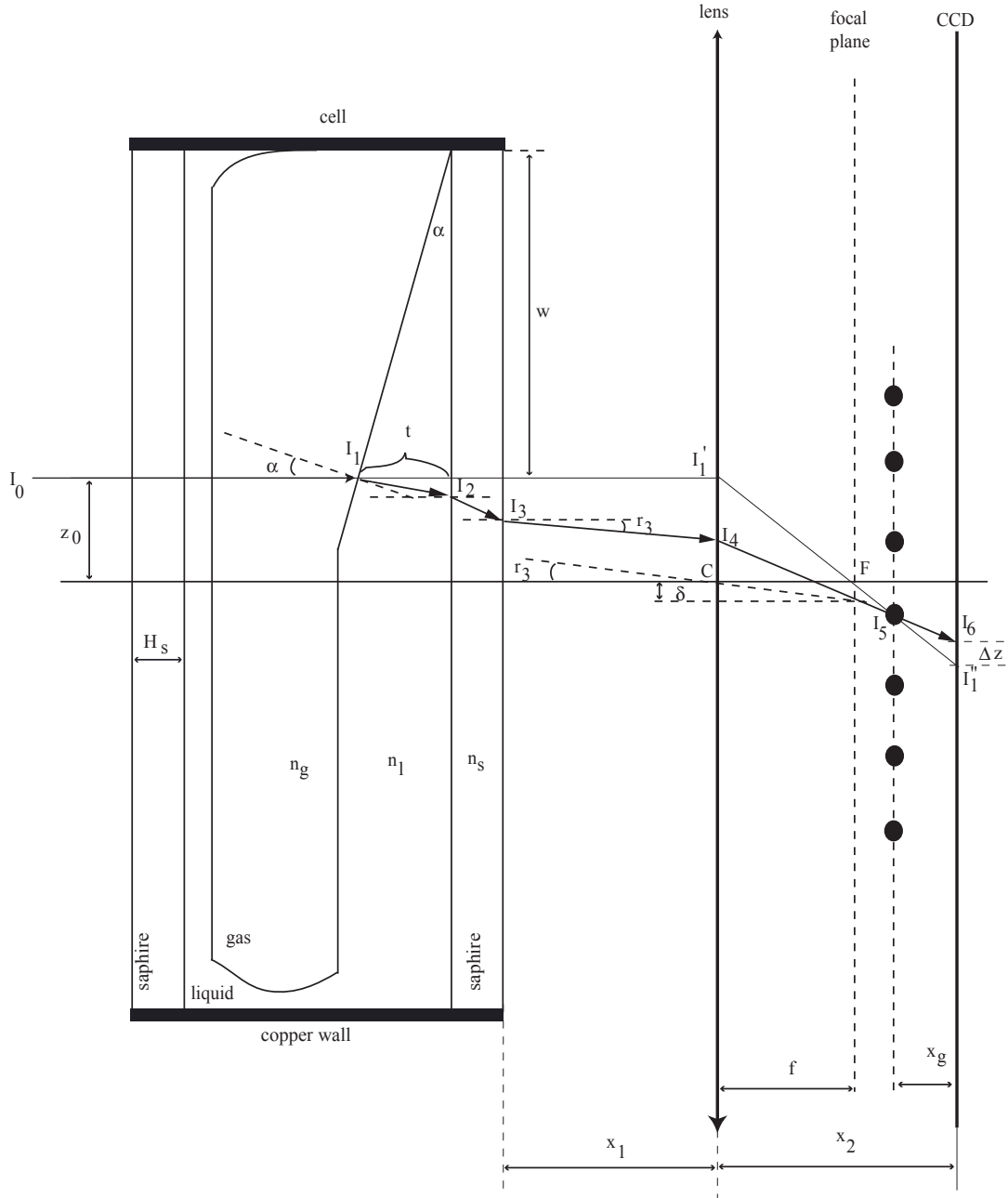
Figure 3.2.1. Ray tracing through the cell and optical system. The tilt angle of the gas-liquid interface is exaggerated for illustration purposes. An incident ray I_0, passing at distance z_0 from the optical axes, would remain parallel to the optical axes if the interface is not tilted with respect to the sapphire windows, and hit the lens plane at I_1'. The ray is further refracted through the focus F and reaches the CCD at I_1''. If the tilt angle α of the gas-liquid interface is non-zero, then the ray starting at I_0 would hit the CCD plane at I_6, following successive refractions. The distortion of the shadow depends on the tilt angle α of the interface and its thickness, t. We computed the film thickness by measuring the displacement of a grid line (Δz) and the width (δ) of the triple contact line.

130

In the presence of a tilted gas-liquid interface, the same incident ray I_0 would pass through the same point I_5 in the grid plane, and hit the CCD at I_6. The displacement of the grid shadow $(I_1''I_6)$ depends on both the tilt angle (α) and the thickness of the gas-liquid interface (t). Since we always observed only single contact line motions, we assumed that only one gas-liquid interface is tilted (Figure 3.2.1), and the tilt angle is α. Let z_0 be the height of an incident ray parallel to the optical axes. At point I_1 Snell's law gives

$$n_g \sin \alpha = n_l \sin r_1, \tag{3.2.1}$$

where n_g is the refraction index of the gas phase, n_l is the refractive index of the liquid and r_1 is the refraction angle at I_1. At the point I_2, applying Snell's law we get

$$n_l \sin (\alpha - r_1) = n_s \sin r_2, \tag{3.2.2}$$

where n_s is the index of refraction of sapphire and r_2 is the refraction angle at I_2. The height of the next incidence point (I_2) is

$$z_2 = z_0 - t\ Tan(\alpha - r_1). \tag{3.2.3}$$

Finally, there is refraction inside the cell

$$n_s \sin r_2 = n_{air} \sin r_3, \tag{3.2.4}$$

where r_3 is the angle of the emergent ray and whose distance from the optical axes is

$$z_3 = z_2 - H_s\ Tan\ r_2 = z_0 - t\ Tan(\alpha - r_1) - H_s\ Tan\ r_2, \tag{3.2.5}$$

where H_s is the thickness of the sapphire window. The emergent ray from the cell hits the convergent lens at z_4, given by

$$z_4 = z_3 - x_1\ Tan\ r_3 = z_0 - t\ Tan(\alpha - r_1) - H_s\ Tan\ r_2 - x_1\ Tan\ r_3, \tag{3.2.6}$$

Using congruent triangles we get the height of the point in the CCD plane where the refracted ray $I_4 I_5$ hits the plane (point I_6)

$$\frac{z_6 - \delta}{z_4 + \delta} = \frac{x_2 - f}{f} \Rightarrow z_6 = \delta + (z_4 + \delta)\frac{x_2 - f}{f}, \tag{3.2.7}$$

where $\delta = f\ Tan\ r_3$ is the height of the crossing point between the refracted ray $I_4 I_5$ and the focal plane. Based on (3.2.6) and (3.2.7) we get the displaced height of the grid shadow at

$$z_6 = (z_0 - t\ Tan(\alpha - r_1) - H_s\ Tan\ r_2 - x_1\ Tan\ r_3 + f\ Tan\ r_3\ )\ \gamma + f\ Tan\ r_3, \tag{3.2.8}$$

where $\gamma = x_2/x_1$ is the magnification of the convergent system L. Based on (3.2.7), the height of the crossing point between the unperturbed ray and the CCD plane will be

$$z_6{}^0 = z_0\ \gamma. \tag{3.2.9}$$

Combining the above relationships, we get the displacement of the grid shadow due to a tilted gas-liquid interface

$$\Delta z_6(t, \alpha) = - (t\ Tan(\alpha - r_1) + H_s\ Tan\ r_2)\ \gamma. \qquad (3.2.10)$$

The displacement Δz of the grid shadow depends on both the tilt angle α and the thickness of the film. From the experimental data such as those shown in Figure 3.2.2 we measured:

1. the displacement ($\Delta z_6(t, \alpha)$) of a fractured grid line shadow

2. the width (δ) of the triple contact line in the image plane. The width (w) of the tilted region can be obtained by using the magnification formula $w = \delta/\gamma$, where γ is the optical system magnification.
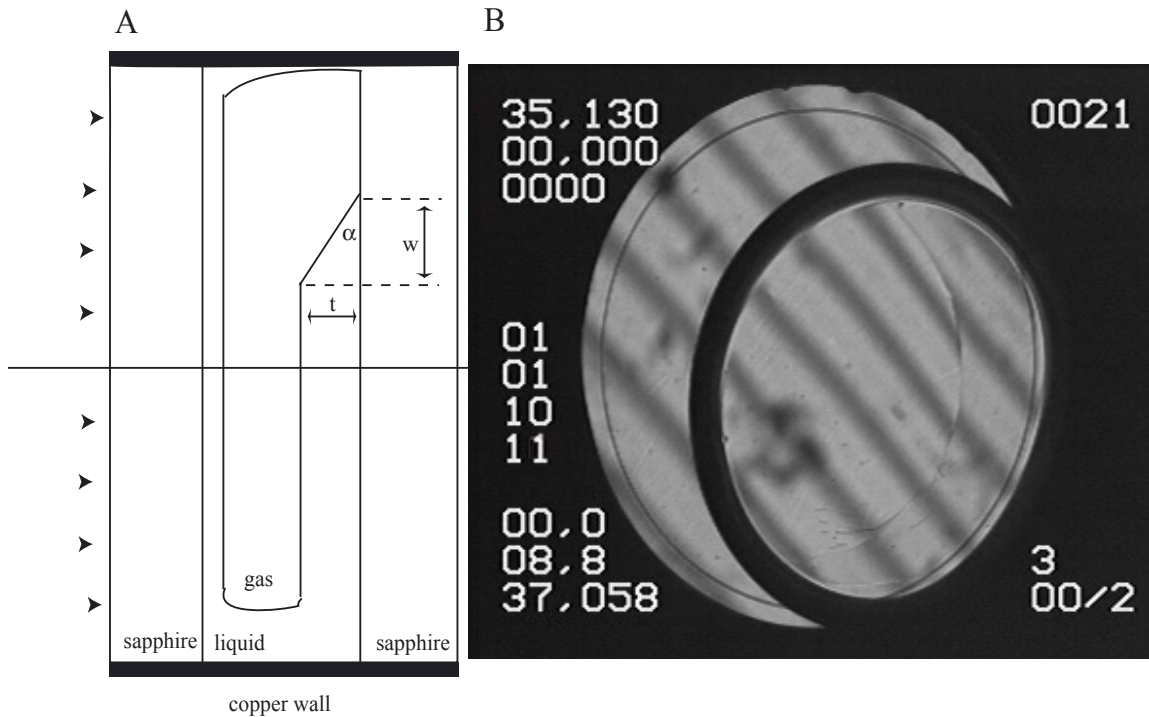
Figure 3.2.2.   The tilted gas-liquid interface due to liquid evaporation leads to a triple contact line for gas-liquid–sapphire (panel A). The tilt angle induces a significant displacement of the grid shadow (panel B). The shadow displacement is proportional to the tilt angle (α) and the thickness (t) of the film.

On the other hand, from Figure 3.2.2 the width of the triple contact line is

$$t = w\ Tan\ \alpha. \qquad (3.2.11)$$

Using the relationship (3.2.11) we eliminate the tilt angle from (3.2.10) and numerically solve the equation for the film thickness (t). The tilted gas-liquid interface and its effect are shown in Figure 3.2.2.

Each captured image has a black reference line drawn parallel to the reference shadows of the grid as shown in Figure 3.2.3. We used two different software products to double-check our results. We used an in-house designed program written in LabVIEW to determine the intensity profile along a particular contour drawn inside the image.
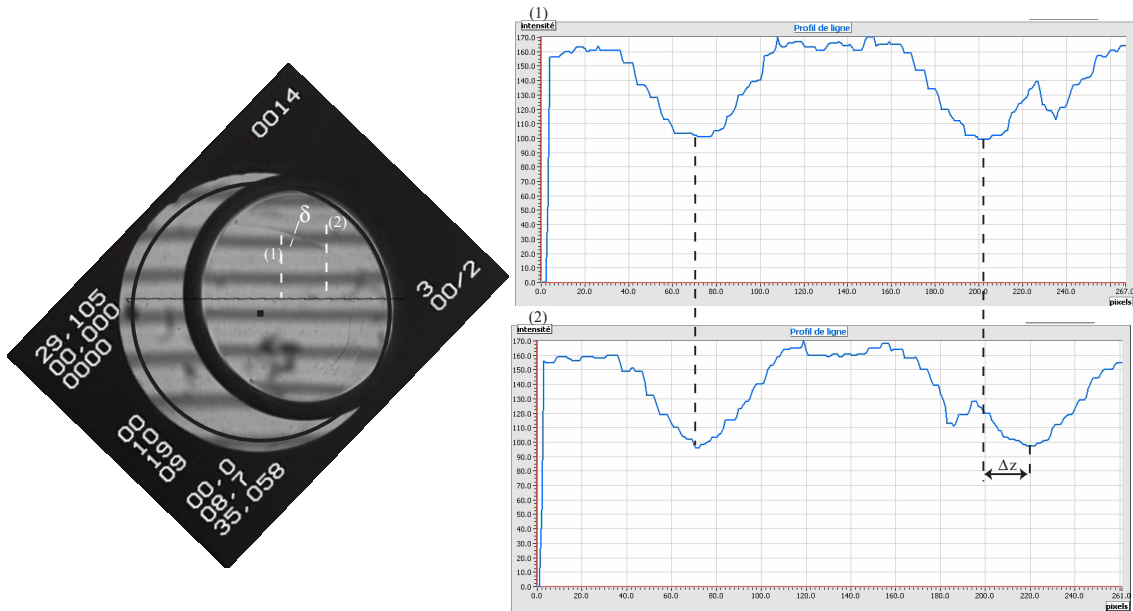
Figure 3.2.3. Experimental determination of grid shadow displacement. A) Two successive lines drawn perpendicular to the unperturbed shadow direction. B) The profile of the intensity corresponds to successive sections of grid. Both white dashed lines, marked (1) and (2), give a minimum of the intensity at the same position for the first grid shadow line above the black dashed reference line. For the second grid shadow line above the black reference line, the position of the minimum intensity is displaced by Δz. The shadow displacement Δz and the width of the contact line between the wetting film and the dry area (δ) are used to estimate the thickness of the film.

Using the black reference line drawn on Figure 3.2.3.A, we determined the middle point of the displaced shadows by localizing the minimum of the intensity profile for each position along the reference line. Figure 3.2.3.A shows two white dotted lines, marked (1) and (2), drawn perpendicular to the black reference line at different positions. The intensity profiles of the two lines (right panels of Figure 3.2.3) show two clear minima. The first minimum corresponds to the middle of the first line crossed above the reference line. The position of the minimum of the first grid shadow line does not change with respect to the black dashed reference line between the two section lines marked (1) and (2) and indicates that this line is continuous and there is no interface to distort it. The position of the minimum for the second grid shadow line crossed by the two

133

vertical lines (1) and (2) occurs at two different positions with respect to the reference axis. By measuring the amount of the displacement, Δz, and using the relationship (3.2.10), we estimated the film thickness.

Similar results were obtained using a MatLab software package. To determine the thickness of the film structure we also need to measure the width of the contact line between the wetting film and the dry area, δ. To determine the width of the contact line we again used both software packages.
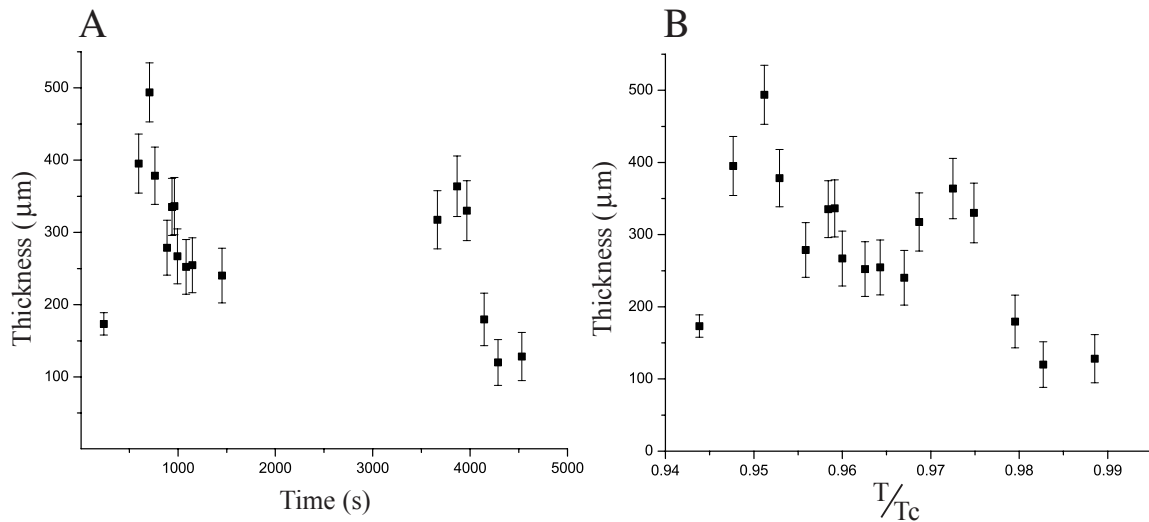
Figure 3.2.4. Dynamics of the film thickness. Estimated thickness of the film structure plotted versus time (panel A) and versus the relative temperature (panel B) for both temperature ramps. The error bars reflect the uncertainty in the measurements of the triple contact line width.

The displacement of the shadow line, Δz, is significantly larger than the width of the contact line (δ) between the wetting film and the dry area. The width of the contact line (δ) is sometimes very small, close to the image resolution limits. As a result, we took 5 to 10 different perpendicular sections to the contact line and determined the average width. Using the average value of the width, we computed, from formulas (3.2.10) and (3.2.11) the thickness of the film. An example of these measurements is shown in Figure 3.2.4 for the two temperature ramps. The biggest error in thickness evaluation is from the uncertainty in the contact line width. Therefore, we computed the thickness of the film for the average width of the contact line and for the average width plus/minus its standard deviation to give the error bars shown in Figure 3.2.4.

134

3.3 Results

The time-dependent temperature, called the temperature profile, consisted of two ramps with a slope of 10 mK/seconds separated by a 40 minute constant temperature plateau (Figure 3.3.1A). Three images from each ramp and one image from the plateau are shown (Figure 3.3.1B-H). During the ramp the contact line often exhibits an apparent periodic change in position. The contact line on the B-H images often advances and retreats with a period of approximately 10-12 seconds corresponding to the heating cycle of the instrument.
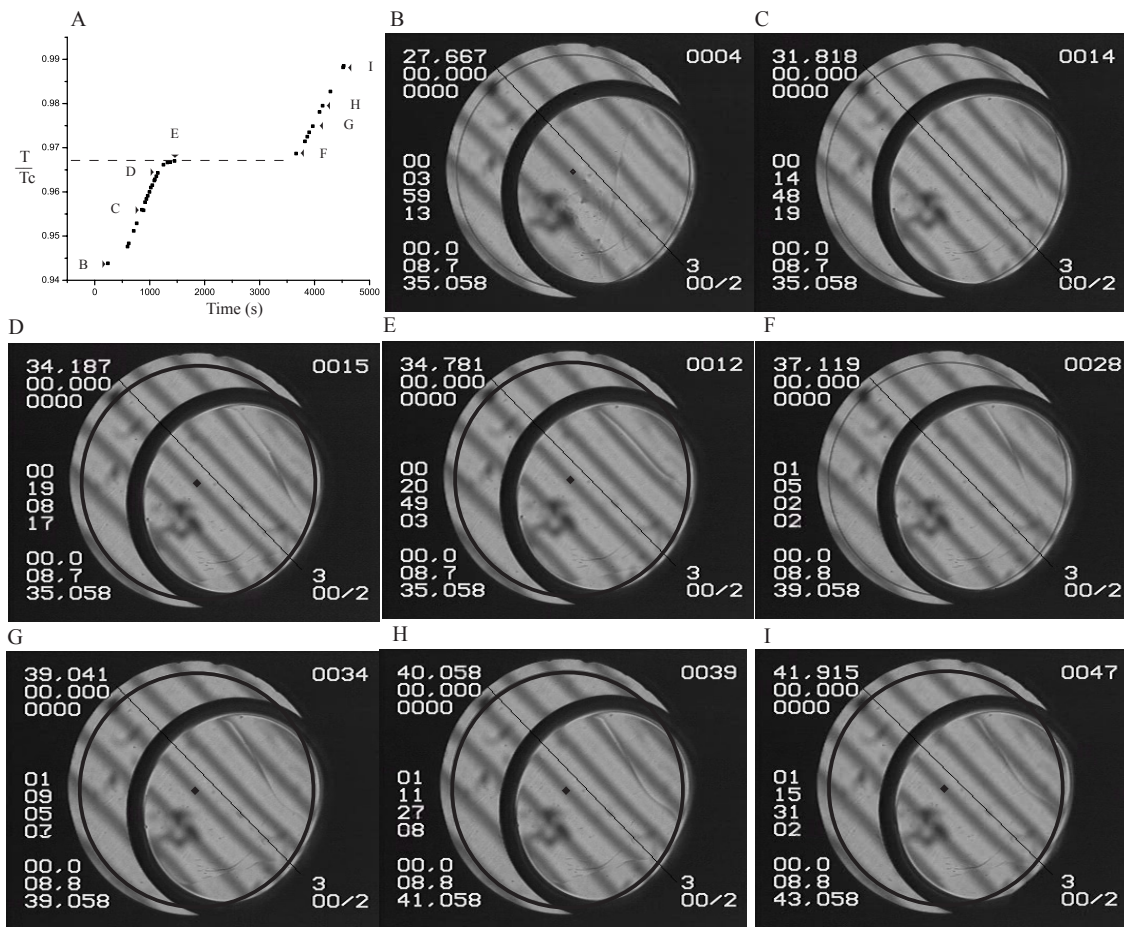
Figure 3.3.1.   Shadow fracture determines the film thickness. A) Relative temperature evolution at the cell wall during heating. The points that correspond to each of the image in the panels B-H are indicated by arrows and corresponding letters on the temperature ramps in panel A.

At the beginning of each heating ramp (Figure 3.3.1A) the grid shadow is not distorted (see also Figure 3.1.3B), indicating a flat wetting film inside the cell. After heating is started, a fast moving line appears from the region where the bubble touches the side-wall. This line propagates to the right as shown in Figure 3.3.2. The right side of the line shows grid shadow distortions while the left side appears flat. We can not directly detect if there is any liquid present on the left side. If there were appreciable liquid after the propagation of such large distortions (contact line) we would expect there to be significant interfacial distortions, too. This implies that there is at least a flat thin liquid film or a "precursor film" to the right of the contact line. The contact line, however, always moves away from the region where the bubble is in contact with the copper side-wall. This is also the region with the largest heat flux and this hotter region would tend to quickly evaporate any thin film to the right of the contact line. In addition, we have observed similar moving lines in other cells where there are some particles deposited on the sapphire windows that act as a defect that clearly pins the contact line as it advances or retreats. Garrabos [Garrabos *et al.*, 2000; Garrabos *et al.*, 2001; Hegseth *et al.*, 2002] observed a striking spreading bubble event that occurs close to the critical temperature, T_c, and reasoned that a strong vapor recoil force that diverges strongly at T_c was pushing the bubble interface. The vapor recoil, also called vapor thrust, is the only probable cause for such a large mechanical force pushing the contact line. According to Nikolayev [Nikolayev *et al.,* 1999], the vapor recoil force is large in the vicinity of a triple contact line. Qualitatively, the liquid-gas temperature is fixed by the saturated vapor pressure, whereas the wall's temperature is higher. Therefore, near the triple contact line, a large temperature gradient occurs. The largest portion of mass transfer also takes place at the contact line. The region behind the triple contact line becomes dry because of evaporation. After less than 30 seconds, the speed of the rapidly moving contact line decreases almost to zero as shown in Figures 3.3.3 and 3.3.4. By continuing the heat transfer to the cell for more than 15 minutes, a slow decrease in the size of the dry area occurs until it stabilizes to an almost constant value (see Figure 3.3.3B). We discuss below these two different regimes of the triple contact line movement.

2.3.1.   Fast moving contact line

At the beginning of both temperature ramps and intermittently during the ramps, a fast moving contact line is seen. This triple contact line slows down as it advances toward the cell center (Figures 3.3.4 and 3.3.5). The initial fast motion is sometimes accompanied by a slight change in the contact angle as shown in Figure 3.1.4B. The heat conductivity for copper is larger than for the sapphire windows [Hegseth *et al*., 2005]; therefore, the film should evaporate on the copper wall sooner than on the sapphire windows. The rapid increase of the dry surface area behind the contact line is the result of fast evaporation.
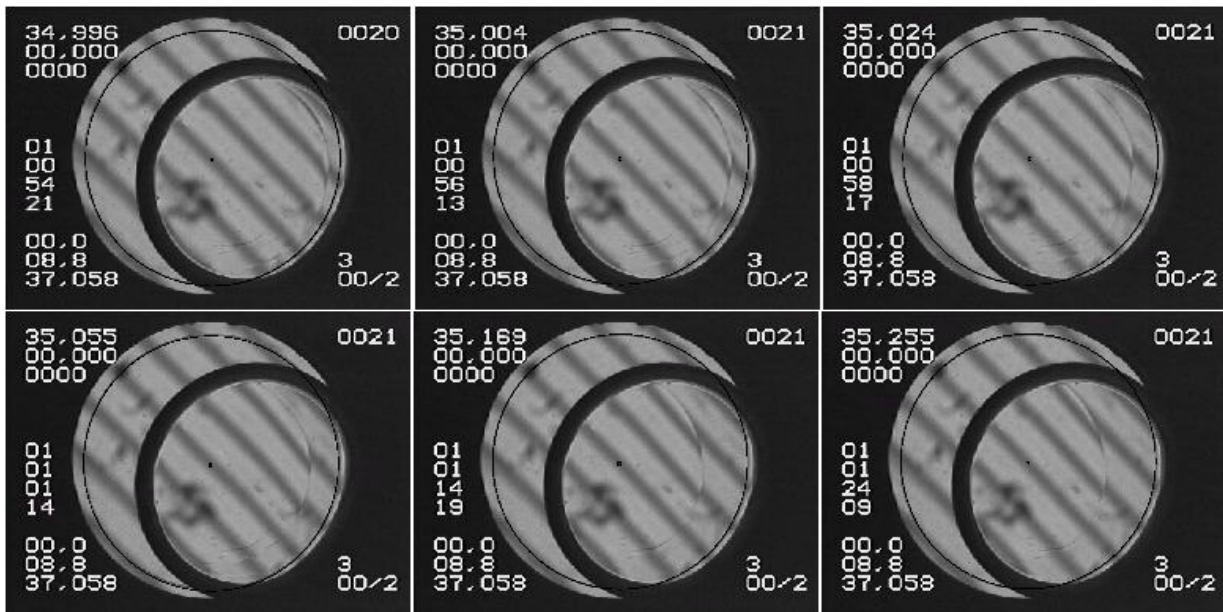
Figure 3.3.2.   Moving contact line. At the beginning of each heating ramp, a fast moving contact line occurs. The dry area behind the triple contact line reaches the maximum surface in less than 30 seconds.

A quantitative measure of the increasing dry area gives the speed of the contact line. To determine this speed we draw a ray from the cell's center perpendicular to the triple contact line. By measuring the successive intersections of the triple contact line with the reference radius we are able to determine the velocity of the contact line along the chosen direction. The measurements in Figure 3.3.3 show that the triple contact line first moves rapidly for approximately 20 seconds and then stops after almost 30 seconds. The explanation is probably that a fast initial evaporation slows down once the gas makes significant contact with the cooler

sapphire window. As a result, the speed of contact line motion decreases until a steady regime is reached.
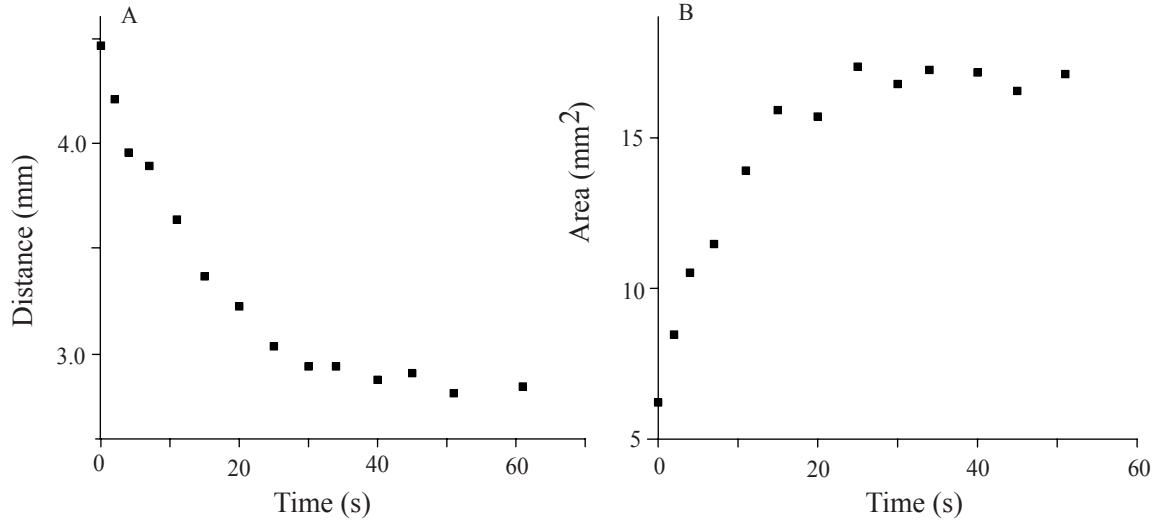
Figure 3.3.3.   Displacement of triple contact line. (A) Distance moved by the contact line towards the center of the cell after heating begins. (B) The corresponding dry area left behind the triple contact.

We used a linear interpolation algorithm to determine the slope of the distance traveled by the moving contact line versus time for the initial region (first 20 seconds) of the heating process [Oprisan, 2003]. The algorithm successively increases the number of points considered for linear interpolation until the linear regression coefficient began decreasing (Figure 3.3.4).

velocity = - 0.067 +- 0.007   mm/s

d(area)/dt = 0.61+-0.05 mm^2/s
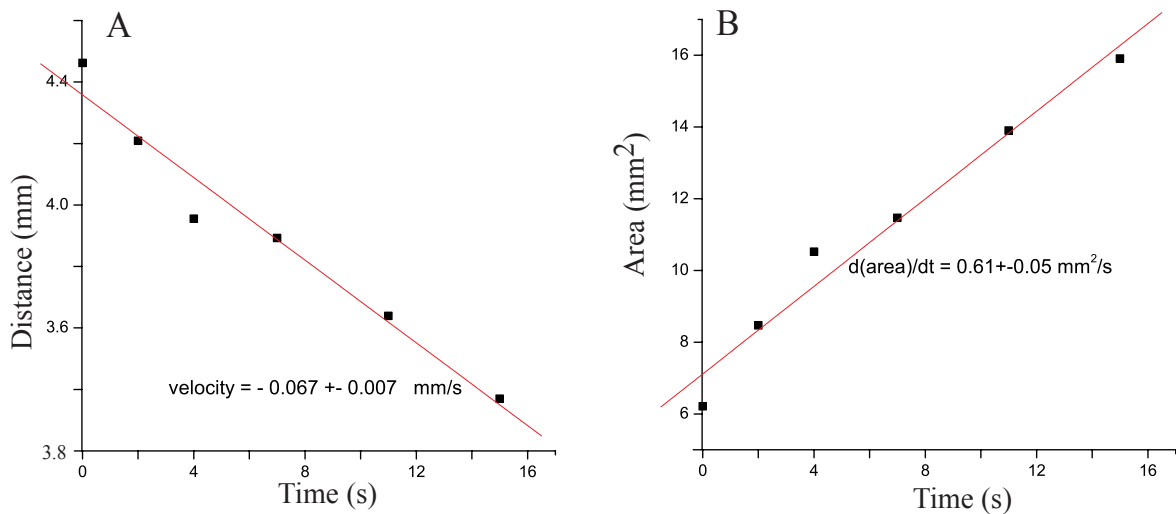
Figure 3.3.4.   The speed of triple contact line. (A) The speed of the moving contact line obtained using linear interpolation. (B) The rate of dry surface area change.

The wetting film thickness versus time and position (measured from the heating wall towards the center of the cell) are plotted in Figure 3.3.5. During the fast advance of the contact line, it appears that the forces near the wall push the fluid to the right where it accumulates [Oprisan, 2003].
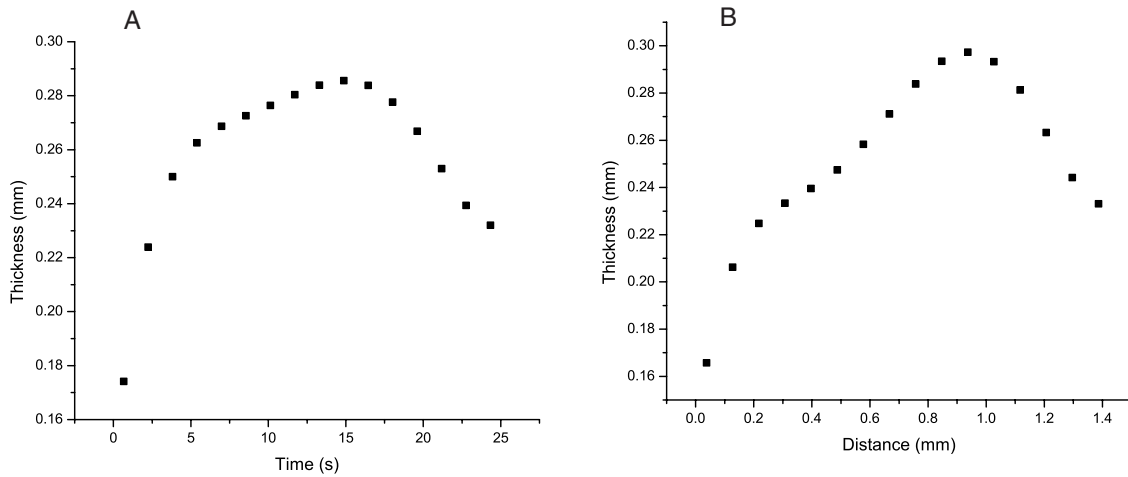
Figure 3.3.5.   Film thickness estimated from shadow fracture. (A) Estimated thickness of the wetting film versus time measured from the beginning of the second heating ramp at the same position in the field of view. (B) The estimated spatial profile of the advancing contact line.

3.3.2. Slow dynamics of the contact line

At the beginning of each contact line advance, the dry area increases rapidly up to a maximum value, as discussed in the previous section. We plotted this maximum dry area over the longer time scale of the ramp as shown in Figure 3.3.6. We note that the area of the bubble is essentially constant during the heating process (Figure 3.3.6 A and B).
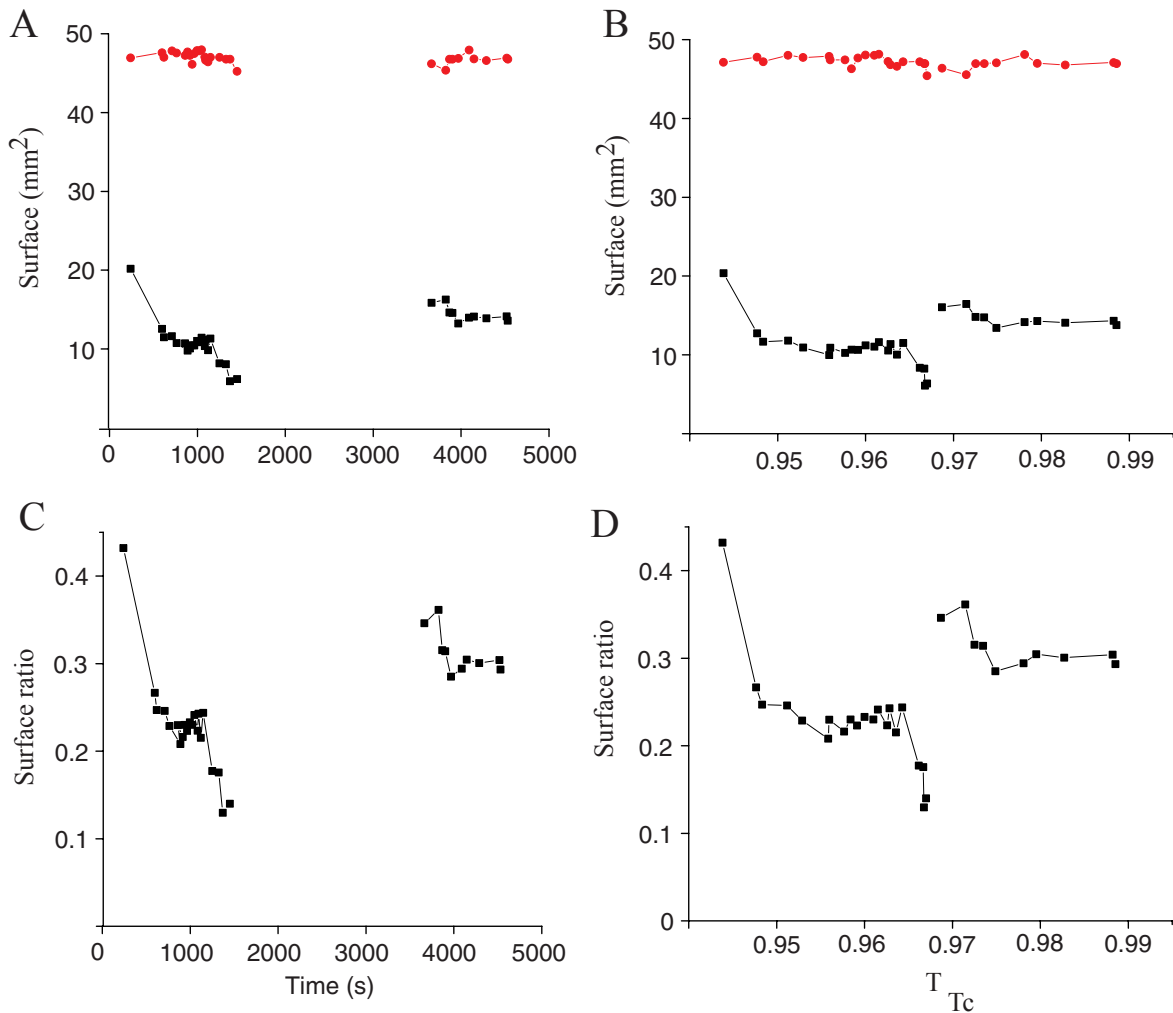
Figure 3.3.6.   Temporal evolution of the area covered by film. The total area covered by the dry surface (black squares on panels A and B) and the area of the gas bubble (red circles on panels A and B) versus time (panel A) and relative temperature (panel B). The total area of the gas bubble is constant during heating (red circles on panels A and B). The relative change in the area of the dry surface versus time (panel C) and versus the relative temperature (panel D) confirms that the main effect of heating is in the dry area shrinking due to evaporation.

On the other hand, the ratio of the dry area versus the total area of the gas bubble, as shown in Figure 3.3.4 C and D, has more complicated behavior. At first, we observed a decrease in the dry area (Figure 3.3.6C and D) but on a long time scale the surface of the dry area stabilizes to a constant value for a large range of the relative temperature (panel D).

Figure 3.3.6 shows that the area/volume ratio of the gas bubble stays constant while the dry area changes [Hegseth *et al*., 2005]. There is also a strong correlation between the estimated film thickness in Figure 3.2.4 and the total film surface area (Figure 3.3.6). This suggests that the liquid film tends to conserve its mass over a long time scale. At different temperatures, a steady state is reached where the film thickness is small (large) and the dry area is small (large), too. The steady state is also accompanied by strong fluctuations in the film thickness after the initial fast advance, suggesting that the steady state is a delicate balance between heat transfer, mass transfer, and mechanical stress [Hegseth *et al*., 2005].

3.4. Conclusions

Convection and the isothermal gas-liquid interface

If a temperature change, δT, appeared along the liquid-gas interface, it would create a surface tension gradient $\delta\sigma = (d\sigma/dT)\delta T$ that would drive a thermal-capillary or a Marangoni flow in the bulk of both fluids [Longhurst, 1973; Moldover *et al.*,1979; Nikolayev *et al.*,1999]. The possible effects of a surface tension gradient were considered in [Garrabos *et al.*, 2000]. It was shown that such effects would be unlikely to cause large-scale bubble deformations. The reasons were as follows: no convection was observed, the interface is essentially at saturation so that any gradients are strongly damped by evaporation and condensation, and if there were convection it would also dampen any δT along the liquid-gas interface [Nikolayev *et al.*, 1999]. Such a flow could modify the shape of the wetted surface and create large sustained contact lines. The same reasons for an isothermal bubble interface, however, also apply to the wetting layer. The proximity of the wetting layer to the heating wall could possibly drive such a gradient. Again, we have not seen any evidence of the steady convection that is required to create and maintain these contact lines in our experiments. As discussed above, we have occasionally seen transient bubbles coalescence. These events, however, only had a small transient influence on the bubble shape and no effect on the wetting layer. The fact that there is no convection far from the critical point shows that the interface is isothermal.

We do not know of any other external force that could produce large macroscopic effects in the presence of an isothermal wetting film. We conclude that the vapor recoil force also causes the receding contact line. This is supported by the observations that the bubble initially responds to the heating with a small impulse and a receding contact line. As noted in [Garrabos *et al.*, 2000], other experiments where the bubble is not pushed against the sidewall, show no bubble spreading. Small bubbles nucleated near the sidewall when the large bubble was near the sidewall. This region also had many coalescent events and a considerable density gradient. Similar coalescent events were also seen close to the contact angle before the rapid bubble spreading appeared. This transient phenomenon stops prior to the rapid spreading, indicating that

contact region has grown and the wetting film has evaporated along the copper sidewall. We conclude that the wall near the contact region is dry [Hegseth *et al*., 2005].

We used the grid-deflection method to estimate the thickness of the wetting film under microgravity conditions. The method has the advantage of being simple while allowing precise quantitative measurements. We approximate the liquid-vapor interface near the contact line as a wedge [Oprisan, 2003], *i.e.*, the contact line is an inclined plane between two parallel planes, where the incline is characterized only by its tilt angle with respect to the sapphire window. Although the estimation of the film structure thickness is in good agreement with previous results, this method could be improved by considering other geometries [Hegseth *et al.,* 2002].

We have shown that the line in the 2D projection of the cell is given by the triple contact line between gas, liquid and the solid sapphire window [Oprisan, 2003]. There is either no film or only a thin precursor film on the sapphire window. The fast motion of the contact line appears to accumulate fluid in front of the line. The steady state line exhibits thickness fluctuations. We have been able to interpret our results using the vapor recoil force [Hegseth *et al*., 2005]. The quantitative details of the heat and mass transfer processes near the triple contact line are challenging problems that exceed the scope of this study. The qualitative explanation for the dynamics of the triple contact line is that the vapor recoil force exerts a stress on the vapor-liquid interface near the contact line.

4. Conclusions

A series of experiments was performed in weightlessness and on Earth to study boiling under microgravity conditions for SF_6, fluctuation under microgravity conditions for SF_6 and binary mixtures on Earth, and phase separation under microgravity conditions for SF_6. To reduce the effects of sedimentation in Earth environments, the binary mixture was prepared using a density matched mixture of methanol and partially deuterated cyclohexane.

The thermo-physical properties of fluids near the critical point are sensitive to small temperature and density fluctuations. The thermodynamic parameters, such as isothermal compressibility, thermal expansion, and specific heat, and transport coefficients such as thermal diffusivity and thermal conductivity, are enhanced near the critical point and exhibit very large or very small values in this region. The microgravity environment was useful in unmasking the transport property and other thermodynamic properties without the contribution of sedimentation and convection.

Pure fluids in the supercritical state have great potential for applications and are used in industry as solvent media instead of organic and halogenated solvents in chemical processes. For example, one of the main aims of research in this area is the use of supercritical carbon dioxide as a solvent because it is environmentally a much more acceptable alternative. Another application of supercritical fluids is in chemical processes and material engineering. A commercial application in this area is supercritical fluid chromatography (SFC), a widely accepted tool in analytical chemistry. SFC is also a useful method for measuring the thermodynamic and transport properties in near critical systems.

Another major application of supercritical fluids concerns the boiling process. Under microgravity condition, the buoyancy force is eliminated and the surface tension varies accordingly to a known universal power law. Near the critical point, fluids exhibit perfect wetting of almost any solid. In the process of boiling under the application of heat, we found a perfectly wetted wall to dry from evaporation, resulting in a liquid-gas-solid triple contact line. In the microgravity environment, a spreading bubble is seen without a large heat transfer because the critical heat flux is much smaller near the critical point. The initial response of a gas bubble to the temperature increase occurs at the edge, where the defocused image of a grid becomes distorted. This distortion propagates and causes a change in the wetting film's thickness. The

144

film's thickness was estimated using the defocused grid method and an edge model approximation. The quantitative data presented here has been observed prior to the critical boiling crisis. A qualitative explanation for the dynamics of the triple contact line is that the vapor recoil force changes the curvature of the vapor-liquid interface and explains the observed correlation between the heat cycle and the periodic movement of the triple contact line.

The direct visualization and analysis of critical fluctuations in pure fluids in microgravity, as well as in a binary mixture on Earth, provides invaluable information about cooperative phenomena and the role played by the thermodynamic fluctuations in determining the critical behavior. Densities fluctuations appear as domains with different intensities compared to the average value of the image intensity and are detectable only near the critical point. The images analysis provides new valuable information regarding the underlying statistical physics of the system. Image processing techniques, such as the radial average power spectrum, allowed us to estimate important characteristics of the fluctuations. For example, we obtained the characteristic length of fluctuations in sulfur hexafluoride and were able to estimate the average temperature difference ΔT_λ. It was found that the ΔT_λ is too small to be detected by the ALICE II instruments because of the finite size effects that significantly limit the ability to estimate the temperature of a near critical fluid from the radial average of the power spectrum. However, if we assume that the correlation length obeys the same power law on both sides of the critical temperature, then their ratio should be independent of any finite size effects. Using this approach, it was possible to determine the position of the critical point by taking the ratio of the characteristic lengths, which were in turn derived directly from the averaged radial power spectrum.

The histograms of the recorded images were also used for estimating the critical temperature. This method has the advantage of avoiding any reference to the spatial correlation of the pixels in the recorded images. Based on the average intensity and the variances of gray levels extracted directly from the histograms of the recorded images, we were able to evaluate the critical temperature. The growth of fluctuating domains near the critical temperature revealed that the log-log plot of the reduced wave number k* versus the reduced time t* follows a linear relationship. The data fit reasonably well and correspond to the early stage of the "universal" growth curve. Data from image analysis of the phase separation for sulfur hexafluoride in the case of the 3.6 mK temperature quench were also used to find the power law and to observe

145

growth dynamics. The early stage power law was also found in this case using the scaled universal units k* and t*. These results, obtained in the absence of gravity effects established a quantitative relationship between the morphology and the "universal" evolution law of the pattern.

The fluctuation dynamics were studied on Earth with binary liquids near the critical point. The analysis of image formations for recorded frames of binary liquid mixture using three different techniques called bright field (BF), phase contrast (PC), and dark field (DF) was performed. The dark and bright regions in the scattering images are areas of more or less light scattering due to the local fluctuation of the mixture concentration. The local fluctuations of concentration cause small variations in the index of refraction that determine changes in the optical path of the transmitted and scattered light. The histograms of the recorded images show Gaussian statistics for BF and PC techniques and a slight difference for the DF images. The fluctuations contrast in the images significantly increase by using a red filter and circular polarizer. The power spectrum method allowed us to estimate the wave numbers for each image. Similarities between the wave numbers were found in the case of BF and PC images regardless of the filters. The plot of the half-width of the histogram versus the size of the averaging filter (L) shows two different regions of qualitatively different behavior. In the first region, the widths of the histogram saturate for a value of the averaging filter size L smaller than a critical value (16 pixels) as a result of correlations between fluctuations. In the second region (>> 20 pixels), the widths of the histogram show a $1/L^x$ dependence. The red filter and the circular polarizer smoothes the transition diagram although the two regions remain separated.

5. References

1.   Ahlers G., 1980, Critical phenomena at low temperature, Rev. Mod. Phys. **52**: 489–503.
2.   Ahlers G., and J. Oh, 2003, Critical Phenomena near Bifurcations in Nonequilibrium Systems, Int. J. Mod. Phys. B **17**: 3899.
3.   Alexander F.J., S. Chen, and D.W. Grunau, 1993, Hydrodynamic spinodal decomposition: Growth kinetics and scaling functions, Phys. Rev. B **48**: 634–637
4.   Andrews T., 1869, On the continuity of the gaseous and liquid state of matter, Phil. Trans. R. Soc. **159**: 575 – 589.
5.   Bailey A.E., and D.S. Cannell, 1993, Spinodal decomposition in a binary fluid, Phys. Rev. Lett. **70**: 2110–2113.
6.   Barker J.A., and D. Henderson, 1976, What is Liquid? Understanding the States of Matter, Rev. Mod. Phys. **48**: 587-671.
7.   Bastea S., and J.L. Lebowitz, 1997, Spinodal Decomposition in Binary Gases, Phys. Rev. Lett. **78** (18): 3499-3502.
8.   Baumberger T., F. Perrot, and D. Beysens, 1992, Kinetics of nucleation and growth in a near-critical binary liquid mixture at rest and under a shear flow, Phys. Rev. A. **46**(12): 7636-7642.
9.   Berg R.F., and M.R. Moldover, 1988, Critical exponent for the viscosity of four binary liquids, Journal of Chemical Physics **89**: 3694-3704.
10.   Berg R.F., and M.R. Moldover, 1990, Critical exponent for the viscosity of carbon dioxide and xenon, Journal of Chemical Physics **93**: 1926.
11.   Berg R.F., and M.R. Moldover, 1990, Critical exponent for viscosity, Phys. Rev. A **42**(12):7183-7186.
12.   Berg R.F., 1993, Thermal Equilibration Near the Critical Point: Effects due to Three Dimensions and Gravity, Phys. Rev. E **48**: 1799.
13.   Beysens D., A. Bourgou, and G. Zalczer, 1976, Journal of Physics Paris **37**: C1.
14.   Beysens D., and G. Zalczer, 1977, Low-frequency spectrum of light multiply scattered by a critical mixture, Phys. Rev. A **15**: 765-772.
15.   Beysens D., M. Gbadamassi, and L. Boyer, 1979, Light-Scattering Study of a Critical Mixture with Shear Flow, Phys. Rev. Lett. **43**: 1253–1256.
16.   Beysens D., 1986, Critical Phenomena, in Materials Sciences in Space, a Contribution to the Scientific Basis of Space Processing, B. Feuerbacher, H. Hamacher, and R.J. Naumann, eds. (Springer, Berlin), p. 191.
17.   Beysens D., J. Straub, and D.J. Turner, 1987, Phase Transitions and Near-Critical Phenomena, in Fluid Sciences and Materials Science in Space, A European Perspective, H. U. Walter, ed. (Springer, Berlin), p. 221.
18.   Beysens D., P. Guenoun, and F. Perrot, 1988, Phase separation of critical binary fluids under microgravity: Comparison with matched-density conditions, Phys. Rev. A **38**: 4173–4185.
19.   Beysens D., P. Guenoun and F. Perrot, 1990, Direct observation of critical fluctuations, J. Phys.: Condens. Matter **2**: SA127-SA133.

20. Beysens D., 1990, Recent Developments in Critical and Near-Critical Point Phenomena, in Proceedings VIIth European Symposium on Materials and Fluid Sciences in Microgravity, ESA SP-295.

21. Beysens D., P. Guenoun, P. Sibille, and A. Kumar, 1994, Dimple and nose coalescences in phase-separation processes. Phys. Rev. E **50**(2):1299-1302.

22. Beysens D., and Y. Garrabos, 2000, Near-critical fluids under microgravity: status of the ESEME program and perspectives for the ISS, 51st lnternational Astronautical Congress, Rio de Janeiro, Brazil, IAF-00-J.3.04.

23. Beysens D., and Y. Garrabos, 2000, The phase transition of gas and liquids, Physica A **281**:361-380.

24. Beysens D., Y. Garrabos, V.S. Nikolayev, C. Lecoutre-Chabot, J.-P. Delville and J. Hegseth, 2002, Liquid-vapor phase separation in a thermocapillary force field, Europhys. Lett. **59** (2): 245-251.

25. Beysens D., V.S. Nikolayev and Y. Garrabos, 2003, Vapour spreading and the boiling crisis, J. Phys.: Condens. Matter **15**: S435-S442.

26. Beysens D., D. Chatain, P. Evesque, and Y. Garrabos, 2005, High-Frequency Driven Capillary Flows Speed Up the Gas-Liquid Phase Transition in Zero-Gravity Conditions, Phys. Rev. Lett. **95**: 034502.

27. Binder K., and D. Stauffer, 1974, Theory for the Slowing Down of the Relaxation and Spinodal Decomposition of Binary Mixtures, Phys. Rev. Lett. **33**: 1006–1009.

28. Binder K., 1987, Theory of first-order phase transitions. Rep. Prog. Phys. **50**:783-859.

29. de Bonta P.W., C.L. Luengo-Hendriksb, M.P.G. van Kempena, and R. Vreeker, 2004, Time evolution of phase separating milk protein and amylopectin mixtures, Food Hydrocolloids **18**: 1023–1031.

30. Bray A., and R. Chang, 1975, Double-scattering correction in the interpretation of Rayleigh scattering data near the critical point of a binary liquid, Phys. Rev. A **12**: 2594-2605.

31. Broide M.L., Y. Garrabos, and D. Beysens, 1993, Nonfractal colloidal aggregation, Phys. Rev. E **47**(5): 3768-3771.

32. Cahn J.W., 1965, Phase separation by spinodal decomposition in isotropic systems. Journal Chemistry Physics **42**: 93.

33. Calmettes P., I. Laguës, and C. Laj, 1972, Evidence of Nonzero Critical Exponent η for a Binary Mixture from Turbidity and Scattered Light Intensity Measurements, Phys. Rev. Lett. **28**: 478–480.

34. Castleman K.R., 1996, Digital Image Processing, Prentice Hall.

35. Chakrabarti A., and J.D. Gunton, 1988, Cell-dynamics approach to late-stage domain growth in phase-separating systems, Phys. Rev. B **37**: 3798–3800.

36. Chang R.F., H. Burstyn, and J.V. Sengers, 1979, Correlation function near the critical mixing point of a binary liquid, Phys. Rev. A **19**: 866–882.

37. Chalyi A.V., A.D. Alekhin, 1971, Application of scaling method to study of light scattering with allowance for gravitational effect, and determination of critical indices from light scattering data, Soviet Phys. JETP **32**(2):181.

38. Chou Y.C., and W.I. Goldburg, 1979, Phase separation and coalescence in critically quenched isobutyric-acid—water and 2,6-lutidine—water mixtures, Phys. Rev. A **20**: 2105–2113.

39. Chu B., 1966, Experiments on the Critical Opalescence of Binary Liquid Mixtures - Elastic Scattering, in Critical Phenomena, ed. M. S. Green and J.V. Sengers, National Bureau of Standards Miscellaneous Publication **273**: 123.

40. Cannell D.S., 1975, Measurement of the long-range correlation length of SF6 very near the critical point, Phys. Rev. A **12**: 225–231.

41. Chimowitz E.H., 2005, Introduction to Critical Phenomena in Fluids, Oxford Univ Press.

42. Cornell S.J., and A.J. Bray, 1996, Domain Growth in a 1-D Driven Diffusive System, Physical Review E **54**: 1153.

43. Cumming A., P. Wiltzius, F.S. Bates, and J.H. Rosedale, 1992, Light-scattering experiments on phase-separation dynamics in binary fluid mixtures, Phys. Rev. A **45**: 885–897.

44. Dahl D., and M.R. Moldover, 1972, Thermal Relaxation Near the Critical Point, Phys. Rev. A **6**: 1915.

45. Damay P., F. Leclercq, P. Chieux, 1989, Critical scattering function in a binary fluid mixture: A study of sodium-deuteroammonia solution at the critical concentration by small-angle neutron scattering, Phys. Rev. B **40**(7): 4696-4708.

46. Damay P., F. Leclercq, R. Magli, F. Formisano, and P. Lindner, 1989, Universal critical-scattering function: An experimental approach, Physical Review B **58**(18): 12038-12043.

47. Debye J., 1968, J. Chem. Phys. **48**: 203.

48. Domb C., 1996, The critical point, - a historical introduction to modern theory of critical phenomena, Taylor and Francis.

49. Eggers J., J. Lister, and H.A. Stone, 1999, Coalescence of Liquid Drops. J. Fluid Mech. **401**: 293.

50. Eggers J., and H.A. Stone, 2004, Characteristic lengths at moving contact lines for a perfectly wetting fluid: the influence of speed on the dynamic contact angle, J. Fluid Mech. **505**: 309.

51. Eggers J., 2005, Contact line motion for partially wetting fluids , Phys. Rev. E **72**: 061605.

52. Fisher M.E., 1982, Critical Phenomena in Lecture Notes in Physics, ed. F.J.W. Hahne (Springer-Verlag, Berlin), Vol. 186, 1.

53. Ford N.C., and G.B. Benedek, 1965, Observation of the Spectrum of Light Scattered from a Pure Fluid Near its Critical Point, Phys. Rev. Lett. **15**: 649–653.

54. Ford N.C., 1985, Light Scattering Apparatus, in Dynamical Light Scattering, Application of Photon Correlation Spectroscopy, R. Pecora, ed. Plenum, New York, p. 7.

55. Fisher M.E., 1967, The theory of equilibrium critical phenomena, Rep. Progr. Phys. **30**:615-730.

56. Furukawa H., 2000, Spinodal decomposition of two-dimensional fluid mixtures: A spectral analysis of droplet growth, Phys. Rev. E **61**: 1423–1431.

57. Gammon R.W., 1987, "Critical Fluid Light Scattering", in The Nation's Future Material Needs, T. Lynch, J. Persh, T. Wolf, and N. Rupert, eds. (Soc. Adv. Mater. & Process Eng., Covina, CA, 1987), proceedings of the 19th International Technical Conference of the Society for the Advancement of Material and Process Engineering (SAMPE).

58. Gammon R.W., 1991, Investigations of Fundamental Phenomena in Microgravity, Proceedings IKI/AIAA Microgravity Symposium (American Institute of Aeronautics and Astronautics, pp. 379-381.

59.   Garrabos Y., B. Le Neindre, P. Guenoun, B. Khalil, and D. Beysens, 1992, Observation of spinodal decomposition in a hypercompressible fluid under reduced gravity, Europhysics Letters **19**: 491.

60.   Garrabos Y., R. Wunenburger, and J. Hegseth, 2000, Critical boiling phenomena observed in microgravity, AIP Conference Proceedings, Volume 504, Issue 1, pp. 737-743.

61.   Garrabos Y., A. Dejoan, C. Lecoutre, D. Beysens, V.S. Nikolayev, and R. Wunenberger, 2001, Piston effect in a supercritical fluid sample cell: a phenomenological approach, Colloque Sciences de la Matiere et microgravite, CNES/CNRS, GDR no 2258, Paris, France, Session: Transport dans les fluides, May 14-15.

62.   Garrabos Y., A. Dejoan, C. Lecoutre, D. Beysens, V.S. Nikolayev, and R. Wunenburger, 2001, Piston effect in a supercritical fluid sample cell: a phenomenological approach of the mechanisms, J. Physique IV (France) **11:** 6-23.

63.   Garrabos Y., C. Lecoutre-Chabot, J. Hegseth, V.S. Nikolayev, D. Beysens, 2001, Gas spreading on a heated wall wetted by liquid, Phys. Rev. E **64**(5): 051602-1–051602-10.

64.   de Gennes P.G., 1985, Wetting: Statics and Dynamics. Review of Modern Physics **75**(3): 827-863.

65.   de Gennes P.G., F. Brochard-Wyart, and D. Quere, 2003, Capillarity and Wetting Phenomena: Drops, Bubbles, Pearls, Waves, Springer.

66.   Goldman D.I., J.B. Swift, and H.L. Swinney, 2004, Noise, coherent fluctuations, and the onset of order in an oscillated granular fluid, Physical Review Letters **92**: 174302.

67.   Golestanian R., and E. Raphael, 2001, Relaxation of a moving contact line and the Landau-Levich effect, Europhys. Lett. **55**(2): 228-234.

68.   Golestanian R., and E. Raphael, 2001, Dissipation in dynamics of a moving contact line, Phys Rev E Stat Nonlin Soft Matter Phys. **64**(3 Pt 1): 031601.

69.   Gonzalez R.C., and R.E. Woods, 2002, Digital Image Processing, Prentice Hall Upper Saddle River, New Jersey.

70.   Grant M., and K.R. Elder, 1999, Spinodal Decomposition in Fluids, Phys. Rev. Lett. **82**(1): 14-16.

71.   Green M.S. (ed.), 1971, Critical Phenomena, Academic Press.

72.   Greer C., and M.R. Moldover, 1981, Thermodynamic Anomalies at Critical Points of Fluids, Annual Review of Physical Chemistry **32**: 233-265.

73.   Grigoriev R.O., 2002, Control of evaporatively driven instabilities of thin liquid films, Physics of Fluids **14**: 1895-1909.

74.   Green M.S. (ed.), 1971, Critical Phenomena, Academic Press.

75.   Guenoun P., D. Beysens, F. Perrot, Y. Garrabos and A. Kumar, 1994, Phase separation in critical and off-critical fluids: specific experimental behaviours at criticality, J. Phys.: Condens. Matter **6**: A199-A203.

76.   Guenoun P, F. Perrot, and D. Beysens, 1989, Microscopic observation of order-parameter fluctuations in critical binary fluids: Morphology, self-similarity, and fractal dimension, Phys. Rev. Lett. **63**(11): 1152-1155.

77.   Guenoun P., D. Beysens, and M. Robert, 1990, Dynamics of wetting and phase separation, Phys. Rev. Lett. **65**: 2406–2409.

78.   Gurfein V., D. Beysens, Y. Garraobs, and B. Le Neindre, 1991, Simple grid technique to measure refractive index gradients, Optics Communications 85.

79.   Hegseth J.J., N. Rashidnia and A. Chai, 1996, Natural convection in droplet evaporation, Phys. Rev. E **54**: 1640–1644.
80.   Hegseth J.J., V.S. Nikolayev, D. Beysens, Y. Garrabos, C. Chabot, 1998, Growth and Morphology of Phase Separating Supercritical Fluids (GMSF), Boiling in Subcritical Fluids, and Critical Fluctuations, Fourth Microgravity and Transport Phenomena Conference, Cleveland, Ohio.
81.   Hegseth J.J., Y. Garrabos, V.S. Nikolayev, C. Lecoutre-Chabot, R. Wunenburger, and D. Beysens, 2002, Gas "wets" a solid wall in orbit, International Journal of Thermophysics **23**: 89 – 101.
82.   Hegseth J., A. Oprisan, C. Lecoutre, D. Beysens, and Y. Garrabos, 2002, Coarsening and growth in phase separation neare the liquid-gas critical point, Annual American Physical Society March Meeting 2002, March 18 - 22, Indianapolis, Indiana.
83.   Hegseth J, D. Beysens, and Y. Garrabos, 2003, Direct imaging of fluctuation near the critical point of binary liquids, Fifteenth Symposium on thermophysical properties Boulder, CO, USA, June 22 - 27.
84.   Hegseth J.J., A. Oprisan, Y. Garrabos, V.S. Nikolayev, C. Lecoutre-Chabot, and D. Beysens, 2005, Wetting film dynamics during evaporation under weightlessness in a near-critical fluid, Phys. Rev. E **72**: 031602.
85.   Jahne B., 1997, Digital image processing: Concepts, algorithms, and scientific applications, Springer-Verlag, Berlin, Heidelberg.
86.   Jain A.K., 1990, Fundamentals of digital image processing, Prentice Hall.
87.   Jany P., and J. Straub, 1987, Thermal Diffusivity of Fluids in a Broad Region Around the Critical Point., Int. J. Thermophys. **12**(8): 165-180.
88.   Hashimoto T., M. Itakura, and H. Hasegawa, 1986, Late stage spinodal decomposition of a binary polymer mixture. 1. Critical test of dynamic scaling in scattering function. Journal Chemistry Physics **85**: 6118–6128.
89.   Hiroshi J., Tsuyoshi K., Y. Nishikawa, T. Hashimoto, and S.T. Hyde, 1997, Curvature Determination of Spinodal Interface in a Condensed Matter System, Phys. Rev. Lett. **78**: 2248–2251.
90.   Hohenberg P.C., and M. Barmatz, 1977, Gravity Effects near the Gas-Liquid Critical Point, Phys. Rev. A **6**: 289.
91.   Hohenberg P.C., B.I. Halperin, 1977, Theory of dynamic critical phenomena. Rev. Mod. Phys. **49**: 435-479.
92.   Houessou C., P. Guenoun, R. Gastaud, F. Perrot, D. Beysens, 1985, Critical behavior of the binary fluids cyclohexane-methanol, deuterated cyclohexane-methanol and of their isodensity mixture: Application to microgravity simulations and wetting phenomena, Phys. Rev. A **32**(3): 1818-1833.
93.   Jayalakshmi Y., B. Khalil, and D. Beysens, 1992, Phase separation under a weak concentration gradient, Phys. Rev. Lett. **69**(21): 3088-3091.
94.   Joshua M., J.V. Maher, and W.I. Goldburg, 1983, Observation of Periodic Spinodal Decomposition, Phys. Rev. Lett. **51**: 196–198.
95.   Joshua M., W.I. Goldburg, A. Onuki, 1985, Periodic spinodal decomposition: Light scattering in the phase-separating and disordered regimes, Phys. Rev. Lett. **54**(11): 1175-1177.
96.   Joshua M., W.I. Goldburg, 1985, Periodic spinodal decomposition in a binary liquid mixture, Physical Review A **31**(6): 3857-3867.

97. Kadanoff L.P.,1976, in Phase Transitions and Critical Phenomena, eds. C. Domb and M.S. Green (Academic, New York, USA), Vol. 5A, Ch. 1, pp. 1-34.

98. Kadanoff L.P., 2000, Statistical Physics: Statics, Dynamics and Renormalization, World-Scientific.

99. Kawasaki K., 1975, in Phase Transitions and Critical Phenomena, C. Domb and M.S. Green, eds. (Academic, New York), Vol. 5a, p. 165.

100. Kawasaki K., 1983, Physica Amsterdam, 118A, 175.

101. Kazi M.H., M. Inui, and K. Tamura, 2002, A study of density fluctuations near the critical point of fluid Se by small angle X-ray scattering, J. Non-Cryst. Solids **312-314**: 279-283.

102. Koga T., and K. Kawasaki, 1991, Spinodal decomposition in binary fluids: Effects of hydrodynamic interactions, Phys. Rev. A **44**: R817–R820.

103. Ley-Koo M., and M.S. Green, 1977, Revised and extended scaling for coexisting densities of SF_6, Physical Review A **16**(6): 2483-2487.

104. Lamorgese A.G., and M. Roberto, 2005, Nucleation and spinodal decomposition of liquid mixtures, Phys. Fluids **17**: 034107.

105. Landau L.D., and E.M. Lifshitz, 1969, Statistical Physics, Addison-Wesley.

106. Laradji M., S. Toxvaerd, and G.M. Ole, 1996, Molecular Dynamics Simulation of Spinodal Decomposition in Three-Dimensional Binary Fluids, Phys. Rev. Lett. **77**(11): 2253-2256.

107. Li W.B., J.V. Sengers, R.W. Gammon, and P.N. Segre, 1995, Measurements of Transport Properties of Liquids with Equilibrium and Nonequilibrium Rayleigh Scattering, Int. J. Thermophys. **16**: 23.

108. Lipa J.A., D.R. Swanson, and J.A. Nissen, 1996, Heat Capacity and Thermal Relaxation of Bulk Helium very near the Lambda Point, Phys. Rev. Lett. **76**: 944–947.

109. Longhurst R.S., 1973, Geometrical and Physical Optics, Longman, London and New York, Third edition.

110. Lunacek J.H., and D.S. Cannell, 1971, Long-Range Correlation Length and Isothermal Compressibility of Carbon Dioxide Near the Critical Point, Phys. Rev. Lett. **27**: 84 .

111. Mac Cormack S., 1951, J. Chem. **29**: 699.

112. Martın A., A.G. Casielles, M.G. Munoz, F. Ortega, and R.G. Rubio, 1998, Two-exponential correlation functions near the critical point of a micellar system, Phys. Rev. E **58**(2).

113. Mitchell J.L., W.B. Pennebaker, 1996, MPEG digital video compression standard, Kluwer Academic Publishers.

114. Moldover M.R., R.J. Hocken, R.W. Gammon, and J.V. Sengers, 1976, Overviews and Justifications for Low Gravity Experiments on Phase Transitions and Critical Phenomena in Fluids, National Bureau of Standards Technical Note 925 (U.S. Government Printing Office, Washington, D.C).

115. Moldover M.R., J.V. Sengers, R.W. Gammon, and R.J. Hocken, 1979, Gravity effects in fluids near the gas-liquid critical point, Rev. Mod. Phys. **51**: 79-99.

116. Mountain R.D., 1966, Spectral distribution of scattered light in a simple fluid. Rev. Mod. Phys. **38**: 20514.

117. Nikolayev V.S., D. Beysens, and P. Guenoun, 1996, New hydrodynamic mechanism for drop coarsening, Phys. Rev. Lett. **76**(17): 3144-3147.

118. Nikolayev V.S., and D. Beysens, 1997, Physics of Fluids **11:** 3227-3234.

119. Nikolayev V.S., and D. Beysens, 1999, Boiling crisis and non-equilibrium drying transition, Europhysics Letters **47**(3): 345 – 351.
120. Nikolayev V.S., D.A. Beysens, G.-L. Lagier, and J. Hegseth, 2001, Growth of a dry spot under a vapor bubble at high heat flux and high pressure, International Journal of Heat and Mass Transfer **44**: 3499 – 3511.
121. Nikolayev V.S., and D. Beysens, 2003, Equation of motion of the triple contact line along an inhomogeneous surface, Europhysics Letters **64**(6): 763 – 768.
122. Nikolayev V.S., A. Dejoan, Y. Garrabos, and D. Beysens, 2003, Fast heat transfer calculations in supercritical fluids versus hydrodynamic approach, Phys. Rev. E **67**: 061202.
123. Nikolayev V.S., D. Beysens, 2004, Boiling crisis: theory, simulation, and experiments in micro-gravity, "Theory and simulations", Bulletin DRFMC No. 4 (Novembre), 44 – 45, CEA Grenoble.
124. Nikolayev V.S., 2005, Dynamics and depinning of the triple contact line in the presence of periodic surface defects, J. Phys. Cond. Matt. **17**(13): 2111 – 2119.
125. Nikolayev V.S., D. Beysens, Y. Garrabos, D. Chatain, and C. Lecoutre, 2005, Bubble spreading during the boiling crisis: modeling and experimenting in microgravity.
126. Oh J., and G. Ahlers, 2003, Thermal-Noise Effect on the Transition to Rayleigh-Benard Convection, Phys. Rev. Lett. **91** (9).
127. Oh J., J. O. de Zarate, J. Sengers, and G. Ahlers, 2004, Dynamics of fluctuations in a fluid below the onset of Rayleigh-Benard convection, Phys. Rev. E **69**: 021106.
128. Ohbayashi K., and B. Chu, 1978, Light Scattering Near the Plait Point of a Ternary Liquid Mixture: Ethanol-Water-Chloroform, J. Chem. Phys. **68**: 5066.
129. Onuki H.H., and R.A. Ferrell, 1990, Fast Adiabatic Equilibration in a Single-Component Fluid Near the Liquid-Vapor Critical Point, Phys. Rev. A **41**: 2256.
130. Onuki H.H., and R. A. Ferrell, 1990, Adiabatic Heating Effect Near the Gas-Liquid Critical Point, Physica A **164**: 245.
131. Onuki A., and S. Puri, 1999, Spinodal Decomposition in Gels. Physical Review E **59**: R1331–R1334.
132. Onuki A., 2002, Phase Transition Dynamics, Cambridge University Press; 1st edition.
133. Onuki A., and A. Furukawa, 2001, Phase transitions of binary alloys with elastic inhomogeneity, Phys. Rev. Lett. **86**(3): 452-455.
134. Oprisan A., S.A. Oprisan, and J. Hegseth, 2002, Computational solution of liquid-gas interface shapes from the refractions of a defocused grid, Annual American Physical Society March Meeting 2002, Indianapolis, Indiana.
135. Oprisan A., 2003, Master thesis, University of New Orleans.
136. Oprisan A., and J. Hegseth, 2003, Moving Contact Lines in Heated Liquid Films, Fifteenth Symposium on thermophysical properties Boulder, CO, USA.
137. Oprisan A., J. Hegseth, D. Beysens, Y. Garrabos, 2003, Moving contact lines in heated liquid films, American Physical Society, Annual APS March Meeting 2003.
138. Ornstein L., and S. Zernike, 1914, Proc. Sect. Sci. K Med. Akad. Wet. **17:** 793.
139. Oron A., S.H. Davis, and S.G. Bankoff, 1997, Long-scale evolution of thin liquid films, Rev. Mod. Phys. **69**: 931–980.
140. Palmer H.J., 1976, The hydrodynamic stability of rapidly evaporating liquids at reduced pressure, J. Fluid Mech. **75**(3): 487-511.

141. Papon P., P.H.E. Meijer, and J. Leblond, 2002, The Physics of Phase Transitions, Springer.
142. Perrot F., P. Guenoun, T. Baumberger, D. Beysens, Y. Garrabos, and B. Le Neindre, 2002, Nucleation and Growth of Tightly Packed Droplets in Fluids, Phys. Rev. Lett. **73**: 688–691.
143. Perrot F., D. Beysens, Y. Garrabos, T. Fröhlich, P. Guenoun, M. Bonetti, P. Bravais, 1999, Morphology transition observed in a phase separating fluid, Physical Review E **59**(3): 3079-3083.
144. Press W.H., 1988, Numerical Recipes in C. The Art of Scientific Computing, Cambridge University Press, Cambridge.
145. Puglielli V.G., and N.C. Ford, 1970, Turbidity measurements in SF_6 near its critical point, Phys. Rev. Lett. **25**: 143.
146. Puri S., and B. Dünweg, 1992, Temporally linear domain growth in the segregation of binary fluids, Phys. Rev. A **45**: R6977–R6980.
147. Qiu X.-L., and G. Ahlers, 2005, Dynamics of Fluctuations below a Stationary Bifurcation to Electroconvection in the Planar Nematic Liquid Crystal N4, Phys. Rev. Lett. **94**: 087802.
148. Rodolfo M. (Ed.), 2002, Physics of Fluids in Microgravity, CRC.
149. Segre P.N., R.W. Gammon, and J.V. Sengers, 1993, Light-Scattering Measurements of Nonequilibrium Fluctuations in a Liquid Mixture, Phys. Rev. E **47**: 1026.
150. Segre P.N., R. Schmitz, and J.V. Sengers, 1993, Fluctuations in Inhomogeneous and Nonequilibrium Fluids under the Influence of Gravity, Physica A **195**: 31.
151. Segre P.N., and J.V. Sengers, 1993, Nonequilibrium Fluctuations in Liquid Mixtures under the Influence of Gravity, Physica A **198**: 46.
152. Sengers A.L., R. Hocken, and J.V. Sengers, 1977, Critical Point Universality and Fluids, Physics Today **12**: 42.
153. Sengers J.V., 1982, Universality of Critical Phenomena in Classical Fluids, in Phase Transitions: Cargese 1980, Maurice Levy, Jean-Claude LeGuillou, and Jean Zinn-Justin, eds. (Plenum Publishing Corp., New York).
154. Sengers A.L., J.M.H. Morrison, and G. Chang, 1983, Critical Behaviour in Fluids and Fluid Mixtures, Fluid Phase Equilib. **14**: 19-44.
155. Sengers J.V., and J.M.H.L. Sengers, 1986, Thermodynamic Behavior of Fluids Near the Critical Point, Annual Review of Physical Chemistry **37**: 189-222.
156. Sengers J.V., 1994, in Supercritical Fluids: Fundamentals for Applications, E. Kiran and J. M. H. Levelt Sengers, Eds., Effects of critical Fluctuation on the Thermodynamics and Transport Properties of Supercritical Fluids (Kluwer, Dordrecht), 231.
157. Siggia E.D., B.I. Halperin, and P.C. Hohenberg, 1976, Renormalization-Group Treatment of the Critical Dynamics of the Binary-Fluid and Gas-Liquid Transitions, Phys. Rev. B **13**: 2110.
158. Siggia E.D., 1979, Late stages of spinodal decomposition in binary mixtures, Phys. Rev. A **20**: 595–605.
159. Stanley H.E., 1971, Introduction to phase transitions and critical phenomena, (Clarendon Press, Oxford, New York).
160. Stanley H.E., 1999, Scaling, universality, and renormalization: Three pillars of modern critical phenomena, Rev. Mod. Phys. **71**: S358–S366.

161. Tafa K., S. Puri, D. Kumar, 2001, Kinetics of domain growth in systems with local barriers, Phys. Rev. E **63**(4 Pt 2): 046115.
162. Tanaka T., 1983, Phase transition and critical phenomena, Domb, Academic press.
163. Tanaka T., 1994, Phys. Rev. Lett. **72**: 1702.
164. Thomas and Schmidt, 1963, Journal of Chemical Phys. **39**: 2506.
165. Tokuyama M., and K. Kawasaki, 1984, Statistical–mechanical theory of coarsening of spherical droplets. Physica A **123**: 386.
166. Tong L.S., 1997, Boiling heat transfer and two phase flow, (Taylor & Francis, New York).
167. Traub J.J., 1964, Iterative Methods of the Solution of Equations, Prentice Hall, Englewood Cliffs, New Jersey.
168. Verlet L., and J.J. Weis, 1972, Equilibrium Theory of Simple Liquids, Phys. Rev. A **5**: 939-952.
169. Walter H.U. (Ed.), 1987, Fluid Science and Materila Science in space, European Space Agency, Springer-Verlag, Berlin, Heidelberg.
170. W. R. White, and P. Wiltzius, 1995, al Space Measurement of Structure in Phase Separating Binary Fluid Mixtures, Phys. Rev. Lett. **75**: 3012–3015.
171. Wyczalkowska K., and J.V. Sengers, 1999, Thermodynamic properties of sulfurhexafluoride in the critical region, The Journal of Chemical Physics **111**(4): 1551-1560.
172. Wilkinson R.A., G.A. Zimmerli, H. Hao, M.R. Moldover, R.F. Berg, W.L. Johnson, R.A. Ferrell, and R.W. Gammon, 1988, Equilibration Near the Liquid-Vapor Critical Point in Microgravity, Physical Review E **57**(1): 436-448.
173. Wong N.C., and C.J. Kobler, 1978, Chem. Phys. **69**: 725.
174. Wu M., G. Ahlers, and D.S. Cannell, 1995, Thermally Induced Fluctuations below the Onset of Rayleigh-Bénard Convection, Phys. Rev. Lett. **75**: 1743–1746.
175. Wunenburger R., Y. Garrabos, C. Lecoutre-Chabot, D. Beysens, and J. Hegseth, 2000, Thermalization of a two-phase fluid in low gravity: heat transferred from cold to hot, Phys. Rev. Lett. **84**: 4100 – 4103.
176. Zang A., and C. Davis, 1991, Journal of Fluid Mechanics **230**: 479.
177. Zappoli B., D. Bailly, Y. Garrabos, B. Le Neindre, P. Guenoun, and D. Beysens, 1990, Anomalous heat transport by the piston effect in supercritical fluids under zero gravity, Phys. Rev. A **41**: 2264-2267.

VITA

Ana Oprisan was born in Neamt, Romania. She graduated from "Alexandru Ioan Cuza" University of Iasi, Romania, in 1987. Her first appointment as a middle and high school physics teacher was in Tecuci, Romania. After six years, she moved to a high school in Iasi, Romania, and continued to teach physics for six more years. She took all the required pedagogical and scientific examinations and achieved the highest level of competence in physics teaching at the high school level. Her research thesis for the first degree teaching achievement described the fractal growth processes. She gave talks at scientific meetings at "Al.I.Cuza" University of Iasi, and APS meetings and published in peer review and proceeding at different conferences. In 1999 she received an award for outstanding teaching, research, and scholarly activity.

In 2001 she was admitted to the Master's program in Physics at the University of New Orleans. She received a teaching (2001-2002) and (2005-2006) and a research assistantship from the Physics Department (2002-2004). She was designated to receive an "Outstanding Teaching Award" from the American Association of Physics Teachers, and the "Bill Good Award" in 2002 and 2006, for excellence in research, from the Physics Department at the University of New Orleans. She is a member of the American Physical Society and the American Association of Physics Teachers.

She received her Master of Science from the Department of Physics in May of 2003.